UCLA
UCLA Electronic Theses and Dissertations

Title

Multi-Field/-Scale Interaction of Neoclassical Tearing Modes with Turbulence and Impact on Plasma Confinement

Permalink

https://escholarship.org/uc/item/0m06d5bg

Author

Bardoczi, Laszlo

Publication Date

2017

Peer reviewed|Thesis/dissertation

eScholarship.org Powered by the California Digital Library
University of California

University of California
Los Angeles

Multi-Field/-Scale Interaction of Neoclassical Tearing Modes with Turbulence and Impact on Plasma Confinement

A dissertation submitted in partial satisfaction
of the requirements for the degree
Doctor of Philosophy in Physics

by

László Bardóczi

2017

© Copyright by
László Bardóczi
2017

Abstract of the Dissertation

Multi-Field/-Scale Interaction of
Neoclassical Tearing Modes with Turbulence
and Impact on Plasma Confinement

by

László Bardóczi
Doctor of Philosophy in Physics
University of California, Los Angeles, 2017
Professor Troy A. Carter, Chair

Neoclassical Tearing Modes (NTMs) are a major impediment in the development of operational scenarios of present toroidal fusion devices. The multi-scale and non-linear interaction of NTMs with turbulence has been an active field of theoretical plasma research in the past decade for its role in plasma confinement. However, little to no experimental effort has been devoted to explore this interaction. As part of this thesis, dedicated experiments were conducted utilizing the full complement of the DIII-D turbulence diagnostics to study the effect of NTM on turbulence as well as the effect of turbulence on NTM growth.

The first localized measurements of long and intermediate wavelength turbulent density fluctuations ($\widetilde{n}$) and long wavelength turbulent electron temperature fluctuations ($\widetilde{T}_e$) modified by magnetic islands are presented. These long and intermediate wavelengths correspond to the expected Ion Temperature Gradient (ITG) and Trapped Electron Mode (TEM) scales, respectively.

Two regimes were observed when tracking $\widetilde{n}$ during NTM evolution: (1) small islands are characterized by steep electron temperature (T_e) radial profile and turbulence levels comparable to that of the background; (2) large islands have a flat T_e profile and reduced turbulence level at the O-point. Radially outside of the large island, the T_e profile is steeper and the turbulence level increased compared to the no or small island case.

It was also found that turbulence is reduced in the O-point region compared to the X-point region. This helical structure of turbulence modification leads to a 15% modulation of $\widetilde{n}^2$ as the island rotates in the lab frame and this modulation is nearly in phase with the T_e modulation.

These measurements were also used to determine the turbulence penetration length scale ($L_{\widetilde{n}}$) at the island separatrix and was found that $L_{\widetilde{n}}$ is on the order of the threshold island width for temperature flattening and turbulence reduction to occur at the O-point. This suggests that the physics of island transition could be related to turbulence penetration into the island.

In addition, a novel, anisotropic, non-linear heat transport model of magnetic islands with spatially non-uniform cross-field thermal diffusivity ($\chi_\perp$) was developed. This model was utilized to derive $\chi_\perp$ at the O-point from measured electron temperature data and it was found that $\chi_\perp$ at the O-point is 1 to 2 orders of magnitude smaller than the background plasma transport. As the anomalously large values of $\chi_\perp$ are often attributed to turbulence driven transport, the reduction of $\chi_\perp$ is consistent with the found turbulence reduction at the O-point.

Complementing the experimental results of turbulence-NTM interaction described in this thesis, qualitative comparisons were carried out for the first time to GENE non-linear gyrokinetic turbulence simulations employing static magnetic islands. These simulations qualitatively replicate the measured 2D response of turbulence as well as the observed scaling with island size.

The consequences of the observed NTM-turbulence interaction on the global plasma confinement were studied via analyses of simultaneous changes in NTM amplitude, plasma pro-

files, turbulence, fluxes and confinement. It was found that the global confinement degradation is intimately linked to the turbulence enhancement outside of the island region (induced by the island).

Experimentally observed local turbulence and transport reduction at the O-point, as well as the effect of global confinement decrease was incorporated in the dynamical equation of NTMs, which shows that the NTM growth rate increases when turbulence and gradients are reduced inside the island (right after the transition from small to large island regime).

Additionally, the shrinking of NTM islands due to strong temperature perturbations associated with Edge Localized Modes was observed. Simultaneous increase in turbulence level at the O-point was also observed and the data suggests that this temporal increase of turbulence level at the O-point accelerates NTM recovery after the ELM-crash. This is facilitated via the fast turbulent cross-field transport that leads to a rapid restoration of the flat profile (and bootstrap current perturbation) at the O-point.

Finally, a series of low torque H-mode experiments were carried out to measure the perturbed ion temperature and toroidal flow profiles via CER across slowly rotating islands. Comparison of the observed flow perturbation to the gyrokinetic simulations suggests that large islands develop a vortex like plasma flow circulating around the O-point.

The dissertation of László Bardóczi is approved.

Neal Crocker

Terry L. Rhodes

Marco Velli

Frank Jenko

Troy A. Carter, Committee Chair

University of California, Los Angeles

2017

"I found that the grown-ups had a terrible time, everybody got tired of what he was doing. Klug was the first grown-up whom I met who loved what he was doing, who did not get tired, and who even enjoyed explaining things to me. That I think is when I made up my mind, very firmly, that I wanted to do something that I really did want to do. Not for anyone else's sake, not for what it may lead to, but because of my inherent interest in the subject."

- Edward Teller

Table of Contents

List of Abbreviations

ITER	**I**nternational **T**hermonuclear **E**xperimental **R**eactor
MHD	**M**agneto**h**ydro**d**ynamics
NTM	**N**eoclassical **T**earing **M**ode
ELM	**E**dge **L**ocalised **M**ode
ITG	**I**on **T**emperature **G**radient mode
ETG	**E**lectron **T**emperature **G**radient mode
TEM	**T**rapped **E**lectron **M**ode
ECE	**E**lectron **C**yclotron **E**mmission
FIR	**F**ar **I**nfra**r**ed Scattering
BES	**B**eam **E**mmission **S**pectroscopy
DBS	**D**oppler **B**acks**s**cattering
CECE	**C**orrelation **E**lectron **C**yclotron **E**mmission
ECH	**E**lectron **C**yclotron **H**eating
LFS	**L**ow **F**ield **S**ide
HFS	**H**igh **F**ield **S**ide
LHS	**L**eft **H**and **S**ide
RHS	**R**ight **H**and **S**ide

LIST OF SYMBOLS

a	plasma minor radius	cm
$\mathrm{B_T}$	toroidal magnetic field	T
f	frequency	rad
$\mathrm{I_P}$	plasma current	MA
$\mathrm{j_{bs}}$	bootstrap current	A
m	poloidal mode number	
n	toroidal mode number	
n	density	10^{19} $\mathrm{m^{-3}}$
$\widetilde{\mathrm{n}}$	turbulent density fluctuation	10^{19} $\mathrm{m^{-3}}$
$\overline{\widetilde{\mathrm{n}}}^2$	turbulent density fluctuation power without island	10^{38} $\mathrm{m^{-6}}$
$\Delta\widetilde{\mathrm{n}}^2$	relative change of turbulent density fluctuation power (relative to $\overline{\widetilde{\mathrm{n}}}^2$)	
$\Delta\widetilde{\mathrm{n}}_0^2$	relative change of rotation averaged turbulent density fluctuation power (relative to $\overline{\widetilde{\mathrm{n}}}^2$)	
$\Delta\widetilde{\mathrm{n}}_1^2$	relative modulation amplitude of turbulent density fluctuation power (relative to $\Delta\widetilde{\mathrm{n}}_0^2$)	
P	power	MW
R	major radius coordinate	cm
$\mathrm{R_\circ}$	major radius of magnetic axis	cm
R_s	major radius of resonant surface	cm
r	minor radius coordinate	cm
r_s	minor radius of resonant surface	cm
$\mathrm{T_e}$	electron temperature	eV

$\widetilde{T}_e$	turbulent electron temperature fluctuation	eV
$\overline{\widetilde{T}_e}^2$	turbulent electron temperature fluctuation power without island	eV^2
$\Delta\widetilde{T}^2_{e,0}$	relative change of rotation averaged turbulent electron temperature fluctuation power (relative to $\overline{\widetilde{T}_e}^2$)	
$\Delta\widetilde{T}^2_{e,1}$	relative modulation amplitude of turbulent temperature fluctuation power (relative to $\overline{\widetilde{T}_e}^2$)	
T_i	ion temperature	eV
$\widetilde{T}_i$	turbulent ion temperature fluctuation	eV
W	island full width	cm
w	island half width	cm
W_c	scale island width	cm
W_{conf}	island width at which confinement degradation is effective	cm
W_{SAT}	saturated island width	cm
W_b	island boundary layer	cm
W_t	threshold island width	cm
z	vertical coordinate	cm
β	plasma beta	
ϕ	toroidal angle	rad
τ_e	energy confinement time	ms
θ	poloidal angle	rad
ξ	helical angle	rad
ω	angular frequency	rad

List of Figures

Acknowledgments

I would like to express my appreciation to my advisor professor Dr. Troy A. Carter and to Dr. Terry L. Rhodes with whom I worked the most during my graduate studies. I would like to thank you for giving me the option to come to and work on DIII-D, the best diagnosed fusion plasma experiment in the world, which I consider as by far the greatest opportunity of my life to grow and become an independent and impactful scientist. Your advice on both research and career have been invaluable and helped me to make my decisions.

Special thanks Dr. A. Bañón Navarro for the collaboration with gyrokinetic simulation studies and professor Dr. Frank Jenko for providing computation resources for these simulations. Thanks to the DIII-D leadership for supporting my experiments by providing the tokamak and the full complement of its diagnostic resources. This thesis was supported by U.S. DOE under Cooperative Agreement DE-FC02-04ER54698.

I thank Dr. Neal Crocker for helpful discussions about numerical mathematical analysis techniques. Thanks to Dr. Tony A. Peebles for mentoring me during the early stage of my research. Thanks to Dr. Choongki Sung for CECE measurements and mentoring me in the CECE lab, Dr. Colin Crystal for CER measurements as well as being the beam coordinator for my experiments and helping me with CER analysis, Dr. Brian Grierson for guidance in transport analysis, Dr. Rob La Haye for discussing NTM physics as well as being directly involved in the slowly rotating NTM experiments, Dr. Craig Petty for being the ECH coordinator as well as for NTM physics discussions and Dr. George McKee for BES measurements. I thank professors Dr. Christoph Niemann, Dr. Marco Velli and Dr. Frank Jenko for serving as my committee members.

Special thanks to my mom and dad for always listening to my frustrations and giving me wise advice during critical times when right decisions were beyond my good judgment. Here, I thank them in Hungarian: *Köszönöm a jó nevelést, mert ez a legtöbb amit egy szülő a gyerekének adhat. Édesanyám, neked külön köszönöm, hogy számíthattam rád.*

Édesapám, neked pedig, hogy türelmesen végighallgattál és segítettél előre lépni, amikor borúsnak láttam a világot; illetve döntést hozni, amikor pillanatnyi nehézségek közepette szükség volt bölcs és megbízható tanácsra.

I am grateful to my wife, Andrea, for her support, patience, humor, love and good food that helped me in devoting my best to this thesis.

Finally, I thank God for letting me through all the difficulties. The 4.5 years of graduate studies as a UCLA student were by far the most difficult *and* the most rewarding times of my life. I have grown professionally and personally the most during this time and I consider it as the most exciting chapter of my life so far.

Vita

2007–2010 B.S. in Physics, Budapest University of Technology and Economics, Budapest, Hungary. Thesis: "Study of turbulence and zonal flows in tokamak plasmas".

2008–2012 Research Assistant, Széchenyi István University, Győr, Hungary. Built a two-dimensional fluid turbulence experiment. Studied turbulence, zonal flows and transport.

2008–2012 Research Assistant, KFKI Research Institute, Budapest, Hungary. TDE development, study of turbulence and GAMs at TEXTOR, comparison with simulations.

2010–2012 M.S. in Physics, Budapest University of Technology and Economics, Budapest, Hungary. Thesis: "Study of turbulence and zonal flows in fusion plasmas"

2012–present Ph.D. candidate in Physics, UCLA, Los Angeles, California, USA
(2012-2014) Teaching Assistant, UCLA, Los Angeles, California, USA
(2014–present)Teaching Assistant, UCLA, Los Angeles, California USA

Publications

1. L. Bardóczi, T. L. Rhodes, T. A. Carter, A. Bañón-Navarro, W. A. Peebles, F. Jenko and G. McKee, *"Modulation of core turbulent density fluctuations by large-scale neoclassical tearing mode islands in the DIII-D tokamak"*
Physical Review Letters **116** (21) 215001 (2016) [DOI]

2. L Bardóczi, T. L. Rhodes, T. A. Carter, N. A. Crocker, W. A. Peebles and B. A. Grierson, *"Non-perturbative measurement of cross-field thermal diffusivity reduction at the O-point of 2/1 neoclassical tearing mode islands in the DIII-D tokamak"* ***Physics of Plasmas***, **23** (5) 052507 (2016) [DOI]

3. L. Bardóczi, T. L. Rhodes, A. Bañón-Navarro, C. Sung, T. A. Carter, R. J. La Haye, C. Petty, C. Crystal and F. Jenko, *"Multi-field/-scale interactions of turbulence with Neoclassical Tearing Mode magnetic islands in the DIII-D tokamak"* ***Physics of Plasmas***, **24** 056106 (2017) [DOI] (invited)

4. L. Bardóczi, T. L. Rhodes, T. A. Carter, R. J. La Haye and G. McKee, *"Shrinking of core Neoclassical Tearing Mode magnetic islands due to Edge Localized Modes and the role of low-k turbulence in island recovery in DIII-D"* ***Physics of Plasmas*** (submitted)

5. A. Bañón-Navarro, L. Bardóczi, F. Jenko, T. A. Carter and T. L. Rhodes, *"Effect of magnetic islands on profiles, flows, turbulence and transport in nonlinear gyrokinetic simulations"* ***Plasma Physics and Controlled Fusion***, **59** (3) 034004 (2017) [DOI]

6. L. Bardóczi, A. Bencze, M. Berta and L. Schmitz, *"Experimental confirmation of self-regulating turbulence paradigm in two-dimensional spectral condensation"* ***Physical Review E***, **90** (6) 063103 (2014) [DOI]

7. L. Bardóczi, M. Berta and A. Bencze, *"Inverse energy cascade and turbulent transport in a quasi-two-dimensional magnetized electrolyte system: An experimental study"* ***Physical Review E***, **85** (5) 056315 (2012) [DOI]

8. S. Zoletnik, L. Bardóczi, A. Kramer-Flecken, Y. Xu, I. Shesterikov, S. Soldatov, G. Anda, D. Dunai, G. Petravich and the TEXTOR Team, *"Methods for the detection of Zonal Flows using one-point and two-point turbulence measurements"* ***Plasma Physics and Controlled Fusion***, **54** (6) 065007 (2012) [DOI]

CHAPTER 1

Introduction

1.1 Motivation

In a fusion power plant, the energy output increases with plasma pressure (p), while the cost of operation increases with magnetic field (B). Therefore, to make commercial fusion viable, one must maximize the plasma beta ($\beta \propto$ p/B^2 $\propto$ a/B$^2\nabla$p, where a is the plasma minor radius and ∇p is the pressure gradient). Neoclassical Tearing Modes (NTM) are large-scale resistive magnetohydrodynamic (MHD) instabilities that form magnetic islands across the nested flux surfaces of tokamaks. NTMs are destabilized by the neoclassical bootstrap current, which is proportional to ∇p. Therefore, NTMs are often unstable in high β tokamak plasmas. In particular, the $m = 2$, $n = 1$ NTM is a major impediment in the development of operational scenarios in present and future toroidal fusion devices as it often degrades confinement and can lead to plasma termination [8, 9]. The multi-scale interaction of large-scale MHD modes with micro-turbulence has been found to play an important role in transport regulation in magnetized plasmas [10] and fluids [11–13] and is suspected to be a key ingredient of the low-to-high confinement mode transition [14]. Magnetic island interaction with plasma turbulence has been observed in simulations [6, 15–29], but experimental observations have been limited so far [30–32]. Improved understanding of NTM physics and interaction with turbulence can lead to improved control of NTMs and plasma performance. Therefore, it can have important implications for future fusion devices, in particular for the International Thermonuclear Experimental Reactor (ITER).

1.2 Tokamaks

A tokamak is a toroidal magnetic device that uses a strong helical magnetic field to confine a plasma. The word "tokamak" is a Russian acronym of "toroidal'naya kamera s magnitnymi katushkami", meaning toroidal chamber with magnetic coils. A schematic view of a tokamak is shown in Figure 1.1.

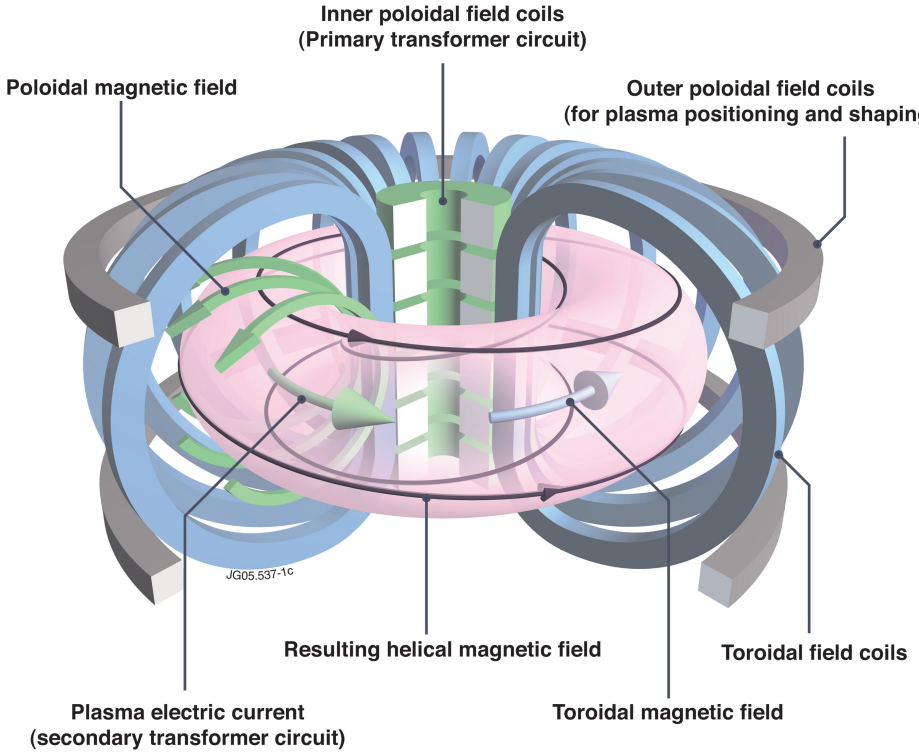

Figure 1.1: Schematic view of a tokamak [1].

The helical magnetic field results from the combination of (i) the toroidal field of currents driven externally in the toroidal field coils and (ii) the poloidal field of the internal toroidal plasma current. The poloidal field coils are used to improve the confinement quality through plasma shaping. A toroidal vacuum chamber isolates the outside air from the plasma (not shown). The plasma is created from injected neutral gas (usually hydrogen or helium) via a large electric field arising from a sudden change of an external transformer current (not shown). Next, auxiliary heating methods are employed (e.g. neutral beams and electron cyclotron waves) to achieve a target plasma.

1.3 Micro-instabilities and transport

The theory of collisional transport in tokamaks has been well-developed and is called neoclassical transport theory [33]. Experimentally measured diffusivities are, however, typically 1 to 2 orders of magnitude larger than neoclassical predictions [34, 35] and therefore, the transport in tokamaks is called "anomalous". It is widely accepted that the anomalous component of the transport is caused by turbulent gyroradius-scale micro-instabilities [36, 37]. Mostly, these are non-linearly interacting drift waves and curvature driven modes. Both are driven by the pressure gradient and are dominantly localized in the low field side, see Fig. 1.2. These instabilities result in small (1%) fluctuations in the electrostatic potential ($\widetilde{\phi}$), density, and temperature, which can lead to heat and particle transport across the nested flux surfaces of tokamaks. Neoclassical theory

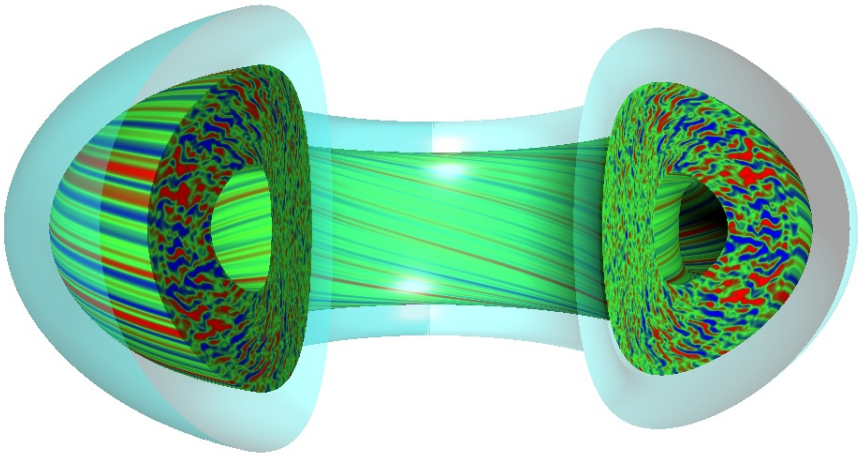

Figure 1.2: Turbulent $\widetilde{\phi}$ in GYRO gyrokinetic simulation [2].

predicts decreasing transport with increasing heating power, however, experiments show the opposite [38]. This is a strong indication that the underlying physics of the transport mechanism is not dominated by collisional transport. Further, the fact that plasma profiles often adopt about the same shape, regardless of the heating profiles, shows that instabilities are able to regulate the profiles. Finally, in the low-to-high confinement transition [39] the abrupt increase of confinement with heating power is accompanied by a significant decrease of core turbulence [40], which is a clear indication that a major fraction

of the anomalous transport is driven by turbulence.

The most common types of micro-instabilities leading to broadband turbulence in tokamaks are the ITG (ion temperature gradient) mode, the TEM (trapped electron mode) and the ETG (electron temperature gradient) mode. These instabilities can couple interchange and drift wave physics. In principle, these modes can be distinguished via their wavenumber and direction of propagation in the E × B plasma frame. However, simulations show that they are not necessarily always distinct: e.g. the TEM can smoothly turn into the ETG mode as a function of wavenumber.

1.3.1 Curvature driven modes

The curvature driven or interchange modes can be purely growing modes without propagation. For a simple mathematical description of the interchange instability, consider a slab perpendicular to the background magnetic field, as shown in Fig. 1.3.

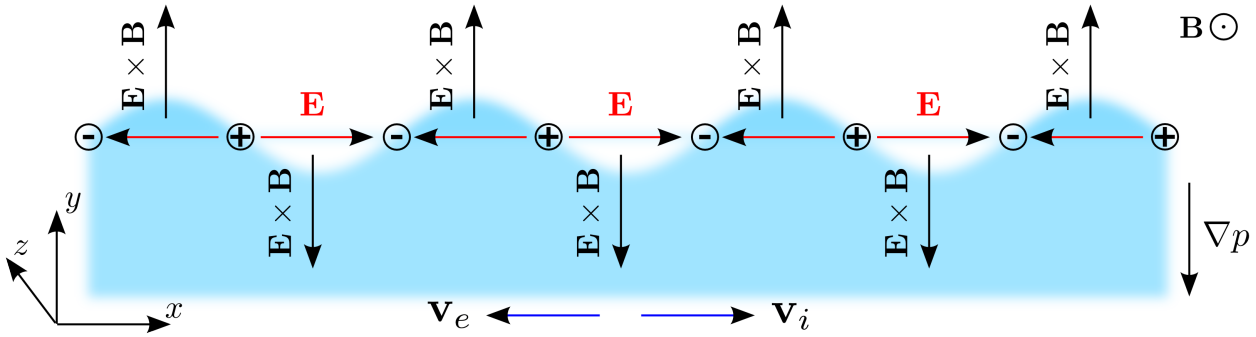

Figure 1.3: Scheme of an interchange mode in a plasma.

Assume a background ∇p perpendicular to B, finite ∇B and field curvature. The combined drift velocity due to the inhomogeneous magnetic field is:

$$\mathrm{v}_D = \mathrm{v}_{\nabla \mathrm{B}} + \mathrm{v}_{\mathrm{R}_c} = \frac{m}{q}\left(\mathrm{v}_{\parallel}^2 + \mathrm{v}_{\perp}^2/2\right)\frac{\mathrm{R}_c \times \mathrm{B}}{\mathrm{B}^2}. \tag{1.1}$$

Here $v_{\nabla B}$ and v_{R_c} are the ∇B and curvature drift velocities, respectively. This combined drift has the opposite sign for electrons and ions. When an initial pressure perturbation is present, this drift leads to a net charge separation and concomitant electric field perturbation (as shown in Fig. 1.3). This electric field leads to a secondary drift, the $E \times B$ drift. The direction of the $E \times B$ drift is such that it amplifies the original ∇p perturbation in the LFS (where ∇p is parallel with ∇B, "unfavorable curvature region") and becomes linearly unstable. On the other hand, the $E \times B$ drift suppresses the initial ∇p perturbation in the HFS (where ∇p is antiparallel with ∇B, "favorable curvature region").

Interchange modes are 2-dimensional, with $k_{\parallel} = 0$. Parallel dynamics becomes important when the unfavorable and favorable curvature regions are connected by the field lines, as is the case in tokamaks. This introduces variations along the field lines, and gives rise, therefore, to 3-dimensional dynamics with $k_{\parallel} > 0$.

Finally, note that this mode has a hydrodynamic version known as the gravitational Rayleigh-Taylor instability. In that case, a heavier fluid is supported against gravity by a lighter fluid. This configuration is unstable to small perturbation; a ripple of the boundary leads to mixing (interchange) of the two fluid layers. An example of a simulation of the Rayleigh-Taylor instability is shown in Fig. 1.4.

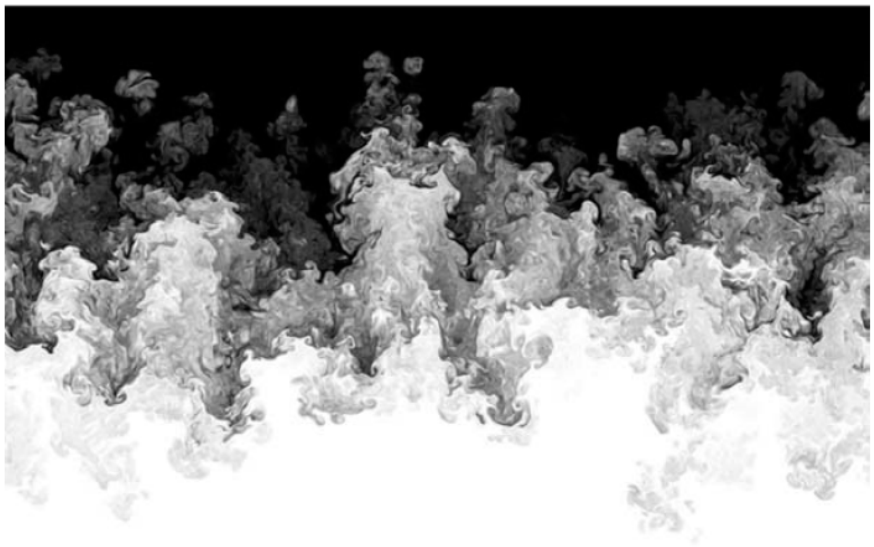

Figure 1.4: Large eddy simulation of the Rayleigh-Taylor instability [3].

1.3.2 Drift waves

Drift waves are intrinsically 3-dimensional instabilities with finite parallel wavenumber. For a simple mathematical description, consider again a plasma slab perpendicular to the background B field [Fig. 1.5]. Assume a uniform background magnetic field in the z-direction, a background pressure gradient in the y-direction and an initial density perturbation. The small electron mass and the fast thermal motion of electrons yields a relation between the electron density and potential, also called as Boltzmannn relation:

$$\frac{\widetilde{\mathrm{n}}}{n} = \mathrm{e}^{\frac{e\phi}{\mathrm{k_B T_e}}} - 1 \approx \frac{e\phi}{\mathrm{k_B T_e}} \tag{1.2}$$

This means that in phase with the density perturbation, an electrostatic potential perturbation develops. The associated E × B drift modifies the phase of this sinusoidal perturbation such that the perturbation effectively shifts in the x-direction. This perturbation, therefore, leads to a wave, propagating in the direction perpendicular to B and ∇p. This wave is called drift wave, and it propagates with the diamagnetic drift velocity $\mathrm{v_{dia}}$.

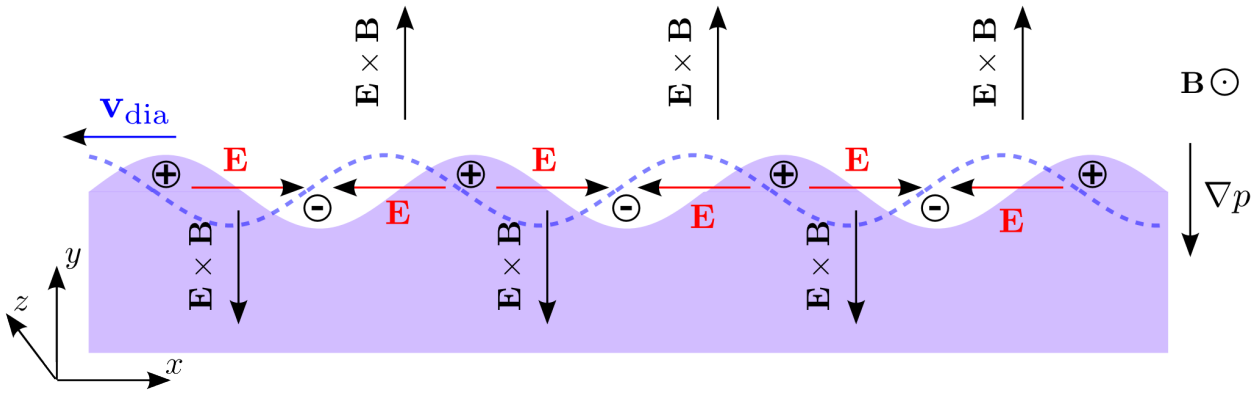

Figure 1.5: Scheme of a drift wave in a plasma.

1.3.3 Ion temperature gradient modes

The ITG mode [41–44] is thought to be a major cause of radial heat and particle transport in tokamaks. ITG modes have low wavenumber ($k_\theta \rho_s < 1$) and propagate in the ion

diamagnetic direction in the plasma frame. In tokamaks, broadband turbulent $\widetilde{n}$ associated with ITG can be measured e.g. locally via Beam Emission Spectroscopy and non-locally via Far Infrared scattering. $\widetilde{T}_e$ in this wavenumber range can be measured via the Correlation Electron Cyclotron Emission diagnostic. ITG modes have a critical gradient [44], below which these modes are stable. The best understood mechanism for the non-linear saturation of ITG provided by self-generated, poloidally and toroidally symmetric potential structures, called zonal flows [10, 14, 45–49].

1.3.4 Trapped electron modes

Toroidal geometry allows the growth of a broad spectrum of modes, which are otherwise stable in e.g. linear devices. One of these modes, the TEM [48, 50, 51] is related to the trapped particle population. This mode leads to turbulence and transport in intermediate wavelengths ($k_\theta \rho_s \lesssim 1$) and has a critical gradient nature. In most cases, TEM is predicted to propagate in the electron diamagnetic direction. TEM-scale $\widetilde{n}$ can be routinely measured via Doppler Backscattering.

1.3.5 Electron temperature gradient modes

The ETG instability [52, 53] leads to fluctuations at electron scales ($k_\theta \rho_s \approx 10$). The ETG mode can be considered isomorphic to the ITG mode. Ions are treated via the Boltzmann relation for the former and electrons are for the latter. ETG modes are also expected to have a critical gradient and have been argued to play an important role in electron heat transport [54].

1.4 Classical tearing modes

Tearing modes in tokamaks are driven by the gradient of the equilibrium plasma current [37]. This instability leads to the tearing and rejoining of the magnetic field lines as a consequence of finite resistivity (hence the name). The new topological objects, formed by the reconnection, are characterized by a confined region of nested flux surfaces, called magnetic islands [Fig. 1.6 (a)].

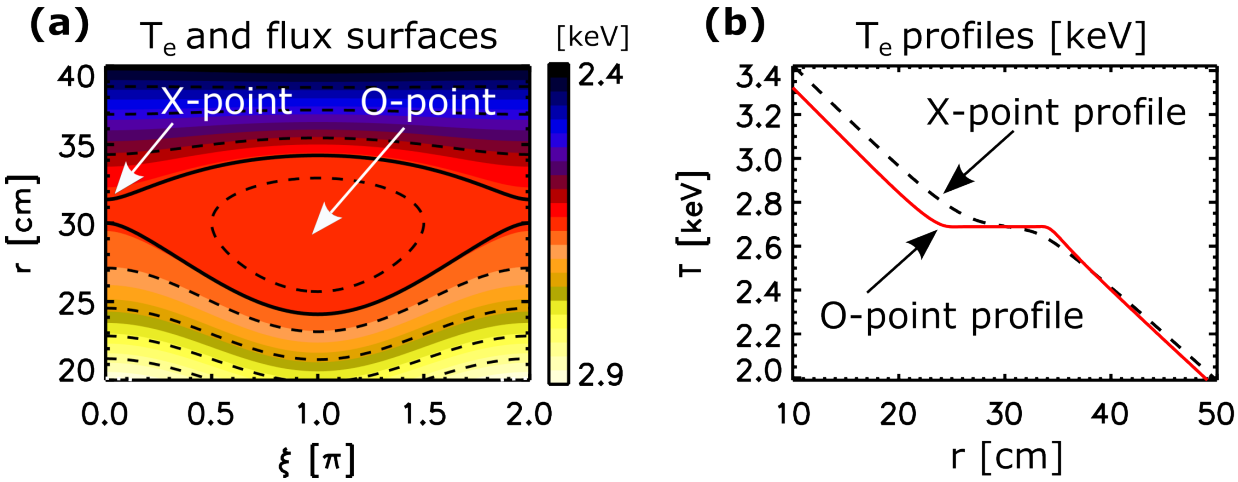

Figure 1.6: (a) Flux surfaces of a magnetic island ($\Omega(r,\xi)$, defined by equation 1.3) and contours of $T_e(\xi,r)$ (solution of equation 1.4). (b) T_e profiles across the O-point and X-point (at $\xi=\pi$ and $\xi=2\pi$, respectively).

1.4.1 Magnetic island structures

Magnetic islands are 3D helical structures having m and n poloidal and toroidal mode numbers, respectively, and are located on rational q surfaces where $q=m/n$. Field lines on rational q surfaces are characterized by a constant pitch (or rotational transform) $\iota=2\pi/q$, where $q=d\phi/d\theta$ (ϕ and θ are the toroidal and poloidal angle, respectively). In the large aspect ratio limit, shift along a field line is a symmetry transformation. This symmetry allows to reduce the poloidal and toroidal coordinates to a single helical coordinate $\xi=m\theta-n\phi$. ξ is perpendicular to the field lines (on the rational surface), m and n are the poloidal and toroidal transits along a field line. The perturbed magnetic flux surfaces of

the island are mapped out by the contours of the normalized flux surface label Ω. Due to the symmetry along the field line, Ω is a function of ξ and r only:

$$\Omega = \frac{8(r-r_s)^2}{\mathrm{W}} + \left(\frac{2A(r-r_s)}{\mathrm{W}} + 1\right)\cos(\xi) \tag{1.3}$$

Here W is the island full width, r_s is the minor radius coordinate of the rational surface where $q = m/n$ and A is a radial asymmetry parameter [55]. The island in Fig. 1.6 (a) is shown in the (ξ, r) plane. In the direction perpendicular to r and ξ, the island is symmetric. The X-points are located at $\xi = 2k\pi$ and the O-points are located at $\xi = (2k+1)\pi$, where k is an integer. The symmetry along the field line extends to O-point into an O-line, with the rotational transform $\iota = 2\pi n/m$ (same that of the local unperturbed field line), see the O-lines of islands with different m/n numbers in Fig. 1.7.

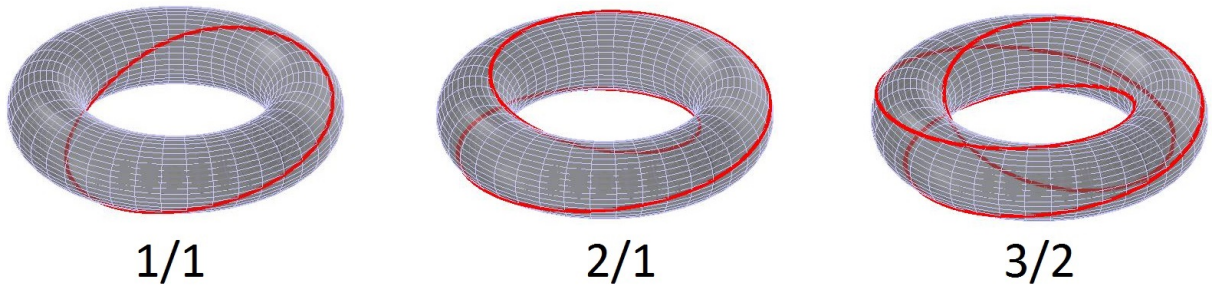

Figure 1.7: Cartoon of 3D helical winding of the magnetic island O-line with different m/n mode numbers.

The reconnection takes place in the X-point region from where the plasma flows toward the O-point region and the island grows until the stabilizing effect of the field line bending leads to saturation.

1.4.2 Theory of heat transport across the islands

Due to the change of field line topology and concomitant changes in heat and particle transport, temperature and pressure perturbations associated with tearing modes also exhibit a 3D helical structure. Heat transport across the island in tokamaks was first

modeled [56] via anisotropic diffusion:

$$\chi_{\parallel}\nabla_{\parallel}^{2}\mathrm{T_e} + \chi_{\perp}\nabla_{\perp}^{2}\mathrm{T_e} = 0 \tag{1.4}$$

Here $\chi_{\perp}$ and $\chi_{\parallel}$ are the perpendicular and parallel electron thermal diffusivities, respectively, with a typical ratio of $\chi_{\perp}/\chi_{\parallel} \approx 10^{-6} - 10^{-8}$. Example numerical solution of the $\mathrm{T_e}(\xi, r)$ contour is shown in Fig. 1.6 (a) and profiles across the O-point and X-point in Fig. 1.6 (b). In this example, $\mathrm{T_e}$ is flat in the O-point region due to the field line structure and fast parallel transport inside the island. Analytic solutions [56] were calculated assuming that $\chi_{\perp}$ is spatially uniform and independent both of W and $\nabla\mathrm{T_e}$ for mathematical simplicity. This assumption allowed the derivation of a critical island width $\mathrm{W_c} = (\chi_{\perp}/\chi_{\perp})^{1/4}\sqrt{\mathrm{R_o L_q}/n}$ ($\mathrm{R_o}$ is the plasma major radius and $\mathrm{L_q}$ is the magnetic shear length at $q = m/n$), which has two fold physical meaning in this theory:

1. The flattening effect of the parallel transport and the gradient restoring effect of the perpendicular transport compete with each other. The effectiveness of the parallel transport depends on the connection length, which is shorter in the O-point region when the islands are larger. This gives rise to a critical island width required for temperature flattening to occur.

2. The connection length diverges as approaching the separatrix from the O-point. This gives rise to a boundary layer, where gradients are maintained and has a width of $\mathrm{W_c}/2$. Essentially, this is the region where perpendicular flux is converted into parallel flux inside the island. This effectively reduces the flat region around the O-point.

Note that $\chi_{\perp}$ itself can depend on turbulence fluctuation levels, which are sensitive to the local gradients. This gives rise to $\chi_{\perp} = \chi_{\perp}(\nabla\mathrm{T})$, which turns the above model (equation 1.4) into a nonlinear partial differential equation. This nonlinear model was developed [Chapter 3] and tested against DIII-D experiments [Chapter 4] as part of this thesis and resulted in a publication in Physics of Plasmas [7].

1.5 Bootstrap current

In a tokamak, particles possessing less then a certain parallel energy are trapped on the LFS (Low Field Side), while particles having higher energy access the HFS (High Field Side). These are called trapped and passing particles, respectively. Trapped particles move on banana orbits, which, together with the background pressure gradient gives rise to a current, called banana current [Fig. 1.8 (left)].

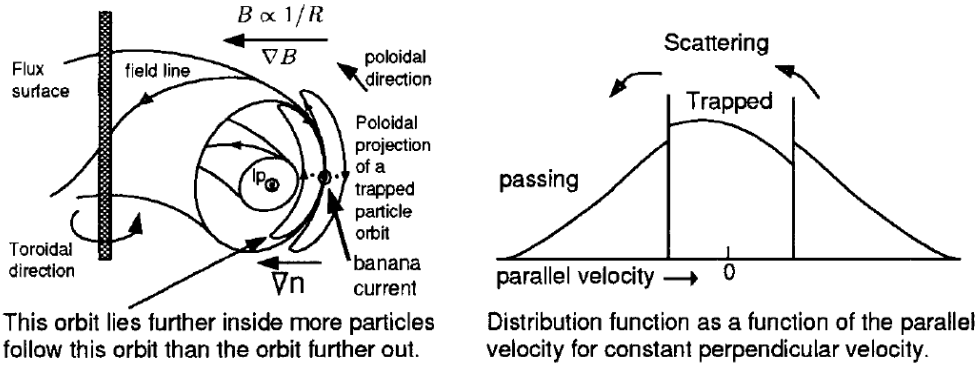

Figure 1.8: The banana current driven by density gradient [4].

Moreover, due to the finite radial width of the banana orbit, the trapped particles are effectively shifted radially outward by about the width of the banana orbit. Due to the background density gradient, this shift leads to an increase of the trapped particle density at any location. The increase in trapped particle population would lead to a discontinuity in the distribution function at the boundary of trapped and passing particles [Fig. 1.8 (right)]. This discontinuity is prevented by collisions between passing and trapped particles but leads to a shift of the full distribution function. This shift is in the opposite direction for electrons and ions, giving rise to a current, called the neoclassical bootstrap current (j_{BS}) [4].

The term neoclassical refers to the fact that this current arises in toroidal geometry (due to trapping of particles). j_{BS} is proportional to the background pressure gradient and also depends on collisionality. Also note that a perturbation of the pressure profile therefore leads to a perturbation of j_{BS} and concomitant magnetic field perturbation which has an

effect on the tearing mode growth [Section 1.6].

1.6 Neoclassical Tearing modes

The flattening of the pressure profile at the O-point leads to a bootstrap current perturbation [57] that reinforces the island. Magnetic islands destabilized by the neoclassical bootstrap current are called NTMs. The modified Rutherford equation [58] (MRE) is often used to study the evolution of the NTM, the simplest form of which (including neoclassical effects), reads:

$$\frac{\mathrm{dW}(t)}{\mathrm{d}t} = \frac{\eta}{\mu_\circ}\left(\Delta' + \mathrm{D_{NC}}\frac{\mathrm{W}(t)}{\mathrm{W_c^2} + \mathrm{W}^2(t)}\right) \tag{1.5}$$

The first term on the RHS describes the classical tearing mode stability, while the second term is the destabilizing bootstrap current term, giving rise to the NTMs. Examples of the solution are shown in Fig. 1.9. Notice that the growth rate is negative when the island width is smaller then a critical island width, therefore a seed island must be generated for the instability to grow. This means that NTMs are linearly stable, non-linearly unstable MHD modes. After the island is generated, it grows until reaches a saturated island width. The growth is faster, the critical island width is smaller and the saturated island width is larger when β is higher in the plasma. Also, there is a critical β, below which NTMs are stable. In fact, NTMs are typically unstable in high-β H-mode discharges. In equation 1.5, η and $\mu_\circ$ are the plasma resistivity and the vacuum permeability, respectively. Δ' is the linear stability parameter [37] and $\mathrm{D_{NC}} = \alpha_1(\nabla_\perp p|_{\text{X-point}} - \nabla_\perp p|_{\text{O-point}})$ is the neoclassical drive proportional to the "missing" pressure gradient at the O-point. $\nabla_\perp p|_{\text{X-point}}$ and $\nabla_\perp p|_{\text{O-point}}$ are the pressure gradient at the X-point and at the O-point, respecively. The numerical coefficient is $\alpha_1 = -2\sqrt{\varepsilon_{\mathrm{TR}}}\mu_\circ \mathrm{L_q}/(\mathrm{B_\theta^2 L_\circ})$, where $\varepsilon_{\mathrm{TR}}$ is the trapped electron fraction and B_θ is the poloidal magnetic field, $\mathrm{L_q}$ is the magnetic field shear length and $\mathrm{L}_\circ$ is the parallel wavelength of the mode.

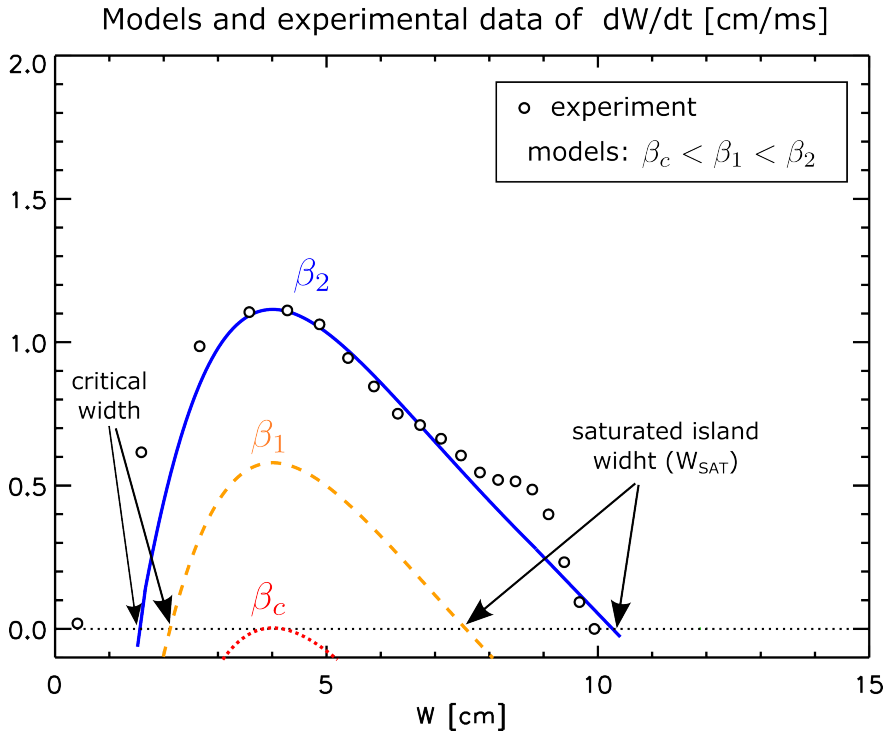

Figure 1.9: Solutions of the modified Rutherford equation (equation 1.5) and experimental data from DIII-D.

This model has been tested against experiments and was found to reasonably agree with observations [7, 59] as also shown in Fig. 1.9 and will be discussed in more depth in Chapter 7. However, notice that turbulent transport enters the MRE via $W_c \propto \chi_\perp^{1/4}$. As mentioned in Section 1.4, finite cross-field transport leads to a boundary layer inside the island, where gradients are partially maintained. This effectively reduces the width of the flat spot and therefore the bootstrap current perturbation which has an impact on the NTM growth.

As part of this thesis work, this model was used to study the effect of turbulence on the NTM growth in Chapter 7.

1.7 Gyrokinetic turbulence simulations with magnetic islands

NTM interaction with plasma turbulence and potential implications on NTM stability has been an active field of theoretical research [6, 15–29] in the past decade. The most complete simulations are achieved via the gyrokinetic approach, where the effect of static magnetic islands has been studied on ITG turbulence [6, 21, 22, 26]. The delta-f approximation is used, in which the distribution function is written as the sum of a Maxwellian background (F) and a perturbation f. The equilibrium is:

$$F = \frac{n}{\pi^{3/2} v_{th}^3} exp\left(-\frac{v_\parallel^2 + 2\mu B/m}{v_{th}^2}\right) \tag{1.6}$$

and the equation prescribing the evolution of f is:

$$\frac{\partial g}{\partial t} + (v_\parallel \mathbf{b} + \mathrm{v}_D)\cdot\nabla f + \mathbf{v}_\chi \cdot \nabla g - \frac{\mu B}{m}\frac{\mathbf{B}\cdot\nabla B}{B^2}\frac{\partial f}{\partial v_\parallel} = S. \tag{1.7}$$

Here μ is the magnetic moment, $v_\parallel$ is the parallel velocity, B is the magnetic field magnitude, m and Z are the particle mass and charge number, respectively. The function $g = f + (Ze/T)v_\parallel \langle A_\parallel \rangle$ contains the parallel component of the vector potential $A_\parallel$. S is the source term and is determined from the equilibrium. The velocities are: (i) motion parallel to the unperturbed, background magnetic field ($v_\parallel \mathbf{b}$), (ii) drift due to inhomogeneous field (v_D) and (iii) motion due to the perturbed electromagnetic field (v_χ). The effect of the island enters the gyrokinetic equation through v_χ, which is a combination of the $\mathbf{E}\times\mathbf{B}$ velocity and the motion along the perturbed magnetic field:

$$\mathrm{v}_\chi = \frac{\mathbf{b}\times\nabla\chi}{B}, \tag{1.8}$$

where $\chi = \langle\phi\rangle - v_\parallel\langle A_\parallel\rangle$. The electrostatic potential ϕ is calculated from the gyrokinetic Poisson equation. Ampére's law is not solved for as the island is not evolved in the

simulation. The perturbed vector potential is simply:

$$A_{\parallel} = A_{\parallel}^{\circ} \mathrm{e}^{i\xi}, \tag{1.9}$$

where $A_{\parallel}^{\circ}$ is the amplitude of the perturbation ($A_{\parallel} \propto W^2$) and $\xi = m\theta - n\phi$ is the helical angle (m and n are the poloidal and toroidal mode numbers of the magnetic island structure).

An example of the instantaneous turbulent density and temperature fluctuations ($\widetilde{\mathrm{n}}$ and $\widetilde{\mathrm{T}}_{\mathrm{e}}$, respectively) across an island is shown in Fig. 1.10

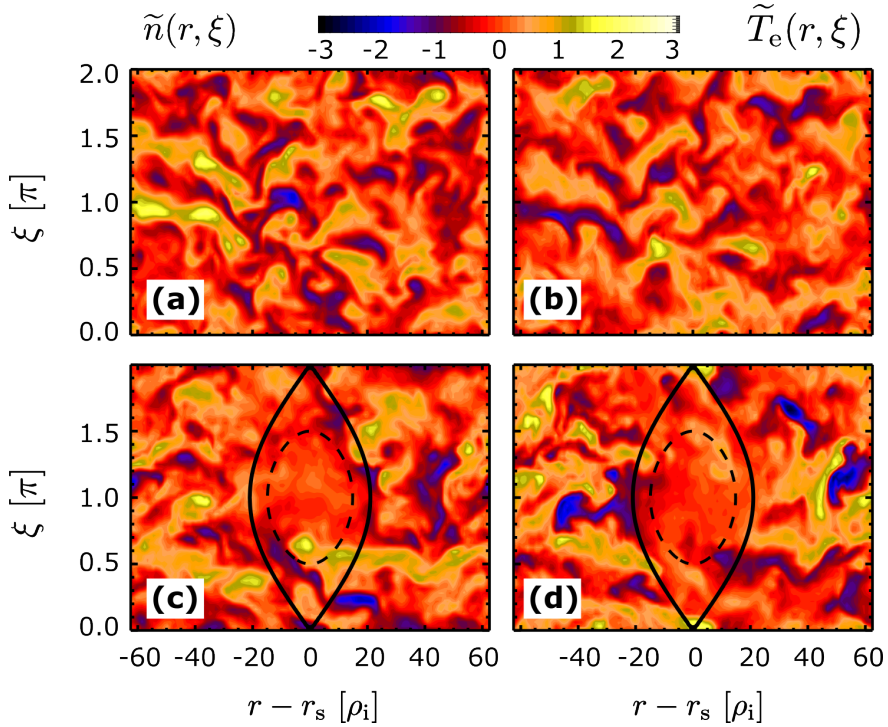

Figure 1.10: GENE gyrokinetic turbulence simulations in 3-dimensional, toroidal geometry: (a,b) instantaneous $\widetilde{\mathrm{n}}$ and $\widetilde{\mathrm{T}}_{\mathrm{e}}$, respectively, (without an island); (c,d) instantaneous $\widetilde{\mathrm{n}}$ and $\widetilde{\mathrm{T}}_{\mathrm{e}}$ with a static island of W = $42\rho_i$.

In Chapter 6, the analysis of non-linear gyrokinetic turbulence simulations with magnetic islands is presented. These simulations were conducted by A. Bañón Navarro of UCLA using the GENE code [52]. The static islands were implemented as in previous GKW (Gyrokinetics at Warwick) simulations (by W. A. Hornsby and coworkers) as described above [60]. The analysis (calculations, figures, etc.) presented in this thesis is my own

original work. This work resulted in a paper in Plasma Physics and Controlled Fusion [6].

1.8 Heat transport measurements across islands

Experimentally, $\chi_\perp$ is often obtained from one-dimensional power balance calculations, e.g. TRANSP [61], where the $m = n = 0$ symmetry of the plasma profiles is a major assumption (m/n are the poloidal/toroidal mode numbers) and the helical perturbation imposed by the island is not taken into account. As the major part of the radial heat flux is driven by parallel transport in the island region, these methods cannot estimate $\chi_\perp$ at the O-point.

Heat/cold pulse propagation experiments [62, 63] have found the reduction of the electron $\chi_\perp$ by about 1 order of magnitude at the O-point of static islands generated by resonant magnetic perturbation. Assuming that the cooling/heating of the island is dominated by the cross-surface heat flux inside the island, a one-dimensional diffusion model was solved and fitted [62, 63] to the transient experimental electron temperature $T_e(t)$. However, these methods infer $\chi_\perp$ reduction at the O-point of externally generated non-rotating magnetic islands (not NTMs) in non-stationary thermal conditions. Interestingly, similar result was derived for the ion $\chi_\perp$ at the O-point of a cooling, locked, tearing driven island after high to low confinement back transition [64].

In stationary thermal conditions $\chi_\parallel$ is important in the island region, hence two-dimensional modeling of the transport is required. In a number of experimental studies [65–69] $\chi_\perp$ was obtained by fitting the numerical solutions of equation 1.4 to experimental T_e data. However, due to the unknown properties of $\chi_\perp$ across the island spatially uniform $\chi_\perp$ was assumed which contradicts the simulations reporting turbulence and concomitant transport reduction at the O-point. The reduction of $\chi_\perp$ at the O-point of NTM islands in stationary thermal conditions has not been confirmed by experiments before.

In order to determine $\chi_\perp$ at the O-point in stationary thermal conditions, a new model was developed [Section 3] and compared to experimental data [Chapter 4] as part of this thesis work. This study found that $\chi_\perp$ is reduced at the O-point by 1-2 orders of magnitude compared to the background and has been published in Physics of Plasmas [7].

1.9 Turbulence and flow measurements across islands

Line-integrated Far Infrared Scattering measurements found reduction of low-k $\widetilde{n}$ in line with the O-point of rotating, tearing driven islands in TEXT [30]. Local turbulence reduction at the O-point of static magnetic islands has been measured in the J-TEXT tokamak via Langmuir-probes [31]. A series of flow measurements across static islands of different size in LHD [5, 70] [Fig. 1.11 (a)] clearly showed the existence of two island regimes: (i) Strong shear flows exist just outside the separatrices of small islands resulting from a flat space potential inside the island; (ii) Large islands are characterized by a vortex flow and curved space potential. The vortex circulates around the O-point and has a radial extent somewhat larger then the island itself.

These results were qualitatively replicated by the GENE simulations [6] as part of this thesis work [Chapter 6], see an example of the vortex mode in Fig. 1.11 (b). The former results were recently replicated by Doppler reflectometry measurements across static islands in the TJ-II [32] stellarator.

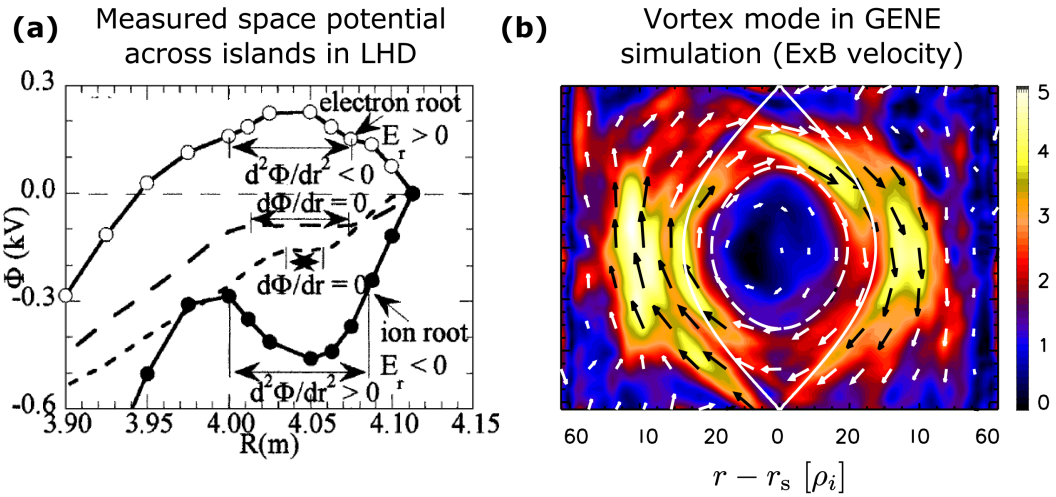

Figure 1.11: (a) Measured potential in LHD [5], (b) vortex in simulation [6].

As part of this thesis work, the flow perturbation around rotating, coupled NTM island chains was measured in low-torque H-mode experiments [Chapter 9]. These results suggest that large NTMs also develop vortex modes.

1.10 Outline of the thesis

First, the DIII-D tokamak, the plasma diagnostics used and data processing techniques are briefly described in Chapter 2.

Next, various heat transport models of magnetic islands are presented in Chapter 3. This effort extends beyond previous work, as a spatially non-uniform electron thermal diffusivity was introduced in an anisotropic heat diffusion model of magnetic islands for the first time.

Island structures are described in Chapter 4 via the analysis of measured 2D (R, ξ) perturbed electron temperature profiles. This is followed by the derivation of the cross-field electron thermal diffusivity in the O-point of the island from T_e data using a heat transport model presented previously in Chapter 3.

The major results of this thesis are presented in Chapter 5: the first localized measurements of low-k and intermediate-k $\widetilde{n}$ and low-k $\widetilde{T}_e$ across naturally growing, freely rotating 2/1 NTM magnetic islands. Differences between O-point and X-point fluctuation levels, fluctuation levels inside vs outside the island region and scaling of turbulence modifications vs island width are all presented. Additionally, these measurements were used to determine the turbulence penetration length scale at the island separatrix.

To help interpreting these experimental observations, GENE gyrokinetic simulations were run to study the effect of magnetic islands on turbulence in Chapter 6. These simulations were carried out by my collaborator A. Bañón Navarro and the output was analyzed by myself. We found that the measured turbulence modifications in DIII-D were qualitatively replicated by these simulations.

Consequences of the observed NTM-turbulence interaction on global plasma confinement were studied via analyses of simultaneous changes in NTM amplitude, plasma profiles, turbulence, fluxes and confinement and are described in Chapter 7. This is followed by discussing the effects of NTM-turbulence interaction on NTM growth rates via the dynamical equation of NTMs.

Additionally, the shrinking of NTM islands due to strong temperature perturbations

associated with Edge Localized Modes was observed and is described in Chapter 8. Simultaneous changes in turbulence levels across the island were also observed and the potential implications of this turbulence level modification on the island recovery is discussed.

Finally, a series of low torque H-mode experiments were carried out to measure the perturbed ion temperature and toroidal flow profiles via CER across slowly rotating islands and the results are presented in Chapter 9.

CHAPTER 2

The DIII-D tokamak, diagnostics and analysis techniques

In this Chapter, the DIII-D tokamak and plasma diagnostics used for island and turbulence studies are briefly introduced. The most commonly used data processing techniques are also discussed here and preliminary examples are shown.

In this thesis work, analysis codes were written from scratch and did not borrow from existing data analysis packages at DIII-D except the profile fitting tool ('GAprofiles') and equilibrium reconstruction fit viewer ('EFITviewer'). This includes complex analysis tools (phase-locking BES and DBS turbulence cross-powers, determination of diffusivities at the O-point of the island from ECE data, partial differential equation solvers, fitting procedures for non-standard functions, etc.) and standard analysis tools (such as calculation of cutoff frequencies, power/coherence/phase spectrum calculations, correlation functions, spectral filtering of signals, etc.).

Reproducible, high-confinement mode experiments were carried out with stationary, long-lived large $m/n = 2/1$ NTM magnetic islands. Plasma fluctuations were monitored on two distinct time and spacial scales: (i) MHD-scale and (ii) turbulent-scale.

The MHD-scale fluctuations are associated with the NTM islands, which have a typical saturated width of 11 cm, toroidal and poloidal mode numbers are $m/n = 2/1$. The islands grow on a time-scale of about 50 ms and rotate with typically 5-15 kHz. The primary diagnostic used for studying the island structure and heat transport is the ECE radiometer, which provides local measurements of T_e. Additionally, T_i profiles across the island are reconstructed from Charge Exchange Recombination (CER) measurements when the island rotation was below 1 kHz. These local measurements are complemented by

external magnetic measurements (Mirnov), which provide the NTM mode numbers as well as the evolution of the magnetic amplitude.

Probed turbulent fluctuations are typically in the range of the ITG and TEM instabilities and are probed up to 7 cm^{-1} in the 50-500 kHz frequency range. The turbulence measurements were focused on the island region and include:

1. Far Infrared scattering: line integrated, low-k $\widetilde{n}$;
2. Beam Emission Spectroscopy: local, low-k $\widetilde{n}/n$;
3. Doppler backscattering: local, intermediate-k $\widetilde{n}$;
4. Correlation Electron Cyclotron Emmission: local, low-k $\widetilde{T}_e$.

Note that the island rotation extends the radially resolved $\widetilde{n}$ and $\widetilde{T}_e$ measurements to 2D (R, ξ) allowing detailed investigation of both the radial and angular dependence of the turbulence power modifications due to the island.

2.1 The DIII-D tokamak

DIII-D is a tokamak developed in the 1980s by General Atomics in San Diego, USA. The mission of the DIII-D Research Program is to establish the scientific basis for the optimization of the tokamak approach to fusion energy production [71]. DIII-D is an

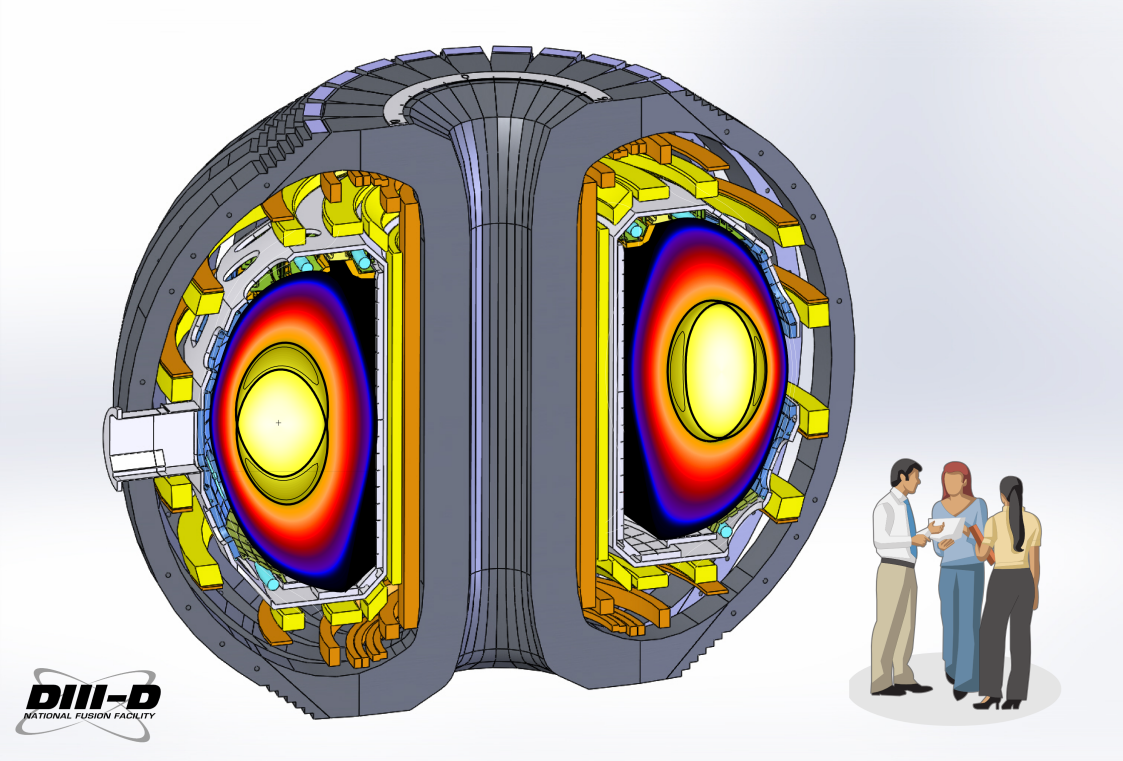

Figure 2.1: Schematic representation of the tokamak showing 2D reconstruction of T_e with magnetic islands in the poloidal plane.

advanced tokamak, characterized by operation at high plasma β through strong plasma shaping, active control of various plasma instabilities (such as NTMs), and achievement of current and pressure profiles that produce high performance. A schematic view of the DIII-D tokamak is shown in Fig. 2.1. The 2D reconstruction of T_e in Fig. 2.1 shows magnetic islands in the poloidal plane.

2.2 Magnetic field measurements via Mirnov-coils

The DIII-D magnetic diagnostic system [71] provides data for real-time equilibrium control, post-shot equilibrium reconstruction, and analysis of MHD fluctuations. The magnetic diagnostic signals come from inductive loops, most of which are connected to analog integrators. Magnetic probes on the inner surface of the vacuum vessel wall measure the local poloidal and toroidal magnetic fields (B_θ and B_ϕ, respectively) [Fig. 2.2]. In this

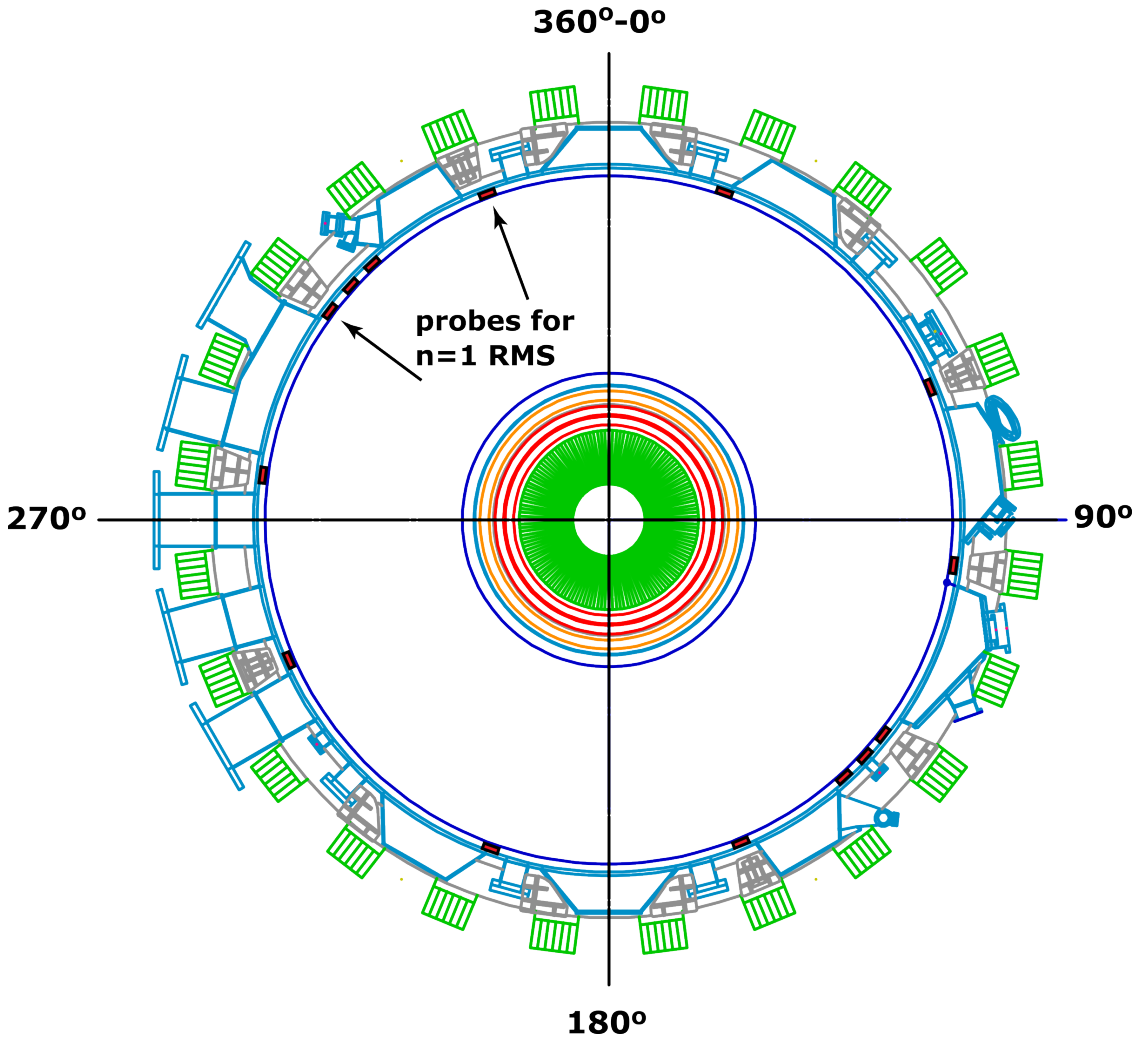

Figure 2.2: A horizontal cross-section of DIII-D at the midplane (z=0). The 14 probes in the low field side toroidal array are shown as red rectangles, with about twice their actual dimensions.

thesis, mainly the RMS of the $n = 1$ component of the B_θ fluctuations are used which is associated with the magnetic amplitude of rotating $m/n = 2/1$ NTM magnetic islands and

is calculated from signals of two magnetic probes separated by 33°. The analysis of a rotating mode takes advantage of the fact that the mode rotates past the sensors many times during the analysis time interval, allowing standard time-domain Fourier analysis techniques to be used. The $n = 1$ magnetic RMS signal is calculated by frequency filtering B_θ to a narrow frequency band where the phase relationship between toroidally offset probes is about $\Omega(\omega) = n\Delta\phi$, where $\Delta\phi$ is the toroidal separation of two probes, $\Omega(\omega)$ is the phase spectrum and ω is the frequency [72]. An example of the time history of the $n = 1$, $n = 2$ and $n = 3$ magnetic RMS signals is shown in Fig. 2.3. In this case, a dominant $n = 1$ mode started growing around 3800 ms, saturated to about 20 G and was stationary for about 1500 ms.

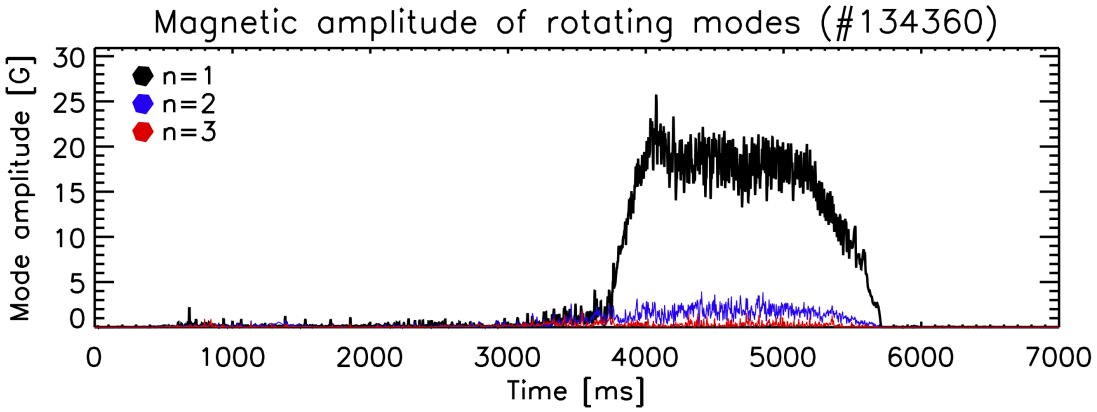

Figure 2.3: Example time history of the $n = 1$, $n = 2$ and $n = 3$ magnetic RMS signals (discharge #134360).

2.3 Electron temperature measurements via Electron Cyclotron Emission Radiometer

In tokamaks, T_e measurement is provided via the cyclotron radiation of thermal electrons. The first harmonic frequency of this radiation is $\omega_c \approx qB/m_e$, where q is the electron charge, B is the magnetic field strength and m_e is the electron mass. As the variation of the toroidal magnetic field in the tokamak follows the $B_T \propto R^{-1}$ relation (R is the major radius coordinate), the frequency resolved detection of the emitted radiation is equivalent with spatially resolved measurement [73, 74]. The power radiated by the gyrating particle relates to the local temperature as:

$$-\frac{dE}{dt} = \frac{\sigma_t B^2 v_\perp^2}{c\mu_\circ}, \text{ where } v_\perp^2 \propto T_\perp \tag{2.1}$$

Note that density fluctuations can mix into this measurement if the probed plasma layer is not optically thick. In this thesis, the ECE measurements were focused on core NTM studies, where this is not a problem. However, electromagnetic waves at frequencies lower or equal to the cutoff frequency can not propagate in the plasma. The radial profiles of the cutoff frequencies can be calculated as:

$$\omega_O(R) = \omega_p \tag{2.2}$$

$$\omega_R(R) = \frac{1}{2}\Big[\omega_c + (\omega_c^2 + 4\omega_p^2)^{1/2}\Big] \tag{2.3}$$

$$\omega_L(R) = \frac{1}{2}\Big[-\omega_c + (\omega_c^2 + 4\omega_p^2)^{1/2}\Big] \tag{2.4}$$

Here ω_O is the cutoff frequency for O-mode polarized radiation and ω_R and ω_L are for right handed and left handed X-mode radiation, respectively. ω_c is the electron cyclotron frequency and ω_p is the plasma frequency:

$$\omega_p = \frac{n_e q^2}{m_e \varepsilon_\circ} \text{ and } \omega_c = \frac{qB}{m_e} \tag{2.5}$$

The density and magnetic field data was taken from Thomson scattering [75] and an equilibrium reconstruction code [76], respectively. The $1/R$ like (blue) lines show the first three harmonics of the radial profile of the electron cyclotron frequency, see Fig. 2.4. The

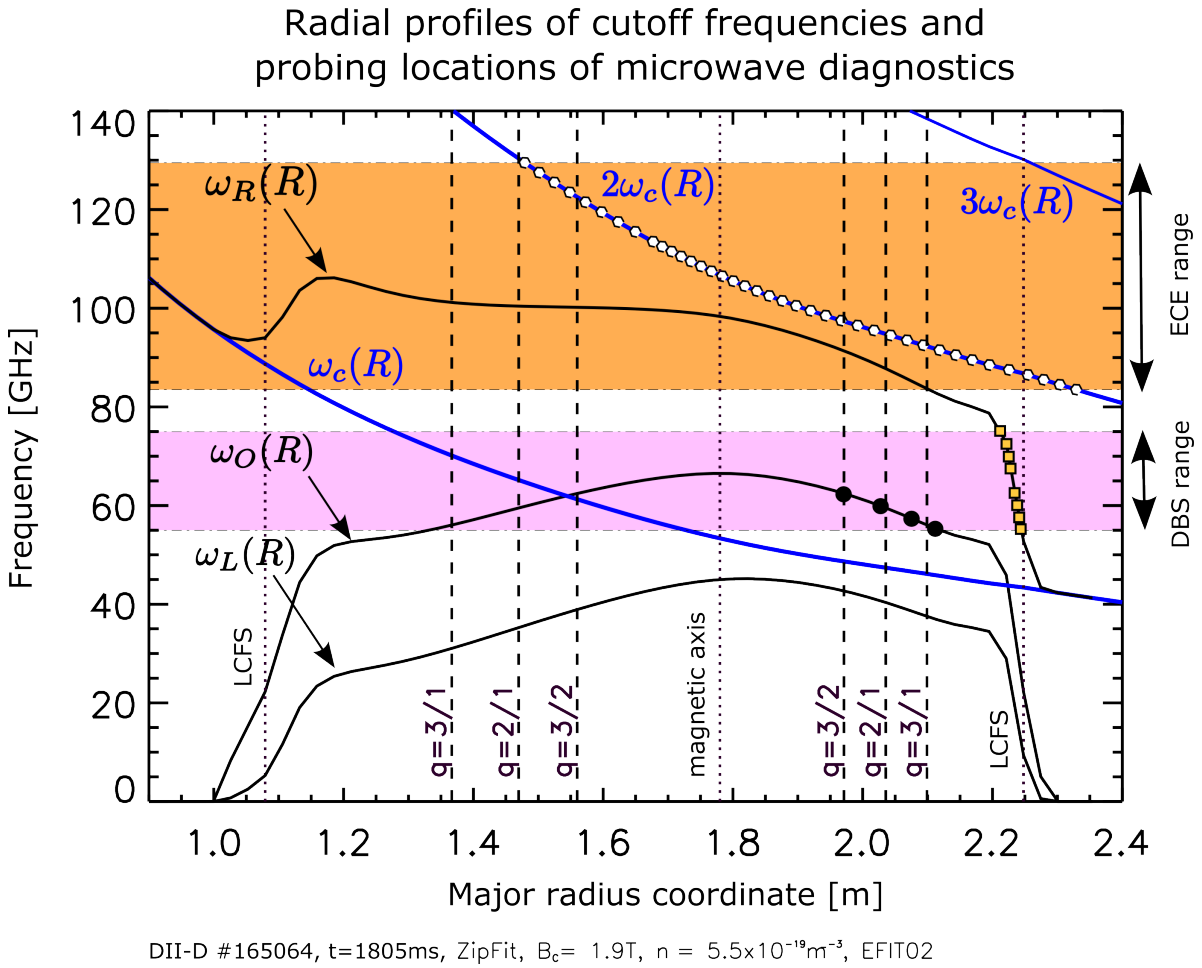

Figure 2.4: Cutoff frequencies at $t = 1805$ ms in #165064 for O-mode and X-mode (black solid lines) polarized microwaves. The first three harmonics of the electron cyclotron frequency profiles are shown with blue solid line. Last closed flux surface (LCFS), magnetic axis and relevant q surfaces are marked by vertical dashed or dotted lines. ECE and Doppler backscattering (DBS) frequency bands are shown with shaded areas and probed frequencies and locations are marked by symbols.

DIII-D electron cyclotron radiometer (ECE [77]) provides T_e from measurements using optically thick, second harmonic (X-mode) electron cyclotron emission in 40 radial locations with a 480 kHz sampling rate in the tokamak mid-plane. The measured ECE frequencies are shown with empty circles and the probed frequency range is highlighted and labeled as "ECE range". As the second harmonic cyclotron frequency is well above the right hand

cutoff, the ECE signals are not cutoff in the presented example. Notice that the probed domain contains the $q = 3/2,\ 2/1$, and $3/1$ rational surfaces thus the $m/n = 3/2,\ 2/1$ and $3/1$ modes can be probed via the ECE system (on the LFS). Additionally, this figure is used to demonstrate approximate probing locations of the Doppler backscattering measurements in O-mode and X-mode polarization, see symbols on the O-mode cutoff and on the right-hand cutoff, respectively, in the frequency range labeled as "DBS range".

The island rotation allows the probing of T_e with respect to ξ (helical phase of the island). In the lab frame $\xi = \omega_\circ t$, where $\omega_\circ/(2\pi) \approx 5 - 15$ kHz is the island frequency, and t is time. This allows a 2D reconstruction of T_e across the island in the R, ξ plane [Subsection 2.3.1]. Further, combining this with the equilibrium profile measurements, one can reconstruct the full 2D perturbed T_e in the poloidal plane [Subsection 2.3.2]. The typical saturated island full width is about 12 cm, see the example of flattened T_e at the $q = 2$ rational surface shown in Fig. 2.5.

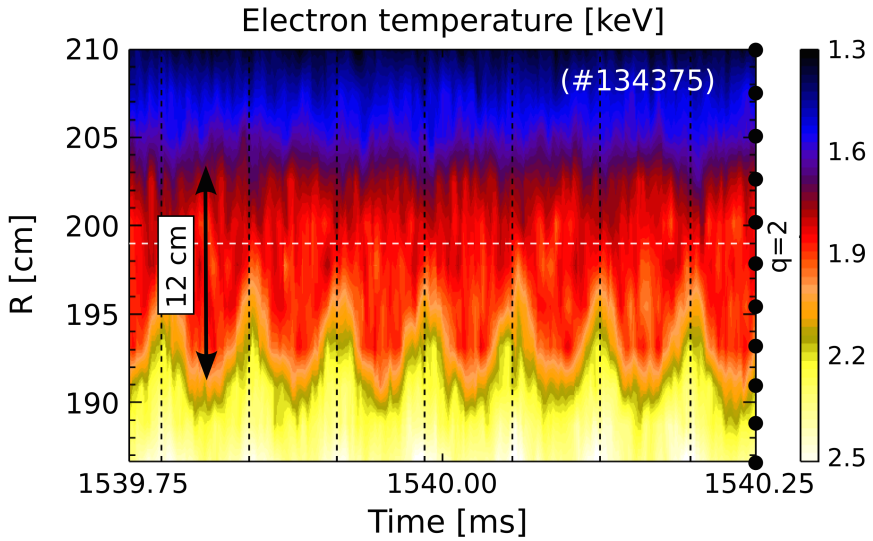

Figure 2.5: Raw ECE data shows T_e flat spots of full width W $\approx$ 12 cm. Circles on the right vertical axis mark the center of the ECE detection locations. The vertical dashed lines mark the X-point times and the light horizontal dashed line indicates the $q = 2$ surface.

The radial resolution of the ECE system is about 0.5 cm and the radial separation of the channels is about 2 cm which sets the size of the smallest detectable islands. This set-up allows the simultaneous probing of T_e at about 5 locations within the island separatrices

when the island full width is about 10 cm. Outside the island separatrices the perturbation $\delta \mathrm{T_e}$ decays on about 10 cm scale which is captured by 5 additional measurement points on each side of the island. In total, typically 15 channels are used to reconstruct the two-dimensional $\mathrm{T_e}$ profile across the island via phase-locking.

2.3.1 Reconstruction of 2D $\mathrm{T_e}$ profiles across the island via phase-locking in the (R, ξ) plane

To obtain the time series of $\mathrm{T_e}(R, \xi)$ first the X-point times t_i were found by constructing a reference signal with Singular Value Decomposition (SVD) calculated from a few ECE signals measured on the inner region of the rational surface. In these signals $\delta \mathrm{T_e}$ has maxima at the X-point times thus t_i can be identified by the maxima of the principal mode SVD signal. After this 100 points were evenly interpolated between each consecutive X-point yielding the t_i^k times ($k = 1, 2, ...100$). Since the ECE system probes in the tokamak mid-plane and a rotating 2/1 mode results 1 island cycle per 2π toroidal rotation, the evenly interpolated t_i^k times within one cycle can be mapped to $\xi_k = 2\pi/100 \cdot k$ helical phases by the $\xi = m\theta - n\phi(t)$ relation. Here $\theta = 0$ is the poloidal angle and ϕ is the toroidal angle of the probing locations in the plasma frame. We neglect here the effect of plasma shaping (i.e. assume that the cylindrical formulation of the magnetic island holds in the tokamak mid-plane), assume that the toroidal rotation frequency is constant within one full toroidal turn-over time ($\approx 70\mu$s) and that it is much larger than the poloidal rotation frequency. As a result the $\mathrm{T_e}$ is parametrized by R, ξ and the X-point times as $\mathrm{T_e}(R_j, \xi_k, t_i)$. The data were then phase-lock averaged using:

$$\langle \mathrm{T_e}(R_j, \xi_k, t_{\mathrm{c}(i)}) \rangle = \frac{1}{\mathrm{N}} \sum_{l=0}^{\mathrm{N}-1} \mathrm{T_e}(R_j, \xi_k, t_{i+l}) \tag{2.6}$$

where the $\langle \cdots \rangle$ brackets stand for averaging, $t_{\mathrm{c}(i)} = (t_{i+N} - t_i)/2$ is the center of the phase locking window $\Delta\tau$ and N is the number of island cycles within this window. The optimal value of $\Delta\tau$ will be obtained in Section 4.2 where the heat transport model will be

compared with experimental data. An example of phase-lock averaged T_e contour and average X-point and O-point T_e profiles are shown in Fig. 2.6. The X-point profile is not flattened but the O-point profile is flattened in about 12 cm radial range as expected from an island [Fig. 2.6 (b)].

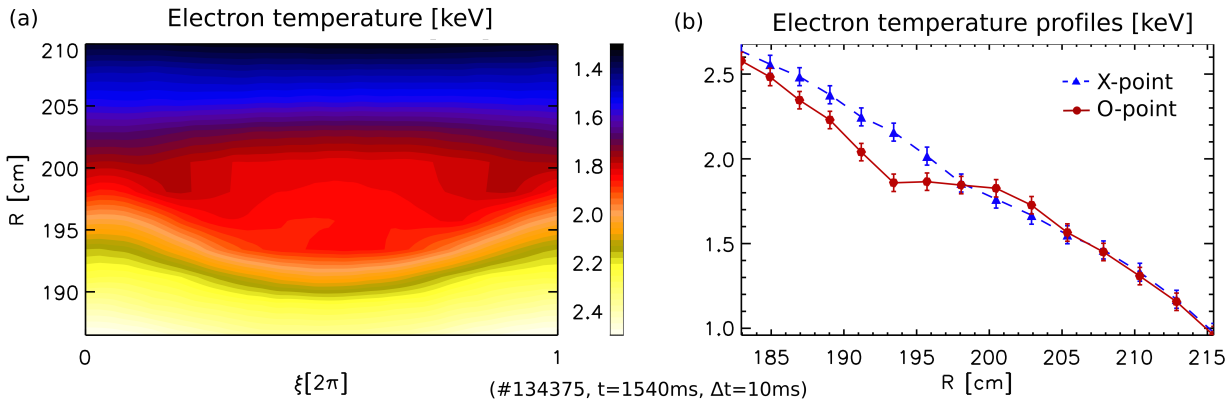

Figure 2.6: (a) $T_e(\xi, R)$ phase-lock averaged over 10 ms (about 150 island cycles using data in Fig. 2.5)), error bars are the standard deviations. (b) $T_e(R)$ across the X-point ($\xi = 0$ or 2π) and O-point ($\xi = \pi$).

2.3.2 Reconstruction of full 2D perturbed T_e profiles in the poloidal plane

T_e is reconstructed in the $R - z$ plane (z is the vertical coordinate) assuming that the equilibrium T_e is a flux function ($\overline{T}_e(\rho)$) and the perturbation due to the island (δT_e) can be written in the convergent Fourier series [56]:

$$\delta T_e(\rho, \xi) = \sum_k B_k(\rho) \cos(k\xi) \tag{2.7}$$

where $B_k(\rho)$ is the amplitude of the k^{th} Fourier harmonic component. The effect of toroidicity and plasma shape on the angular dependence of $B_k(\rho)$ is not considered. Typically $B_k(\rho)/B_{k+1}(\rho) \approx 10$, therefore higher order harmonics are neglected, leading to:

$$T_e(\rho, \xi) \approx \langle T_e(\rho) \rangle_\xi + B_1(\rho) \cos(\xi). \tag{2.8}$$

The mean part $\langle \mathrm{T_e}(\rho)\rangle_\xi = \overline{\mathrm{T}}_\mathrm{e}(\rho) + B_0(\rho)$ is obtained by averaging $\mathrm{T_e}(\rho,\xi)$ vs ξ (ECE and Thomson scattering). $B_1(\rho)$ was obtained via Fourier analysis of $\mathrm{T}(\rho,\xi)$. At a given toroidal angle ($\phi_\circ$), θ is related to ξ as $\xi = m\theta - n\phi_\circ$, giving $\mathrm{T_e}(\rho,\theta)$. Finally, the mapping of $\mathrm{T_e}(\rho,\theta)$ to the $R-z$ plane is done via the $\theta = \theta(R,z)$ and $R = R(\rho)$ relations given by EFIT [76] (magnetic equilibrium reconstruction code). FIG. 2.7 (e) shows the plasma shape and $\mathrm{T_e}(R,z)$ after NTM saturation.

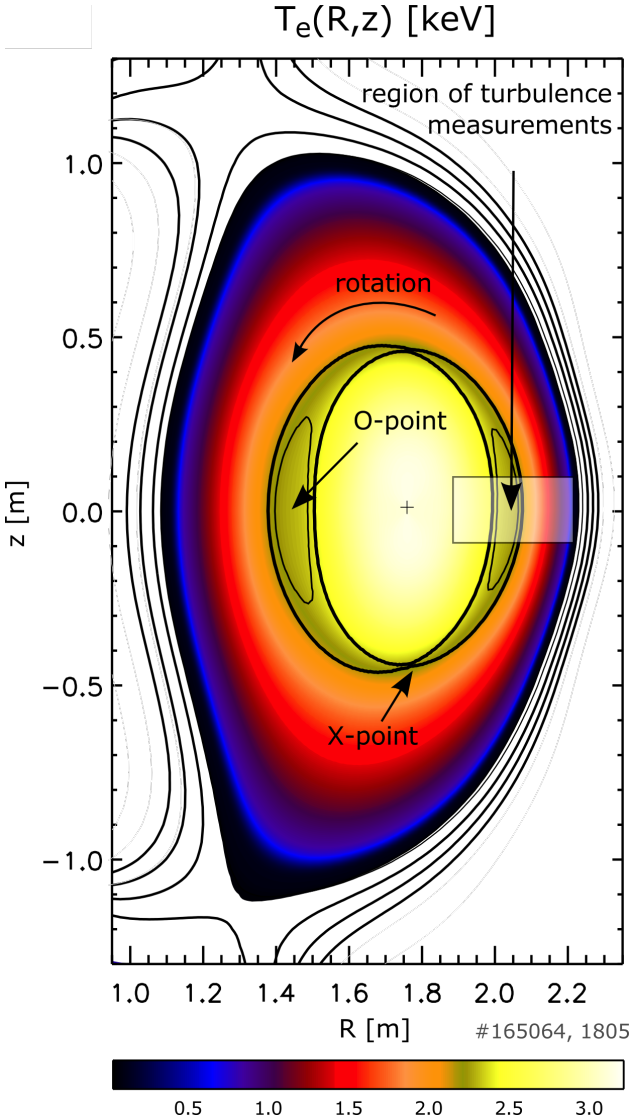

Figure 2.7: Plasma shape (EFIT), $\mathrm{T_e}(R,z)$ reconstructed from 1D ECE data and over plotted the $\Omega = 1$ (island separatrix, defined by eq. 2.9) and $\Omega = 0$ contours (thin and thick solid lines around $\mathrm{T_e} \approx 2.3$ keV, respectively).

The 2/1 islands have flat T_e profile at the O-point and are centered at $q = 2$ ($\rho \approx 0.35$). Ω maps out the perturbed flux surfaces of the island:

$$\Omega = 8X^2 + (2AX + 1)\cos(\xi) \tag{2.9}$$

The separatrix is at $\Omega = 1$, see FIG. 2.7 (e). Here $X = (R - R_s)/W$ and $A \approx -0.6$ is a dimensionless parameter that quantifies the radial asymmetry [55] of the island. The region of turbulence measurements was centered around the island structure in the outboard mid-plane, see the highlighted area in FIG. 2.7.

2.4 Line integrated low-k turbulent density fluctuation measurements via Far Infrared scattering

The FIR system [78] utilizes an O-mode microwave beam that is scattered by density fluctuations $\widetilde{n}$ along the $\phi = 60°$ chord 7.6 cm above the mid-plane. The scattered radiation is detected near 0° scattering angle which selects $\widetilde{n}(k)$ in the $k_\theta < 1\text{cm}^{-1}$ wavenumber range, where k is the wavenumber of $\widetilde{n}$ in the vertical direction in the lab frame and nearly perpendicular to the magnetic field. At $q = 2$ the ion-gyroradius (ρ_i) is approximately 0.7 cm, so that $k_\theta \rho_i < 0.7$ which is a typical range of the ITG instability. As scattering occurs everywhere along the beam trajectory, the FIR system is a line integral measurement in the mid-plane. The low-k FIR scattering system is then a good monitor of $\widetilde{n}$ along this chord encompassing the radial location and extent of the 2/1 tearing mode, see an illustration in Fig. 2.8 (a) and example data in Fig 2.8 (b).

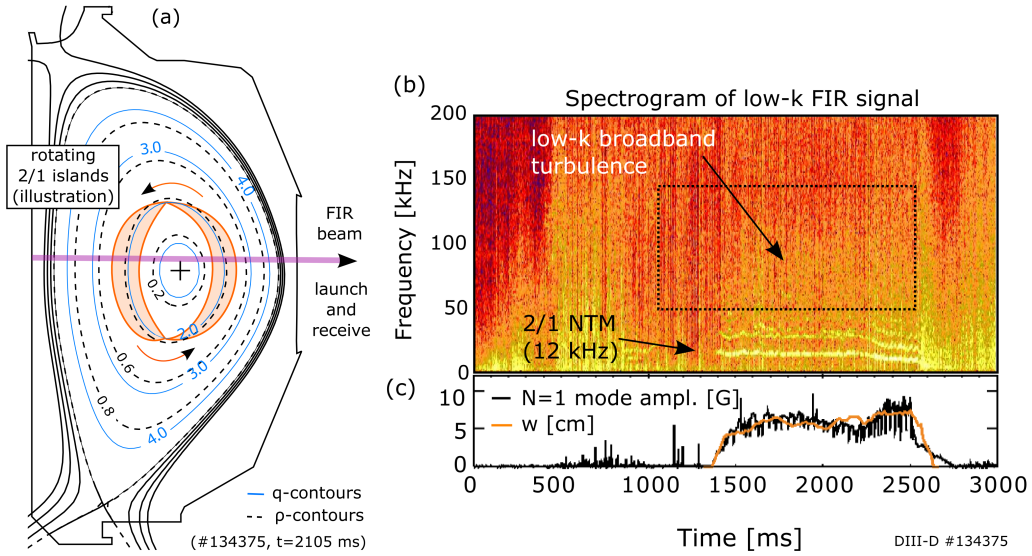

Figure 2.8: (a) FIR geometry shown in the poloidal plane of the tokamak. Over plotted are q (dark dashed) and ρ (light solid) contours. (b) Spectrogram of FIR signal showing coherent density fluctuations at the NTM frequency (12 kHz and higher harmonics) and low-k broadband density fluctuations. (c) $n = 1$ magnetic RMS and the island half width (obtained from ECE data + modeling, see Chapter (4)).

2.5 Local low-k turbulent density fluctuation measurements via Beam Emission Spectroscopy

The BES system [79] detects relative density fluctuations $\widetilde{\mathrm{n}}/\mathrm{n}|_{\mathrm{BES}}$ locally by measuring the light emission from the neutral beam at $\phi = 150°$, 3.6 cm above the mid-plane. The radial locations of the channels are adjustable and were set to cover the $m/n = 2/1$ island region [Fig. 2.9]. The BES system is sensitive to localized, long-wavelength density fluctuations of $k_\theta < 1$ cm^{-1} corresponding to the ITG wavenumber range ($k_\theta \rho_i < 0.7$) similarly to the FIR system. The typical separation between the analyzed 26 channels is about 1 cm, the radial and poloidal localization is about 1 cm.

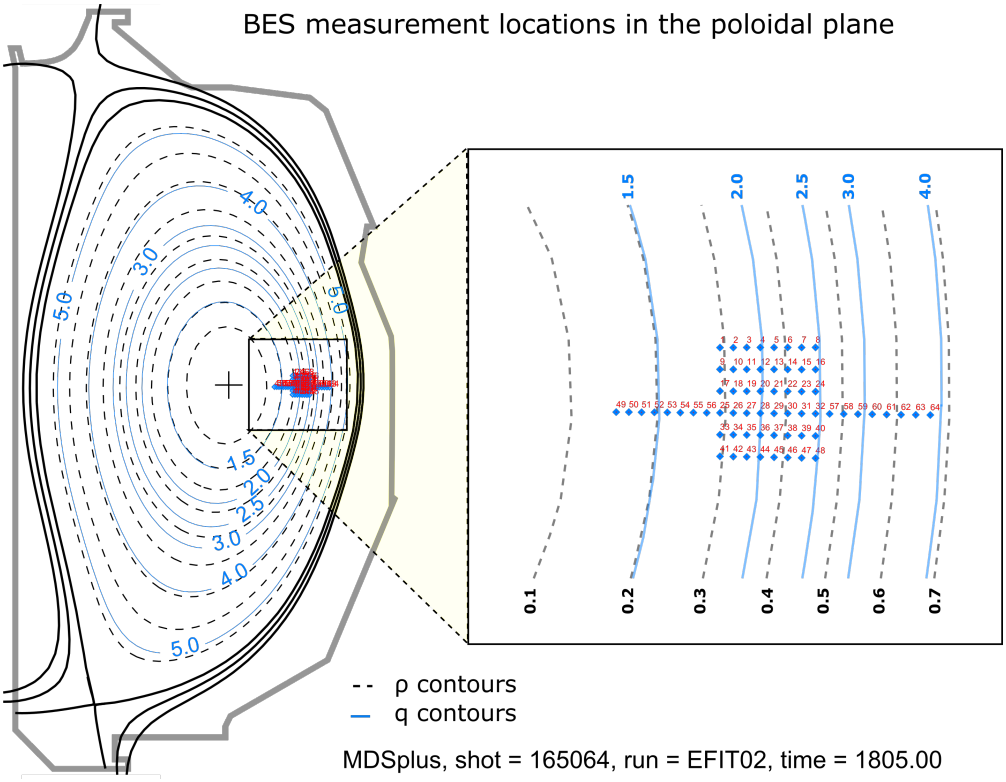

Figure 2.9: BES measurement locations in the poloidal plane. An array of 6 by 8 channels were centered on the $q = 2$ surface monitoring the $m/n = 2/1$ island region. Complementing this, two linear arrays of 8 channels (16 in total) were probing fluctuations on each side of the island 4 mm above the mid-plane.

Data processing

In discharge #165064 two signals of $\widetilde{\mathrm{n}}/\mathrm{n}|_{\mathrm{BES}}$ measured at the same radial coordinate but offset poloidally by 1.4 cm are coherent below 200 kHz [FIG. 2.10]. The linear phase below 200 kHz (with zero intercept) shows that $\widetilde{\mathrm{n}}/\mathrm{n}|_{\mathrm{BES}}$ in this range is due to poloidally propagating broadband density fluctuations. Above 200 kHz the signals are dominated by photon and electronic noise as seen from the low level of coherence and incoherent phase. Below 50 kHz the BES spectra exhibit a coherent peak at the NTM frequency (5 kHz) and at higher harmonics due to the modulation of $\mathrm{n}(t)$ by the rotating island. Therefore, data is analyzed in the $f = 50 - 200$ kHz range only. Note that the BES photon noise has a near white spectrum and the total power of the photon noise is proportional to the density. Therefore, a slow modulation of the density leads to the slow modulation of the signal level in the $f = 50 - 200$ kHz range through the photon noise modulation. To remove this spurious contribution, the turbulence power was calculated using the nearest neighbor cross-powers. As the BES channels are separated radially by about $1.25\rho_i$, the photon noise is uncorrelated between neighboring channels but the turbulence is correlated.

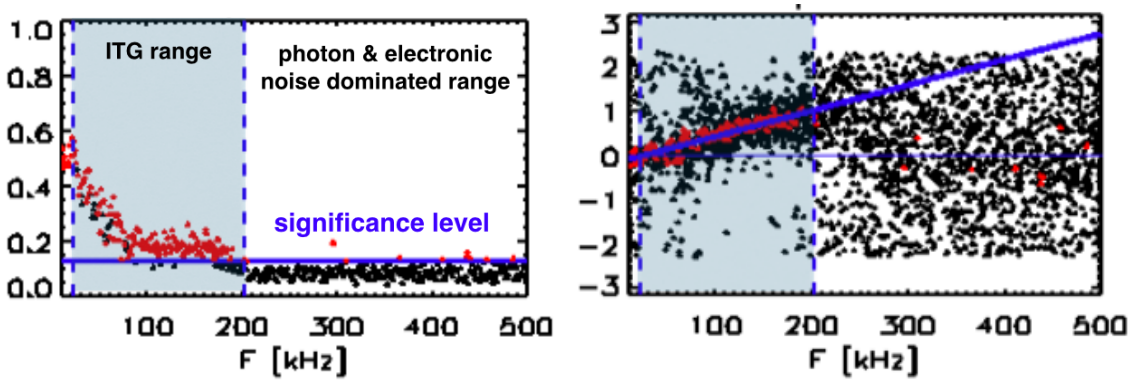

Figure 2.10: (a) Coherence and (b) phase across poloidally offset BES channel pairs averaged over the array of 6 channels. Points, where the coherence is larger or equal to the significance are colored. Below 200 kHz, only those points are colored that approximately follow a linear phase relationship.

2.6 Local intermediate-k turbulent density fluctuation measurements via Doppler backscattering

The DBS system launches a microwave beam into the plasma with oblique incidence and measures the the electric field component of the backscattered microwave. Plasma density fluctuations whose $k_\perp$ satisfies the Bragg condition $k_\perp = -2k_i$ backscatter the incident beam (momentum conservation). Therefore, the backscattered electric field is used as proxy for the amplitude of density fluctuations $\widetilde{\mathrm{n}}(k_\perp)$. Here $k_\perp$ is the wavenumber of density fluctuations perpendicular to the magnetic field, k_i is the local probing wave vector determined by the launch angle α relative to $\hat{n}$ as $k_i = k_\circ \sin(\alpha)$, where $k_\circ$ is the wavenumber of the incident microwave beam in vacuum and $\hat{n}$ is the normal vector of the cutoff surface [80]. The radial wavenumber of the microwave beam decreases during inward propagation and vanishes at the probed surface, see examples of calculated beam trajectories in Fig. 2.11.

Due to the matching condition and the varying beam wavenumber along the trajectory, the different Fourier components of the backscattered signal originate from different locations along the path. Plasmas with a turbulence k-spectrum following power law, enhance the scattered amplitude around the cutoff layer and suppress everywhere else. This provides a good spatial localization of the backscattered amplitude.

Due to energy conservation in the backscattering process, the frequency of the backscattered signal is Doppler shifted by $f_D = k_\perp v_\perp/(2\pi)$. This allows the determination of turbulence propagation velocity $v_\perp$. This is often dominated by a global $\mathbf{E} \times \mathbf{B}$ flow, thus flow velocity and electric field information can be extracted from the time trace of the the Doppler-shift [47]. See an example of the power spectrum of the DBS signal in FIG. 2.12. Additionally to the Doppler-shifted signal component (about 5 MHz wide Gaussian-like peak centered around 2 MHz), a zero mean frequency component is present which is a combination of a line integral of scattering along the beam, reflection from the tokamak inner walls, background radiation and electronic noise. This zero mean frequency

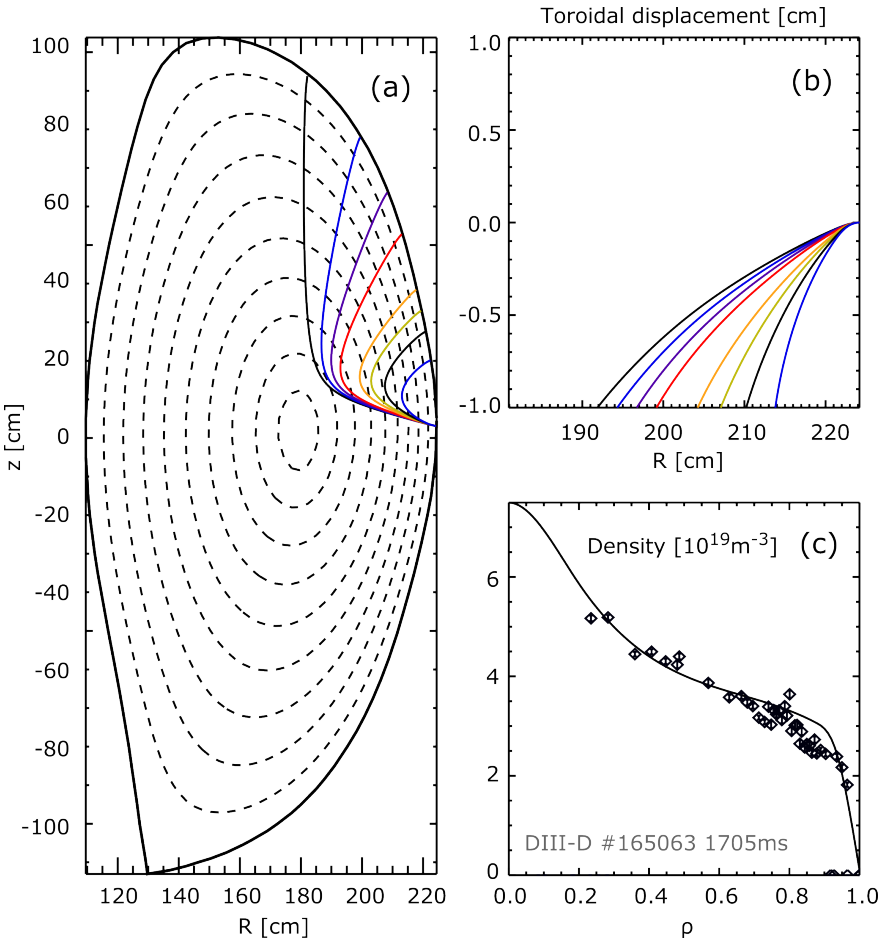

Figure 2.11: Example of a GENRAY output showing DBS beam trajectories in (a) the poloidal plane and in (b) the toroidal plane. (c) Measured density (via Thomson scattering) and fitted profile used as input to GENRAY (cubic spline).

component is often referred to as "noise", as it can not be used to derive local turbulence characteristics at the cutoff surface.

The DBS system installed on DIII-D [81, 82] measures in the $\Delta f = 55 - 75$ GHz frequency range with 8 evenly separated channels. In the presented discharges, $\tilde{n}$ probed by the DBS system is typically in the $2 < k_\theta \rho_s < 5$ range and is likely due to the TEM instability as indicated by GENE gyrokinetic simulations ($\rho_s = \sqrt{m_i T_e/(qB)}$ is the ion sound Larmor radius, m_i is the ion mass, q is the ion charge and B is the magnetic field strength). The probing locations can be varied by adjusting polarization, magnetic field and plasma density.

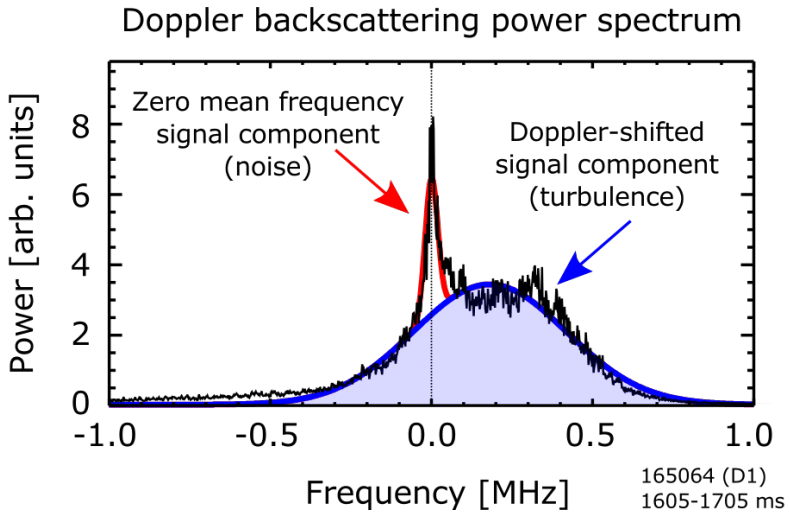

Figure 2.12: Example of raw DBS power spectrum and fitted Gaussians defined by equation 2.10.

Data processing

The zero mean frequency component is subtracted by fitting a double Gaussian to the DBS power spectrum $\mathrm{P}(f)$ defined by $\mathrm{P}_{\mathrm{fit}}(f)$ as:

$$\mathrm{P}_{\mathrm{fit}}(f) = \mathrm{A}_0 \mathrm{e}^{-f^2/\sigma_0^2} + \mathrm{A}_D \mathrm{e}^{-(f-f_\mathrm{D})^2/\sigma_\mathrm{D}^2} \tag{2.10}$$

The 5 free parameters are fitted simultaneously: A_0 and σ_0 are the amplitude and width of the zero-mean frequency noise component, respectively, A_D, σ_D and f_D are the amplitude, width and Doppler-frequency of the Doppler-shifted turbulence component, respectively. The fitted components compare well with the raw DBS data, see FIG. 2.12. The power of the Doppler-shifted component is analyzed thereafter, referred to as the turbulence power $\widetilde{\mathrm{n}}^2_{\mathrm{DBS}}(t) = \mathrm{A}_\mathrm{D}(t)\sigma_\mathrm{D}(t)$.

Determination of probing locations and probed wavenumbers

Probing locations and wavenumbers were determined via GENRAY, which is a general ray tracing code for the calculation of electromagnetic wave propagation and absorption in the geometrical optics approximation [83]. For a given launched wave (defined by the frequency

and polarization) GENRAY returns the probing location in the poloidal plane (R, z) as well as the toroidal displacement and the wavenumber (k) of the probed plasma density fluctuation $(\widetilde{\mathrm{n}}(k))$. Images of the beam trajectory are shown in Fig. 2.11 (a) and (b). The input density profile is generated through a cubic spline interpolation of Thomson scattering data [Fig. 2.11 (c)]. In Fig. 2.11, the measurement locations and probed wave numbers cover the $\rho = 0.18 - 0.65$ radial range and $4.0\ \mathrm{cm}^{-1} < k < 11.5\ \mathrm{cm}^{-1}$ wave number range, respectively, such that longer wavelengths are probed further out.

2.7 Local low-k turbulent electron temperature fluctuation measurements via Correlation Electron Cyclotron Emission

Radial profiles of broadband $\widetilde{\mathrm{T}}_\mathrm{e}$ turbulence are obtained with the new 8-channel DIII-D CECE radiometer [84], which is similar to the earlier 2-channel system [40]. This system receives second harmonic X-mode ECE radiation emitted from the plasma in the frequency range 72-108 GHz, 7.6 cm above the tokamak mid-plane. The spectral decorrelation technique [85] is used to obtain true $\widetilde{\mathrm{T}}_\mathrm{e}$ distinct from the thermal background noise. Coherent modes observed at low frequency ($f < 50\,\mathrm{kHz}$) are excluded from the fluctuation level calculation. In these plasma, the eight measurement locations of the CECE system cover the $\rho = 0.4 - 1.0$ radial range. Example coherence spectrum of $\widetilde{\mathrm{T}}_\mathrm{e}$ fluctuations is shown in FIG. 2.13 with and without islands.

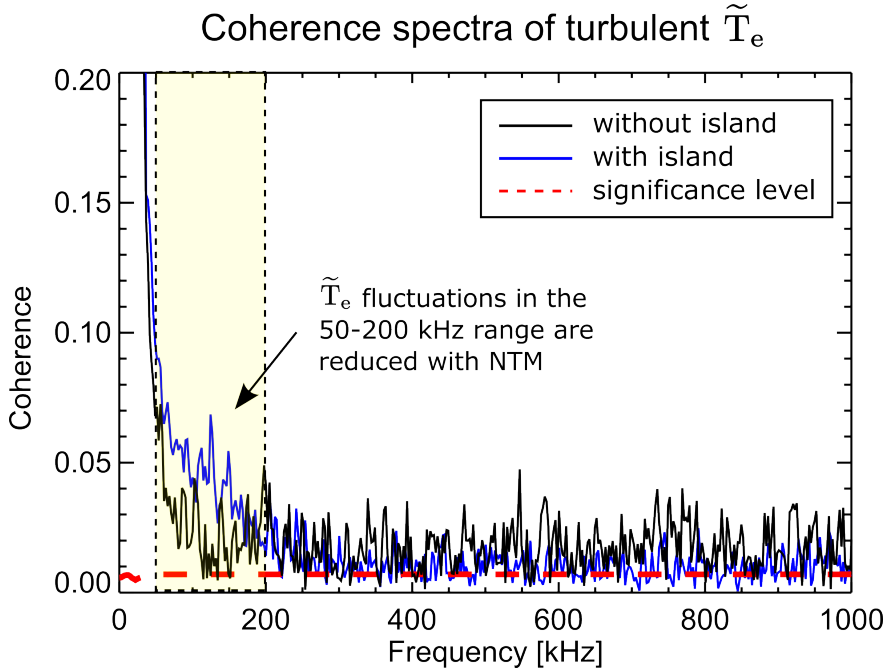

Figure 2.13: Coherence spectrum of CECE signals at $\rho = 0.45$, $\approx 1 - 2$ cm from $q = 2$, averaged over typically 150 ms in 16 similar discharges (165057 - 165154) showing significant turbulent $\widetilde{\mathrm{T}}_\mathrm{e}$ fluctuations without island in the $50 - 200$ kHz range. These fluctuations are reduced when the island grows to about 5 G (W $\approx$ 6 cm).

2.8 Effect of ELMs on profile and turbulence measurements

Finally, it is worthwhile to mention that Edge Localized Modes (ELMs) can lead to spurious fluctuations in a broad spectral range in every profile and turbulence measurement. To avoid this contribution, only ELM-free times were analyzed. The excluded time windows were selected using the amplitude of the D_α signal, which exhibits a peak after each ELM crash, see an example in Fig. 2.14 together with the D_α signal. The critical signal level, above which a peak in the D_α signal is considered an ELM, as well as the excluded window width (τ_{ex}) were set such that analysis results reported here are independent of these parameters. The excluded windows are shaded with light color in Fig. 2.14. For the turbulence analysis, the data in ELM-free windows was combined into a single signal and characteristic quantities (such as fluctuation amplitude) were determined from this ELM-free signal.

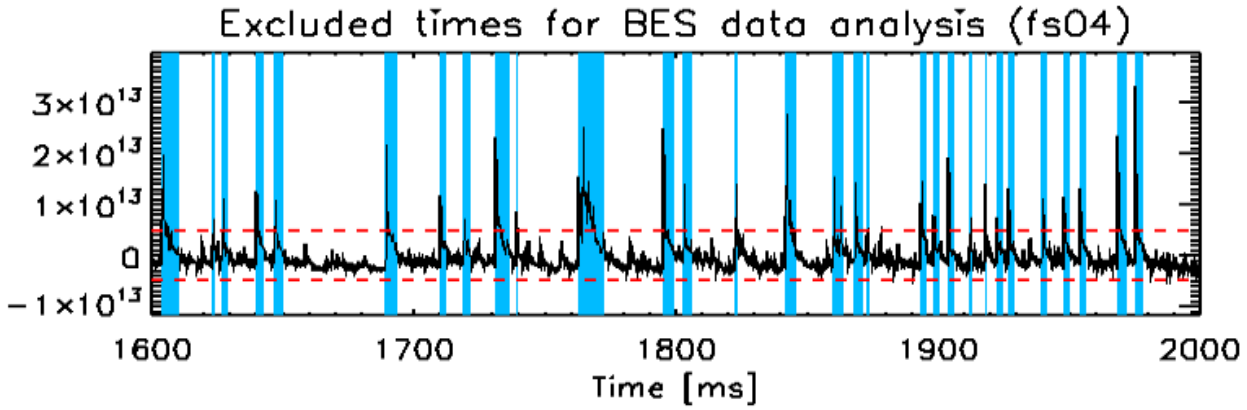

Figure 2.14: Example of excluded windows and D_α signal.

CHAPTER 3

Heat transport model of magnetic islands

Gyrokinetic simulations predict the reduction of turbulent fluctuations and cross-field heat transport across the island O-point [6, 19, 21, 60]. As the anomalously high $\chi_\perp$ is often attributed to turbulence, the simulations suggest an interesting relationship between the decreased fluctuations and $\chi_\perp$ at the O-point of the islands. In qualitative agreement, recent experiments have reported decreased low-k turbulence at the O-point of naturally arising, rotating NTM islands [86, 87]. The turbulence driven cross-field transport has implications on NTM stability, hence, determination of $\chi_\perp$ at the O-point of NTM islands is of timely interest.

As mentioned before [Section 1.8], available transport codes (e.g. TRANSP) can not be used to determine $\chi_\perp$ due to the assumed simple geometry (m=n=0) in the codes. So far only perturbative experiments have investigated the transport at the O-point of static islands generated by resonant magnetic perturbations in L-mode tokamak plasmas and in stellarators.

Measurements of $\chi_\perp$ at the O-point of NTM islands in stationary thermal conditions have not been reported by experiments before.

In this chapter, 4 cases of the heat transport will be modeled:

1. Stationary, anisotropic diffusion with spatially uniform $\chi_\perp$ in the absence of thermal sources and sinks (similar to previous studies [65–69])

2. Stationary, anisotropic diffusion with spatially non-uniform $\chi_\perp$ in the absence of thermal sources and sinks (for the first time [7]).

3. Stationary, anisotropic diffusion with spatially uniform $\chi_\perp$ in the presence of heat sources and sinks (for the first time [88]).

4. Transient, one-dimensional diffusion with spatially uniform $\chi_\perp$ in the absence of thermal sources and sinks (similar to previous studies [62–64]).

These models (2 and 4) will be used in Chapter 4 and Chapter 8 to derive $\chi_\perp$ at the O-point of $m/n = 2/1$ NTMs in stationary and transient thermal conditions, respectively.

3.1 Spatially uniform cross-field thermal diffusivity

Model assumptions:

Here stationary, anisotropic heat transport is assumed, governed by diffusion in the absence of heat sources and sinks:

$$\nabla_\parallel(\chi_\parallel \nabla_\parallel \mathrm{T}) + \nabla_\perp(\chi_\perp \nabla_\perp \mathrm{T}) = 0 \tag{3.1}$$

In tokamaks parallel heat transport is typically not diffusive but is instead convective. However a diffusive transport model can be used by adopting a flux limited expression [66] for $\chi_\parallel$. Here the determination of $\chi_\perp$ at the O-point is in focus for which it is not necessary to determine the numerical value of $\chi_\parallel$. In eq. (3.1) constant electron density profile is assumed across the island region ($\mathrm{n_e} = \text{const.}$) which is reasonable as the equilibrium density profile is relatively flat in the experiments, hence the perturbation due to the magnetic island is also small ($\delta \mathrm{n_e} \approx 0$). The perturbed magnetic flux surfaces of the island are mapped out by the contours of the normalized flux surface label Ω:

$$\Omega = 2X^2 + (\mathrm{A}X + 1)\cos(\xi) \tag{3.2}$$

Here $X = (r - r_\mathrm{s})/\mathrm{w}$ is the normalized radial coordinate and ξ is the helical angle ($\xi = m\theta - n\phi$, where ϕ is toroidal and θ is the poloidal angle). r is the minor radius

coordinate, r_s is the resonant surface location, w is the island half width and the dimensionless parameter A is a correction to the perturbed flux function that breaks up the radial $\Omega(X) = \Omega(-X)$ symmetry of the island [55]. The X-point is located at $\xi = 0$ or 2π ($X = -\mathrm{A}/4$, $\Omega = 1 - \mathrm{A}^2/8$) and the O-point is located at $\xi = \pi$ ($X = \mathrm{A}/4$, $\Omega = -1 - \mathrm{A}^2/8$). The $\Omega = 1$ surface is the separatrix of the island. The effect of the parameter A is shown in Fig. 3.1, namely:

1. when $\mathrm{A} < 0$ the island is elongated toward the magnetic axis [Fig. 3.1 (a)],
2. $\mathrm{A} = 0$ describes a symmetric island [Fig. 3.1 (b)] and
3. the island is elongated toward the edge plasma when $\mathrm{A} > 0$ [Fig. 3.1 (c)].

.

Equation (3.1) is written in the perturbed magnetic field of the radially asymmetric island (defined by equation (3.2)):

$$\left[\left(X + \frac{\mathrm{A}}{4}\cos(\xi)\right)\left.\frac{\partial}{\partial\xi}\right|_X + \frac{\mathrm{A}X + 1}{4}\sin(\xi)\left.\frac{\partial}{\partial X}\right|_\xi\right]^2 \mathrm{T} + \tag{3.3}$$

$$\frac{\partial}{\partial X}\left(\frac{\mathrm{w_c^4}}{\mathrm{w}^4}\frac{\partial \mathrm{T}}{\partial X}\right) = 0 \tag{3.4}$$

where the explicit form of $\nabla_\parallel$ for arbitrary values of A was derived in previous work [68] and $\nabla_\perp = \mathrm{w}^{-1}\partial/\partial X$. The scale island width $\mathrm{w_c}$ is related to the transport anisotropy ($\chi_\perp/\chi_\parallel$):

$$\mathrm{w_c} = \sqrt{\frac{\mathrm{R_o L_q}}{n}}\left(\frac{\chi_\perp}{\chi_\parallel}\right)^{1/4} \tag{3.5}$$

where $\mathrm{L_q} = \mathrm{q}(\partial \mathrm{q}/\partial r)^{-1}$ is the magnetic shear length at $\mathrm{r_s}$, $\mathrm{R_o}$ is the major radius of the tokamak, and n is the toroidal mode number of the tearing mode. Spatially uniform $\chi_\parallel$ is assumed.

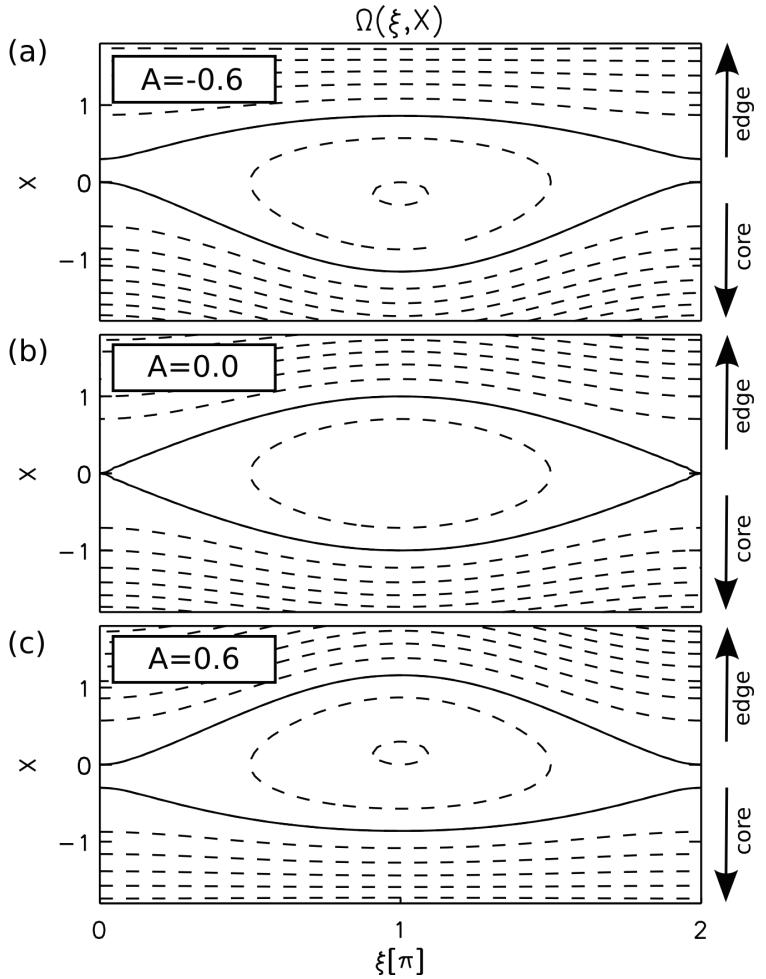

Figure 3.1: The effect of the asymmetry parameter A on the shape of the island: (a) A=-0.6, (b) A=0, (c) A=0.6. Note that direction of plasma edge/core are shown by arrows. The island separatrix ($\Omega = 1$) is marked by the solid line, other flux surfaces ($\Omega = -1, 0, 2, 3, \cdots$) are marked by dashed lines. ($\xi = m\theta - n\phi$ is the helical angle and $X = (r - r_s)/w$ is the normalized radial coordinate.)

Solution method:

Equation (3.3) was solved numerically using the pseudospectral method [89] as follows. The Fourier series of the trial solution

$$T(X, \xi) = \sum_{n=0}^{15} T_n^M(X)\cos(n\xi) \tag{3.6}$$

is substituted into equation (3.3). Here $T_n^M(X)$ is the n^{th} Fourier harmonic amplitude of the model solution (hence the superscript M). Next, equation (3.3) is turned into a set of

coupled equations of harmonic modes with Fourier's method. This eigenvalue problem is solved numerically with second order finite difference scheme on the $X = [-6, 6]$ and $\xi = [0, 2\pi]$ domain.

Example solutions:

Examples of the solution are shown in Fig. 3.2. Note that the radial width of the flat spot at the O-point varies with $\chi_\perp$ at fixed island width. This can be seen clearly from the variation of the radial distance between the maxima of the 1st Fourier harmonic amplitude as $\chi_\perp$ is varied at fixed w. This example illustrates that the radial extent of the T_e flat spot can overestimate or underestimate the magnetic island width w. In this case, the difference is 5 cm when $w_c \propto \chi_\perp^{1/4}$ is varied by a factor of 4.5, meaning that $\chi_\perp$ is varied by about 2 orders of magnitude.

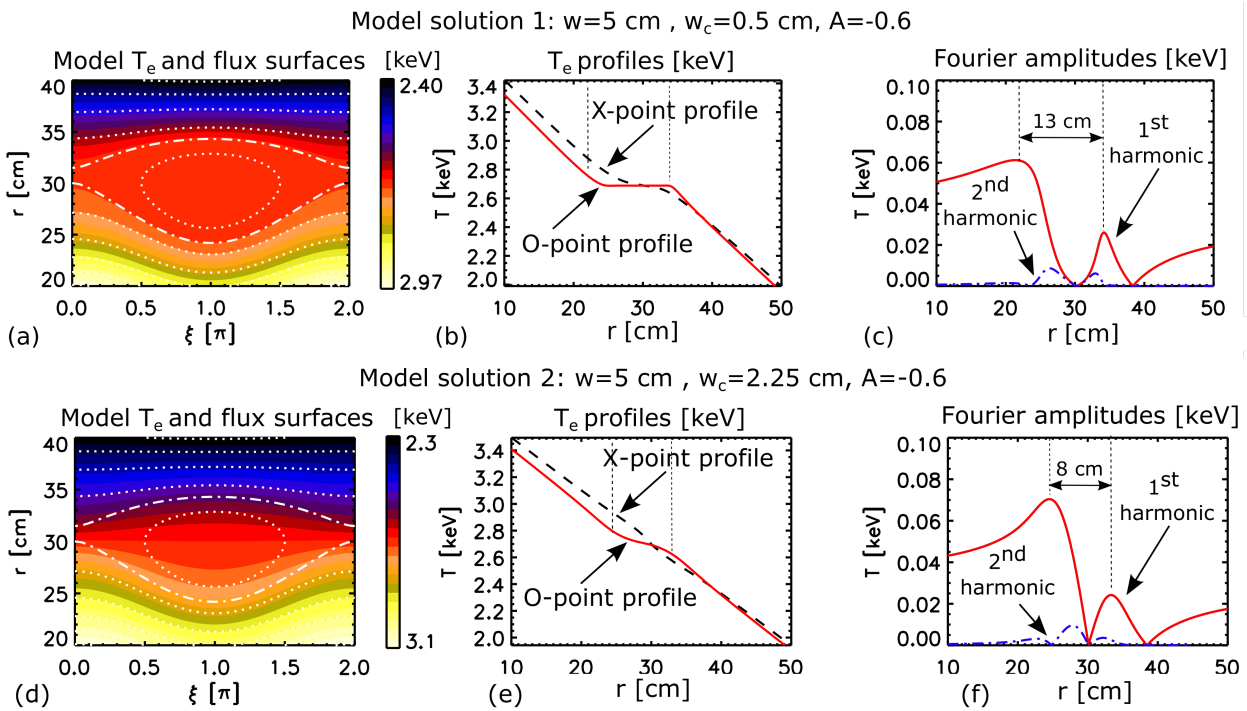

Figure 3.2: Stationary solutions of the heat transport model (eq. (3.1)) with w = 5 cm, A=-0.6 and (a-c) $w_c = 0.5$ cm and (d-f) $w_c = 2.25$ cm.

3.2 Spatially non-uniform cross-field thermal diffusivity

In this section a model for a non-uniform $\chi_\perp$ is presented. The spatial variation of $\chi_\perp$ is assumed to be proportional to the local $\nabla_\perp \mathrm{T_e}$, modeling the effect of temperature gradient driven turbulence in the transport. The effect of spreading/penetration [90] and convection of turbulence into the island is not considered here.

Model assumptions:

Spatially non-uniform $\chi_\perp$ is employed in the form:

$$\chi_\perp(\nabla_\perp \mathrm{T}, \nabla_\perp \mathrm{n}) = \chi_\perp^N + \chi_\perp^A(\nabla_\perp \mathrm{T}, \nabla_\perp \mathrm{n}), \tag{3.7}$$

where the neoclassical contribution ($\chi_\perp^N$) is assumed to be constant across the island region but the anomalous contribution ($\chi_\perp^A$) is an unknown function of the turbulence drives. One can Taylor expand $\chi_\perp^A$ up to first order about zero with respect to $\nabla_\perp \mathrm{T}$ and $\nabla_\perp \mathrm{n}$:

$$\chi_\perp^A(\nabla_\perp \mathrm{T}, \nabla_\perp \mathrm{n}) \approx \mathrm{a_T} \nabla_\perp \mathrm{T} + \mathrm{a_n} \nabla_\perp \mathrm{n}, \tag{3.8}$$

where $\mathrm{a_T}$ and $\mathrm{a_n}$ are the (constant) coefficients of the expansion. $\chi_\perp/\chi_\parallel << \mathrm{D}_\perp/\mathrm{D}_\parallel$ implies [56] that $\nabla_\perp \mathrm{n}$ is practically constant across the layer and this constant can be incorporated in the spatially uniform part of $\chi_\perp$ ($\mathrm{D}_\perp$ and $\mathrm{D}_\parallel$ are the perpendicular and parallel particle diffusivities). Finally equation (3.7) is written as:

$$\chi_\perp \approx \chi_\perp^{(0)}\left(1 + \varepsilon \widetilde{\mathrm{F}}(\nabla_\perp \mathrm{T})\right) \tag{3.9}$$

where $\chi_\perp^{(0)}$ is the spatially uniform contribution to $\chi_\perp$ and ε is a single new dimensionless parameter that controls the magnitude of the spatial variation $\widetilde{\mathrm{F}}$. $\widetilde{\mathrm{F}}$ is linear, dimensionless function of $\nabla \mathrm{T}$. Note that the particular form of $\widetilde{\mathrm{F}}$ can be chosen freely. For mathematical

convenience the following expression is used:

$$\widetilde{\mathrm{F}} = -\frac{\nabla_\perp \mathrm{T} - \mathrm{mean}\{\nabla_\perp \mathrm{T}\}}{\max\{\nabla_\perp \mathrm{T}\} - \min\{\nabla_\perp \mathrm{T}\}} \tag{3.10}$$

$\widetilde{\mathrm{F}}$ has zero mean value and the magnitude of the variation is normalized to unity. With this form of $\widetilde{\mathrm{F}}$ the fit parameter ε describes the sensitivity of $\chi_\perp$ with respect to $\nabla_\perp \mathrm{T}$.

The transport equation with spatially non-uniform $\chi_\perp$ now reads:

$$\chi_\parallel \nabla_\parallel^2 \mathrm{T} + \chi_\perp^{(0)} \nabla_\perp^2 \mathrm{T} = -\varepsilon \chi_\perp^{(0)} \nabla_\perp (\widetilde{\mathrm{F}} \nabla_\perp \mathrm{T}) \tag{3.11}$$

which is a non-linear partial differential equation with the non-linearity on the right hand side arising due to the effect of the magnetic island on turbulence driven transport. The equation conveniently transforms into the spatially uniform $\chi_\perp$ model when $\varepsilon \to 0$, i.e. when the latter effect is neglected. The explicit form of $\nabla_\perp^2$ and $\nabla_\parallel^2$ were shown in eq. 3.3.

Solution method:

The $\chi_\perp \propto \nabla_\perp \mathrm{T_e}$ model turns the diffusion equation into a nonlinear problem which is solved via a fix point iteration method: the solution process is started from the solution of the spatially uniform case ($\varepsilon = 0$) $\mathrm{T}^{(0)}$ which yields the approximation for the diffusivity $\widetilde{\chi}_\perp^{(1)}$ using expressions (3.9)-(3.10). Here the superscript refers to the sequence of approximations. The $\varepsilon \neq 0$ problem is then solved with $\widetilde{\chi}_\perp^{(1)}$ to obtain $\mathrm{T}^{(1)}$. The process is then successively repeated to generate the $\widetilde{\chi}_\perp^{(k)}$ and $\mathrm{T}^{(k)}$ series until they converge.

Example solutions:

Examples of the O-point profiles of the spatially non-uniform model $\chi_\perp$ and the the first harmonic amplitude of the solution ($\mathrm{T}_1^{\mathrm{M}}(X)$) are shown in Fig. 3.3 (a) and (b) as ε varies, respectively.

The shape of $\mathrm{T}_1^{\mathrm{M}}(X)$ is preserved at the O-point while the rate of decay of $\mathrm{T}_1^{\mathrm{M}}(X)$ is

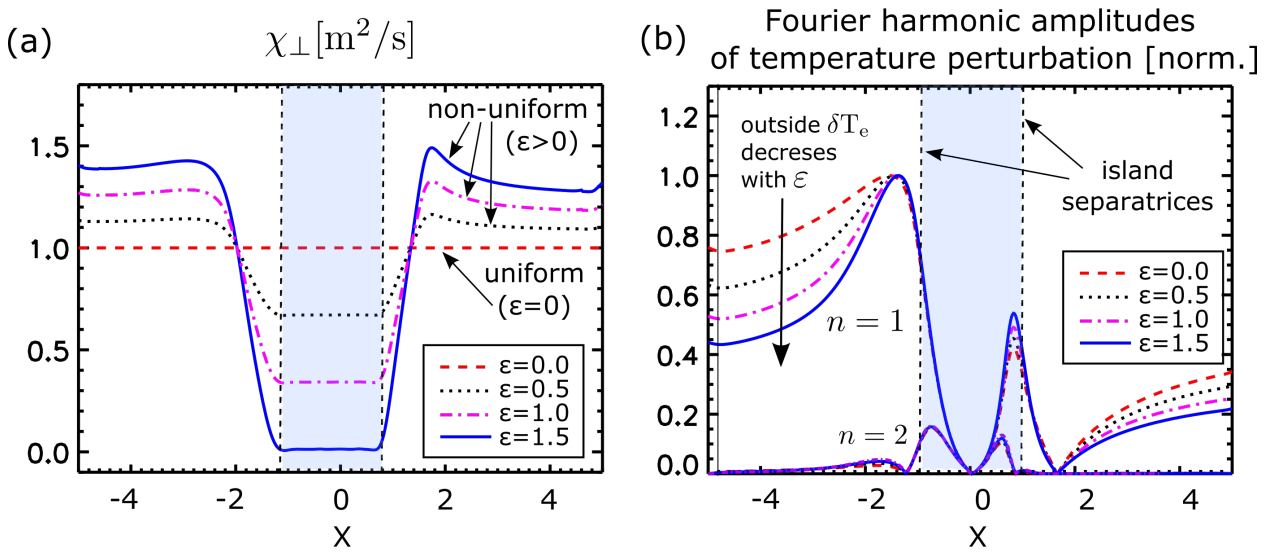

Figure 3.3: (a) Dependence of $\chi_\perp$ on $X = (r - r_s)/w$ as the parameter ε is varied (here $\chi_\perp^{(0)} = 1$ [m^2/s] for clarity). (b) Dependence of the $n = 1$ and $n = 2$ Fourier harmonic amplitudes of the temperature perturbation δT on X as ε is varied (maxima are normalized to unity). Note that δT decreases outside of the island as ε is increased, while it stays about the same inside the island. (Other parameters are fixed and experimentally relevant: A=-0.6, $w_c = 0.1w$.)

enhanced at $|X| > 1$ and it is controlled by the new parameter ε. This shows that the flattening of T at the O-point region is still effective as $\chi_\perp$ is suppressed inside the island even though $\chi_\perp$ of the background plasma is relatively large.

As the cross-field heat flux through the O-point is small even with uniform $\chi_\perp$ (due to $\nabla_\perp T$ is small), a decrease of $\chi_\perp$ at the O-point leads to little difference in the overall transport. Therefore, experimental determination of ε is difficult.

3.3 Effect of heat sources and sinks

Model assumptions:

The heat transport equation with heat sources and sinks reads:

$$\left[\left(X+\frac{\mathrm{A}}{4}\cos(\xi)\right)\frac{\partial}{\partial\xi}\bigg|_X+\frac{\mathrm{A}X+1}{4}\sin(\xi)\frac{\partial}{\partial X}\bigg|_\xi\right]^2\mathrm{T_e}+\frac{\mathrm{w_c^4}}{\mathrm{w^4}}\frac{\partial^2\mathrm{T_e}}{\partial X^2}=\frac{\partial\mathrm{T_e}}{\partial t}-\frac{\mathrm{P}}{(\mathrm{f}/2)\mathrm{n_e q_e}\chi_\parallel\mathrm{w}^2} \tag{3.12}$$

Here both $\chi_\parallel$ and $\chi_\perp$ are assumed to be spatially uniform for simplicity as in previous studies [65, 67, 68]. P is the power density of the heat source/sink. $\mathrm{P}>0$ represents a heat source and $\mathrm{P}<0$ represents a sink; for example:

- neutral beam heating,
- electron cyclotron heating ,
- heating or cooling due collisional coupling of electrons to ions or neutrals and
- cooling via radiation.

f and $\mathrm{q_e}$ are the degrees of freedom and charge of an electron, respectively, and $\mathrm{n_e}$ is the electron density which is assumed to be flat.

The model heat source/sink used here is uniform vs ξ and Gaussian vs. X with a half width of $\sigma_X=3$:

$$\mathrm{P}(X)=\mathrm{P_\circ}\left(\mathrm{e}^{-X^2/2\sigma_X^2}-\mathrm{e}^{-1/2}\right) \tag{3.13}$$

Here $\mathrm{P_\circ}$ is the maximum of the power density of the heat source/sink. $\mathrm{P}(X)$ is centered about the resonant surface, it vanishes at the boundaries of the domain (at $X=\pm3$) and is experimentally reasonable as: (1) it is broader than the island region, hence localized peaking of the profile is not expected solely due to the spatial variation of $\mathrm{P}(X)$; (2) It is uniform with respect to ξ. Although auxiliary heating sources (ECH and/or neutral beam

heating) are poloidally and toroidally localized in the lab frame, this localization is removed in the island frame due to island rotation.

Solution method:

First, the stationary problem was solved without heat sources via the pseudo-spectral method as described previously. Next, the inhomogeneity (heat source) was included and fixed-point iteration was employed starting from the solution of the homogeneous equation as proxy for the solution of the inhomogeneous equation. This mathematical method is the same as the one used to solve the problem with spatially non-uniform $\chi_\perp$.

Example solutions:

Experimentally relevant parameter values are (e.g.) w = 5 cm, $P_\circ = 0.5$ W/cm^3, $n_e = 3.5 \times 10^{19} m^{-3}$, $\chi_\parallel = 10^8$ m^2/s, $\chi_\perp = 1.7$ m^2/s without ECH and $\chi_\perp = 5$ m^2/s with ECH. Example solutions are shown in FIG. 3.4 with symmetric magnetic flux surfaces (A = 0).

In the absence of heat sources, T_e is flat across the O-point as expected [FIG. 3.4 (a)] but a peak (ΔT_{PEAK}) develops at the O-point when the heat source is imposed [FIG. 3.4 (b)] (defined by equation 3.13). The peak is slightly asymmetric since the $X < 0$ side of the island (and the peak) is in thermal contact with a hotter plasma region (via finite $\chi_\perp$) while the $X > 0$ side is in contact with a colder plasma region. This asymmetry is more pronounced when $\chi_\perp$ is increased e.g. by a factor of 3 as in FIG. 3.4 (c). Interestingly, a heat sink (due to e.g radiation) leads to a valley at the O-point [FIG. 3.4 (d) and (h)]. Based on these model solutions, the following general statements can be made about the peak ΔT_{PEAK} at the O-point:

1. A heat source can lead to the peaking of T_e at the O-point of magnetic islands with nested flux surfaces. This peaking would not be observed in islands without nested flux surfaces, e.g. in a situation where chaotic field lines are present in the island

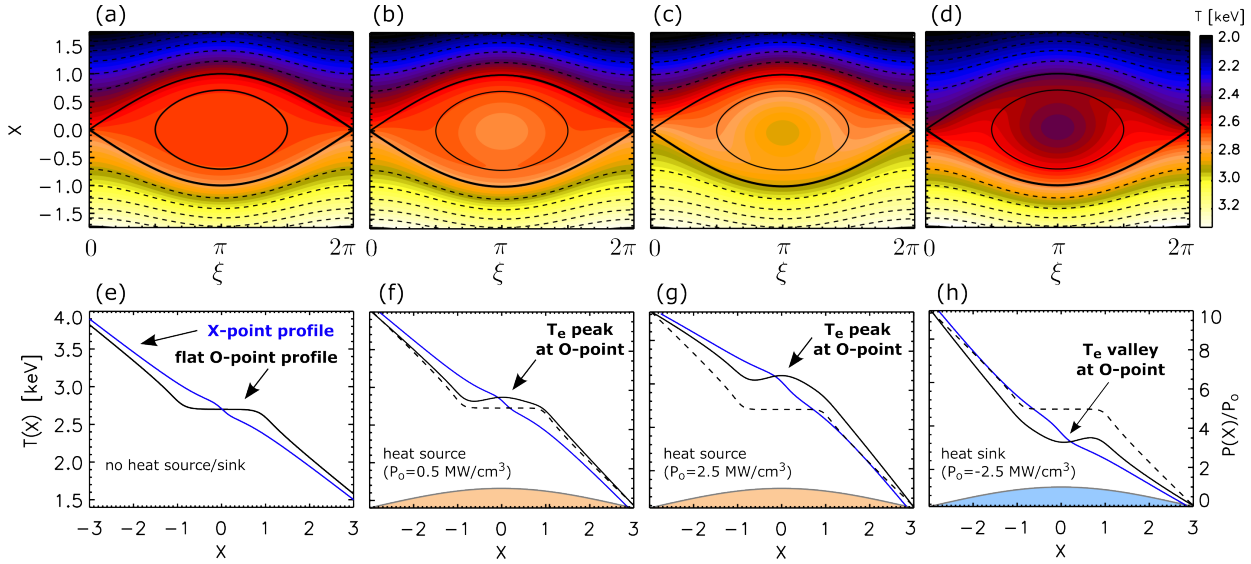

Figure 3.4: Stationary solutions of the heat transport model (eq. (3.12)). (a,e) No heat source ($P_\circ = 0$ MW/cm^3). (b,f) small heat source ($P_\circ = 0.5$ MW/cm^3), (c,g) large heat source ($P_\circ = 2.5$ MW/cm^3) and (d,h) heat sink ($P_\circ = -2.5$ MW/cm^3). Contours of $T_e(X, \xi)$ and contour lines of the magnetic island flux ($\Omega(X, \xi)$) are shown in (a)-(d) ($\Omega = 0$ thin solid line, $\Omega = 1$ thick solid line, separatrix of island and $\Omega > 1$ dashed lines). Profiles across the X-point and the O-point are shown in (e)-(h) with solid lines. Dashed lines are the O-point profiles without heat source/sink for comparison in (f)-(h).

region. Hence, the peak indicates that the island has nested flux surfaces.

2. Since $\chi_\perp$ is spatially uniform in this model, the T_e peak is not due to a reduced $\chi_\perp$ at the O-point, but is instead, a topological effect. It follows that a T_e peaking at the O-point alone does not indicate $\chi_\perp$ reduction inside the island.

3. The peak is asymmetric about the resonant surface even when the island and the heat source/sink are symmetric. This asymmetry is due to the background ∇T_e (i.e. different T_e on the two sides of the island).

4. A heat sink (e.g. radiation or energy exchange with a cold ion or neutral population) leads to a valley at the O-point.

Notice that ∇T_e is altered at the boundaries when a heat source/sink is present. This follows from integrating eq. (3.1) with respect to X over the full domain. In other words, the heat outflow is increased compared to the inflow as a result of the heat source/sink.

3.4 Heat transport dynamics

As mentioned before, if the thermal source or sink is turned off, the temperature at the O-point should flatten. In this subsection, we focus on the dynamics of the temperature profile flattening inside the island after a heat source is removed.

Model assumptions:

As heat can be driven through the island separatrices via cross-field transport only, the parallel term in equation (3.12) can be dropped when studying the evolution of the temperature peak at the O-point. This leads to a simple time-dependent radial heat diffusion equation [62, 64] which is used to derive $\chi_\perp$ at the O-point without adopting an expression for $\chi_\parallel$:

$$\frac{\chi_\perp}{w^2}\frac{\partial^2 \mathrm{T}}{\partial X^2} = \frac{\partial \mathrm{T}}{\partial t} - \frac{\mathrm{P}}{(\mathrm{f}/2)\mathrm{n_e q_e}} \tag{3.14}$$

Solution method:

The inhomogeneous equation (equation (3.14)) can be turned into a homogeneous equation for the variable $\Delta \mathrm{T_{PEAK}}$ assuming P is static and spatially uniform in the plasma layer:

$$\Delta \mathrm{T_{PEAK}}(X,t) = \mathrm{T}(X,t) + \frac{\mathrm{P_1} w^2}{2\chi_\perp} x^2 - \mathrm{P_2} t + a_1 x + a_2 \tag{3.15}$$

The 2^{nd} and 3^{rd} terms on the RHS describe the effect of the heat source on the background profile with the $\mathrm{P_1}$ and $\mathrm{P_2}$ constants ($\mathrm{P_1} + \mathrm{P_2} = 2\mathrm{P}/(\mathrm{f\, n_e q_e})$ is constrained). This background consists of a static parabolic part (consistent with FIG. 3.4 (f),(g) and (h)) and a linearly evolving spatially uniform part. The 4^{th} and 5^{th} terms can be added freely as equation (3.14) is second order in X and first order in t. The value of a_1 and a_2 must be chosen to satisfy initial and boundary conditions.

Example solutions:

A particular solution of the homogeneous equation for $\Delta \mathrm{T}_{\mathrm{PEAK}}$, describing a decaying Gaussian peak centered at the O-point, is:

$$\Delta \mathrm{T}_{\mathrm{PEAK}}(X,t) = \frac{\Delta \mathrm{T}^{\circ}_{\mathrm{PEAK}}}{\sigma(t)/\sigma_{\circ}} \mathrm{e}^{-X^2/(2\sigma(t)^2)} \tag{3.16}$$

where $\sigma(t) = \sqrt{\sigma_{\circ} + (t - t_{\circ})/\tau}$ with the decay time scale $\tau = (W/2)^2/\chi_{\perp}$. $\Delta \mathrm{T}^{\circ}_{\mathrm{PEAK}}$ and $\sigma_{\circ}$ are the amplitude and width of the peak at $t = t_{\circ}$, respectively. Experimentally relevant values are $\Delta \mathrm{T}^{\circ}_{\mathrm{PEAK}} \approx 0.2 - 0.4$ keV and $\sigma_{\circ} \approx 0.7$.

The decay rate of this peak at $X = 0, t = 0$ is:

$$\frac{1}{\Delta \mathrm{T}_{\mathrm{PEAK}}} \frac{\partial \Delta \mathrm{T}_{\mathrm{PEAK}}}{\partial t} = -\frac{\chi_{\perp}}{\mathrm{W}^2 \sigma_{\circ}^2/2} \tag{3.17}$$

Larger $\chi_{\perp}$ therefore leads to faster decay and $\chi_{\perp}$ can be obtained by fitting expression (3.16) to experimental data.

3.5 Discussion

In this chapter a series of heat transport models of magnetic islands were presented. First, stationary, two-dimensional, anisotropic heat transport was investigated as in previous works. Next, this model was generalized by employing spatially non-uniform $\chi_{\perp}$ and the dependence of the perturbed $\mathrm{T_e}$ was derived vs the spatial non-uniformity of $\chi_{\perp}$. The effect of heat sources was studied thereafter, assuming stationary thermal conditions, also for the first time. This analysis found that a heat source can lead to the peaking of $\mathrm{T_e}$ when the island has nested flux surfaces. This model shows that temperature peaking occurs even if the cross-field thermal diffusivity is not reduced at the O-point, i.e. the peak is a topological effect. Finally, a relationship between $\chi_{\perp}$ and the time history of the peak evolution was derived for a case when the heat source (or sink) is turned off.

CHAPTER 4

Measurements of cross-field electron thermal diffusivity at the O-point of magnetic islands

In this section the heat transport model of magnetic islands employing spatially non-uniform $\chi_\perp$ is used (Section 3.2) to derive $\chi_\perp$ at the O-point from electron temperature data measured across 2/1 NTM islands in DIII-D. It was found that $\chi_\perp$ at the O-point is 1 to 2 orders of magnitude smaller than the background plasma transport, in qualitative agreement with gyrokinetic predictions [60]. As the anomalously large values of $\chi_\perp$ are often attributed to turbulence driven transport, the reduction of the O-point $\chi_\perp$ is consistent with turbulence reduction found in recent experiments.

4.1 Experimental overview

$m/n = 2/1$ NTMs were studied in a H-mode DIII-D discharge (#134375). Typical plasma parameters are: major radius $R_\circ = 1.74$ m, minor radius $a = 0.56$ m, elongation 1.84. The toroidal magnetic field was $B_T = 1.9$ T and a steady ramp rate of plasma current (I_p) was maintained with a maximum of 1.1 MA [Fig. 8.1 (a)]. The heat transport is analyzed in the $\Delta t = 1500 - 1900$ ms window where the NTM is quasi-stationary. The line averaged core density (interferometry data [91]) was about $3.4 \cdot 10^{19} m^{-3}$ [Fig. 8.1 (b)] in the analyzed window. The ion temperature (T_i, Charge Exchange Recombination data [92]) was comparable with the electron temperature (T_e, ECE and Thomson scattering data) at $R = 199$ cm (which corresponds to the center of magnetic islands on the low field side after NTM onset), see Fig. 8.1 (c). The normalized plasma beta ($\beta_N = \beta a B_T / I_p$) was growing

linearly, similarly to I_p [Fig. 8.1 (d)]. The minimum safety factor (q_{MIN}) reached 2 around 1350 ms [Fig. 8.1 (e)] near the time that a dominant $n = 1$ magnetic mode began to grow: Fig. 8.1 (f) shows the amplitude of the $n = 1$ toroidal harmonic component of magnetic fluctuations measured by Mirnov coils. The island rotation frequency was about 15 kHz resulting in 6000 island cycles within the analyzed window providing a large statistical ensemble for the heat transport study.

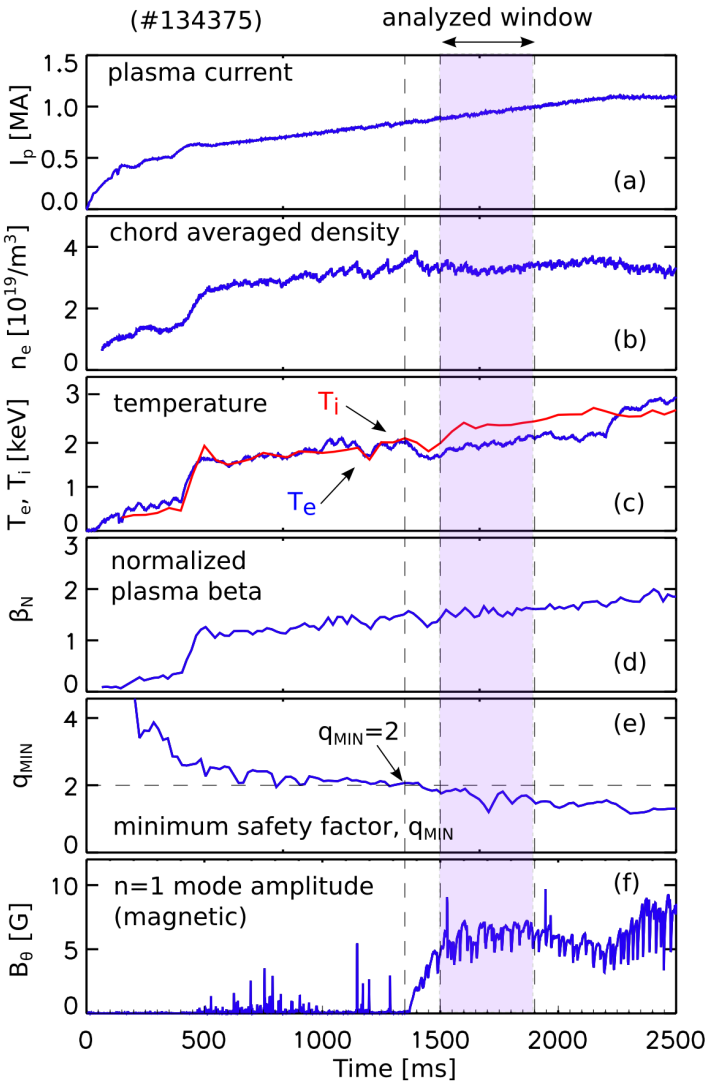

Figure 4.1: Time trace of (a) plasma current, (b) density, (c) T_i and T_e at R = 199 cm (center of 2/1 island), (d) normalized plasma beta, (e) minimum safety factor and (f) n = 1 mode amplitude (magnetic signal).

Representative n, T_e, T_i and q-profile averaged over 20 ms are shown in Fig. 4.2. These

profiles do not show flat spots as the islands make about 300 periods during the window used for averaging. However the temperature profile across the O-point reconstructed in 2D via phase-locking shows flat spot at q=m/n (see later in Fig. 4.4).

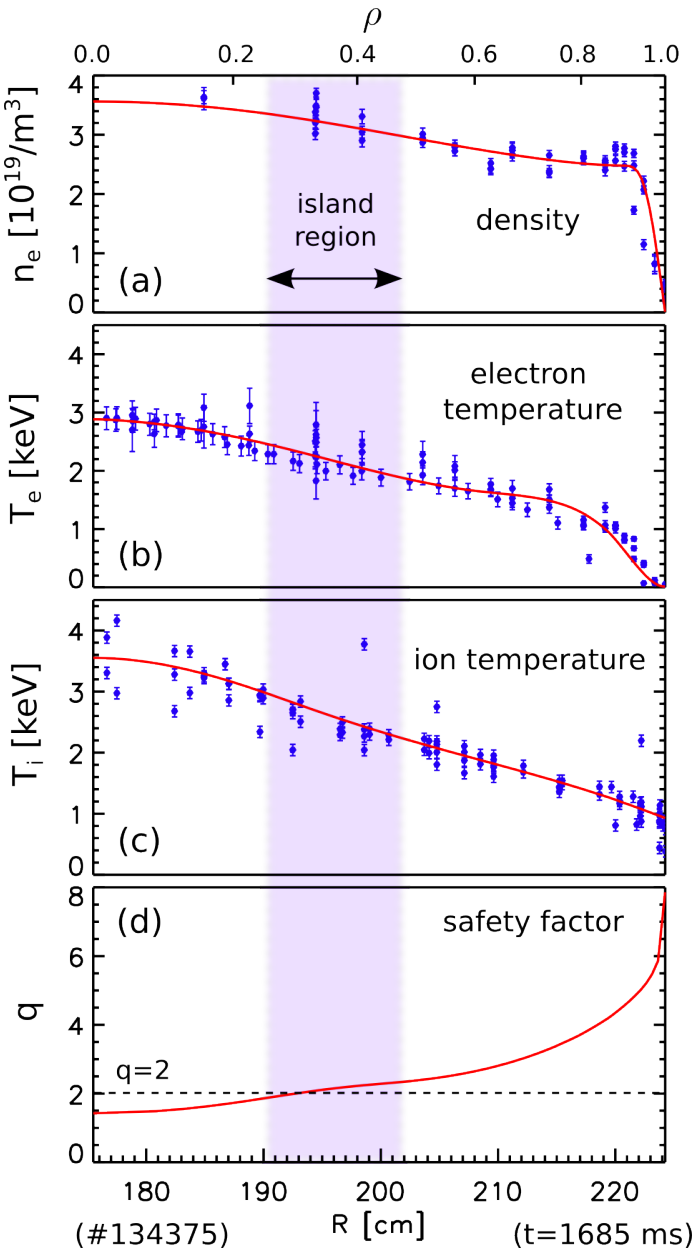

Figure 4.2: Experimental profiles at $t = 1685$ ms averaged over $\Delta t = 20$ ms after NTM onset: (a) chord averaged density, (b) T_e, (c) T_e and (d) q. The solid lines are spline fits on (a), (b) and (c).

The island structure and heat transport are analyzed using the DIII-D electron cyclotron

radiometer [77] that provides local T_e. The typical saturated island full width is about 12 cm, see the example of flattened T_e at the $q = 2$ rational surface shown in Fig. 9.4 (repeat of Fig. 2.5). The good alignment of the magnetic islands with the $q = 2$ rational surface and the $n = 1$ toroidal mode number [Fig. 8.1 (f)] is consistent with an $m/n = 2/1$ tearing mode.

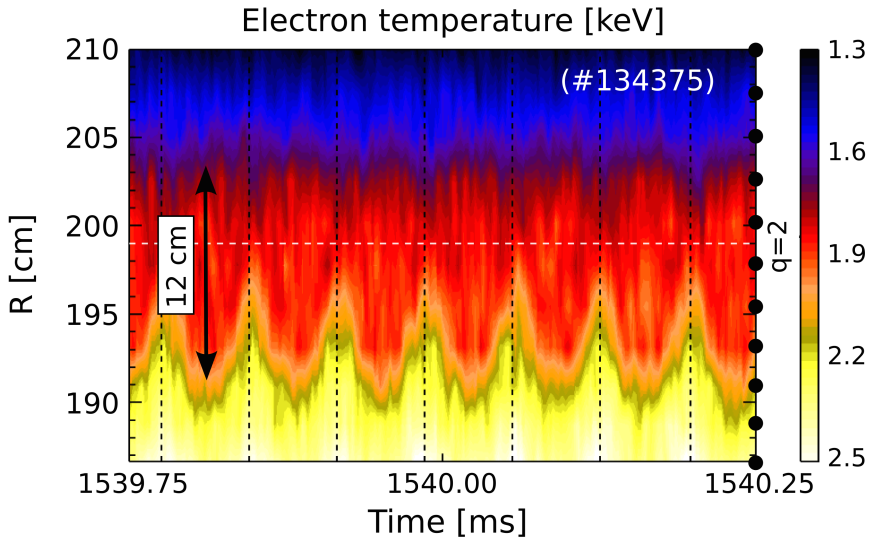

Figure 4.3: Raw ECE data shows T_e flat spots of full width W $\approx$ 12 cm. Circles on the right vertical axis mark the center of the ECE detection locations. The vertical dashed lines mark the X-point times and the light horizontal dashed line indicates the $q = 2$ surface.

The 2D T_e profile across the island was reconstructed via phase-locking the raw T_e data via the method described in Subsection 2.3.1. The optimal value of the phase locking time $\Delta\tau$ will be obtained in Subsection 4.2 where the heat transport model will be compared with experimental data. An example of phase-lock averaged T_e contour and average X-point and O-point T_e profiles are shown in Fig. 4.4 (repeat of Fig. 2.6. The X-point profile is not flattened but the O-point profile is flattened in about 12 cm radial range as expected from an island [Fig. 4.4 (b)].

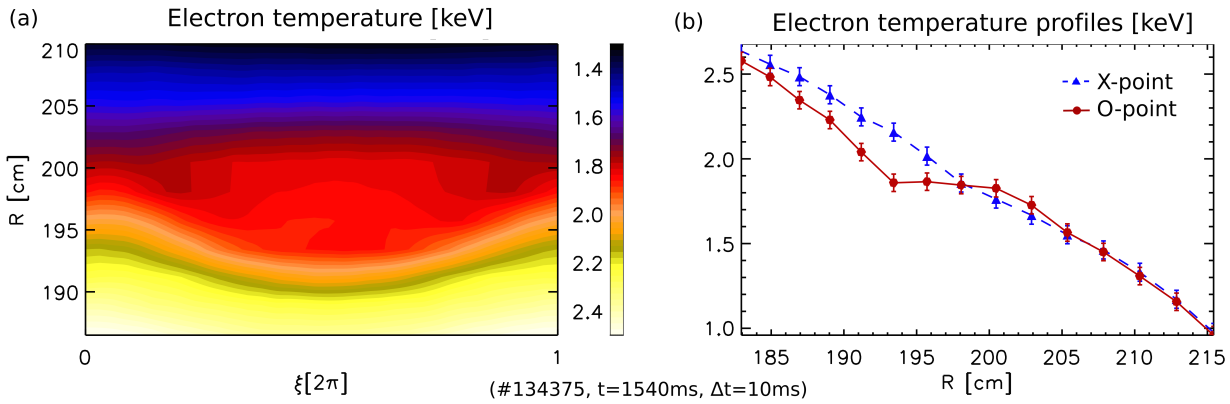

Figure 4.4: (a) $T_e(r, \xi)$ phase-lock averaged over 10 ms (about 150 island cycles using data in Fig. 9.4)), error bars are the standard deviations. (b) $T_e(r)$ across the X-point ($\xi = 0$ or 2π) and O-point ($\xi = \pi$).

4.2 Determination of island fit parameters

To obtain the sensitivity of $\chi_\perp$ to $\nabla_\perp T_e$ (i.e. ε) and other island parameters (w and A), the first harmonic of the model solution $T_1^M(r_j)$ (see eq. (3.6)) was fitted to the first harmonic of the phase-lock-averaged ECE temperature $\langle T_1(r_j, t_{c(i)})\rangle$ with chi-square ($\overline{\chi}^2$) minimization:

$$\overline{\chi}^2 = \sum_{j=1}^{15} \frac{(T_1^M(r_j) - \langle T_1(r_j, t_{c(i)})\rangle)^2}{\sigma_1^2(r_j, t_{c(i)})} \tag{4.1}$$

where $\langle T_1(r_j, t_{c(i)})\rangle$ and $\sigma_1(r_j, t_{c(i)})$ are the mean value and the standard deviation of the $n = 1$ component of the angular decomposed ($\xi \to n$) T_e, respectively. The determination of higher-order harmonics is less accurate due to their small values compared to the first harmonic amplitudes [56]. Also, mode coupling [93, 94] could contribute to the second harmonic which can not be captured by a single island model. $\langle T_1(r_j, t_{c(i)})\rangle$ was calculated from the phase-lock averaged T_e (defined by equation (2.6)), while the standard deviation $\sigma_1(r_j, t_{c(i)})$ was calculated from the first harmonics of each island within the phase-locking windows:

$$\sigma_1^2(r_j, t_{c(i)}) = \frac{1}{N} \sum_{l=0}^{N-1} \Big(\langle T_1(r_j, t_{c(i)})\rangle - T_1(r_j, t_{i+l}) \Big)^2 \tag{4.2}$$

$\sigma_1(r_j, t_{c(i)})$ is interpreted as the measurement error and it is attributed to small variations of the island within the window, residual of various plasma phenomena which are not phase

coupled to the NTM (e.g. small scale fluctuations due micro-turbulence, edge localized modes, Alfvén waves, etc.) and noise of the diagnostic (dominated by amplifier noise). As the solution of the model is parametrized by the set $\{\mathrm{w}, \chi_\perp/\chi_\parallel, \mathrm{A}, \mathrm{r_s}, \nabla_\perp \mathrm{T}(r_s)\}$, the minimum of $\overline{\chi}^2$ yields the best fit value of each parameter for each phase-lock averaged $\mathrm{T_e}$ profile, i.e. the time series of the parameters.

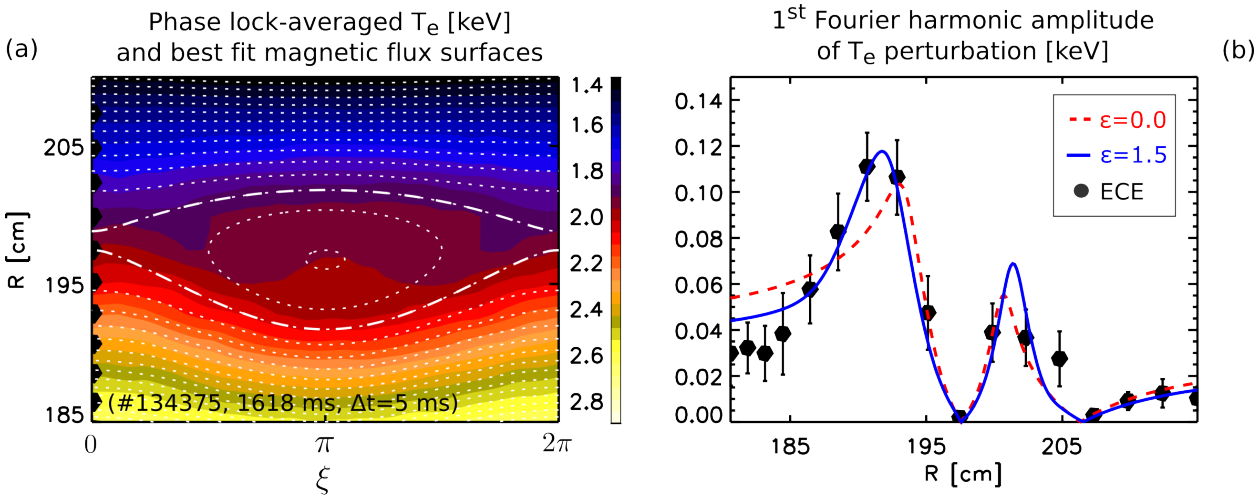

Best fit parameters with ε=0.0: w=4.0 cm, w_C=0.6 cm, A=-0.45, $Chisqr_{RED}$=2.5
Best fit parameters with ε=1.5: w=5.0 cm, w_C=0.8 cm, A=-0.55, $Chisqr_{RED}$=1.5

Figure 4.5: Comparison of experimental $\mathrm{T_e}$ data with the solutions of the diffusion models. (a) Phase-lock averaged $\mathrm{T_e}$ and Ω. (b) Amplitude of 1st Fourier harmonic of experimental $\delta\mathrm{T_e}$ and the best fit solution of the transport model with spatially uniform $\chi_\perp$ ($\varepsilon = 0$) and with spatially non-uniform $\chi_\perp$ ($\varepsilon = 1.5$).

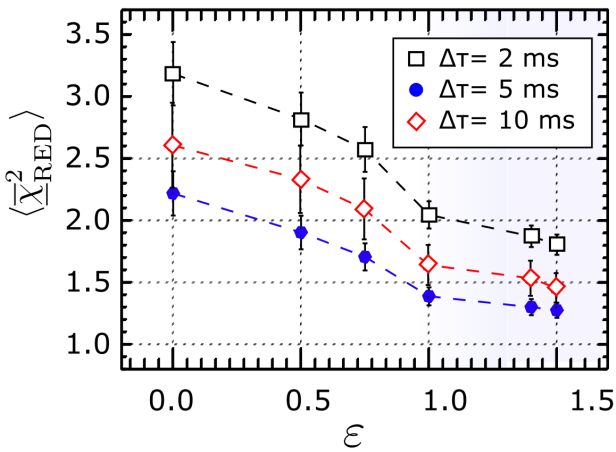

Figure 4.6: Higher ε (corresponding to smaller $\chi_\perp$ at O-point) leads to better fits.

Example of the experimental $\mathrm{T_e}$ and the best fit solution are shown in Fig. 4.5 (a) and (b).

The T_e contour together with Ω of the best fit at $\varepsilon = 1.5$ is shown in Fig. 4.5 (a). The first harmonic of T_e is shown in Fig. 4.5 (b) together with the best fit solution at $\varepsilon = 0.0$ and $\varepsilon = 1.5$. The $\varepsilon = 1.5$ model predicts an island half width of w =5 cm and the island is peaked toward the core plasma as in references [66, 68] with asymmetry parameter $A = -0.55$. The scale island width is w_c=0.8 cm. The island width is typically smaller by about 20% with uniform $\chi_\perp$ ($\varepsilon = 0.0$), and the transport anisotropy is $\chi_\perp/\chi_\parallel \approx 2 \cdot 10^{-7}$. The standard deviations of the fit parameters w, w/w_c and A were estimated to about 20% while the standard deviation of $\chi_\perp/\chi_\parallel$ is 1 order of magnitude. Using a window of 5 ms for phase-locking (75 island cycles) the uncertainties of the mean values of w, w/w_c and A within a phase-locking window are about $20\%/\sqrt{74} \approx 2.3\%$ and the uncertainty of the mean of $\chi_\perp/\chi_\parallel$ is about 30%.

The agreement between the experimental data and the numerical solution is significantly better with non-uniform $\chi_\perp$ in the range $R < 195$ cm, [Fig. 4.5 (b)]. We point out that the first Fourier harmonic amplitude measured via Thomson scattering in MAST [68] (top right panel in Fig. 7) systematically deviates from the best fit solution of the spatially uniform $\chi_\perp$ model as here [Fig. 4.5 (b)].

To determine the sensitivity of $\chi_\perp$ to $\nabla_\perp T_e$ the best fits of the model at different values of ε are compared using the reduced chi-square test: $\underline{\overline{\chi}}^2_{\mathrm{RED}} = \underline{\overline{\chi}}^2 \cdot \nu^{-1}$, where ν is the number of observations (15) minus the number of fit parameters (5). Typically $\underline{\overline{\chi}}^2_{\mathrm{RED}} >> 1$ indicates a poor fit, i.e. the difference between the observation and the model is larger than the measurement error. $\underline{\overline{\chi}}^2_{\mathrm{RED}} > 1$ indicates that the model has not completely captured the data or the measurement errors were underestimated. $\underline{\overline{\chi}}^2_{\mathrm{RED}} < 1$ indicates over-fitting or that the measurement errors were overestimated. Finally, $\underline{\overline{\chi}}^2_{\mathrm{RED}} \approx 1$ is obtained when the agreement between observations and model estimates is comparable with the measurement errors [95]. $\langle \underline{\overline{\chi}}^2_{\mathrm{RED}} \rangle$ calculated at 6 different values of ε (averaged in the $\Delta t = 1500 - 1900$ ms window corresponding to 6000 island cycles) shows that the best fit solution is obtained in the range $\varepsilon = 1.0 - 1.5$ regardless of the phase-locking time $\Delta\tau$ [Fig. 4.6]. However, $\langle \underline{\overline{\chi}}^2_{\mathrm{RED}} \rangle$ has a minimum at $\Delta\tau = 5$ ms, giving the best value of the

phase-locking time for the transport study. On one hand, if the island evolves/moves radially on $\Delta\tau > 5$ ms timescale then the phase-locked island is smeared enough to prevent the model from capturing the data. On the other hand, when $\Delta\tau < 5$ ms the phase-locking is not effective enough, i.e. other plasma phenomena not phase-locked to the island persists in the data.

$\langle \overline{\chi}^2_{\mathrm{RED}} \rangle$ of the fit is $2.2 \pm 3\%$ (where $\pm 3\%$ is the standard deviation of $\langle \overline{\chi}^2_{\mathrm{RED}} \rangle$) at $\varepsilon = 0.0$ and it gradually decreases as $\chi_\perp$ at the O-point is decreased until it saturates around $1.27 \pm 3\%$ in the range $\varepsilon = 1.0 - 1.5$ [Fig. 4.6]. This shows that the spatially non-uniform $\chi_\perp$ model is a better fit to the experimental data. Given the large statistical sample size and that $\langle \overline{\chi}^2_{\mathrm{RED}} \rangle$ at $\varepsilon = 1.5$ is consistently smaller then at $\varepsilon = 0.0$ by about 50% it can be concluded that $\chi_\perp$ is reduced at the O-point and the best fit value is $\varepsilon \approx 1.5$. Next, we identify the lower and upper bounds of the best estimator of ε. $\varepsilon > 1.5$ is unphysical as it describes $\chi_\perp < 0$ at the O-point and the lowest possible value of $\chi_\perp$ is set by neoclassical transport (a physical constraint). This gives the upper bound of the estimation: $\varepsilon \leq 1.5$. To obtain the lower bound the time series of $\overline{\chi}^2_{\mathrm{RED}}$ are analyzed. For example, one can differentiate between two fits obtained with two different values of ε (ε_1 and ε_2) if the following inequality is satisfied:

$$|\langle \overline{\chi}^2_{\mathrm{RED}}(t, \varepsilon_1) \rangle - \langle \overline{\chi}^2_{\mathrm{RED}}(t, \varepsilon_2) \rangle| \tag{4.3}$$

$$> |\sigma_{\varepsilon_1} + \sigma_{\varepsilon_2}| \tag{4.4}$$

where σ_{ε_1} and σ_{ε_2} are the uncertainties of $\langle |\overline{\chi}^2_{\mathrm{RED}}(t, \varepsilon_1)| \rangle$ and $\langle |\overline{\chi}^2_{\mathrm{RED}}(t, \varepsilon_2)| \rangle$, respectively. The $\overline{\chi}^2_{\mathrm{RED}}(t, \varepsilon)$ series are not fully stochastic as slow variations of the plasma profiles have a common imprint in them. This non-stochastic, time dependent contribution leads to the increase of the standard deviations σ_ε which prevents one from distinguishing the fits in the $\varepsilon = 1.0 - 1.5$ range [Fig. 4.6]. To distinguish between the fits in this range we remove this

common time dependent contribution by analyzing the differences:

$$\Delta\overline{\chi}^2_{\mathrm{RED}} = \overline{\chi}^2_{\mathrm{RED}}(\varepsilon_\circ) - \overline{\chi}^2_{\mathrm{RED}}(\varepsilon) \tag{4.5}$$

Here $\varepsilon_\circ = 1.5$ and ε can take values between 0.0 and 1.4. We are looking for the highest value of ε for which $\langle\Delta\overline{\chi}^2_{\mathrm{RED}}\rangle$ is inconsistent with zero, i.e. where the fit is significantly different from the $\varepsilon = 1.5$ fit. When $\varepsilon < 1.4$ the $\langle\Delta\overline{\chi}^2_{\mathrm{RED}}\rangle$ is inconsistent with zero which is seen from the fact that $\langle\Delta\overline{\chi}^2_{\mathrm{RED}}\rangle$ is larger then the standard deviation of $\langle\Delta\overline{\chi}^2_{\mathrm{RED}}\rangle$, see Fig. 4.7. Fig. 4.7 (a) shows the probability distribution functions (PDF) of $\Delta\overline{\chi}^2_{\mathrm{RED}}$ and

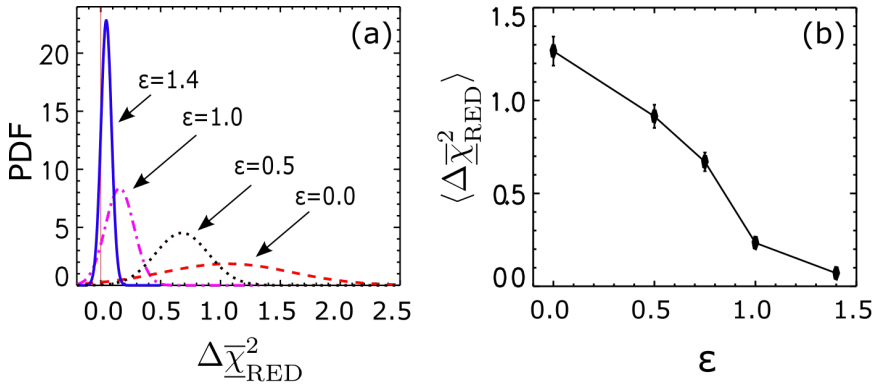

Figure 4.7: (a) Probability distribution functions (PDF) of the differences defined by eq. (4.5) and (b) the mean values of the distributions (error bars indicate the standard deviation of the mean).

Fig. 4.7 (b) shows that $\langle\Delta\overline{\chi}^2_{\mathrm{RED}}\rangle$ goes to nearly zero when $\varepsilon = 1.4$. As 80 independent fits are obtained in the 400 ms window (using $\Delta\tau = 5$ ms windows for the phase locking) and the width of the distributions are about 0.5-0.05 the uncertainties of $\langle\Delta\overline{\chi}^2_{\mathrm{RED}}\rangle$ are relatively small $\approx 5 \times 10^{-2-3}$ allowing one to constrain ε in the 1.5-1.4 range. In the following we estimate the absolute value of $\chi_\perp$ at the island O-point by fitting the $\varepsilon = 1.4$ and $\varepsilon = 1.5$ model predictions outside the island to $\chi_\perp$ obtained with TRANSP power balance calculation.

4.3 Determination of $\chi_\perp$ at the O-point of the island

TRANSP is a time-dependent transport analysis code used for energy, particle and momentum transport calculations [61]. TRANSP uses the experimentally measured density, T_e, T_i, impurity density, rotation and radiation profiles to calculate local radial transport coefficients assuming $m = n = 0$ symmetry. The sampling rate of the radial electron thermal diffusivity profile resulting from the power balance calculation $\chi_{\mathrm{TRANSP}}^{Power\ b.}$ as well as the neoclassical value $\chi_{\mathrm{TRANSP}}^{Neoclass.}$ is limited to 20 ms due to the temporal resolution of the equilibrium magnetic field reconstruction. This in fact corresponds to about 300 island cycles. As such, the O-point and X-point profile data are averaged and a spline fit is used as input for TRANSP [see examples on Fig. 4.2]. As discussed in the introduction TRANSP can not determine the cross-field diffusivity across the island, hence we do not try to capture short spatial details of the profile by the fitting procedure but to estimate the transport of the background plasma outside of the island region.

Also, the equilibrium magnetic field reconstruction used by TRANSP does not incorporate the $m/n = 2/1$ perturbation imposed by the island. Hence the TRANSP output is interpreted as the radial electron thermal diffusivity of the background plasma. The power balance calculation yields $\chi_{\mathrm{TRANSP}}^{Power\ b.} \approx 1.7\ \mathrm{m}^2/\mathrm{s}$ and the neoclassical value is $\chi_{\mathrm{TRANSP}}^{Neoclass} \approx 0.01\ \mathrm{m}^2/\mathrm{s}$ at $q = 2$ [Fig. 4.8].

The two-dimensional diffusion model studied here predicts $\chi_\perp/\chi_\parallel \propto w_c^4$ ratio only (equation (3.5)), not $\chi_\perp$ and $\chi_\parallel$ separately. $\chi_\parallel$ is often estimated with a semi-classical formula [66]. Given the best fit value of ε we do not need to estimate $\chi_\parallel$ as equations (3.9) and (3.10) directly yield the ratio $R_\perp = \chi_\perp^{\mathrm{O}}/\chi_\perp^{\mathrm{B}}$, where $\chi_\perp^{\mathrm{O}}$ is the cross-field diffusivity at the O-point and $\chi_\perp^{\mathrm{B}}$ is that of the background plasma (i.e. $\chi_\perp^{\mathrm{B}} = \chi_\perp|_{X\approx -2}$). Requiring the electron heat flux of the two-dimensional model outside the island region to match the TRANSP power balance calculation result, i.e setting $\langle\chi_\perp^{\mathrm{B}}\rangle = \langle\chi_{\mathrm{TRANSP}}^{Power\ b.}\rangle$, yields the

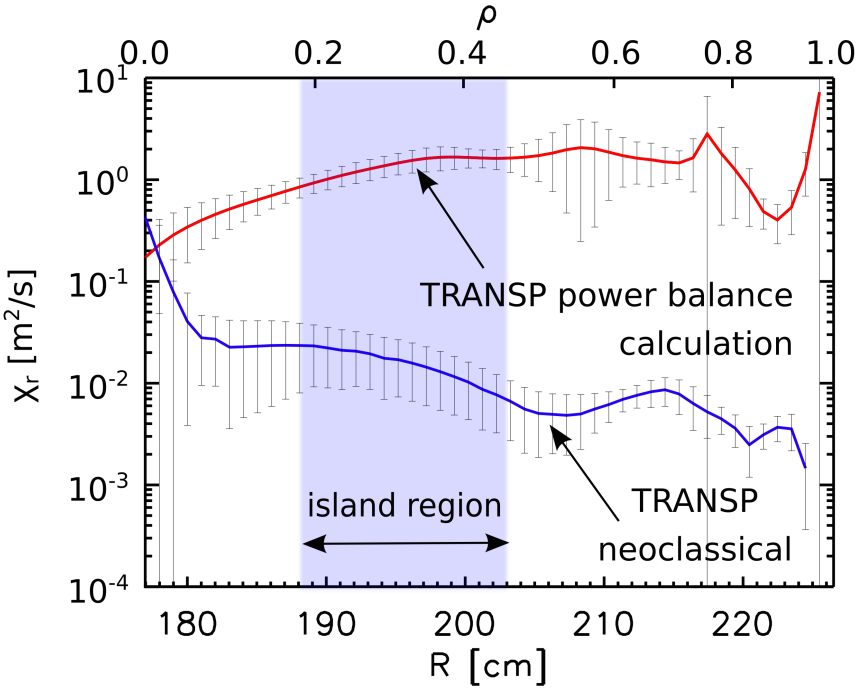

Figure 4.8: Radial electron thermal diffusivity profiles calculated by TRANSP. (Δt =1500-1900 ms).

estimation of $\chi_\perp$ at the O-point:

$$\chi_\perp^{\mathrm{O}} = \langle \chi_{\mathrm{TRANSP}}^{Power\ b.} \rangle \mathrm{R}_\perp \tag{4.6}$$

Using this prescription the time series of $\chi_\perp^{\mathrm{O}}$ are shown in Fig. 4.9 for $\varepsilon = 1.4$ and 1.5. Due to equation (4.6) $\langle \chi_\perp^{\mathrm{B}} \rangle$ agrees with the TRANSP result. Inside the island the model predicts $\chi_\perp$ reduction and $\chi_\perp^{\mathrm{O}}$ approaches $\chi_{\mathrm{TRANSP}}^{Neoclass.}$ as ε goes to 1.5. $\overline{\chi}^2_{\mathrm{RED}}$ decreases gradually as $\chi_\perp$ is decreased, as follows from Fig. 4.6. As $1.4 < \varepsilon < 1.5$ the estimated value of the electron cross-field thermal diffusivity at the O-point is 0.1 m^2/s $< \chi_\perp <$ 0.01 m^2/s (as indicated by the shaded region in Fig. 4.9), i.e. $\chi_\perp$ is decreased by about 1 to 2 orders of magnitude at the island O-point compared to the background plasma. This result is consistent with heat pulse propagation studies which found the reduction of $\chi_\perp$ at the O-point of static islands by 1 order of magnitude in LHD [62] and TEXTOR [63]. Finally, we point out that the heat flux across the island region in this procedure is fixed when ε is

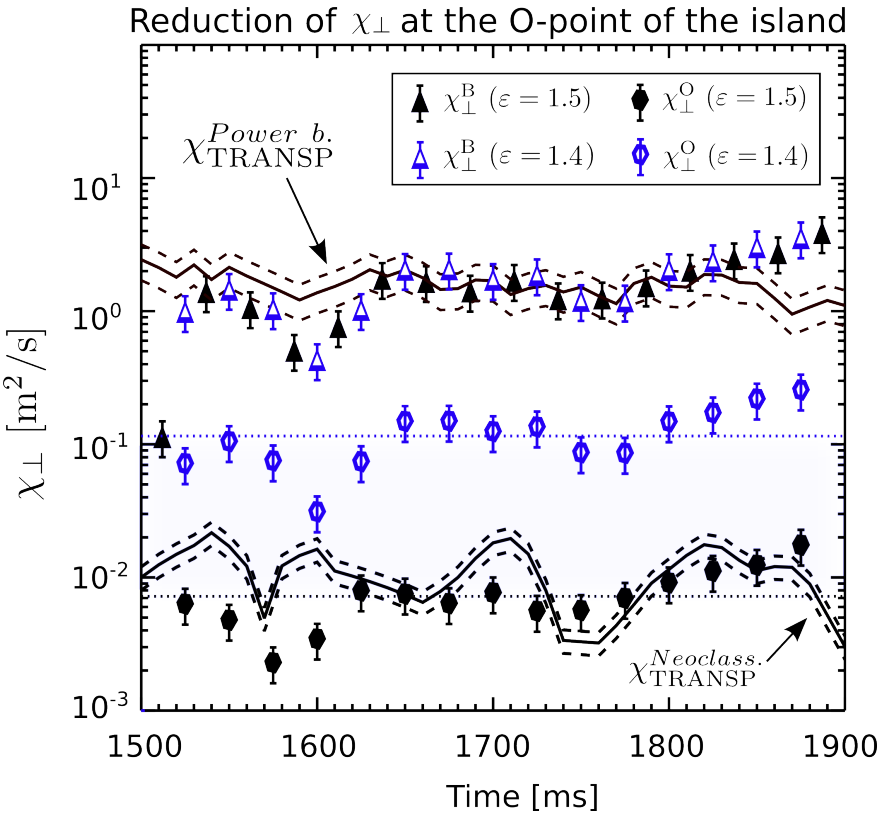

Figure 4.9: $\chi_\perp$ obtained with the two-dimensional transport model at $\varepsilon = 1.4$ and 1.5 is compared with the TRANSP prediction ($\chi_\perp^B$ and $\chi_\perp^O$ are the cross-field thermal diffusivities outside the island and at the O-point, respectively).

varied as the gradient of the solutions at the boundary is matched to experimental data and $\chi_\perp$ outside the island region is matched to $\chi_{TRANSP}^{Power\ b.}$.

4.4 Discussion

A heat transport model of magnetic islands employing spatially non-uniform $\chi_\perp$ was used to derive $\chi_\perp$ at the O-point of 2/1 NTM islands from experimental T_e data. $\overline{\chi}^2_{RED}$ of the fit decreases gradually by about a factor of 2 as $\chi_\perp$ at the O-point approaches the neoclassical limit. $\chi_\perp$ at the island O-point falls in the range 0.01-0.1 m^2/s while $\chi_\perp$ of the background plasma is about 1.7 m^2/s. Interestingly, in heat pulse propagation studies [62, 63] it was found that $\chi_\perp$ is reduced by about 1 order of magnitude at the O-point of islands generated by resonant magnetic perturbation. In those cases, an anomalous $\chi_\perp$ is

reasonable as the deposited heat at the O-point modifies ∇T_e and ∇T_i (turbulence drives), hence it is expected to increase $\chi_\perp$ itself.

CHAPTER 5

Modifications of turbulence fluctuation power across magnetic islands

This chapter reports the first localized measurements of low-k $\widetilde{n}$ (via BES and FIR), intermediate-k $\widetilde{n}$ and low-k $\widetilde{T}_e$ (via CECE) being modified by naturally growing, freely rotating 2/1 NTM magnetic islands in the DIII-D tokamak. These measurements show that mean turbulence levels (averaged over the island rotation) as well as gradients of T_e, T_i and n are not modified when the island width (W) is smaller than a threshold of $W_t \approx 5$ cm. On the other hand, when $W > W_t$ the reduction of the mean turbulence levels is observed radially inside the island region in sync with radially localized reduction of mean ∇T_e, ∇T_i and ∇n. Radially outside the island region an enhancement of the mean fluctuation levels is observed along with radially localized increase of mean gradients. Finally, $\widetilde{n}$ is reduced at the O-point compared to the X-point when the islands are large [86] leading to a 15% modulation of the turbulence envelope across the island that is nearly in phase with the temperature modulation.

These measurements also allow the determination of turbulence penetration length scales $L_{\widetilde{n}}$ and $L_{\widetilde{T}_e}$ at the island separatrix. Turbulence penetration is predicted to affect NTM stability via (i) increasing the seed island width (W_c) required for neoclassical growth [27] and (ii) partially restoring the pressure gradient (∇p) and bootstrap current (j_{BS}) at the O-point of large islands [7]. Beyond NTM stability, $L_{\widetilde{n}}$ and $L_{\widetilde{T}_e}$ may provide insight into turbulence spreading considering that the interior of the island is a more stable region for drift waves compared to the exterior.

The material of this Chapter has been presented in an APS invited talk (2016) and will be

published in the associated Physics of Plasmas paper.

This Chapter is organized as follows. The experimental overview is given in Section 5.1. The effects of magnetic islands on turbulence are described in Section 5.3 and the scaling of the effects vs. island width as well as turbulence spreading is discussed in Section 5.4.

5.1 Experimental overview

Low- and intermediate-k $\widetilde{\mathrm{n}}$ and low-k $\widetilde{\mathrm{T}}_\mathrm{e}$ was studied across naturally occurring and rotating 2/1 NTMs in reproducible, stationary H-mode plasma conditions utilizing the full complement of DIII-D turbulence diagnostics. The major radius of the magnetic axis was R=179 cm, minor radius a=58 cm, elongation was 1.85. A steady plasma current of 1 MA was maintained [FIG 5.1 (a)], in the stationary state the chord averaged density was $3.8 \times 10^{19}\mathrm{m}^{-3}$ [FIG 5.1 (b)] (interferometry [91]), the toroidal magnetic field was $\mathrm{B_T} = -2.05$ T, normalized plasma beta was 2 ($\beta_\mathrm{N} = \beta\, a\mathrm{B_T}/\mathrm{I_P}$) and neutral beam power was 8 MW. $\mathrm{T_e}$ and $\mathrm{T_i}$ were about 2.6 keV in the stationary state at $q = 2$ [FIG 5.1 (c)]. The major radius coordinate and the square root of the normalized toroidal flux surface label of the $q = 2$ rational surface was $R_\mathrm{s} = 203$ cm and $\rho = 0.42$, respectively. Mirnov coils at the tokamak edge show that the $n = 1$ magnetic amplitude initially grows to 12 G [FIG 5.1 (d)] and the associated 2/1 island full width was W $\approx$ 11 cm, rotating at 5 kHz and well aligned with the $q = 2$ surface. The onset of these NTMs do not always correlate with MHD events (e.g. sawtooth crashes or Edge Localized Modes), therefore it could be the case that they are driven by turbulence [96].

β_N has decreased during the NTM growth phase as indicated by the decrease of n and $\mathrm{T_e}$ in FIG 5.1 (b) and (c). This decrease of β_N then led to the decrease of the NTM amplitude, followed by a quasi-stationary state of about 3 seconds. The island structure was monitored via the DIII-D ECE radiometer [77]. As mentioned before, these islands saturated to a full width of about W = 11 cm, determined by fitting the solutions of a heat transport model of magnetic islands [Section 4.2] to the experimentally determined $B_1(\rho)$. This method is applicable when the island size is larger than the radial resolution of the ECE measurement

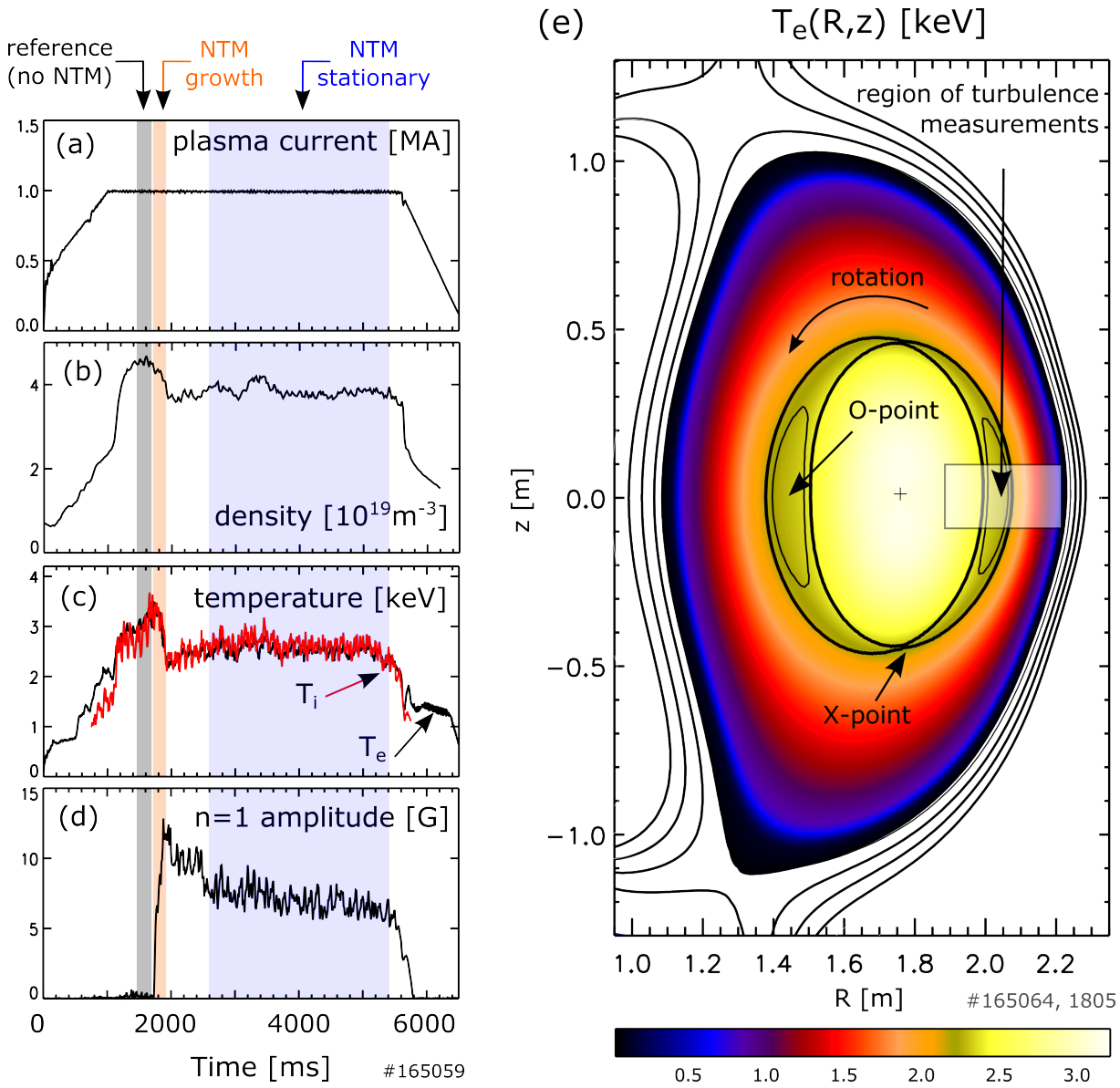

Figure 5.1: Time history of (a) plasma current, (b) chord averaged electron density, (c) T_e and T_i at $q = 2$, (d) $n = 1$ amplitude (magnetic RMS). (e) Plasma shape (EFIT), $T_e(R, z)$ reconstructed from 1D ECE data and over plotted the $\Omega = 1$ (island separatrix) and $\Omega = 0$ contours (thin and thick solid lines around $T_e \approx 2.3$ keV, respectively).

and when the island is at least partially flattened, which is the case for islands larger then 5 cm. The determination of W was extended to the range of small islands by combining this method with external magnetic measurements [59]. T_e is reconstructed in the $R - z$ plane as described in Subsection 2.3.2, see Fig. 5.1 (repeat of Fig. 2.7).

Radially resolved turbulence measurements were performed via BES, DBS and CECE.

Three windows were used for analysis which are highlighted in FIG 5.1 (a-d):

1. A reference window of 50 ms before NTM onset is used to obtain equilibrium quantities (e.g. unperturbed radial profile of $\widetilde{\mathrm{n}}$ and $\widetilde{\mathrm{T}}_\mathrm{e}$).

2. Scaling of changes in turbulence vs island width is studied during the NTM growth phase.

3. Finally, a long window during stationary NTM is used for CECE analysis which requires long data series.

5.2 Plasma profiles and unstable drift waves (GENE)

The profiles of $\mathrm{n_e}$ (Thomson scattering [75]), $\mathrm{T_e}$ (ECE and Thomson scattering) and $\mathrm{T_i}$ (Charge Exchange Recombination [92]) are shown in FIG. 5.2 (a)-(c) averaged over 20 ms (100 island turnover times) before NTM onset and after the magnetic island has grown to a size of about $\mathrm{W} = 9$ cm but not yet saturated. These profiles are steep without an island but are flattened at $q = 2$ with island. Consequently, the inverse scale lengths $\mathrm{L_n^{-1}} = \mathrm{n}^{-1}\partial_R \mathrm{n}$, $\mathrm{L_{Te}^{-1}} = \mathrm{T_e^{-1}}\partial_R \mathrm{T_e}$ and $\mathrm{L_{Ti}^{-1}} = \mathrm{T_i^{-1}}\partial_R \mathrm{T_i}$ are reduced inside and tend to be increased outside of the island region, see FIG. 5.2 (d)-(f). As the inverse scale lengths act as turbulence drives, $\widetilde{\mathrm{n}}$ and $\widetilde{\mathrm{T}}_\mathrm{e}$ reduction inside and increase outside the island region is expected.

Determining the type of unstable drift-waves across the island requires nonlinear gyrokinetic simulations with magnetic islands and plasma parameters ($\mathrm{T}_e/\mathrm{T}_i$, $\nabla \mathrm{T}_e$, $\nabla \mathrm{T}_i$, $\nabla \mathrm{n}$, geometry, rotation, etc.) carefully matched to the experiment. This is beyond the scope of this thesis but will be the focus of future work. To identify the type of dominant micro-instabilities of the background plasma at $q = 2$ before NTM onset, the growth rates and frequencies of the fastest growing micro-instabilities were calculated via linear GENE gyro-kinetic simulations [52] [FIG. 5.3] using the experimental profiles measured before NTM onset [FIG. 5.2]. These flux-tube simulations were run on ion- and electron-scales ($k_\theta \rho_s = 0.1 - 100.0$), used two fully kinetic species (deuterons and electrons) and included

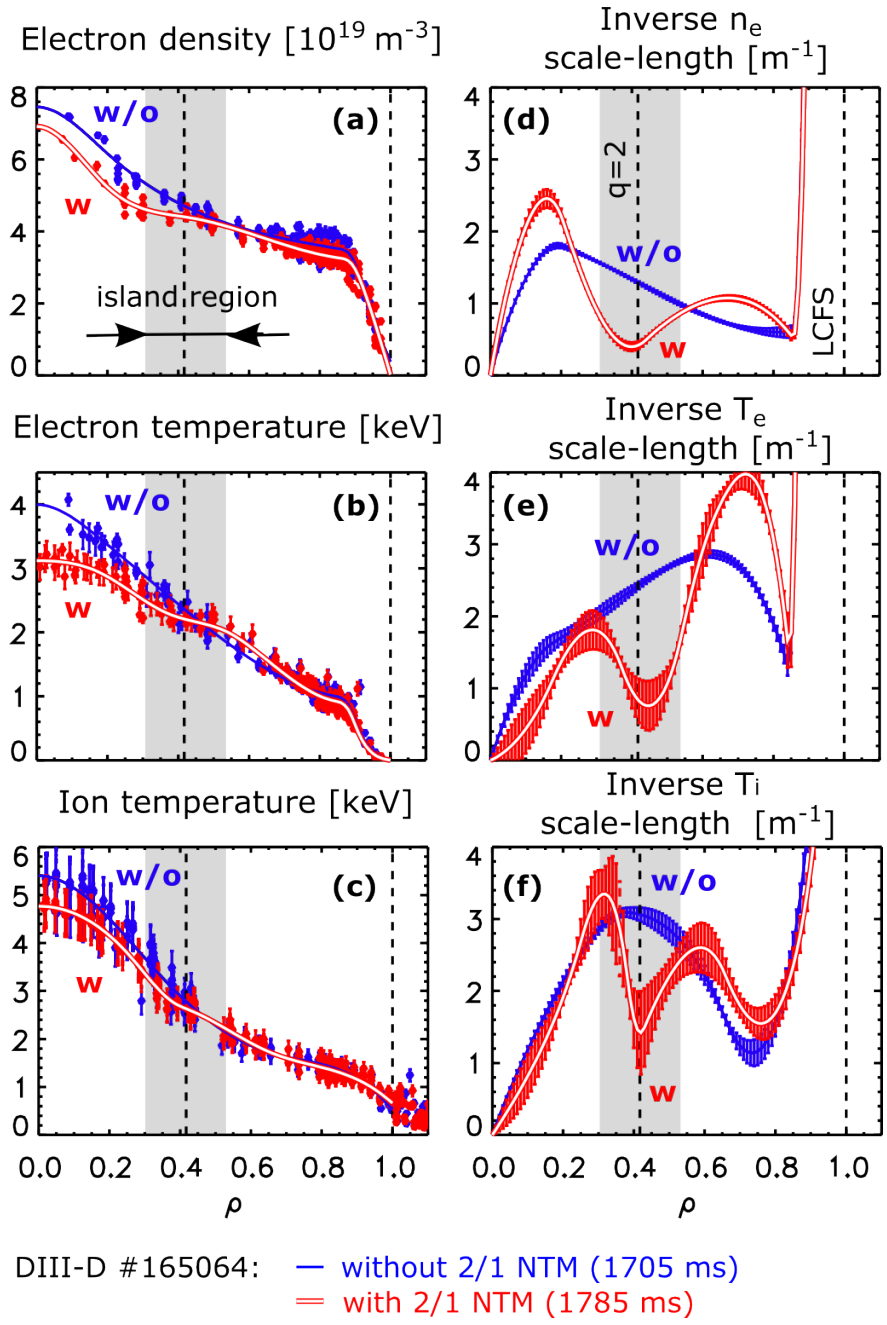

Figure 5.2: Rotation averaged plasma profiles and inverse scale lengths before NTM onset (w/o) and after NTM saturation (w): (a) n_e, (b) T_e and (c) T_i, (d) L_n^{-1}, (e) L_{Te}^{-1} and (f) L_{Ti}^{-1}. The profiles are fitted with cubic splines to determine the scale lengths.

electromagnetic effects. Here k_θ is the poloidal wavenumber and $\rho_s = c_s/\omega_i \approx 0.4$ cm, where $c_s = \sqrt{T_e/m_i}$, and m_i and ω_i are the ion mass and cyclotron frequency, respectively. A dominant ion mode in the range of the Ion Temperature Gradient (ITG) instability that

propagates in the ion diamagnetic direction was found at long wavelengths ($k_\theta \rho_s < 2$), while at shorter wavelengths in the range of Trapped Electron Mode (TEM) and Electron Temperature Gradient (ETG) instabilities ($2 < k_\theta \rho_s < 100$) the dominant mode propagates in the electron diamagnetic direction [FIG. 5.3]. In contrast, the simulations show that all modes are stable when using the profiles after NTM saturation [FIG. 5.2]. This suggest that all modes are linearly stable at the O-point of the islands.

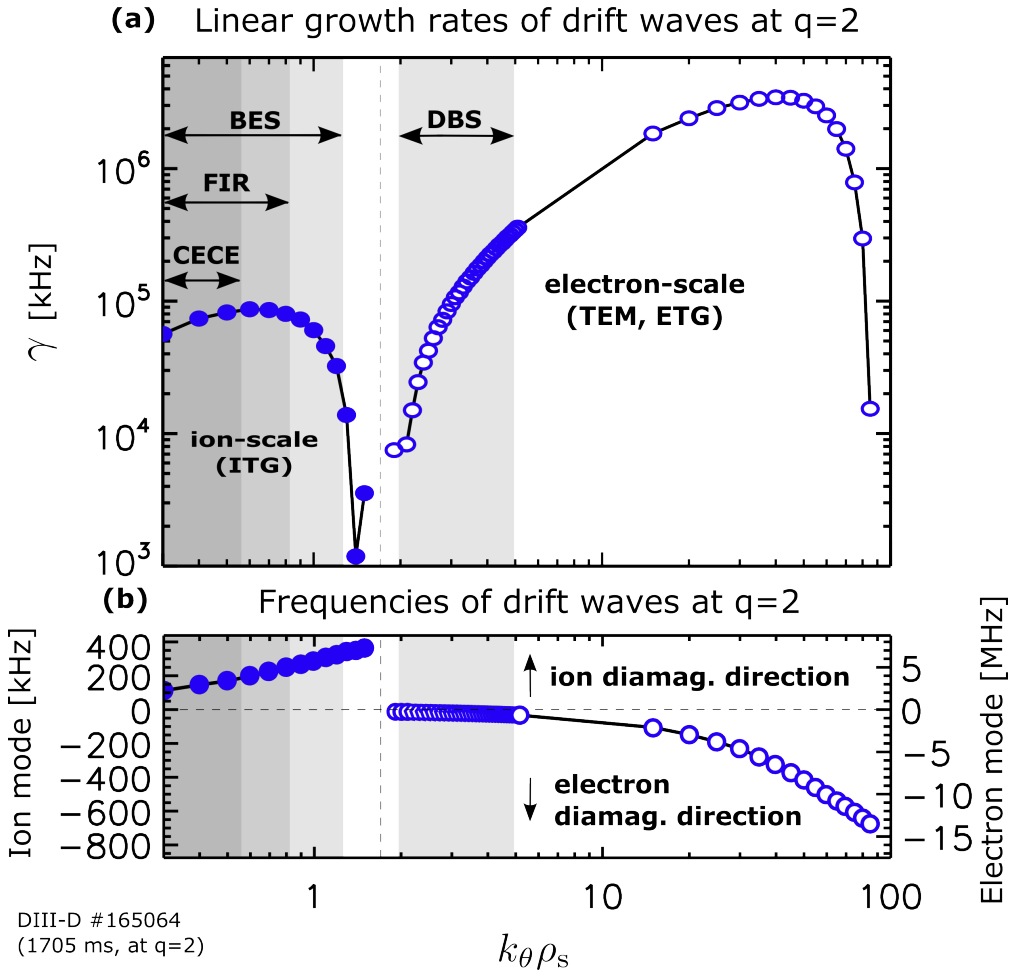

Figure 5.3: (a) Linear growth rates and (b) frequencies of unstable drift waves at $q = 2$ *before* NTM onset via GENE (see input experimental profiles in FIG. 5.2). Ion modes are shown with filled circles, electron modes are shown with open circles. Shaded columns mark the sensitivity range of the turbulence diagnostics.

BES, FIR and CECE are sensitive in the $k_\theta \rho_s < 1.0$, $k_\theta \rho_s < 0.7$ and $k_\theta \rho_s < 0.5$ range, respectively [FIG. 5.3]. Hence, the fluctuations probed by these diagnostics are presumably due to ITG turbulence. Complementing these low-k measurements, DBS is sensitive in the

$2 < k_\theta \rho_s < 5$ range, and therefore the probed DBS fluctuations are potentially due to TEM or low-k ETG turbulence.

5.3 Effect of islands on turbulent fluctuation power

The turbulent fluctuation power ($\widetilde{n}^2(R,\xi)$) is written as the sum of the unperturbed radial profile ($\overline{\widetilde{n}^2}(R)$) in the NTM-free plasma and the perturbation ($\delta\widetilde{n}^2(R,\xi)$) due to the island:

$$\widetilde{n}^2(R,\xi) = \overline{\widetilde{n}^2}(R) + \delta\widetilde{n}^2(R,\xi) \tag{5.1}$$

$\widetilde{n}^2(R,\xi)$ is obtained from a series of 10 ms windows during island evolution and $\overline{\widetilde{n}^2}(R)$ is determined from the reference window of 50 ms before NTM onset; see these windows in FIG. 5.1 (a-d). Note that $\overline{\widetilde{n}^2}(R) \geq 0$ but $\widetilde{n}^2(R,\xi) = \widetilde{n}^2(R,\xi) - \overline{\widetilde{n}^2}(R)$ can be negative if the fluctuation level after NTM onset decreases below the level measured before NTM onset. As turbulence is driven by gradients, it is reasonable to look at the perturbation ($\delta\widetilde{n}^2(R,\xi)$) in a Fourier series pertaining terms up to the $k = 1$ harmonic component:

$$\delta\widetilde{n}^2(R,\xi) \approx \widetilde{n}_0^2(R) + \widetilde{n}_1^2(R)\cos(\xi + \Delta\xi_1(R)) \tag{5.2}$$

$\widetilde{n}_0^2(R)$ is the radial profile of the helically averaged part of the perturbation ($k = 0$ response) and is obtained simply by the $\widetilde{n}_0^2(R) = \langle\widetilde{n}^2(R,\xi)\rangle_\xi - \overline{\widetilde{n}^2}(R)$ relation where $\langle\cdots\rangle_\xi$ stands for averaging over ξ which is accomplished in practice by averaging over time (recall that $\xi = \omega_\circ t$ and therefore $\langle\cdots\rangle_\xi \equiv \langle\cdots\rangle_t$). Note, that $\widetilde{n}_0^2(R)$ can be either positive or negative, corresponding to an average increase or decrease, respectively. $\widetilde{n}_1^2(R) \geq 0$ is the amplitude and $\Delta\xi_1(R)$ is the phase of the $k = 1$ component of the perturbation (vs. T_e) and are calculated via standard Fourier analysis in the stationary state. Finally, radial variations unrelated to island physics (e.g. electronic amplifier calibration factors) are removed from the data by calculating the percentage change of $\widetilde{n}_0^2(R)$ and $\widetilde{n}_1^2(R)$ relative to

before NTM onset:

$$\Delta\widetilde{\mathrm{n}}_0^2(R) = \frac{\widetilde{\mathrm{n}}_0^2(R)}{\overline{\widetilde{\mathrm{n}}^2}(R)}, \quad \text{and} \quad \Delta\widetilde{\mathrm{n}}_1^2(R) = \frac{\widetilde{\mathrm{n}}_1^2(R)}{\overline{\widetilde{\mathrm{n}}^2}(R)} \tag{5.3}$$

Similar definitions hold for $\widetilde{\mathrm{T}}_\mathrm{e}$. In this paper, the effect of magnetic islands on turbulence is characterized by the $\Delta\widetilde{\mathrm{n}}_0^2(R), \Delta\widetilde{\mathrm{n}}_1^2(R)$ and $\Delta\xi_1(R)$ dimensionless radial profiles. The evolution of $\Delta\widetilde{\mathrm{n}}_0^2(R)$ during island growth is presented in Subsection 5.3.1 together with $\Delta\widetilde{\mathrm{T}}_{\mathrm{e},0}^2(R)$ obtained in the stationary regime. $\Delta\widetilde{\mathrm{n}}_1^2(R)$ and $\Delta\xi_1(R)$ were calculated in the stationary regime and are presented in Subsection 5.3.2. Finally, the full 2D turbulence response is discussed in Subsection 5.3.3.

5.3.1 Rotation averaged part of turbulence response

NTM growth and saturation takes place in about 100 ms [FIG. 5.1 (d)] providing 10 independent windows of ≈ 10 ms data to study turbulence response to islands of full width ranging from $0 - 11$ cm. Contours of $\mathrm{T_e}(R, \xi)$ are shown at 3 distinct stages during island evolution in FIG. 5.4: (a) small island right after NTM onset ($\mathrm{W} = 3$ cm), (d) intermediate island during NTM growth ($\mathrm{W} = 6$ cm) and (g) large island right after saturation ($\mathrm{W} = 9$ cm). Contours of the perturbed magnetic flux function at $\Omega = -1, 0, 1$ are over plotted on $\mathrm{T_e}(R, \xi)$ (recall that $\Omega = 1$ is the separatrix of the island). The following observations are made in these stages of the NTM evolution:

- **When the island is small ($\mathrm{W} \approx 3$ cm)**

  $\mathrm{L_{Te}^{-1}}$ and $\mathrm{L_{Ti}^{-1}}$ [FIG. 5.4 (b)] are not modified substantially at R_s (i.e. profiles are not flattened) which is consistent with expectation as the gradient restoring effect of cross-field turbulent transport can effectively compete with the flattening effect of the parallel transport in small islands [56]. In accord with these profiles, $\Delta\widetilde{\mathrm{n}}_0^2 \approx 0$ both in the low- and intermediate-k $\widetilde{\mathrm{n}}$ range, indicating that small islands do not affect turbulence [FIG. 5.4 (c)].

- **When the island is mid-sized ($\mathrm{W} \approx 6$ cm)**

  $\mathrm{L_{Te}^{-1}}$ and $\mathrm{L_{Ti}^{-1}}$ decrease inside and slightly increase outside the island [FIG. 5.4 (e)]. In

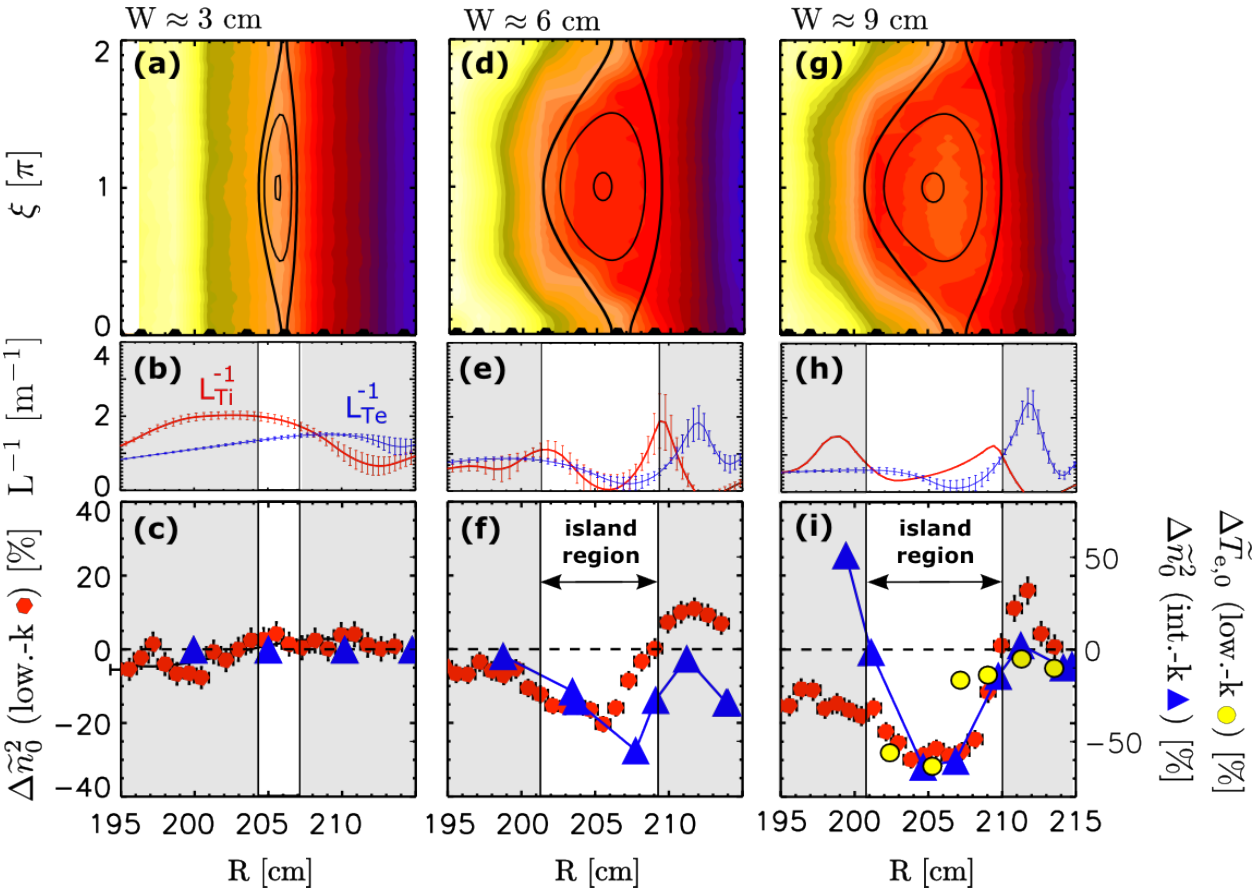

Figure 5.4: T_e, inverse temperature length-scales (L^{-1}) and turbulent fluctuations across a growing 2/1 magnetic island. (a-c) small island, (d-f) intermediate island and (g-i) large island. Top row shows contours of the phase-locked T_e. Radial locations of the measurements are marked by dark semicircles at $\xi = 0$. Over plotted are the island flux surfaces at $\Omega = 1$ (thick line - separatrix) and $\Omega = -1, 0$ (thin line). Middle row shows the inverse length-scales of T_e and T_i. Bottom row shows the % change of rotation averaged low-k $\Delta\tilde{n}_0^2$ (hexagons), intermediate-k $\Delta\tilde{n}_0^2$ (triangles) and low-k $\Delta\widetilde{T}_{e,0}$ (circles) relative to before NTM onset. Note that the vertical axis of low-k $\Delta\tilde{n}_0^2$ is on the left but that of intermediate-k $\Delta\tilde{n}_0^2$ and low-k $\Delta\widetilde{T}_{e,0}$ is on the right.

turn both the low- and intermediate-k $\Delta\widetilde{n}_0^2$ decrease inside the island region and the low-k $\Delta\widetilde{n}_0^2$ increases outside of the island region at large major radii [FIG. 5.4 (f)].

- **Finally, when the island is large (W $\approx$ 9 cm)**

  L_{Te}^{-1} and L_{Ti}^{-1} further decrease inside and increase outside the island region [FIG. 5.4 (h)]. $\Delta\widetilde{n}_0^2$ of in the low-k range decreases to about -30% while that in the intermediate-k range decreases to about -60% [FIG. 5.4 (i)]. Therefore the intermediate-k $\Delta\widetilde{n}_0^2$ has 2$\times$ stronger response than the low-k $\Delta\widetilde{n}_0^2$. Notice, that the scale of low-k $\Delta\widetilde{n}_0^2$ is shown on the left, while that of intermediate-k $\Delta\widetilde{n}_0^2$ is shown on the right side of the figure.

  To compare the trends of fluctuations of different scales and fields in FIG. 5.4 (i), instead of the quadratic quantity $\Delta\widetilde{T}_{e,0}^2$, the linear quantity $\Delta\widetilde{T}_{e,0}$ is plotted:

$$\Delta\widetilde{T}_{e,0} = (\widetilde{T}_e - \overline{\widetilde{T}_e})/\overline{\widetilde{T}_e}. \tag{5.4}$$

  Here $\overline{\widetilde{T}_e}$ is calculated before NTM onset and $\widetilde{T}_e$ is calculated from a window of 3 s during the stationary state. The reduction of of low-k $\Delta\widetilde{T}_{e,0}$ inside the island region is about 2$\times$ the reduction of low-k $\Delta\widetilde{n}_0^2$. Follows, that the decrease of low-k $\Delta\widetilde{T}_{e,0}^2$ is about 4$\times$ the decrease of the low-k $\Delta\widetilde{n}_0^2$.

Note, that the DBS measurement relies on the backscattering of a microwave beam at a cutoff surface, which is usually assumed to be a symmetric ($m = n = 0$) toroidal surface. However, the island leads to a dominantly $m/n = 2/1$ spatial modulation of the flux surfaces (and cutoff surface), which can, in principle, have an imprint on the DBS signal even when turbulence is not affected by the island. This issue has been investigated with a simple analytic calculation, which indicates that $\Delta\widetilde{n}_0^2$ can be in fact increased but not decreased solely due to the cutoff modulation.

5.3.2 Turbulence modulation

In this section, the dimensionless radial profiles of the relative amplitude and phase of turbulence power modulation are reported ($\Delta\widetilde{\mathrm{n}}_1^2$ and $\Delta\xi_1$ respectively). The modulation is studied via BES and FIR and the fluctuations are denoted as $\widetilde{\mathrm{n}}|_{\mathrm{FIR}}$ and $\widetilde{\mathrm{n}}/\mathrm{n}|_{\mathrm{BES}}$, respectively.

The island rotates with 14.5 kHz as seen from the spectrum of $\widetilde{\mathrm{B}}$ [Fig. 5.5 (a)]. Similarly to $\mathrm{T_e}$, it is expected that n is also flattened at the O-point [56], hence n measured in the lab-frame is expected to be modulated due the island rotation. This 14.5 kHz modulation is seen in the spectrum of $\widetilde{\mathrm{n}}|_{\mathrm{FIR}}$ [Fig. 5.5 (b)] and $\widetilde{\mathrm{n}}/\mathrm{n}|_{\mathrm{BES}}$ [Fig. 5.5 (c)] measured 0.3 cm inside R_{s}.

For reference, comparisons are made with $\widetilde{\mathrm{n}}|_{\mathrm{FIR}}$ measured before NTM onset and with $\widetilde{\mathrm{n}}/\mathrm{n}|_{\mathrm{BES}}$ measured during the same window (with NTM) but further out where the effect of the island is not dominant ($\rho \approx 0.75$, 17 cm away from R_{s}).

Before NTM onset there is no coherent peak at 14.5 kHz in the spectrum of the reference $\widetilde{\mathrm{B}}$ and $\widetilde{\mathrm{n}}|_{\mathrm{FIR}}$ [Fig. 5.5 (a) and (b)] and the spectrum of the reference $\widetilde{\mathrm{n}}/\mathrm{n}|_{\mathrm{BES}}$ shows no coherent modulation either [Fig. 5.5 (c)]. Hence the peak at 14.5 kHz seen in the $\widetilde{\mathrm{n}}|_{\mathrm{FIR}}$ and $\widetilde{\mathrm{n}}/\mathrm{n}|_{\mathrm{BES}}$ spectra is identified as the local density profile modulation due to the island rotation. Cross-correlation analysis of $\widetilde{\mathrm{n}}|_{\mathrm{FIR}}$ with $\widetilde{\mathrm{B}}$ and $\widetilde{\mathrm{n}}/\mathrm{n}|_{\mathrm{BES}}$ with $\widetilde{\mathrm{B}}$ confirms this point. Besides the coherent peak at 14.5 kHz (and higher harmonics) the $\widetilde{\mathrm{n}}|_{\mathrm{FIR}}$ and $\widetilde{\mathrm{n}}/\mathrm{n}|_{\mathrm{BES}}$ signals possess broadband fluctuations up to about 500 kHz attributed to the effect of broadband turbulent density fluctuations [Fig. 5.5 (b) and (c)]. Next the modulation of turbulence was investigated by analyzing the envelope of the fluctuations in the $\Delta f = 100 - 500$ kHz range (shaded in Fig. 5.5 (b) and (c)). The envelope $\Psi_{\widetilde{n}}^{\mathrm{FIR}}(t)$ of $\widetilde{\mathrm{n}}(t)|_{\mathrm{FIR}}$ is calculated as:

$$\Psi_{\widetilde{\mathrm{n}}}^{\mathrm{FIR}}(t) = \left(\int_{100\ \mathrm{kHz}}^{500\ \mathrm{kHz}} \widetilde{\mathrm{n}}(f)|_{\mathrm{FIR}} \cdot \mathrm{e}^{i2\pi f t} \mathrm{d}f \right)^2 \tag{5.5}$$

where f is the frequency and $\widetilde{\mathrm{n}}(f)|_{\mathrm{FIR}}$ is the Fourier transform of $\widetilde{\mathrm{n}}(t)|_{\mathrm{FIR}}$. The envelope of $\widetilde{\mathrm{n}}(t)/\mathrm{n}(t)|_{\mathrm{BES}}$ and $\widetilde{\mathrm{B}}(t)$ are calculated similarly and denoted as $\Psi_{\widetilde{\mathrm{n}}/\mathrm{n}}^{\mathrm{BES}}(t)$ and $\Psi_{\widetilde{\mathrm{B}}}(t)$,

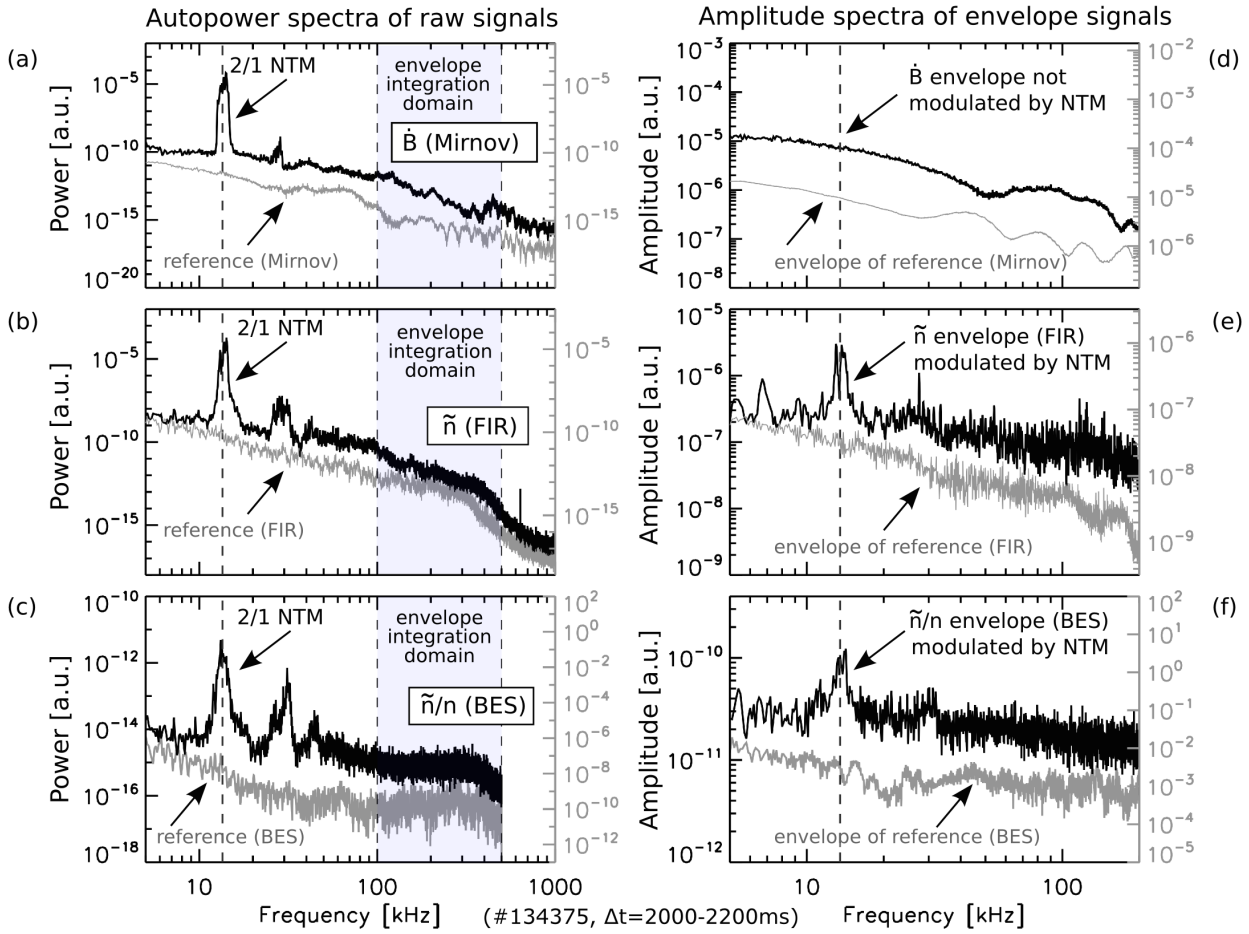

Figure 5.5: Power spectrum of (a) $\widetilde{\mathrm{B}}$ (Mirnov), (b) $\widetilde{\mathrm{n}}|_{\mathrm{FIR}}$ and (c) $\widetilde{\mathrm{n}}/\mathrm{n}|_{\mathrm{BES}}$. Amplitude spectrum of the corresponding envelope signals: (d) envelope of $\widetilde{\mathrm{B}}$, (e) envelope of $\widetilde{\mathrm{n}}|_{\mathrm{FIR}}$ and (f) envelope of $\widetilde{\mathrm{n}}/\mathrm{n}|_{\mathrm{BES}}$. Note that the magnetic and FIR reference signals (light color) were measured before NTM onset, while the reference BES signal was measured during NTM but further out (17 cm away from R_{s} showing the radial and temporal localization of the NTM.

respectively, while the Fourier transforms are $\Psi^{\mathrm{FIR}}_{\widetilde{\mathrm{n}}}(f)$, $\Psi^{\mathrm{BES}}_{\widetilde{\mathrm{n}}/\mathrm{n}}(f)$ and $\Psi_{\widetilde{\mathrm{B}}}(f)$, respectively. $\Psi_{\widetilde{\mathrm{B}}}(f)$ has no coherent peak at 14.5 kHz, hence the measured broadband $\widetilde{\mathrm{B}}(t)$ is not modulated by the rotating island [Fig. 5.5 (d)]. This is consistent with expectation as the magnetic field B_θ of a poloidal harmonic component of the perturbed current located at r_{s} decays as $\mathrm{B}_\theta(\mathrm{b}_\circ) \propto (r_{\mathrm{s}}/\mathrm{b}_\circ)^{m+1}$, where $\mathrm{b}_\circ$ is the probing location. Therefore the measured broadband magnetic fluctuations originate from the edge plasma, not from the island region.

$\Psi^{\mathrm{FIR}}_{\widetilde{\mathrm{n}}}(f)$ and $\Psi^{\mathrm{BES}}_{\widetilde{\mathrm{n}}/\mathrm{n}}(f)$ [Fig. 5.5 (e) and (f)] exhibit a clear peak at the NTM frequency (and

additionally at the second harmonic frequency) showing the modulation of broadband turbulence across the island. The envelopes of the reference signals show no turbulence modulation (without island), as expected [Fig. 5.5 (e) and (f)].

Both the FIR and BES systems detect the reduction/increase of the broadband turbulent density fluctuations at the O-point/X-point region of the island. As the diagnostics are separated toroidally and poloidally, they probe different phases of the island at a given instant of time [Fig. 5.6].

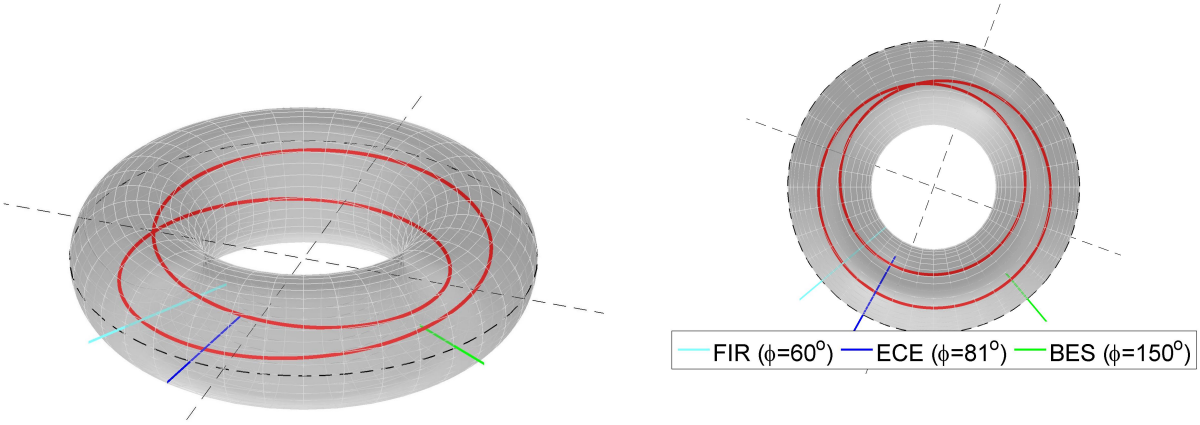

Figure 5.6: The ECE, BES and FIR diagnostics are separated toroidally and poloidally, which gives rise to an effective phase lag in the local fluctuations induced by the rotating island. (Cartoon. Dashed lines are in the tokamak midlplane, solid red line marks the O-line of the $m/n = 2/1$ island. Left: 3D view, right: top view.)

Due to the island rotation this offset translates to an effective time lag: $\Delta t = \Delta\xi/\omega$, where $\Delta\xi = -n(\Delta\phi - 2\pi\iota^{-1}\Delta\theta)$, ω is the NTM frequency and ι is the rotational transform. Given the probing locations the helical phase differences are $\Delta\xi|_{\mathrm{FIR}} = -12^\circ$ and $\Delta\xi|_{\mathrm{BES}} = -84^\circ$, the time lags are $\Delta t|_{\mathrm{FIR}} = 2.3\ \mu$s and $\Delta t|_{\mathrm{BES}} = 1.6\ \mu s$ relative to the $\mathrm{T_e}$ measurement. $\Psi^{\mathrm{FIR}}_{\tilde{\mathrm{n}}}(t)$ and $\Psi^{\mathrm{BES}}_{\tilde{\mathrm{n}}/\mathrm{n}}(t)$ were shifted by $\Delta t|_{\mathrm{FIR}}$ and $\Delta t|_{\mathrm{BES}}$, respectively, and bandpass filtered to $\Delta f = 10 - 50$ kHz. These signals are shown in Fig. 5.7 together with $\mathrm{T_e}$ inside ($R_\mathrm{s} > R = 194.7$ cm) and outside ($R_\mathrm{s} < R = 204.3$ cm) the $q = 2$ surface.

The minima/maxima of $\Psi^{\mathrm{FIR}}_{\tilde{\mathrm{n}}}(t)$ and $\Psi^{\mathrm{BES}}_{\tilde{\mathrm{n}}/\mathrm{n}}(t)$ are close to the minima/maxima of $\mathrm{T_e}(R < R_\mathrm{s})$ which correspond to the O-point/X-point passing-by-times. The measured phase lags are $\Delta\xi|_{\mathrm{FIR}} = -12.06^\circ$ (0.5% difference from the estimated -12°) with $\gamma \approx 0.5$

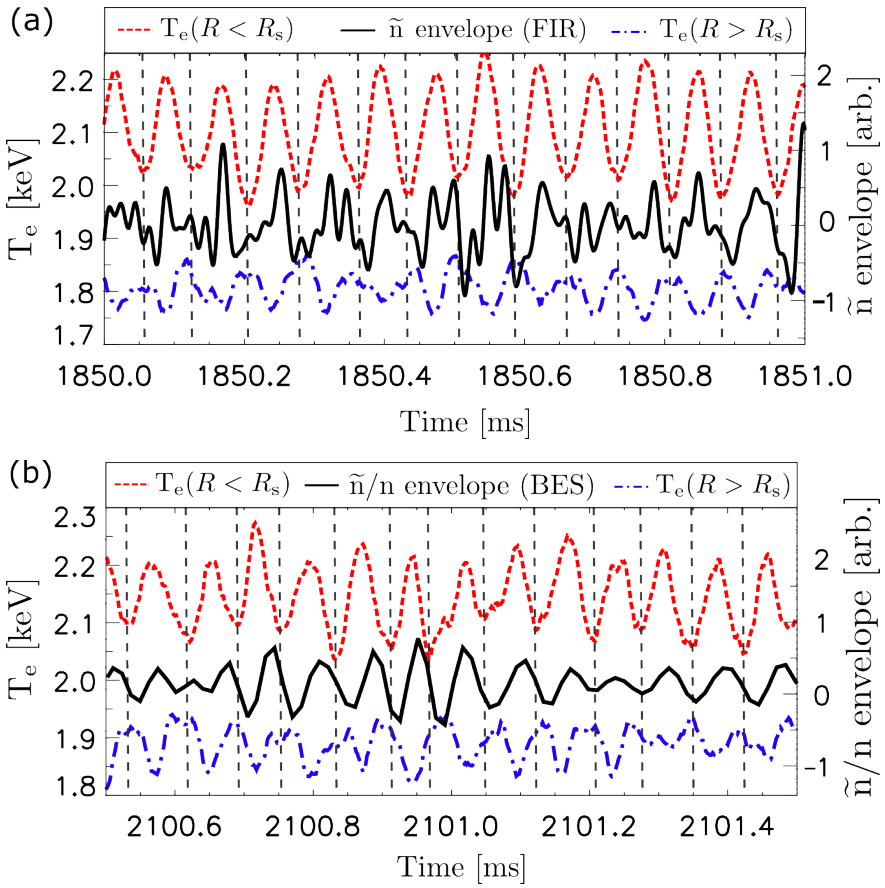

Figure 5.7: T_e outside ($R_s < R = 204.3$ cm) and inside ($R_s > R = 194.7$ cm) $q = 2$ and the envelope of (a) $\tilde{n}|_{FIR}$ and (b) $\tilde{n}/n|_{BES}$. O-point passing-by-times are marked by vertical dashed lines (134375).

coherence (0.14 significance level) and $\Delta\xi|_{BES} = -90°$ (6% difference from the estimated $-84°$) with $\gamma \approx 0.67$ coherence at 14.5 kHz (0.22 significance level). Here $\Psi^{BES}_{\tilde{n}/n}(t)$ was calculated using the nearest neighbor cross-powers, which removes any spurious contributions of photon noise modulation present in the BES signal. As the BES channels are separated radially by about $1.25\rho_i$, the photon noise is uncorrelated between neighboring channels but the turbulence is correlated.

Small differences between the calculated and measured phases can be explained as r_s changes over time by about 2 cm (8%) resulting in a small change in $\Delta\theta$. Another, also small contribution comes from the phase asymmetry of the island [55]: the typical phase difference between two T_e signals measured on the same side of the island is $\leq 4°$.

Turbulence is modulated by a maximum between 13-14% and this modulation is confined

to the island region [Fig. 5.8 (a)] (the island region is determined by the maximum radial distance between the island separatrices as mentioned previously).

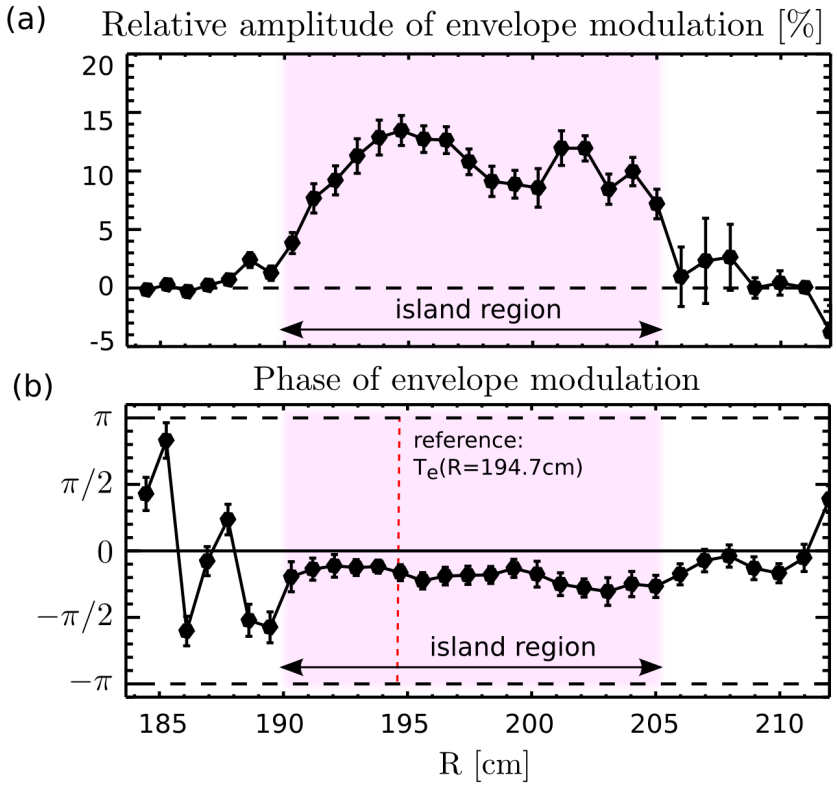

Figure 5.8: (a) Modulation amplitude of broadband turbulence relative to the mean fluctuation levels (BES) and (b) phase of modulation relative to $\mathrm{T_e}(R < R_\mathrm{s})$ (134375).

The modulation has near constant phase across the island region. This is consistent with gradient driven turbulent fluctuations being modulated by the rotating island since $\nabla \mathrm{T_e}$, $\nabla \mathrm{T_i}$ and $\nabla \mathrm{n}$ exhibit no phase jump at R_s. Fig. 5.8 (b) shows that the relative phase between turbulence modulation and $\mathrm{T_e}(R < R_\mathrm{s})$ is nearly constant and near zero across the island. As $\mathrm{T_e}(R < R_\mathrm{s})$ has minima at the O-point region the near zero phase means that turbulent fluctuations are smaller at the O-point region ($\widetilde{\mathrm{n}} \approx 3.6 \times 10^{17}$ m^{-3}) and larger at the X-point region ($\widetilde{\mathrm{n}} \approx 4.4 \times 10^{17}$ m^{-3}), i.e the modulation shown in Fig. 5.8 (a) is in fact a reduction of the O-point $\widetilde{\mathrm{n}}/\mathrm{n}|_\mathrm{BES}$ below the X-point $\widetilde{\mathrm{n}}/\mathrm{n}|_\mathrm{BES}$.

Finally, note that a similar analysis can not be obtained for $\widetilde{\mathrm{T}}_\mathrm{e}$ as the CECE analysis requires longer windows for integration than are available in the dataset due to the fast NTM growth.

5.3.3 Full 2D effects of islands on turbulence

To obtain a radially *and* helically resolved turbulence measurement [FIG. 5.9], 50 ms BES data (corresponding to about 250 island rotation cycles) was binned into a set of 19 $\xi = \omega_{\circ} t$ windows in the large island regime (W $\approx$ 9 cm), where $\xi(t)$ was obtained from $T_e(t)$ signals. As turbulence is driven by gradients, this data is directly compared to ∇T_e

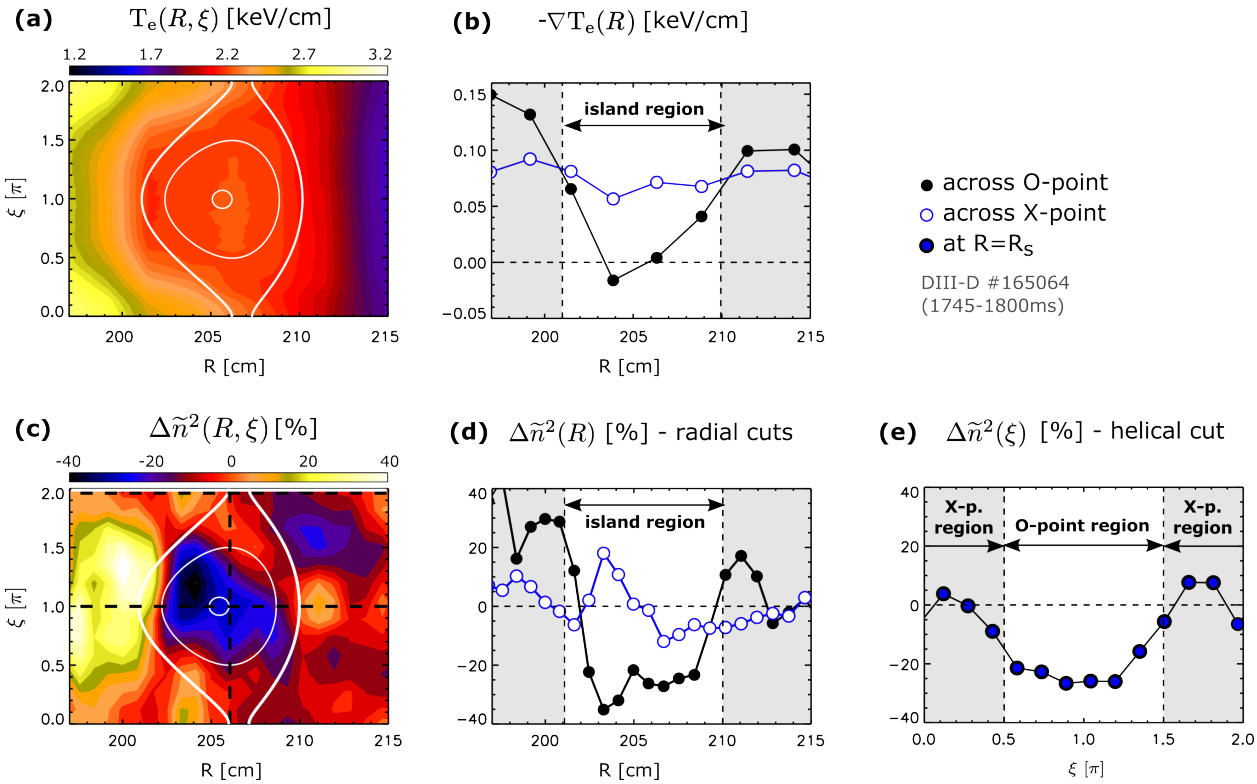

Figure 5.9: (a) Phase-lock averaged $T_e(R,\xi)$. (b) $-\nabla T_e(R)$ across the O-point ($\xi = \pi$) and X-point ($\xi = 0, 2\pi$). Percentage change of low-k $\tilde{n}^2$ relative to before NTM onset ($\Delta\tilde{n}^2(R,\xi)$): (c) 2D contour in the (R,ξ) plane, (d) radial profiles across O-point and X-point and (e) helical cut at R_s = 206 cm. O-point region is $\Omega < 0$, X-point region is $\Omega > 0$ in (e). The island flux surfaces at $\Omega = -1, 0, 1$ are over plotted in (a) and (c) with light solid lines.

that was calculated with the same method and in the same time window: (1) $T_e(R,\xi)$ contour is shown in FIG. 5.9 (a), profiles of ∇T_e across the O-point and X-point are shown in FIG. 5.9 (b); (2) 2D (not rotation averaged) $\Delta\tilde{n}^2(R,\xi) = \delta\tilde{n}^2(R,\xi)/\widetilde{\tilde{n}^2}(R)$ contour is shown in FIG. 5.9 (c), profiles across the O-point and X-point are shown in FIG. 5.9 (d). $\tilde{n}^2$ is reduced at the O-point region by a maximum of about 35% and is increased by about

20% close to the X-point region, in qualitative agreement with simulations [6, 19, 26, 28, 97]. Outside the island, along a radial chord encompassing the O-point, $\widetilde{n}^2$ is increased by about $20-30\%$, see the O-point profile in FIG. 5.9 (d). The X-point profile [FIG. 5.9 (c)] shows a maximum of 20% increase inside the island region, however this is not aligned with the X-point of $\Omega(R,\xi)$. These changes of $\widetilde{n}^2$ are reasonable, considering the profiles of ∇T_e [FIG. 5.9 (b)] as well as the average profiles and turbulence drives shown previously in FIG. 5.2.

A helical cut at $R_s = 206$ cm [FIG. 5.9 (e)] shows that the difference between X-point and O-point $\widetilde{n}^2$ gives rise to a modulation of $\widetilde{n}^2$ with about 30% amplitude due to the island rotation in the lab frame (recall that $\xi = \omega_o t$). Note that the symmetry of $\widetilde{n}^2$ about $\xi = \pi$ indicates near zero phase with respect to L_{T_e} as in FIG. 5.7 and 5.8.

5.4 Scaling of turbulence modifications with island size

This section presents the degree of the turbulence reduction (increase) and its dependence on local gradients as well as on scaling with islands size during NTM growth. FIG. 5.10 (a) shows that T_e is not flattened substantially as long as the island is smaller than a threshold size of $W_t \approx 5$ cm. When $W > W_t$, ∇T_e progressively decreases inside the island region and increases outside the island region as the island grows in accord with the predictions of a heat transport model of magnetic islands [56]. Comparing the helically averaged turbulence reduction inside the island region (minimum of $\Delta\widetilde{n}_0^2$) and enhancement outside the island region (maximum of $\Delta\widetilde{n}_0^2$) with ∇T_e, a simple linear relationship is observed with a correlation coefficient of 91% (low-k) and 82% (intermediate-k) [FIG. 5.10 (b) and (e)]. It follows, that $\widetilde{n}$ tracks the evolution of ∇T_e. As shown in FIG. 5.10 (c) and (f), $\widetilde{n}$ is not modified when $W < W_t$, but $\widetilde{n}$ progressively decreases inside the island region and increases outside the island region when $W > W_t$. This data shows the existence of two regimes during NTM evolution:

Small islands characterized by steep O-point T_e profile and turbulence level comparable

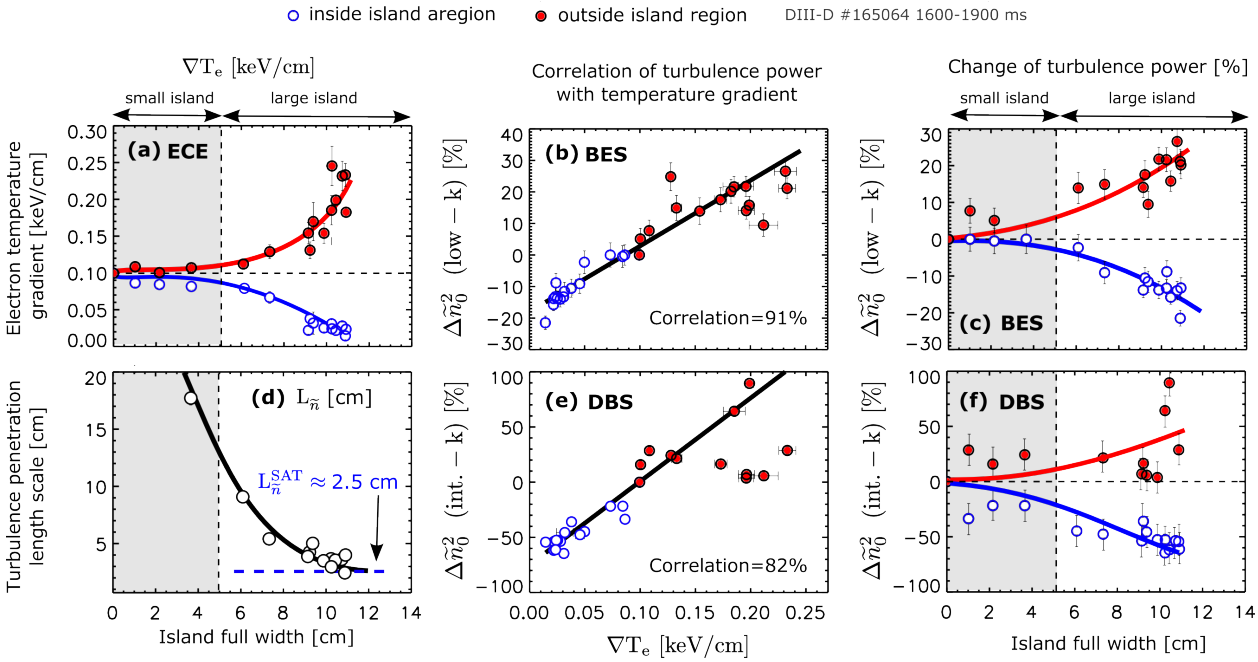

Figure 5.10: (a) Helically averaged ∇T_e shows little to no change when $W < W_t$ ($W_t \approx 5$ cm) but a gradual decrease inside and increase outside the island region when $W > W_t$. (b) and (e) show that low-k and intermediate-k $\Delta\tilde{n}_0^2$ are correlated with ∇T_e, respectively. (c) and (f) show that the scaling of reduction (increase) of low-k and intermediate-k $\Delta\tilde{n}_0^2$ vs W is similar to that of ∇T_e, i.e. little change when $W < W_t$ but gradual decrease inside and increase outside the island region when $W > W_t$. (d) Turbulence penetration length scale (defined in eq. (5.6) vs W.

to that of the background.

Large islands characterized by flat T_e profile and reduced turbulence level at the O-point, but steeper T_e profile and increased turbulence level outside the island.

Transition from small to large island occurs when W exceeds a threshold of $W_t \approx 5$ cm. A previous analytical study [56] estimated $W_t = (\chi_\perp/\chi_\perp)^{1/4}\sqrt{R_\circ L_q/n}$ assuming that $\chi_\perp$ is spatially uniform and independent of W and ∇T_e ($R_\circ$ is the plasma major radius and L_q is the magnetic shear length at $q = m/n$). However, as the ratio of turbulent and neoclassical $\chi_\perp$ is typically order 10^2 and as turbulence is sensitive to local gradients, the physics of W_t is likely linked to critical gradient phenomenon. Moreover, beyond local stability conditions, turbulence is also affected by spreading [90] which allows turbulence to penetrate to the O-point region from outside the island. This could increase $\chi_\perp$ and therefore ∇T_e which could feed back to increase fluctuations non-linearly. Therefore, a

lower estimate for W_t could be given by twice the turbulence penetration length-scale (due to penetration from both sides of the island). The penetration length-scale of the turbulent fluctuations into the island region was estimated from the helically averaged BES fluctuation data as:

$$L_{\widetilde{n}} = \left(\frac{1}{\widetilde{n}_0^2} \frac{\partial \widetilde{n}_0^2}{\partial r} \right)^{-1} \Bigg|_{R-R_s=W/2} \tag{5.6}$$

As such, here $L_{\widetilde{n}}$ is the length-scale of the rotation averaged $\widetilde{n}^2$ evaluated at the boundary of the island region. This definition is not identical, but similar to that given in a recent simulation study [27]. Note that as long as $W < L_{\widetilde{n}}$, turbulence penetrating through e.g. the inner separatrix of the island leads to fluctuations in the vicinity of the outer separatrix (and vice versa). This effect is eliminated by looking at the asymptotic behavior of $L_{\widetilde{n}}(W)$ in the large island regime. FIG. 5.10 (d) shows that $L_{\widetilde{n}}$ approaches $L_{\widetilde{n}}^{SAT} \approx 2.5$ cm as the island saturates. As significant turbulence reduction can take place when $W > 2L_{\widetilde{n}}^{SAT}$, the lower estimate of the threshold is $W_t \approx 2L_{\widetilde{n}}^{SAT} \approx 5$ cm. This compares well with the observed threshold for $\widetilde{n}$ reduction and T_e flattening.

It is worthwhile to note that the ion banana width is about 3 cm at $q = 2$. As trapped particles at the island separatrices partially restore the local gradients, the transition from small to large island regimes could be related to the step size of trapped particle transport. Further, neoclassical effects on islands get washed out when islands are smaller than the ion banana width.

5.5 Discussion

A series of controlled H-mode experiments have been dedicated in DIII-D to measure the effect of naturally occurring, freely rotating 2/1 NTM islands on plasma turbulence. Local measurements of low- and intermediate-k $\widetilde{\mathrm{n}}$ via BES and DBS, respectively, and low-k $\widetilde{\mathrm{T}}_{\mathrm{e}}$ via CECE show reduction of fluctuation levels in the region of magnetic islands for the first time [FIG. 5.4]. Fluctuations are increased at the X-point region as well as outside the island region (where gradients are elevated) [FIG. 5.9]. The dependence of turbulence increase/reduction on local gradients as well as scaling with islands size was also presented [FIG. 5.10]. It was found that significant profile flattening and turbulence modification occurs when the island width is larger than a threshold island width of $\mathrm{W_t} \approx 5$ cm. Based on these observations, 2 regimes have been identified:

Small island regime when $\mathrm{W} < \mathrm{W_t}$. Temperature flattening is minor and turbulence is not modified. Cross-field transport inside the island is presumably anomalous.

Large island regime when $\mathrm{W} > \mathrm{W_t}$. Temperature is significantly flattened and turbulence is reduced inside and increased outside the island. Cross-field transport inside the island is on the order of neoclassical transport [7].

The physics of transition from small to large island regimes remains an open question for future investigations. Here,it was found that transition occurs when the island width exceeds the characteristic length-scale of turbulence penetration into the island [FIG. 5.10 (d)].

It was reported that turbulence is modulated (due to the island rotation) and this modulation is confined to the island region [FIG. 5.8 (a)] in discharge #134375. In contrast, a modulation outside of the island region is observed in discharge #165064, as seen from the fact that $\Delta\widetilde{\mathrm{n}}^2(r,\xi)$ is increased in line with the O-point compared to that in line with the X-point [FIG. 5.9 (d)]. This difference between the two discharges could be e.g. due to the interaction of turbulence with sheared flows connected to the $m/n = 2/1$ component of the electric field. This process is closely analogous to the familiar effect of

zonal flows on drift-wave turbulence and has been predicted theoretically [15] and reported in global nonlinear gyrokinetic particle-in-cell simulations [18]. Shear flows outside of the island have been observed around static magnetic islands in stellarators [5, 32] but have not yet been studied around rotating NTM islands in tokamaks.

Finally, the observed turbulence modifications in the large island regime can have direct implications for understanding the interaction between turbulence and large-scale NTMs as well as the reduction of plasma confinement by NTMs:

Turbulence reduction at O-point as the local gradient at the O-point is determined by the $\chi_\perp/\chi_\parallel$ ratio ($\chi_\perp$ and $\chi_\parallel$ being the perpendicular and parallel diffusivities), reduced turbulent cross-field transport modifies local gradients and concomitant bootstrap current perturbation. This enters the modified Rutherford equation (MRE) which governs the evolution of the NTM.

Turbulence enhancement outside the island likely leads to increased radial heat and particle fluxes which play a role in decreasing the confinement as well as the bootstrap current.

Inclusion of turbulence effects in the MRE and the impact of NTM-turbulence multi-scale interaction on plasma confinement will be the focus of Chapter 7.

CHAPTER 6

Magnetic islands in nonlinear gyrokinetic simulations

The simulations presented in this section were conducted by A. Bañón the of UCLA using the GENE code [52]. The analyses (calculations, figures, etc.) presented here are my own original work.

6.1 Introduction

Static magnetic islands have been implemented in GENE nonlinear gyrokinetic simulations in 3-dimensional, toroidal geometry to study the effect of static magnetic islands on ion-scale turbulence. This was accomplished by introducing a static $m/n = 3/2$ radial magnetic field perturbation through the parallel component of the vector potential [6]. GENE self-consistently solves the gyrokinetic-Maxwell system of equations on a fixed grid in five dimensional phase space (plus time). Two particle species (deuterons and electrons) were used including electromagnetic effects. The equilibrium magnetic configuration (large aspect-ratio, circular model equilibrium) is characterized by a safety factor of $q = 1.5$, magnetic shear of $\hat{s} = 0.16$ and inverse aspect ratio of $\epsilon = 0.19$, $R/L_{Ti} = R/L_{Te} = 6.9$, $R/L_n = 2.2$. These parameters are similar to the "Cyclone DIII-D base case parameter set" [44] (discharge #81499) as in other gyrokinetic simulations [26, 60]. As such, these simulations can only be compared qualitatively to the DIII-D experiments presented in this thesis. Therefore, here the simulation results are presented in arbitrary units.
These simulations are started out with constant gradients which drive the ITG modes unstable. Next, the turbulent cross-field transport and the fast parallel transport inside the island lead to the modification of the initially imposed profile such that gradients are

reduced at the O-point but increased outside the island region. The modified gradients in turn can lead to turbulence modification, which feeds back into the transport and profile evolution in a self-consistent way. After the system has come to statistical equilibrium, the simulation is continued for a time much longer then the turbulence correlation time. For the analysis presented in this thesis, the stationary part of the simulations are analyzed. Note, that the equilibrium profiles are fixed through the boundary conditions, as the characteristic global confinement time-scale of H-mode plasmas is much longer than the time-scale of these simulations. However, the profiles quickly modify inside and around the island due to the parallel transport which has a much shorter time-scale than the global confinement.

6.2 Plasma profiles

The stationary state is characterized by an $m = 3, n = 2$ static perturbation (magnetic field, $\mathrm{T_e}, \mathrm{T_i}$, etc.) as well as ITG turbulence and shear flows. In this section, the characteristics of the $\mathrm{T_e}, \mathrm{T_i}$ and n profiles are described. Subsequent sections focus on flows, turbulence and transport across the island.

Small islands maintain a finite $\nabla \mathrm{T_e}(r)$ and $\nabla \mathrm{T_i}(r)$ across the O-point while large islands are almost flat, see Fig. 6.1 (a), similarly to a diffusive transport model of magnetic islands [56]. The threshold island width required for temperature flattening is $\mathrm{W_t} \approx 33\rho_\mathrm{i}$. Interestingly, the flat region of $\mathrm{T_i}(r)$ [Fig. 6.1 (a)] is shifted from the O-point of the large island by about $5\rho_i$. In contrast, the flat region of $\mathrm{T_i}(r)$ is centered about r_s when the island is small. This shift has been observed in these gyrokinetic simulations for the first time and is potentially linked to finite banana width effects.

Fig. 6.1 (b) shows the logarithmic gradients around the O-point (averaged over $\Omega < -0.5$) normalized to the equilibrium logarithmic gradient (R/L_0). In the large island regime, the flattening of $\mathrm{T_i}(r)$ in the O-point region is less than that of $\mathrm{T_e}(r)$ but the trends vs. W are similar. Finally, the flattening of $\mathrm{n}(r)$ is marginal, which could be due to trapped particles that do not follow the field lines inside the island, maintaining a steep density profile at the

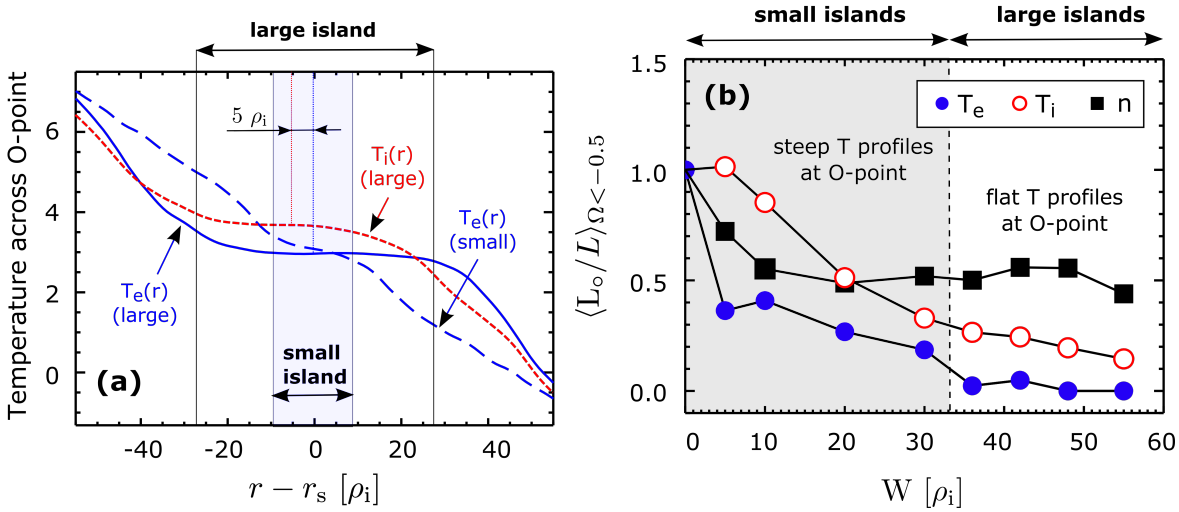

Figure 6.1: (a) Time averaged electron and ion temperature profiles across the O-point. Small islands maintain a finite temperature gradient at the O-point while large islands are completely flat. (b) Logarithmic gradients around the O-point ($\Omega < -0.5$) vs the island width.

O-point in contrast to passing particles.

6.3 Flow perturbations

In this section, the mean $E \times B$ flow ($\mathbf{v}_{E\times B}$) is described. The helical component (v_ξ), radial component (v_r) and flow magnitude $v_{E\times B}$ are calculated from the electrostatic potential (ϕ) at $\theta = 0$ as follow:

$$\langle v_\xi \rangle_t = \left\langle \frac{1}{B}\frac{\partial \phi}{\partial r} \right\rangle_t \quad \text{and} \quad \langle v_r \rangle_t = \left\langle -\frac{1}{B}\frac{\partial \phi}{R\partial \xi} \right\rangle_t \tag{6.1}$$

$$\langle v_{E\times B} \rangle_t = \left\langle \sqrt{v_\xi^2 + v_r^2} \right\rangle_t \tag{6.2}$$

where $\langle \cdot \rangle_t$ represents the time average. It is worth noting that ϕ has a fluctuating part $\tilde{\phi}$ and a mean component $\langle \phi_{n=2} \rangle$ due to the island. The shear (ω_E) of the helical $E \times B$ flow is calculated from the radial derivative of v_ξ:

$$\langle \omega_E \rangle_t = \left\langle \left| \frac{1}{B}\frac{\partial^2 \phi}{\partial r^2} \right| \right\rangle_t, \tag{6.3}$$

The absolute value of $\partial_r^2\phi$ was used here as negative and positive shear have the same effect on turbulence.

Two examples of $v_{E\times B}$ are shown as contours on Fig. 6.2 (a) and (c) for different island widths. Here, the over plotted arrows represent the vectors of $\mathbf{v}_{E\times B}$. Small islands develop a strong, localized shear flow just outside of the island, which is parallel with the separatrices, as seen from the contour of $v_{E\times B}$ [Fig. 6.2 (a)] and from the radial profiles of v_ξ and ω_E across the O-point [Fig. 6.2 (b)]. On the contrary, when $\mathrm{W} > \mathrm{W_t}$, a peaked ϕ develops at the O-point leading to a vortex-like $E \times B$ plasma flow circulating around the O-point inside and outside the island separatrices [Fig. 6.2 (c)]. The radial extent of this vortex is comparable to W/2 on each side of the island as seen from the radial profiles of v_ξ and ω_E across the O-point in Fig. 6.2 (d). The onset of this flow occurs simultaneously with the flattening of the temperature profiles and, therefore, with the shift of $\mathrm{T_i}(r)$. The direction of the circulation is random at mode onset, the magnitude fluctuates over time and even random reversals occur. Outside the separatrices, the vortex flow magnitude and shear are typically both larger than the localized shear flow of small islands, but ω_E is reduced by about a factor of 3 at the O-point when $\mathrm{W} > \mathrm{W_t}$. The transition point from small to large island regime is most clearly seen in v_ξ, which reverses on one side of the island at the transition point [Fig. 6.2 (e)]. Therefore, $\mathrm{W_t}$ is obtained from the discontinuity of v_ξ vs W. Finally, ω_E is about constant when $\mathrm{W} < \mathrm{W_t}$, but increases about linearly with W when $\mathrm{W} > \mathrm{W_t}$ [Fig. 6.2 (f)]. Vortex-like plasma flow has been observed in previous simulations [22, 60] and in LHD experiments [5, 70] via CER across static magnetic islands. The physics of the transition and the dependence of $\mathrm{W_t}$ on various plasma conditions (such as plasma shape, collisionality, trapped particle fraction, temperature ratio, equilibrium gradients, E × B shear, island rotation, etc) is beyond the scope of this work and remains therefore a topic for future investigations. However, it is *conjectured* here, that the different ion and electron pressure at the O-point (established by the shift) drives a current through the island separatrices, which, interacts with the background magnetic field and spins the plasma about the O-point, leading to the vortex.

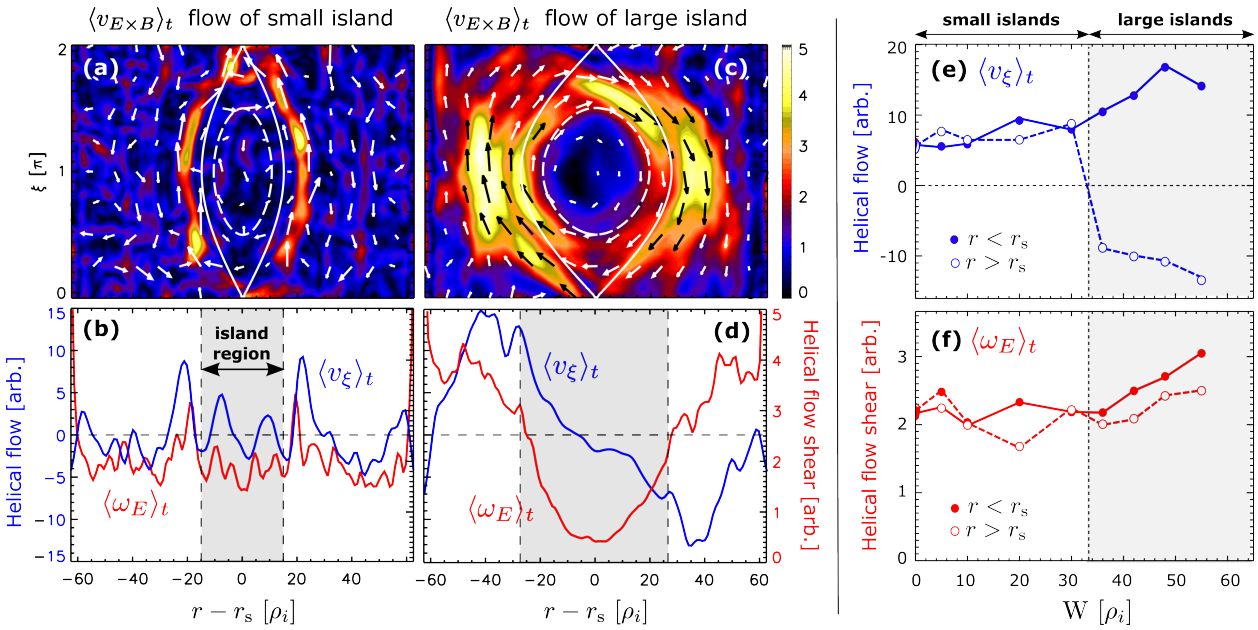

Figure 6.2: (a) Helical flow and (b) shear flow around an island of $W = 30\rho_i$ showing symmetric flow structure. (c) Helical flow and (d) shear flow around an island of $W = 55\rho_i$ showing a vortex mode centered at the O-point. (e) Flow and (f) shear versus island width for values taken left of the resonance surface ($r_s < r$) and right ($r_s > r$).

6.4 Impact of islands on ITG-turbulence

In this section, ITG-scale density $\widetilde{n}(r,\xi)$ and temperature $\widetilde{T}_e(r,\xi)$ fluctuations are investigated, as these can be measured in the core of H-mode tokamak plasmas and are therefore experimentally relevant.

Example contours of the instantaneous turbulent fluctuations $\widetilde{n}(r,\xi)$ and $\widetilde{T}_e(r,\xi)$ are shown in Fig. 6.3 for three cases: (a,b) without island for reference ($W = 0$), (c,d) for a small island ($W = 20\rho_i$) and (e,f) for a large island ($W = 40\rho_i$). Turbulent fluctuations are calculated from the simulation output ($n(r,\xi,t)$) by removing the static MHD-perturbation:

$$\widetilde{n}(r,\xi,t) = n(r,\xi,t) - \langle n(r,\xi,t)\rangle_t, \tag{6.4}$$

and similarly for $\widetilde{T}_e(r,\xi)$. As it was shown previously in Fig. 6.1, the $T(r)$ profiles are not flattened at the O-point in the small island regime. Accordingly, little to no reduction of turbulent fluctuations is seen at the O-point, compare Figs. 6.3 (a) and (b) to Figs. 6.3 (c)

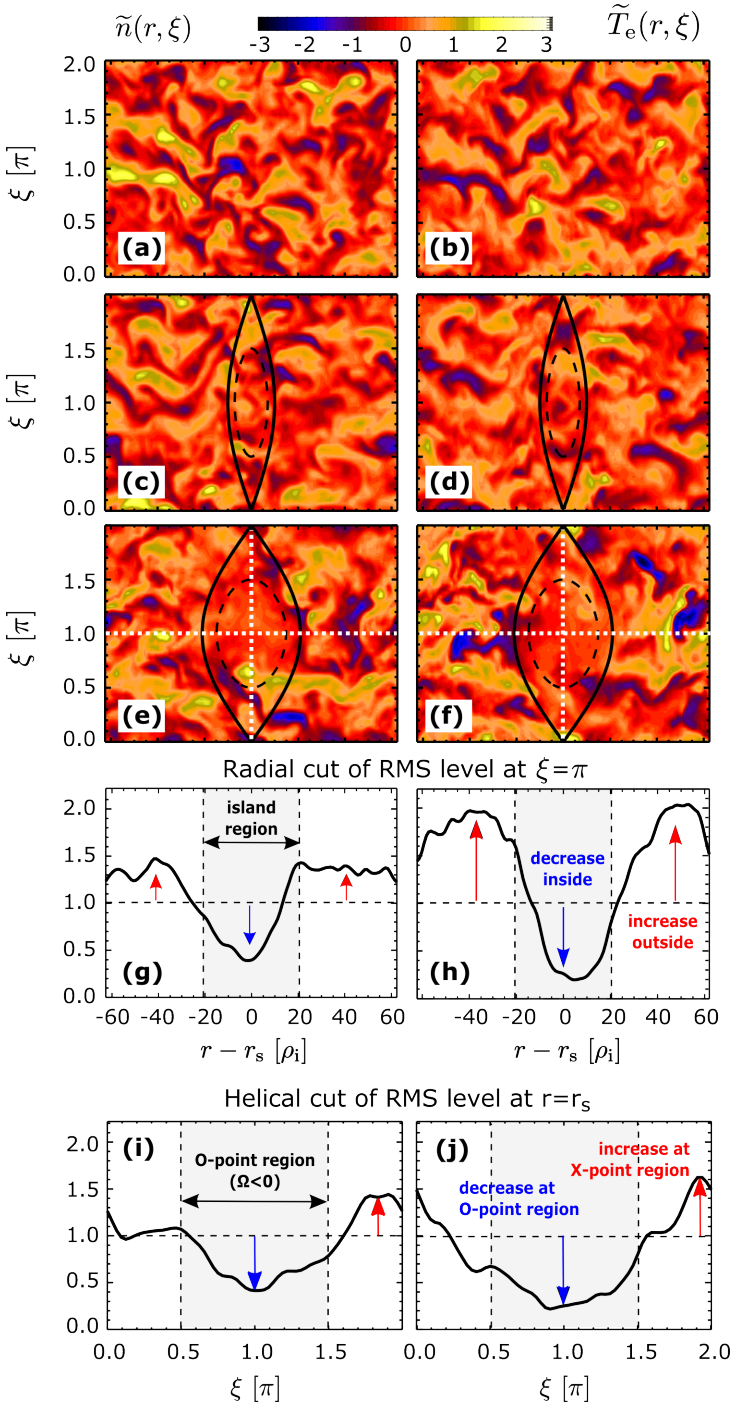

Figure 6.3: Contours of instantaneous turbulent fluctuations without an island (a,b), with an island of W = 20 ρ_i (c,d) and with an island of W = 55 ρ_i (e,f). $\widetilde{n}(r,\xi)$ and $\widetilde{T}_e(r,\xi)$ are shown in the left and right columns, respectively. (g) and (h) show radial cuts of the RMS level across the O-point of the large island ($\xi = \pi$, see dotted light horizontal line on (e,f)). (i) $\widetilde{n}(r,\xi)$ and (j) $\widetilde{T}_e(r,\xi)$ are helical cuts of the RMS level along the resonant surface of the large island ($r = r_s$, see dotted light vertical line on (e) and (f)).

and (d), respectively. In contrast, fluctuations are substantially decreased in the O-point region of large islands [Figs. 6.3 (e) and (f)]. Radial profiles of the RMS $\widetilde{\mathrm{n}}(r,\xi)$ and $\widetilde{\mathrm{T}}_\mathrm{e}(r,\xi)$ across the O-point [Figs. 6.3 (g) and (h), respectively] show as much as about 50% reduction of $\widetilde{\mathrm{n}}$ inside and increase outside a large island of $\mathrm{W} = 40\rho_i$, and a stronger response (about 70%) for $\widetilde{\mathrm{T}}_\mathrm{e}$. Finally, by looking at the fluctuations at the resonant surface ($r = r_s$) [Fig. 6.3 (i) and (j)], it is clear that $\widetilde{\mathrm{n}}$ and $\widetilde{\mathrm{T}}_\mathrm{e}$ are significantly reduced at the O-point and slightly increased at the X-point. Note that the reduction at the O-point is more pronounced than the increase at X-point, resulting in average, in a reduction of the fluctuations across the resonant surface.

The power of turbulent density and temperature fluctuations are calculated from the GENE simulation output as:

$$\widetilde{\mathrm{n}}^2(r,\xi) = \int \widetilde{\mathrm{n}}^2(r,\xi,t)\,\mathrm{d}t \quad \text{and} \quad \widetilde{\mathrm{T}}_\mathrm{e}^2(r,\xi) = \int \widetilde{\mathrm{T}}_\mathrm{e}^2(r,\xi,t)\,\mathrm{d}t. \tag{6.5}$$

$\widetilde{\mathrm{n}}^2$ and $\widetilde{\mathrm{T}}_\mathrm{e}^2$ is written in the form of a Fourier series focusing on the $n_i{}^{\mathrm{th}}$ helical harmonic component of the perturbation, similarly to the experiments:

$$\widetilde{\mathrm{n}}^2(r,\xi) = \overline{\widetilde{\mathrm{n}}^2}(r) + \sum_{n_i=0}^{\infty} \widetilde{\mathrm{n}}_{n_i}^2(r)\cos(n_i\xi + \Delta\xi_{n_i}^{\widetilde{\mathrm{n}}}(r)) \approx \overline{\widetilde{\mathrm{n}}^2}(r) + \widetilde{\mathrm{n}}_0^2(r) + \widetilde{\mathrm{n}}_1^2(r)\cos(\xi + \Delta\xi_1^{\widetilde{\mathrm{n}}}(r)) \tag{6.6}$$

Note that $n_i\xi = n_i(m\theta - n\varphi)$, where $\theta = 0$ and therefore the $n_i = 1$ helical harmonic corresponds to the toroidal mode number of the island structure, in this case $n = 2$. Here, $\overline{\widetilde{\mathrm{n}}^2}(r)$ is the unperturbed radial profile of the turbulent fluctuation power in the island-free simulation:

$$\overline{\widetilde{\mathrm{n}}^2}(r) = \Big(\langle\widetilde{\mathrm{n}}^2(r,\xi,t)\rangle_{t,\xi}\Big)\Big|_{\mathrm{W}=0}. \tag{6.7}$$

$\widetilde{\mathrm{n}}_0^2(r)$ is the radial profile of the $n = 0$ component of the perturbation, $\widetilde{\mathrm{n}}_1^2(r)$ and $\Delta\xi_1^{\widetilde{\mathrm{n}}}(r)$ are, respectively, the radial profiles of the amplitude and phase of the $n_i = 1$ helical harmonic component of the turbulence power modulation. A similar expansion is carried

out for $\widetilde{\mathrm{T}}_{\mathrm{e}}^2(r,\xi)$. As mentioned in Chapter 5 (Section 5.3), turbulence measurements are subject to various diagnostic uncertainties (such as electronic amplifier calibration factors), which are unrelated to island physics. To remove such factors, we use the change of $\widetilde{\mathrm{n}}_0^2(r)$ and $\widetilde{\mathrm{n}}_1^2(r)$ relative to the fluctuation power before NTM onset:

$$\Delta\widetilde{\mathrm{n}}_0^2(r) = \frac{\widetilde{\mathrm{n}}_0^2(r)}{\overline{\widetilde{\mathrm{n}}^2}(r)} \quad \text{and} \quad \Delta\widetilde{\mathrm{n}}_1^2(r) = \frac{\widetilde{\mathrm{n}}_1^2(r)}{\overline{\widetilde{\mathrm{n}}^2}(r)} \tag{6.8}$$

and similarly for $\widetilde{\mathrm{T}}_{\mathrm{e}}$.

The reduction of $\Delta\widetilde{\mathrm{n}}_0^2(r)$ and $\Delta\widetilde{\mathrm{T}}_{\mathrm{e},0}^2(r)$ inside and increase outside the island region is observed [Fig. 6.4 (a) and (b), respectively] and this effect increases with increasing island width for $\mathrm{W} > \mathrm{W}_{\mathrm{t}}$ [Fig. 6.4 (c) and (d)]. In the large island regime, $\Delta\widetilde{\mathrm{n}}_0^2(r)$ is decreased

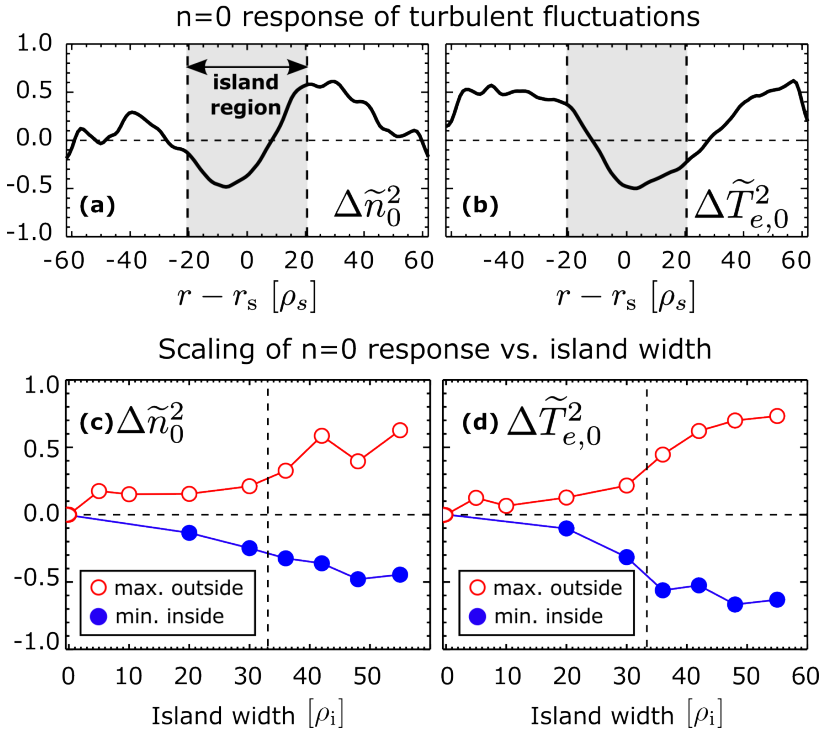

Figure 6.4: $n = 0$ response of turbulence: (a) $\Delta\widetilde{\mathrm{n}}_0^2(r)$ and (b) $\Delta\widetilde{\mathrm{T}}_{\mathrm{e},0}^2(r)$. Scaling of the minimum (inside the island, filled circles) and maximum (outside of the island, empty circles) of (c) $\Delta\widetilde{\mathrm{n}}_0^2(r)$ and (d) $\Delta\widetilde{\mathrm{T}}_{\mathrm{e},0}^2(r)$ vs. the island width.

inside and increased outside the island region by as much as 50% and as much as 70% for $\Delta\widetilde{\mathrm{T}}_{\mathrm{e},0}^2(r)$. This change in the fluctuations is in qualitative agreement with expectations

based on the decreased gradients at $r = r_s$ shown previously in Figs.6.1 (a) and (b). Note that outside the island, the increase of the fluctuations is due to an increase of the gradient since the shear flow is also increased in this region. However, inside the island, the reduction of the fluctuations is attributed to the smaller gradient since the shear flow has also been reduced in that region (see Fig. 6.2(d)). In other words, changes in the fluctuations are opposite from what is expected due to changes in the flow shear but are consistent with changes of the gradients. It is important to mention that this could be different in experimental conditions if, for instance, an additional background shear is present outside of the island due to the plasma rotation, so that the effect of the flow shear could dominate the effect of the drive.

The relative modulation amplitudes are shown in [Figs. 6.5 (a) and (b)]. Inside the island

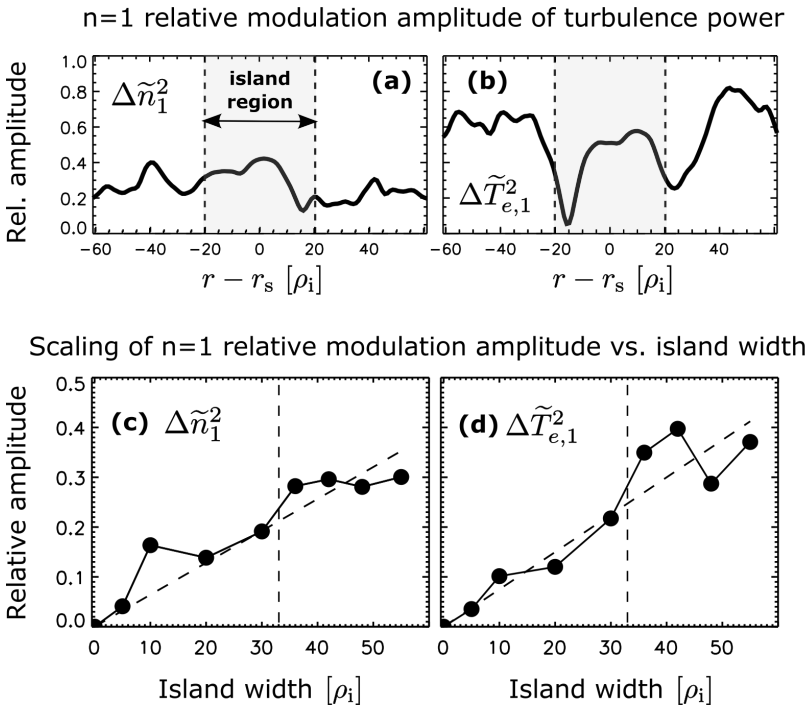

Figure 6.5: Relative modulation amplitude (a) $\Delta\widetilde{\mathrm{n}}_1^2(r)$ and (b) $\Delta\widetilde{\mathrm{T}}_{\mathrm{e}}^2(r)$ ($n_i = 1$ response). Scaling of relative modulation amplitude (c) $\Delta\widetilde{\mathrm{n}}_1^2(r)$ and (d) $\Delta\widetilde{\mathrm{T}}_{\mathrm{e}}^2(r)$ vs. W.

region, the maximum relative modulation amplitude $\Delta\widetilde{\mathrm{n}}_1^2(r)$ and $\Delta\widetilde{\mathrm{T}}_{\mathrm{e},1}^2(r)$ is about $40 - 50\%$. The amplitude progressively increases with W following the linear relation $\Delta\widetilde{\mathrm{n}}_1^2(\mathrm{W}) \approx 0.65\ \mathrm{W}\rho_i^{-1}$ [%] and $\Delta\widetilde{\mathrm{T}}_{\mathrm{e},1}^2(\mathrm{W}) \approx 0.75\ \mathrm{W}\rho_i^{-1}$ [%] [Fig. 6.5 (c) and (d)]. This

nonzero modulation inside the island is due to differences in the turbulent drive between the O-point and X-point. In this region, the phase of this modulation $\Delta\xi_1^{\tilde{n}}(r)$ and $\Delta\xi_1^{\tilde{T}_e}(r)$ is near zero (with respect to $\cos(\xi)$) [Fig. 6.6 (a) and (b)]. The phase in the island region is near zero regardless of the island size: $\Delta\xi_1^{\tilde{n}}(W) \approx \Delta\xi_1^{\tilde{T}_e}(W) \approx 0$ [Fig. 6.6 (c) and (d)]. Finally, outside of large islands, a nonzero modulation with a phase close to π (left side) and $-\pi$ (right side) is also observed. This phase is due to an increase of fluctuations outside of the island in line with the O-point, and the different sign between the two sides is due to the effect of the vortex flow on turbulence distribution around the island.

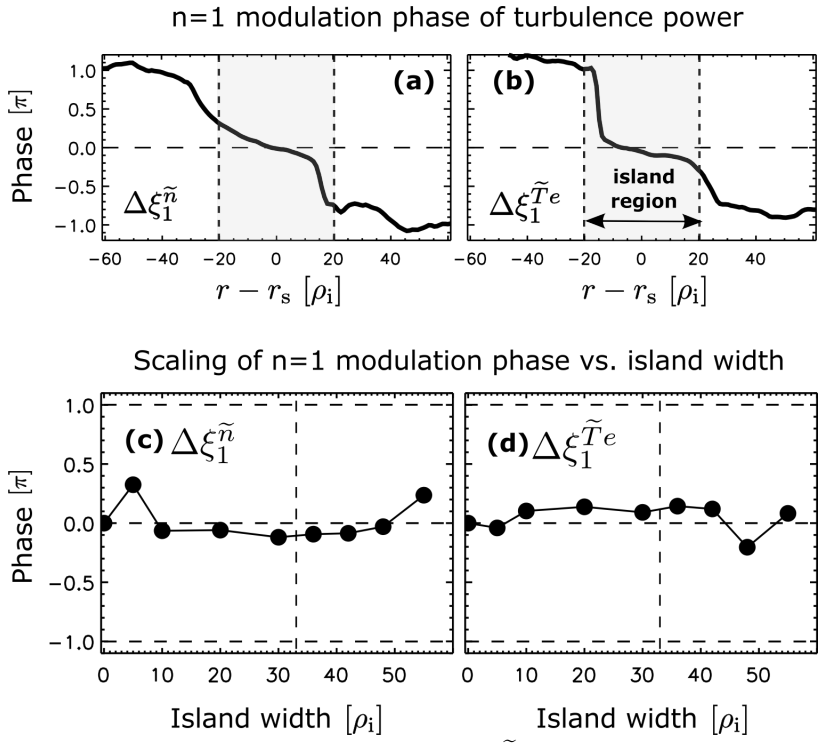

Figure 6.6: Modulation phase (a) $\Delta\xi_1^{\tilde{n}}$ and (b) $\Delta\xi_1^{\tilde{T}_e}$ (n_i=1 response). Scaling of relative modulation amplitude (c) $\Delta\xi_1^{\tilde{n}}$ and (d) $\Delta\xi_1^{\tilde{T}_e}$ vs. island width.

6.5 Transport

In gyrokinetic turbulence simulations without islands, the total radial particle flux, as well as electron and ion heat fluxes ($\Gamma_{\rm tot}$, $Q_{e,\rm tot}$ and $Q_{i,\rm tot}$, respectively) are driven by turbulence. In contrast, when static magnetic islands are present, three different mechanisms combine to drive radial fluxes: (1) turbulent flux ($\Gamma_{\rm turb}$) due to ITG modes ($n > 2$), (2) convection (Γ_v) by the vortex mode ($n = 2$) and (3) free streaming along the field in the radial direction (Γ_p) due to the finite radial field perturbation. Therefore, the total radial particle flux in the presence of a static magnetic island can be written as:

$$\Gamma_{\rm tot} = \Gamma_{\rm turb}(r) + \Gamma_v(r) + \Gamma_p(r), \tag{6.9}$$

and a similar expression applies for the heat fluxes. The turbulent fluxes were calculated from the GENE simulation output in normalized unit as:

$$\Gamma_{\rm turb}(r,\xi) = \langle \widetilde{n}\tilde{v}_r \rangle_t, \tag{6.10}$$

$$Q_{e,\rm turb}(r,\xi) = \frac{3}{2}\langle (\widetilde{n} + \widetilde{T}_e)\tilde{v}_r \rangle_t, \tag{6.11}$$

$$Q_{i,\rm turb}(r,\xi) = \frac{3}{2}\langle (\widetilde{n} + \widetilde{T}_i)\tilde{v}_r \rangle_t, \tag{6.12}$$

where $\tilde{v}_r$ is calculated using $\tilde{\phi}$ (i.e. the fluctuating part of ϕ). In the vicinity of the simulation box boundary (at e.g. $r_b = r_{\rm s} + 55\rho_i$) the transport is dominantly driven by turbulence, since the field perturbation as well as the radial component of the vortex flow is small ($\Gamma_v(r_b) \approx \Gamma_p(r_b) \approx 0$), leading to $\Gamma_{\rm tot}(r_b) \approx \Gamma_{\rm turb}(r_b)$. In a stationary state ($\partial_t n = 0$), therefore $\partial_r \Gamma_{\rm total} = 0$ due to continuity. Therefore, $\Gamma_{\rm tot} \approx \Gamma_{\rm turb}(r_b)$. Thus, the total particle flux is:

$$\Gamma_{\rm tot} \approx \left(\frac{1}{2\pi} \int_0^{2\pi} \Gamma_{\rm turb}(\mathrm{r},\xi)\mathrm{d}\xi \right)\Bigg|_{r=r_b}. \tag{6.13}$$

On the other hand, the turbulent radial particle flux at the O-point is defined as:

$$\Gamma^{\mathrm{O}}_{\mathrm{turb}} = \left(\int_{\Omega<0} \Gamma_{\mathrm{turb}}(r,\xi)\mathrm{d}\xi \right)\Bigg|_{r=r_s}. \tag{6.14}$$

In the following, when W = 0, these quantities are marked with a bar as $\bar{\Gamma}_{\mathrm{tot}}$ and $\bar{\Gamma}^{\mathrm{O}}_{\mathrm{turb}}$. The dimensionless quantities $\Gamma_{\mathrm{tot}}/\bar{\Gamma}_{\mathrm{tot}}$ and $\Gamma^{\mathrm{O}}_{\mathrm{turb}}/\bar{\Gamma}^{\mathrm{O}}_{\mathrm{turb}}$ reflect the effect of the islands. A similar analysis also holds for the heat fluxes. Finally, the convective Γ_v and parallel fluxes $\Gamma_{p,s}$ for a given species s are defined as:

$$\Gamma_v(r,\xi) = \langle \widetilde{n}_{n=2}\tilde{v}_{r,n=2}\rangle_t, \tag{6.15}$$

$$\Gamma_{p,s}(r,\xi) = \langle \widetilde{u}_{\parallel,s}\tilde{B}_x\rangle_t, \tag{6.16}$$

where $\widetilde{u}_{\parallel,s}$ is the fluctuating parallel current.

When $\mathrm{W} > \mathrm{W_t}$, $\Gamma^{\mathrm{O}}_{\mathrm{turb}}/\bar{\Gamma}^{\mathrm{O}}_{\mathrm{turb}}$ and $Q^{\mathrm{O}}_{e,\mathrm{turb}}/\bar{Q}^{\mathrm{O}}_{e,\mathrm{turb}}$ progressively decrease by about 1-2 orders of magnitude as W is increased [Fig. 6.7]. This reduction of turbulent transport at the O-point is in accordance with qualitative expectation since fluctuations are significantly decreased at the O-point of large islands [Figs. 6.4 (c) and (d)]. $\Gamma_{\mathrm{tot}}/\bar{\Gamma}_{\mathrm{tot}}$ does not vary when W is varied which is due to a nearly 0 cross-phase between $\widetilde{\mathrm{n}}$ and $\partial_\xi\widetilde{\Phi}$. The same holds for $Q_{e,\mathrm{tot}}/\bar{Q}_{e,\mathrm{tot}}$ as long as $\mathrm{W} < \mathrm{W_t}$. However, when $\mathrm{W} > \mathrm{W_t}$ the total electron heat flux increases with W and reaches $Q_{e,\mathrm{tot}}/\bar{Q}_{e,\mathrm{tot}} \approx 3$ at $\mathrm{W} = 55\ \rho_i$. Similarly, $Q_{i,\mathrm{tot}}/\bar{Q}_{i,\mathrm{tot}} \approx 3$ and the electron and ion channels compare as $Q_{i,\mathrm{tot}}/Q_{e,\mathrm{tot}} \approx 2$. This increase in the total heat flux is due to the increased turbulence level outside the island (inside the island the parallel transport dominates the transport). Therefore, these simulations indicate that the turbulence increase around islands can be the mechanism leading to increased radial transport observed in high performance fusion plasma experiments with large NTM magnetic islands.

Finally, in case of the largest island ($W = 50\rho_i$), 20% of the total fluxes is driven by turbulent transport localized at the X-point region ($\Gamma_{\mathrm{turb}}/\Gamma_{\mathrm{tot}} \approx 0.2$, $Q_{e,\mathrm{turb}}/Q_{e,\mathrm{tot}} \approx 0.2$ and $Q_{i,\mathrm{turb}}/Q_{i,\mathrm{tot}} \approx 0.2$). The remaining 80% is split equally between parallel transport and

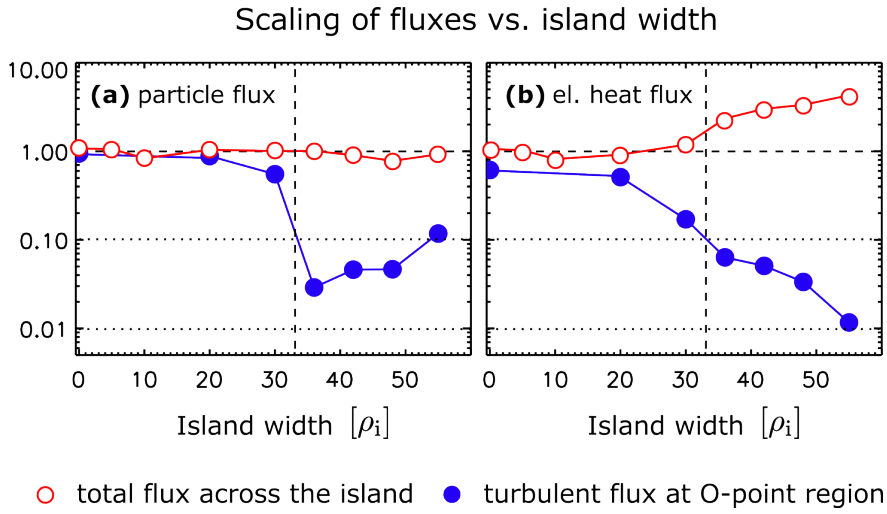

Figure 6.7: Scaling of (a) particle and (b) electron heat flux vs island width: total flux across the island (empty circles) and local turbulent heat flux at O-point region (filled circles).

the vortex mode.

6.6 Effect of radial asymmetry on shear flows and turbulence regulation

It has been found by a previous study [27] that ITG-turbulence can penetrate into the island (where ITGs can be stable) via turbulence spreading [90]. The increased fluctuation level in a boundary layer of a few centimeters leads to increased turbulent transport across the island separatrices. This leads to steeper temperature profiles [7] at the O-point which has a stabilizing effect on NTMs [4, 58]. However, a strong ω_E at the island separatrices is expected to regulate turbulence penetration into the island. Understanding the effect of flow shear on turbulence is important as it can lead to turbulence and transport regulation in plasmas with NTMs and has a potential impact on NTM stability. In the following, we study the effect of shear flows (developed at the island separatrices) on turbulence penetration into the magnetic island. The flow magnitude is controlled via the radial asymmetry of the island (A), which is a new feature in gyrokinetic turbulence simulations and is studied here for the first time.

In these simulations, a gradual increase/decrease of ϕ, v_ξ and ω_E is observed asymmetrically about r_s as A is varied. The largest perturbations are observed for $n = 2$ in the O-point profiles in the vicinity of the island separatrices, see Fig. 6.8. The intersection points of the radial chord encompassing the O-point with the island separatrix are:

$$r_{1,2} = r_s \mp \mathrm{W}/2(1 \mp \mathrm{A}/4 + (\mathrm{A}/4)^2/2), \ \xi = \pi. \tag{6.17}$$

For instance, when $\mathrm{A} < 0$ the magnitude of the perturbation of ϕ, v_ξ and ω_E increases

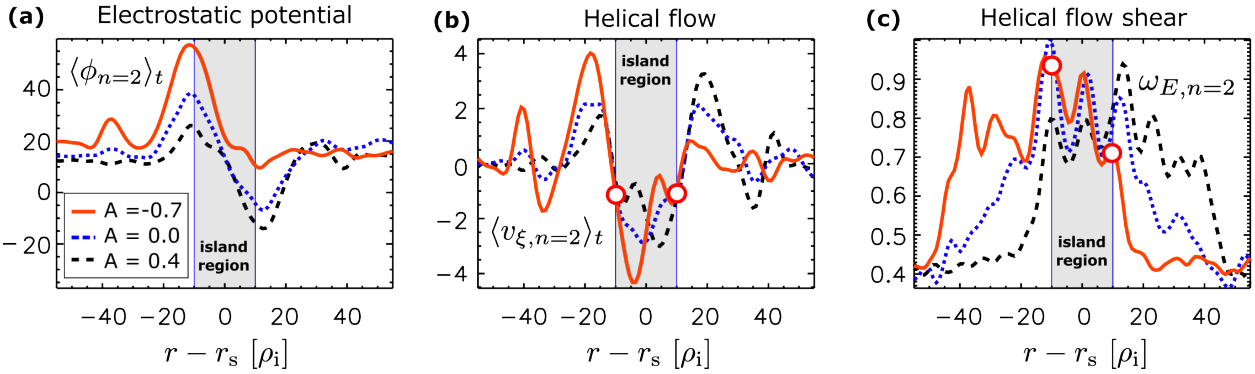

Figure 6.8: Effect of radial asymmetry (A) on the radial profiles of (a) electrostatic potential (ϕ), (b) binormal flow (v_ξ) and (c) flow shear (ω_E) across the O-point of the island for $n = 2$. Circles on (b) and (c) show that the flow is comparable but the flow shear is different on the separatrices of the asymmetric island.

around r_1 and decreases around r_2. At the same time, ITG-scale fluctuations are significantly reduced (about 35%) around r_1 compared to r_2, see the RMS of $\widetilde{\mathrm{T}}_\mathrm{i}$ in Fig. 6.9 (a). This asymmetry in $\widetilde{\mathrm{T}}_\mathrm{i}$ (and other fluctuation profiles such as $\widetilde{\mathrm{T}}_\mathrm{e}$, $\widetilde{\mathrm{T}}_\mathrm{i}$ and $\widetilde{\phi}$) is possibly resulting from the asymmetric ω_E.

To further investigate the relationship between $\widetilde{\mathrm{T}}_\mathrm{i}$ and ω_E, we use correlation analysis employing a simple model [45, 98] of turbulent structures moving in the helical direction and having Gaussian shape both in space and time. In this model one can calculate the autocorrelation time (τ_corr) of turbulent fluctuations as a function of the turbulence structure lifetime (τ_life) and the velocity dependent transit time (τ_v):

$$\tau_\mathrm{corr} = \frac{\tau_\mathrm{life}\tau_v}{\sqrt{\tau_\mathrm{life}^2 + \tau_v^2}}. \tag{6.18}$$

The transit time is $\tau_v = s_\xi / v_\xi$, where s_ξ is the spatial correlation length of the turbulent structures in the flow direction. From this model, it is clear that at fixed τ_v, the variations of $\tau_{\rm corr}$ provide information about the variations of $\tau_{\rm life}$, which can reflect the effect of ω_E. Figs. 6.8 (b) and (c) clearly show that $v_\xi(r_1) \approx v_\xi(r_2)$ but $\omega_E(r_1) > \omega_E(r_2)$ when A $= -0.7$, i.e. the helical flow is comparable but the shear of this helical flow is different on the separatrices. As such, a difference in $\tau_{\rm corr}$ can reflect a difference in $\tau_{\rm life}$ (not τ_v). The autocorrelation functions of $\widetilde{\phi}(r_1, t)$ and $\widetilde{\phi}(r_2, t)$ in Fig. 6.9 (b) show that $\tau_{\rm corr}$ is shorter in the high shear region by about 40% compared to the low shear region ($\tau_{\rm corr}(r_1) = 0.7$ and $\tau_{\rm corr}(r_2) = 1.2$). Therefore it is reasonable to attribute the reduction of fluctuations on the separatrix (at r_1) to the local increase of ω_E. This shows that the shear flow at the island separatrix reduces turbulence penetration into the island. As such, ω_E can lead to more flat islands and therefore to more unstable NTMs. Interestingly, there is no progressive change in $\widetilde{\rm T}_{\rm i}$ vs. A outside of the island where ω_E strongly depends on A.

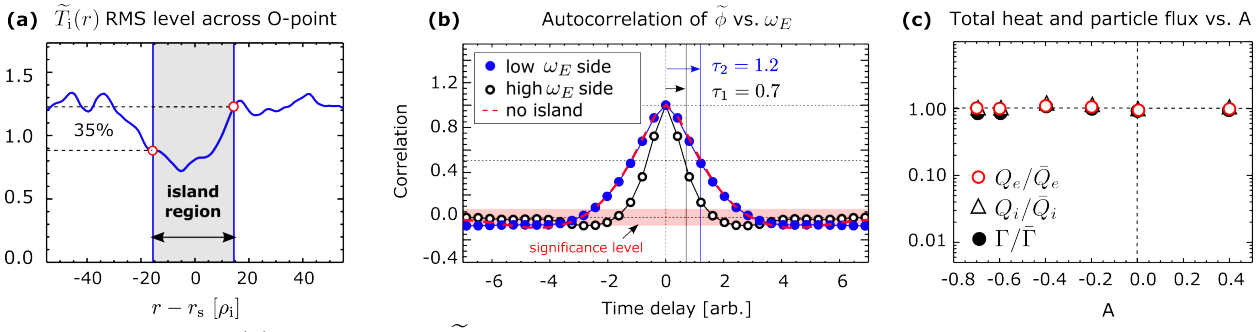

Figure 6.9: (a) RMS level of $\widetilde{\rm T}_{\rm i}$ across the O-point of an asymmetric island of $A = -0.6$. (b) Autocorrelation function of ITG-scale turbulent electrostatic potential fluctuations ($\widetilde{\phi}$) show shorter turbulence life-time ($\tau_{\rm corr}$) in the high-shear region by about 40% compared to the low-shear region. (c) Total heat and particle fluxes across the island region vs. A.

This could be due to simultaneous changes in gradients or zonal flow amplitude in this region, i.e. the turbulence decreasing effect of ω_E is balanced by changes of either one or both of turbulence driving effect of $\nabla {\rm T}_{\rm i}$ and shear effect of turbulence generated zonal flows. Finally, there is no change in the total particle and heat fluxes vs. A [Fig. 6.9 (c)]. This is an interesting result and it might follow from the continuity of $\Gamma_{\rm tot}$, $Q_{e,{\rm tot}}$ and $Q_{i,{\rm tot}}$ in a stationary regime: $\widetilde{\rm T}_{\rm i}(\Delta r_1) < \widetilde{\rm T}_{\rm i}(\Delta r_2)$ would lead to $Q_{i,{\rm tot}}(\Delta r_1) < Q_{i,{\rm tot}}(\Delta r_2)$ (here Δr_1 and Δr_2 refer to the $r < r_1$ and $r > r_2$ domains, respectively). Due to continuity, we

will have that $\partial_t \mathrm{T_i} \neq 0$, and therefore $\mathrm{T_i}$ would decrease at Δr_2, leading to the increase of $\nabla \mathrm{T_i}$ at Δr_1. This increase of gradients would lead to the increase of $\widetilde{\mathrm{T}}_\mathrm{i}(\Delta r_1)$ until $Q_{i,\mathrm{tot}}(\Delta r_1) = Q_{i,\mathrm{tot}}(\Delta r_2)$ is reached and the system comes to a steady state with $\partial_t \mathrm{T_i} = 0$. The $Q_{i,\mathrm{tot}}(\Delta r_1) = Q_{i,\mathrm{tot}}(\Delta r_2)$ constraint requires $\widetilde{\mathrm{T}}_\mathrm{i}(\Delta r_1) = \widetilde{\mathrm{T}}_\mathrm{i}(\Delta r_2)$. Therefore, the system reaches the steady state equilibrium when the turbulence drive balances the shear.

6.7 Discussion

In this Chapter, experimentally relevant quantities of the simulation output were analyzed, aiming to provide guidelines for interpreting experimental data and as a first step in validation of turbulence-island simulations.

In summary, we have investigated the effect of static magnetic islands on ITG turbulence in non-linear GENE gyrokinetic simulations in 3-dimensional toroidal geometry. Depending on the island width, two regimes have been observed, with a threshold of $\mathrm{W_t} = 33\rho_i$. These two regimes show distinct features in profiles, flows, turbulence and transport, and their main features are briefly summarized in the following. In the small island regime ($W < \mathrm{W_t}$), finite gradients across the O-point and strong localized shear just outside the island are present. In accordance with that, little or none reduction of turbulent (temperature and density) fluctuations are seen at the O-point. This also leads to practically unchanged total transport levels. In the large island limit ($W > \mathrm{W_t}$), the temperature profiles are almost flat while the flattening in the density profile is minimal. Here, the flattening of the ion temperature profile is less than the electron temperature profile, and the flat spot of the ion temperature profile is shifted from the O-point by a few ρ_i. In this regime, a vortex flow develops that circulates around the O-point.

Inside/outside the island region, a decrease/increase of the fluctuation levels was observed, with a stronger response in $\widetilde{\mathrm{T}}_\mathrm{e}$ than $\widetilde{\mathrm{n}}$. These modifications of turbulence level are consistent with changes in gradients and shear flows in those regions. Accordingly, both turbulent radial particle and heat fluxes are reduced at the O-point while only the total heat transport is increased across the island region. Finally, the effect of flow shear on

turbulence was studied by implementing an asymmetric island in gyrokinetic simulations for the first time. The asymmetry of the $n = 2$ electrostatic potential perturbation as well as the associated helical flow shear scales with the asymmetry parameter. This asymmetric shear reduces turbulence penetration into the island on the side where the shear is increased. This shows that shear flows at the island separatrices can reduce turbulence penetration making the NTMs more unstable.

As future work, we will perform global gyrokinetic simulations with magnetic islands for a DIII-D discharge, and compare quantitatively several experimentally measurable quantities, which will help in further improving the predictive capabilities of the numerical simulations and interpreting results from present day experiments.

CHAPTER 7

Effect of NTM-turbulence interaction on global plasma confinement and NTM growth

7.1 Introduction

The effect of saturated NTMs on the global energy confinement time (τ_e) was quantified by the Chang-Callen belt model [99] which has predicted a linear relationship between τ_e and the saturated island width W_{SAT}. This belt model, however, neither informs about the dynamics *nor* the physics of the transition of the plasma to the new equilibrium with an embedded NTM. In this Chapter it is shown that the evolution of β links the global confinement degradation to the observed O-point flattening and turbulence enhancement (outside of the island but induced by the island) [Section 7.2].
Next, experimentally observed local turbulence effects as well as global equilibrium changes are incorporated in the MRE [Section 7.3], namely:

- **Local effect**: flattening of O-point pressure profile has impact on bootstrap current perturbation δj_{bs}: when the island is small $W_c = 5$ cm but when the island is large $W_c = 1.2$ cm.
- **Global effect**: turbulence driven transport decreases the core T_e and n which lead to: (a) increase of $\eta \propto T_e^{-3/2}$ and (b) decrease of bootstrap current j_{bs}.

This generalized MRE is then tested against measured NTM growth rates.

7.2 Physics of confinement degradation by NTMs

The experiments analyzed in this Chapter are identical to those presented in Chapter 5, see the time series of P_B (beam power), T_e, T_i, n and $n = 1$ magnetic amplitude in FIG. 7.1. As P_B is ramped up in steps after the plasma start-up, T_e, T_i and n progressively increase. A sharp increase in T_e, T_i and n around 1100 ms (P_B increasing from ≈ 5 MW to 8 MW) indicates the low-to-high confinement mode transition (LH-transition). Following the transition, T_e, T_i and n are quasi-stationary or slightly increase before the $m/n = 2/1$ NTM starts growing (1st window). During the first part of the NTM growing phase (before the dashed line in the 2nd window), T_e, T_i and n do not change significantly. However, during the second part of the NTM growing phase, T_e and T_i drop by about 30% and n drops by about 10%, which are both significant changes. Therefore, T_e, T_i and n display a qualitatively different behavior during the early stage of the NTM evolution compared to the later stage. As the NTM saturates in the 3rd window, T_e, T_i and n also saturate (to a lower level then before NTM onset) and remain quasi-stationary.

Plasma confinement is often quantified in terms of $\beta = p/p_B$, where p is the kinetic pressure and p_B is the magnetic pressure. In order to track the evolution of the core confinement, one can use p when p_B is fixed. Here changes in confinement are tracked via the product of the chord averaged core n and T_e measured on axis. This is only a proxy for β, but reflects qualitative changes in the confinement and is sampled fast enough (500 kHz) to look at changes on the time-scale of NTM evolution in contrast to the relatively slow sampled β or τ_e.

First, notice that even though $\chi_\parallel$ is large in the O-point region, the saturated island leads to no 'extra transport' (3rd window) compared to before NTM onset (1st window). This is counter intuitive, as both β_N and τ_e has decreased and therefore the confinement has been degraded by the NTM. In fact, confinement degradation is constrained in the window of growing NTM *only* (2nd window). This point is substantiated in the following.

At constant input power the plasma is in a quasi stationary state before NTM onset (1st window). After NTM saturation (3rd window) the plasma is also in a stationary state, but

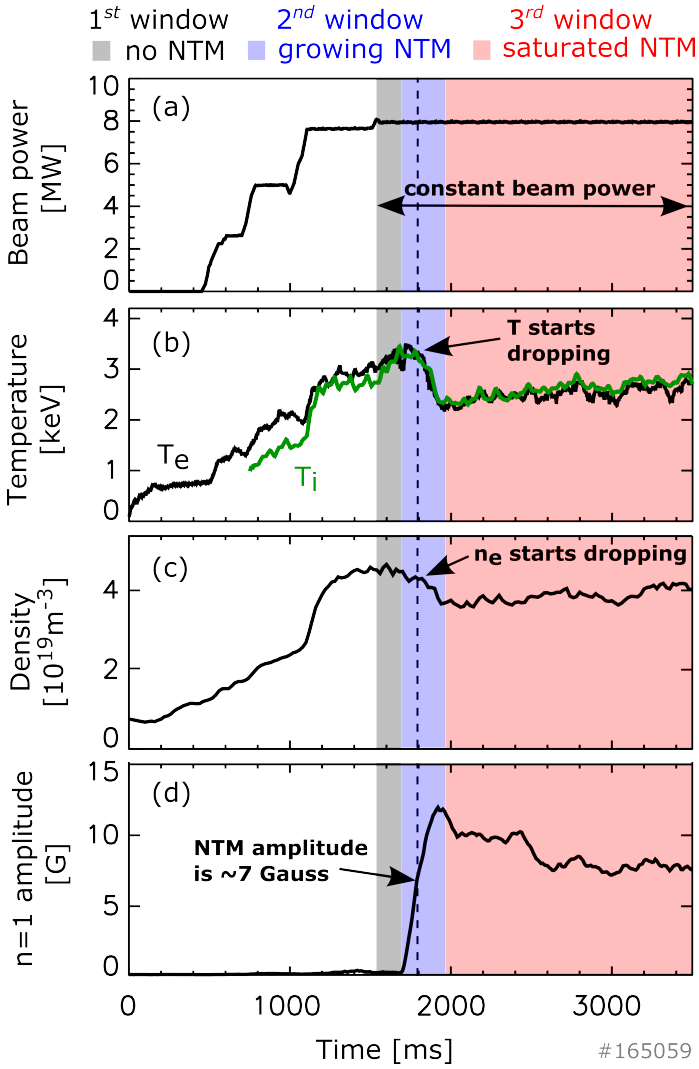

Figure 7.1: (a) Input beam power, (b) chord averaged core density (interferometry), (c) electron and ion temperature at $q = 2$ (ECE and CER, respectively) and (d) $n = 1$ magnetic amplitude (Mirnov).

characterized by lower confinement as seen from the drop of T_e, T_i and n. In both of these stationary states, radial fluxes balance the same input power. Therefore, radial fluxes after NTM saturation match those before NTM onset. In accord, gradients outside the island region after NTM saturation is comparable to that before NTM onset, see FIG. 7.2 (a) and (b).

The physics allowing this counter intuitive transport is as follows. The large $\chi_{\|}$ alone can not lead to 'extra' transport because energy conservation requires the parallel fluxes going inside the island to be equal to the cross-field fluxes going through the island separatrices

(on both sides of the island). In other words, parallel fluxes are limited by perpendicular fluxes. This limit is realized by the reduction of $\nabla_{\parallel} T_e$ inside the island (i.e. flattening) until $\chi_{\parallel} \nabla_{\parallel} T_e = \chi_{\perp} \nabla_{\perp} T_e$ is satisfied. So, the overall transport in the stationary state is determined by $\chi_{\perp} \nabla_{\perp} T_e$ outside of the island region, which is the same as before NTM onset.

Global plasma evolution, therefore, from the first stationary state (without island) to the second stationary state (with island) is realized by elevated radial transport in a limited time window only. Also, energy conservation requires the radial transport to be elevated not only inside the island but in every radial section of the whole plasma during this time. Inside the island, this transport is carried along the field, while outside of the island, the radial transport must be carried across the nested flux surfaces.

Focusing on the transient state, FIG. 7.2 (a) and (b) show that gradients are increased outside the island during NTM evolution (solid line). These elevated gradients are due to the fact that the parallel transport time-scale is much shorter then the global confinement time, flattening the O-point before p could change on axis. ∇T_e is a turbulence drive and the elevation of it is consistent with observed increase of turbulence in the experiments. Therefore, it is likely that the 'extra' transport outside the island region is linked to the observed increase of gradient driven instabilities, which is also supported by the GENE simulations (Chapter 6). This increase in $\chi_{\perp} \nabla_{\perp} T_e$ up shifts the limit on $\chi_{\parallel} \nabla_{\parallel} T_e$ across the island, leading to overall increase of the fluxes in every radial segment of the plasma. These two combined effects: the fast parallel transport inside the island and the increased turbulent transport outside the island leads to the degradation of the global confinement. To further support this point, notice that the confinement degradation is a strongly non-linear function of the island width. Namely, $T_e(t)$, $T_i(t)$ and $n(t)$ are about constant up to the point when the NTM amplitude reaches about 7 G (marked with dashed line in FIG. 7.1) and decrease only when the NTM amplitude is larger then 7 G. This effect is more pronounced, when looking at the conditional averaged pressure vs W calculated from a series of 10 similar discharges during NTM growth [FIG. 7.2 (c)]. p does not change

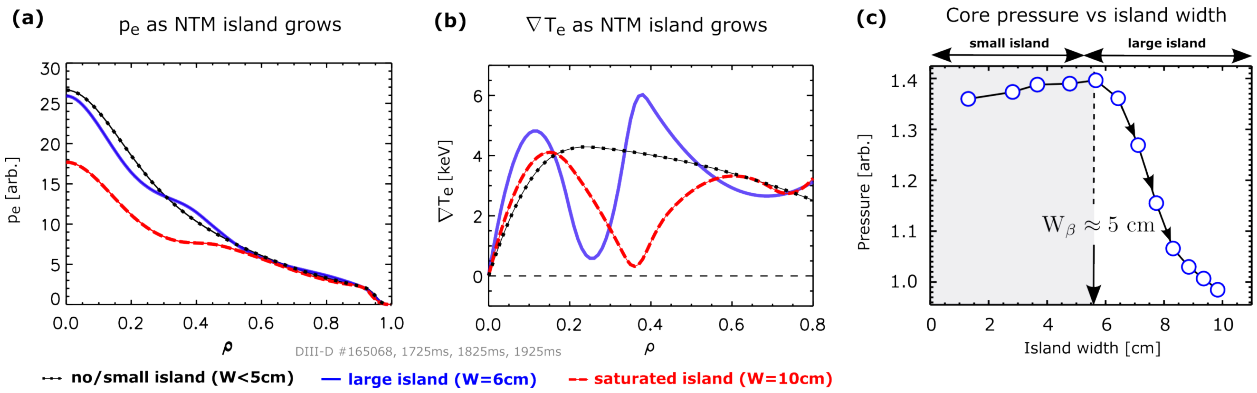

Figure 7.2: Evolution of (a) $p(r)$ and (b) $\nabla T_e(r)$ during island growth: $W < W_{conf}$ (dotted), $W \approx W_{conf} \approx 5$ cm (solid) and $W \approx W_{SAT} \approx 10$ cm (dashed). Note that ∇T_e is elevated outside of the island region when $W_t < W < W_{SAT}$. (c) p conditional averaged vs W. This shows a non-linear global confinement response to the island: p decreases only when $W > W_{conf} \approx 5$ cm.

before the island reaches a width of $W_{conf} \approx 5$ cm but decreases *only* when $W > W_{conf}$. I.e. the confinement degradation is linked to a characteristic island width W_{conf}, and this has about the same magnitude as the observed threshold island width W_t. Recall that W_t is the island width required for T_e flattening (steepening) and turbulence decrease (increase) to occur inside (outside) the island region. Due to the causal relationship between W_t and W_{conf} (beyond numerical agreement), it is reasonable to make the equation $W_{conf} \equiv W_t$. It worths mentioning explicitly the following:

- Radially localized increase of fluctuations at the X-point region *alone* can not lead to decrease of confinement (due to continuity).
- The fact that the confinement does not decrease when $W \approx W_{SAT}$ clearly shows that the parallel transport *alone* does not facilitate any changes in β (due to limits imposed by $\chi_\perp \nabla_\perp T_e$ at the island separatrix).
- Confinement degradation (as a dynamical process) requires elevated radial fluxes outside of the island region (in addition to inside the island) for a certain amount of time as illustrated in the cartoon in FIG. 7.3. Therefore, turbulent transport plays a key role in the β drop.

Finally, the new equilibrium (with NTM) is stable (even though β did increase before

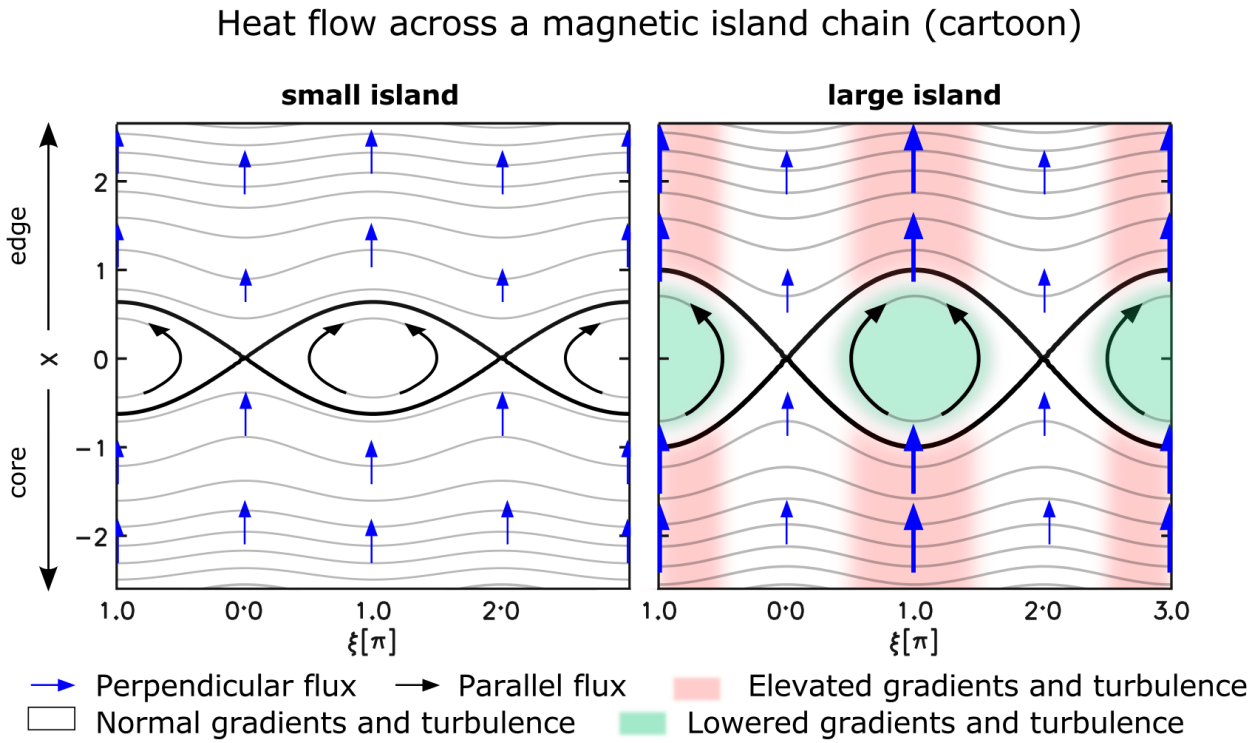

Figure 7.3: Cartoon of transport across a magnetic island: radial fluxes increase due to elevated gradients and concomitant turbulence increase outside of large islands (in line with the O-point). Here $X = (r - r_s)/\mathrm{W_t}$ is a normalized radial coordinate and $\xi = m\theta - n\phi$ is the helical coordinate with θ and ϕ being the poloidal and toroidal angles, respectively. (a) Small island with no profile and flux modification, (b) large island with modified gradients and fluxes.

NTM onset at this same value of β and input power) because an increase in β would increase W and therefore it would increase the fluxes which would decrease β. I.e. this equilibrium is stabilized by the form of the mutual dependence of β and W.

7.3 Turbulence effects in the NTM growth

NTM evolution has been modeled without turbulence effects within the framework of the modified Rutherford equation [59, 100] (MRE), where the major destabilizing mechanism is due to the perturbation of the neoclassical bootstrap current [4] ($\delta \mathrm{j_{bs}}$) arising from pressure flattening at the O-point [58]. Turbulence can affect the NTM growth as the cross-field transport reduces $\delta \mathrm{j_{bs}}$ (via reducing the flat spot at the O-point, see Chapter 1). This

effect has been included in the MRE via the critical island width $W_c \propto \chi_\perp^{1/4}$ with the assumption that $\chi_\perp$ is unaffected by the island [56]. Therefore, the effect of NTM-turbulence interaction on NTM growth rates has not been investigated before. Recall that the physical meaning of W_c is two fold: (i) the threshold (W_t) for transition from small to large island regime and (ii) the width of the island boundary layer (W_b). Hence, the $\chi_\perp$ = const. approximation implies $W_c = W_t = W_b$.

On contrary, turbulence experiments (Chapter 5) and simulations (Chapter 6) show that magnetic islands can lead to the reduction of turbulence levels at the O-point region, which implies that W_c is not a constant but depends on W itself. It was found in Chapter 5 that $W_t \approx 5$ cm, while the boundary layer of saturated islands is of order $W_b \approx 1$ cm as observed in several mid-sized tokamaks [7, 68, 69] (Chapter 1). This means that $W_c = W_t$ when the islands are small, but later on $W_c = W_b$ when the islands saturate. This reduction in W_c ($W_t > W_b$) is likely arising due to turbulence decrease and concomitant $\chi_\perp$ reduction at the O-point region when the island goes through the transition, both of which effects have been reported before (Chapter 5 and 4, respectively). The dependence of W_c on W is an important observation as W_c directly enters the MRE which governs the evolution of the NTM. In this section, the effect of $W_c(W)$ will be investigated on NTM growth using the MRE.

Further, the decrease of plasma β due to the NTM leads to changes in the resistivity (η) as well as in the bootstrap current (j_{bs}). These effects also feed back in the evolution of the NTM. The MRE reads:

$$\frac{dW}{dt} = \frac{\eta}{\mu_\circ}\left(\Delta' + \frac{D_{NC}W}{W^2 + W_c^2}\right) \tag{7.1}$$

The experimental dW/dt is shown in FIG. 7.4 with circles. The solution of equation 7.3 assuming constant $W_c = 1.2$ cm and fixed β is shown in FIG. 7.4 (dashed green). Clearly, this equation describes subcritical islands as seen from the fact that the growth rate is negative around $W = 0$. When $W_c = 0$, dW/dt diverges around zero (dashed black). When

$W_c = 5$ cm, the predicted growth (dashed red) is close to the experimental points.

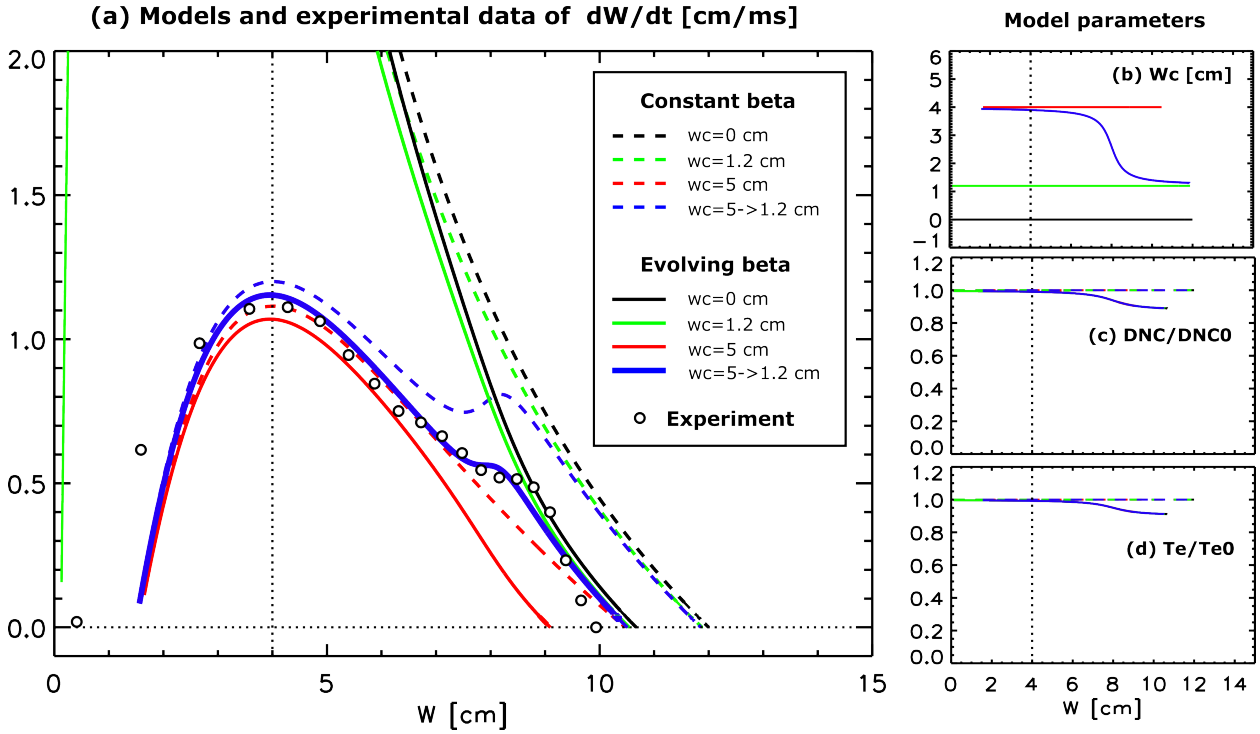

Figure 7.4: (a) Experimental dW/dt (circles) and solutions of the modified Rutherford equation with/without turbulence effects for 4 cases: $W_c = 0$ (black), $W_c = 1.2$ cm (green), $W_c = 5$ cm (red) and evolving W_c (blue). These are shown with evolving β (solid) and fixed β (dashed). Notice that the MRE with turbulence effects (solid blue) compares well with the measured dW/dt. Model $D_{NC}(W), T_e(W)$ and $W_c(W)$ are shown in (b), (c) and (d), respectively.

Notice, that maximum growth occurs at $W = W_c$, which allows the determination of the W_c parameter simply from the time history of W without profile or turbulence measurements. The average of 10 discharges shown in Fig. 7.4 shows $W_c \approx 4$ cm, in good agreement with that obtained via turbulence and profile measurements in Chapter 5. This observation is important as it helps to distinguish the solutions with $W_c = 1.2$ cm and $W_c = 5$ cm. The maximum at $W_c \approx 4$ cm supports the solution with $W_c \approx 5$ cm when the island is small.

However dW/dt has a clear "knee" after $W > W_t$. This means that dW/dt slightly increases off the $W_c = const.$ line after $W > W_t$ has been passed, which indicates that W_c has reduced after $W > W_t$. Clearly, this feature is not captured by the constant W_c model. In order to capture this "knee", two (local and global) transport effects will be

incorporated in equation 8.9 as follows:

- **Local effect (decrease of $\chi_\perp$ at O-point)**: $\mathrm{W_c} = \mathrm{W_t} \approx 5$ cm in small island regime but $\mathrm{W_c} = \mathrm{W_b} \approx 1.2$ cm in large island regime.
- **Global effect (confinement degradation)**: (i) increase of $\eta \propto \mathrm{T_e^{-3/2}}$ and (ii) decrease of $\delta \mathrm{j_{bs}} \propto \mathrm{D_{NC}}$.

Smooth transitions of $\mathrm{W_c}, \mathrm{T_e}$ and $\mathrm{D_{NC}}$ are assumed in the following form:

$$f(\mathrm{W})/f_\circ = 1 - \Delta f \left(\frac{\mathrm{atan}(\mathrm{a_1}(\mathrm{W} - a_2))}{\pi} + \frac{1}{2} \right) \tag{7.2}$$

Here f can be either $\mathrm{W_c}, \mathrm{T_e}$ or $\mathrm{D_{NC}}$. $f_\circ = f|_{\mathrm{W}=0}$ and Δf is the magnitude of the change during the transition. Clearly, $f(\mathrm{W})|_{\mathrm{W}\to\infty} = f_\circ + \Delta f$. The parameters a_1 and a_2 control the speed and the location of the transition vs W. $a_1 \approx 1.5$ and $a_2 = 2\mathrm{W_t}$ result in a moderately steep transition when W passes $\mathrm{W_t}$. These model $\mathrm{D_{NC}(W)}, \mathrm{T_e(W)}$ and $\mathrm{W_c(W)}$ are shown in FIG. 7.4 (b), (c) and (d), respectively. The MRE to solve now is:

$$\frac{\mathrm{dW}}{\mathrm{d}t} = \frac{\eta(\mathrm{W})}{\mu_\circ} \left(\Delta' + \frac{\mathrm{D_{NC}(W)\,W}}{\mathrm{W}^2 + \mathrm{W_c(W)}^2} \right) \tag{7.3}$$

This form of the MRE is consistent with measured $\mathrm{W_c}$ as well as includes the dynamics of η and $\mathrm{j_{bs}}$. Solutions are plotted with evolving $\mathrm{W_c}$ (blue) as well as fixed $\mathrm{W_c} = 5$ cm (red), evolving β (solid) and fixed β (dashed) for comparison [FIG. 7.4]. These solutions show that the MRE with local and global turbulence effects (solid blue) compares well with the measured $\mathrm{dW/d}t$ and (in contrast to the MRE without turbulence effects) can qualitatively and quantitatively replicate the following observations:

1. Turbulence decreases $\mathrm{dW/d}t$ when $\mathrm{W} < \mathrm{W_t}$
2. Decrease of $\mathrm{W_c}$ (due to reduction of turbulence at the O-point) increases $\mathrm{dW/d}t$ after the island has passed the transition point
3. Subsequent drop of β further decreases $\mathrm{dW/d}t$.

In terms of a fusion plasma experiment, not the growth rate itself but W_{SAT} is the important parameter as it determines whether the tokamak can be operated safely or not, i.e. if the torque (T_{isl}) slowing the NTM rotation will lead to locking and subsequent disruption since $T_{isl} \propto W_{SAT}^4$. The global effect decreases W_{SAT} by about 3 cm. This effect is partially compensated by the local effect which increases W_{SAT} by about 1.5 cm. The cumulative effect of turbulence is therefore a decrease of W_{SAT} by about 1.5 cm ($\approx 10\%$), which is favorable as it reduces the chance of NTM locking and subsequent disruption, but also leads to decreased confinement.

7.4 Discussion

In this Chapter it has been shown that the dynamics and the physics of the confinement degradation is clearly linked to turbulence increase outside of the island region [87] (induced by the island). Namely, the T_e profiles show that the island increases ∇T_e outside of the island when W is slightly larger then W_t. This results from the fast parallel transport flattening T_e at the O-point before T_e on axis could decrease. This increase of ∇T_e (and increased turbulence) is responsible for the increased transport. The increased transport decreases the confinement and the gradients until the fluxes balance the constant input power. This non-linear, multi-scale process brings the plasma to a new equilibrium, which is characterized by the same input power, fluxes and gradients as before NTM onset, but with lower β and a ≈ 10 cm wide $m/n = 2/1$ magnetic island.

Next, experimentally observed local turbulence effects as well as global equilibrium changes have been incorporated into the MRE. This qualitatively and quantitatively replicated the observed increase of NTM growth when turbulence was reduced at the O-point.

In a fusion experiment, W_{SAT} determines whether the tokamak can be operated safely or not. The cumulative effect of turbulent transport is a decrease of W_{SAT} by about 1.5 cm ($\approx 10\%$), on the price of decreasing the confinement. As the drag on the island (due to eddy currents generated in the wall by the rotating island) scales with W_{SAT}^4, One can see the decrease of confinement as 'favorable', since it decreases the chances of NTM locking and disruption. These observations also suggests that we can avoid small islands becoming large by driving turbulence at $q = m/n$ (e.g. via ECH), providing an opportunity for scenario development.

CHAPTER 8

Shrinking of magnetic islands due to ELMs and the role of turbulence in island recovery

8.1 Introduction

The multi-scale interaction of small-scale turbulence with the large-scale NTM during the NTM growth phase was reported in Chapters 5 and 7. On the other hand, quasi-periodic shrinking of saturated core $m/n = 2/1$ NTM islands due to coupling to type-I ELMs have been observed previously [101]. However, the physics of coupled island and local turbulence dynamics during the ELM cycle has not been explored yet. Cold pulses linked to the ELM crash propagate to the island region, which could lead to significant perturbations of the otherwise nearly flat T_e inside the island. The concomitant increase of gradients at the O-point (and decrease of δj_{BS}) could be the key physics resulting in the island shrinking. On the other hand, a turbulence increase in sync with increased gradients at the O-point could increase the NTM recovery rate via accelerating the relaxation of the T_e perturbation at the O-point via turbulent cross-field transport.

To address the above hypothesis, the response of $m/n = 2/1$ islands and low-k turbulence to type-I ELMs has been studied. The islands respond with the peaking of T_e at the O-point, leading to increased ∇T_e when the cold pulses reach the island region. In sync, the island width shrinks by as much as 30%, presumably due to changes in δj_{BS} at the O-point due to peaked T_e. Next, the T_e peak relaxes via anomalous cross-field transport and the island recovers simultaneously, suggesting a key role of the peak in the stability of the NTM. Following the ELM crash, local measurements of low-k $\tilde{n}$ via Beam Emission Spectroscopy (BES) show increased turbulence at the O-point when local gradients are

increased, which offers an explanation for the observed anomalous transport. Therefore, these measurements indicate that turbulent cross-field transport accelerates NTM recovery after an ELM crash by relaxing ∇p and thus restoring δj_{BS} at the O-point.

Finally, to investigate this possible relationship between turbulence and NTM growth, it is shown that the modified Rutherford equation [58] (modeling the evolution of the NTM) coupled with the predator-prey equations [10] (modeling the evolution of local turbulence power and pressure gradient at the O-point) can replicate the above observations. In this coupled model, turbulence accelerates NTM recovery via relaxing ∇p and therefore restoring δj_{BS} at the O-point.

These new observations have importance (i) in the frontier of experimental research and gyrokinetic simulations of multi-scale interaction of NTMs with micro-turbulence, and (ii) in developing a more complete understanding of ELM and core NTM coupling, especially in regard of the island shrinking and recovery during the ELM cycle. In addition, the key physics of the relationship between the T_e peak and NTM stability has potentially far-reaching consequences, such as NTM control via pellet injection in large fusion devices, for example in the International Thermonuclear Experimental Reactor (ITER). The material of this Chapter has been submitted for publication to Physics of Plasmas [88].

8.2 Experimental overview

$m/n = 2/1$ NTMs and turbulence were studied in the DIII-D tokamak in two similar H-mode discharges (#134360 and #134375). Discharge #134375 [FIG. 8.1] was described previously in Chapter 4, where heat transport was studied across the island. In the following, the $2200 - 2500$ ms window is in focus, when the islands were heated by 3 MW ECH [FIG. 8.1 (e)]. In this discharge, magnetic islands were monitored via the ECE radiometer and turbulent density fluctuations ($\widetilde{n}$) were probed across the islands locally via BES (Beam Emission Spectroscopy [102]) and non-locally via FIR (Far Infrared scattering [78]).

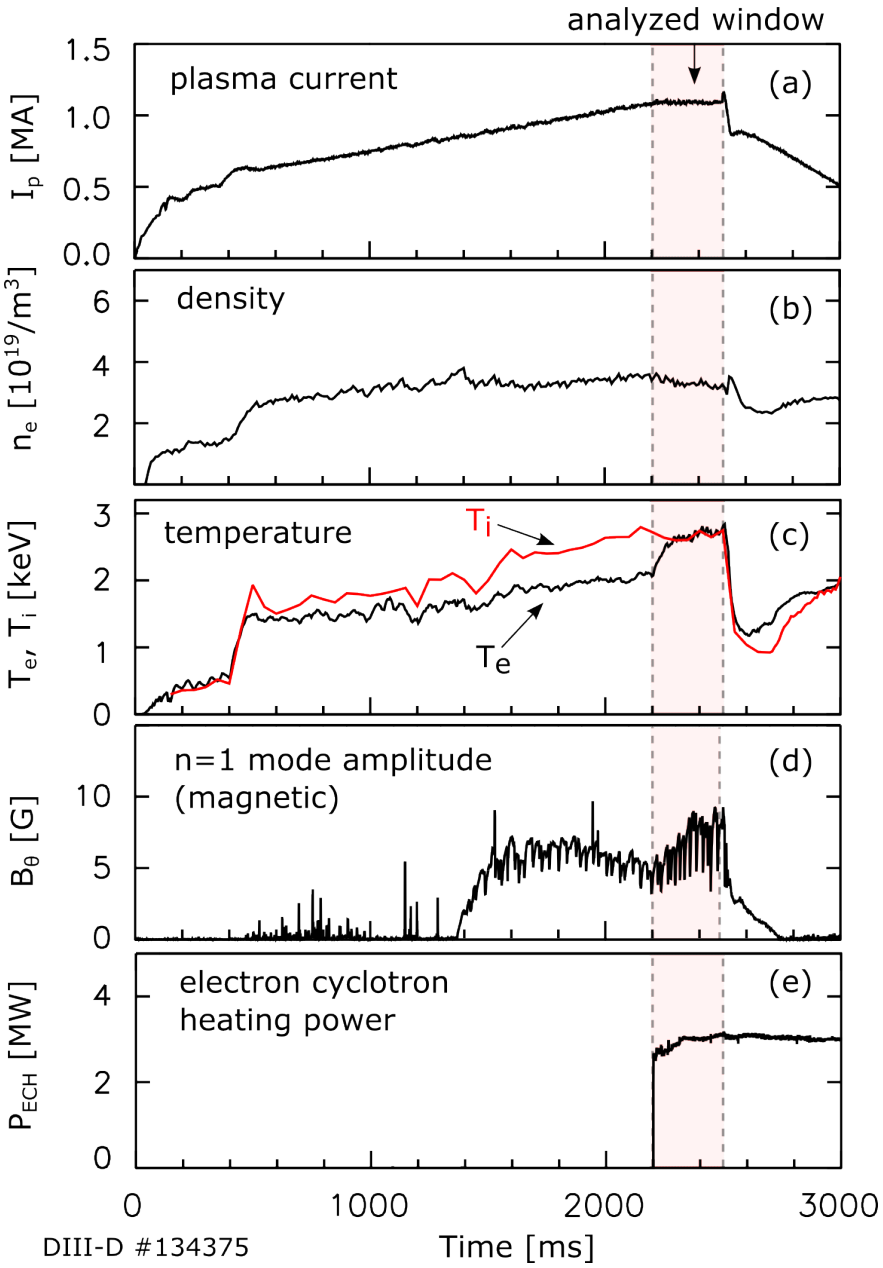

Figure 8.1: Time histories of the studied H-mode plasma discharge: (a) plasma current, (b) density, (c) T_i and T_e at R = 199 cm (center of 2/1 island), (d) n = 1 mode amplitude (magnetic signal) and (e) electron cyclotron heating power. Note that the analyzed window is shaded.

Local turbulence measurements via BES

To avoid spurious photon noise contributions, $\widetilde{n}^2(t)_{\rm BES}$ was calculated from radially offset, nearest neighbor cross-powers:

$$\widetilde{n}^2(t)_{\rm BES} = \int_{100\ \rm kHz}^{500\ \rm kHz} \widetilde{n}_1(\omega,t)_{\rm BES}\, \widetilde{n}_2^*(\omega,t)_{\rm BES}\, d\omega \tag{8.1}$$

Here $\widetilde{n}_1(\omega,t)_{\mathrm{BES}}$ and $\widetilde{n}_2(\omega,t)_{\mathrm{BES}}$ are the short-time Fourier transforms of two neighboring BES signals ($\widetilde{n}_1(t)_{\mathrm{BES}}$ and $\widetilde{n}_1(t)_{\mathrm{BES}}$) near $q = 2$ (* stands for complex conjugation). Note that $\widetilde{n}^2(t)_{\mathrm{BES}}$ is calculated from frequencies (f) much higher then the NTM frequency ($f > 100$ kHz) to avoid contributions form the modulation of the density profile itself caused by the rotating island. Therefore, $\widetilde{n}^2(t)_{\mathrm{BES}}$ is associated with broadband low-k turbulence power. Next, making use of the island rotation and using the ECE signals as reference, the $\widetilde{n}^2(t)_{\mathrm{BES}}$ was extended to $\widetilde{n}^2(t,\xi)_{\mathrm{BES}}$ by mapping time (t) to the helical coordinate (ξ) within each island cycle as in a previous study of magnetic islands [7]. The sampling frequency of the helically resolved $\widetilde{n}^2(t,\xi)_{\mathrm{BES}}$ is then lower than that of $\widetilde{n}^2(t)_{\mathrm{BES}}$ and is equal to the island rotation frequency (9 kHz). Finally the $\widetilde{n}^2(t,\xi)_{\mathrm{BES}}$ signal was phase lock-averaged in the O-point region:

$$\widetilde{n}^2_O(t)_{\mathrm{BES}} = \frac{1}{\pi}\int_{\pi/2}^{3\pi/2} \widetilde{n}^2(t,\xi)_{\mathrm{BES}} d\xi \tag{8.2}$$

Here the O-point region is defined as $\Omega < 0$, which at fixed r corresponds to $\pi/2 < \xi < 3\pi/2$. $\widetilde{n}^2_O(t)_{\mathrm{BES}}$ is therefore the power of broadband, low-k turbulent density fluctuations at the O-point region of the island.

Line integrated turbulence measurements via FIR

The low-k turbulent $\widetilde{n}$ measured via FIR is denoted as $\widetilde{n}(t)_{\mathrm{FIR}}$. The line integrated and rotation averaged broadband fluctuation power was calculated from the FIR signal as:

$$\widetilde{n}^2(t)_{\mathrm{FIR}} = \int_{100\ \mathrm{kHz}}^{500\ \mathrm{kHz}} \widetilde{n}(\omega,t)_{\mathrm{FIR}}\, \widetilde{n}^*(\omega,t)_{\mathrm{FIR}}\, d\omega \tag{8.3}$$

Here $\widetilde{n}(\omega,t)_{\mathrm{FIR}}$ and is the short-time Fourier transform of the FIR signal $\widetilde{n}(t)_{\mathrm{FIR}}$.

T_e measurements via ECE

The contours of T_e were reconstructed by phase-locking the radially resolved ECE data over 0.5 ms windows (4 island turnover time) via the method described in Subsection 2.3.1,

see examples in [FIG. 8.2] (a), (b) and (c). The full width of the island is about W = 10 cm, determined by fitting the solutions of the heat transport model to T_e data (Chapters 3 and 4 [7]).

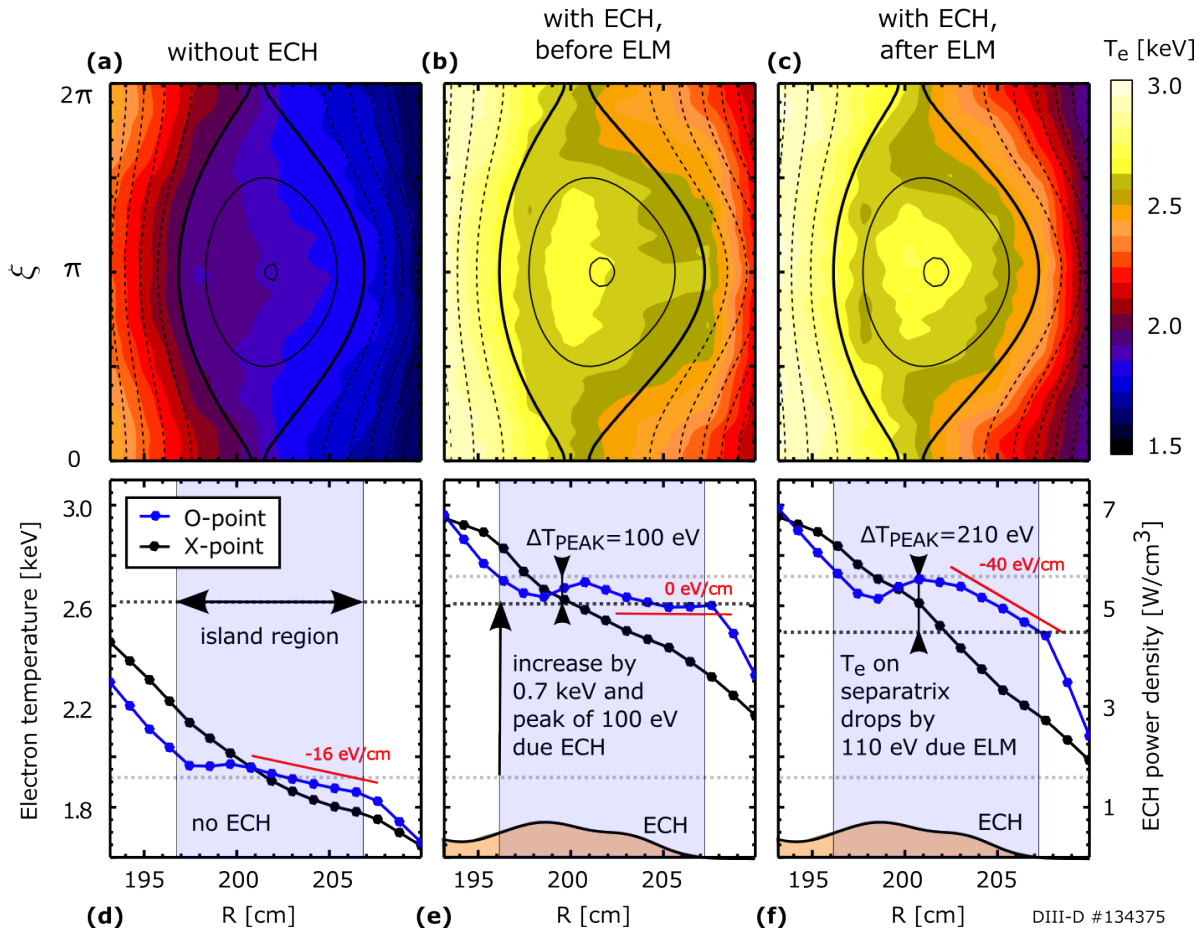

Figure 8.2: Contours of $T_e(R, \xi)$ in the experiment and contour lines of the magnetic island flux function ($\Omega(R, \xi)$) determined by fitting [7] the solutions of equation (3.3) to $T_e(R, \xi)$. (a) flat island without ECH; (b) increased and peaked T_e at the O-point due to static ECH between two ELMs; (c) T_e drops on island outer separatrix after an ELM leading to larger effective peak and a temperature gradient of -40 eV over a significant radial range inside the island. (d), (e) and (f) show radial profiles of T_e across the O-point and X-point corresponding to (a),(b) and (c), respectively. Note that the ECH power density is shown in (e) and (f).

8.3 Structure of $T_e(r, \xi)$ with heat sources and sinks

Three distinct type of $T_e(r, \xi)$ profiles have been observed across the islands, resulting from a combination of a heat source (ECH) and a sink (ELM):

1. First, the island is almost flat in the absence of ECH [FIG. 8.2 (a) and (d)]. This is similar to the solution of the homogeneous heat transport model shown in FIG. 3.4 (a) and (e) [Section 3.3].

2. The background T_e is elevated by ≈ 0.7 keV when $\approx 0.5 \mathrm{W/cm^3}$ ECH is heating the island region [FIG. 8.2 (b) and (e)]. In addition, a $\Delta T_{PEAK} \approx 100\,\mathrm{eV}$ is established at the O-point. This is qualitatively expected from the model presented in Section 3.3, compare with FIG. 3.4 (b) and (f). ΔT_{PEAK} is calculated from the phase-locked ECE contour by subtracting T_e of the outer separatrix ($R \approx 207\,\mathrm{cm},\ \xi = \pi$, proxy for T_e at X-point) from T_e at the O-point ($R \approx 201.5\,\mathrm{cm},\ \xi = \pi$). Note that, according to the heat transport analysis of islands with peaked T_e in Subsection 3.3, the T_e peak at the O-point suggests that field lines inside the island are not chaotic but form nested flux surfaces.

3. Right after an ELM crash, T_e rapidly drops on the island separatrix by $\approx 110\,\mathrm{eV}$. At this time the O-point T_e has not yet changed, leading to an effective $\Delta T_{PEAK} = 210\,\mathrm{eV}$ [FIG. 8.2 (c) and (f)]. Next, this peak equilibrates via cross-field transport that drives heat from the O-point region through the island separatrices as in the model described in Subsection 3.4.

Note that broad-band thermal emission is often observed in ECE signals during an ELM crash leading to a false increase in the signal level in the edge plasma. The observation described above relies on core measurements ($\rho \approx 0.4$), and in fact reports a decrease of T_e after the ELM crash which is inconsistent with spurious broadband emission.

8.4 Peaking of O-point T_e and island shrinking due to type-I ELMs

In this subsection, the dynamics of ΔT_{PEAK} is described which is modulated by type-I Edge Localized Modes. ΔT_{PEAK} was calculated from each island cycle, giving a time history with 9 kHz sampling rate (limited by the island rotation frequency), see FIG. 8.3 (a). $\Delta T_{PEAK}(t)$ reflects the statements drawn from the $T_e(r, \xi)$ contours [FIG. 8.2]. Namely, the island is almost flat ($\Delta T_{PEAK} \approx 0$) when the ECH is off ($t < 2200$ ms), and a peak develops ($\Delta T_{PEAK} \approx 0.25$ keV) after the ECH is switched on at 2200 ms.
$\Delta T_{PEAK}(t)$ undergoes quasi-periodic oscillations of about 0.15 keV (on top of a base value of ≈ 0.25 keV during the ECH heating phase) [FIG. 8.3 (a) and (b)]. Note that these oscillations of $\Delta T_{PEAK}(t)$ are not due to the island rotation as the timescale of these oscillations is ≈ 30 ms while the island turnover time is about 0.12 ms. These oscillations align with the peaks of the divertor D_α signal [FIG. 8.3 (d)] originating from type-I ELMs showing that a strong coupling exists between ELMs and the core NTM. ELMs are edge magnetohydrodynamic instabilities leading to the quasi-periodic collapse of the H-mode pedestal [39]. This collapse results in a perturbation that propagates from the edge plasma to the $q = 2$ surface. In turn, T_e drops at the island separatrix resulting in a cold pulse that travels *around* the island via fast parallel transport (instead of penetrating all the way to the O-point via slow cross-field transport). This leads to the fast drop of T_e at the X-point which is followed by a slower drop of T_e at the O-point, see FIG. 8.3 (c). The difference between T_e at the X-point and at the O-point thus suddenly increases as shown in FIG. 8.3 (b), consistent with the contours shown in FIG. 8.2 (b) and (c). After the ELM crash, this peak relaxes via cross-field transport (since parallel transport can not drive heat across the nested flux surfaces of the island).
In sync with the ELMs and O-point peaking, the NTM magnetic amplitude decreases by as much as 50% (from 8 G to 4 G; the magnetic island width shrinks by about 30%) [FIG. 8.3 (e)]. This shrinking is possibly due to the increased gradients (due to ΔT_{PEAK}) and decreased δj_{BS} at the O-point. Reduced δj_{BS} at the O-point of 3/2 islands after an

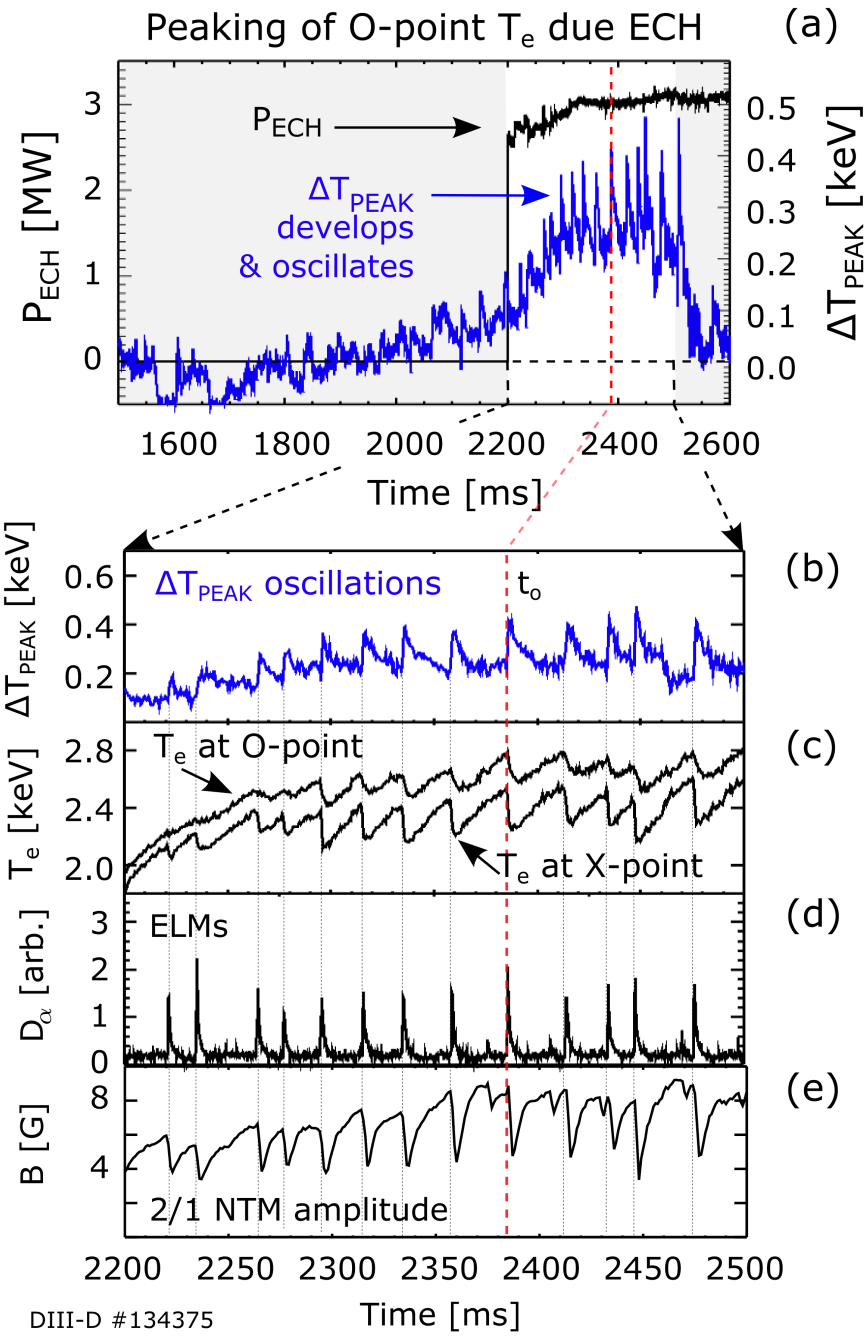

Figure 8.3: (a) Time series of temperature peak at O-point (ΔT_{PEAK}) and ECH heating (P_{ECH}). (b) Expanded view of ΔT_{PEAK} during ECH heating. (c) Time series of T_e at O-point (upper) and at X-point (lower). (d) Divertor D_α signal and (e) 2/1 NTM amplitude ($n = 1$ magnetic RMS). Expanded view around $t_\circ = 2385.5$ ms is shown in FIG. 8.4.

ELM crash was reported previously [103]. Therefore, the transport mechanism relaxing this peak (and restoring δj_{BS}) has potentially a key role in the NMT growth rate when a

saturated NTM magnetic island is recovering after an ELM perturbation. One potential cross-field transport mechanism is linked to low-k fluctuations at the O-point which were measured locally via BES (Beam Emission Spectroscopy) and non-locally via FIR (Far Infrared scattering) [Section 8.5].

8.5 Transport, turbulence and island dynamics during an ELM cycle

In this section, cross-field transport inside the island, local turbulent fluctuations at the O-point and island recovery during an ELM cycle is presented. For this purpose, a window of 20 ms is analyzed in depth [FIG. 8.4] around a large ELM crash at $t_\circ = 2385.5$ ms (marked with vertical dashed line in FIG. 8.3).

8.5.1 Cross-field transport at the O-point

The perturbative $\chi_\perp$ was determined at the O-point by fitting expression (3.16) of the 1D transient heat transport model to the experimentally measured time history of the decaying ΔT_{PEAK}. An expanded view of $T_e(t)$ at the X-point and at the O-point is shown in FIG. 8.4 (a) and ΔT_{PEAK} in shown in FIG. 8.4 (b) (at $t_\circ = 2385.5$ ms). The fitted analytic solutions of the model (solid lines) compare well with the experimental X-point T_e, O-point T_e and ΔT_{PEAK} (circles). The fit estimates $\chi_{\perp,O}^{Pert.} \approx 2$ m^2/s at the O-point and $\chi_{\perp,X}^{Pert.} \approx 10$ m^2/s at the X-point. In comparison, the power balance electron thermal diffusivity of the background plasma at q=2 (not that of the island) is $\chi_{TRANSP}^{Power\ b.} \approx 6\,$m^2/s and the neoclassical cross-field electron thermal diffusivity is $\chi_{TRANSP}^{Neoclass.} \approx 10^{-2}\,$m^2/s, estimated via TRANSP [61]. $\chi_{TRANSP}^{Power\ b.}$ is reasonably close to both $\chi_{\perp,X}^{Pert.}$ and $\chi_{\perp,O}^{Pert.}$ and $\chi_{\perp,X}^{Pert.} > \chi_{TRANSP}^{Power\ b.}$ as expected. This is an interesting result as it shows that $\chi_\perp$ at the O-point is anomalous when T_e is peaked in contrast to flat islands, where $\chi_\perp$ is reduced by 1-2 orders of magnitude [7] (compared to $\chi_\perp$ of the background plasma).

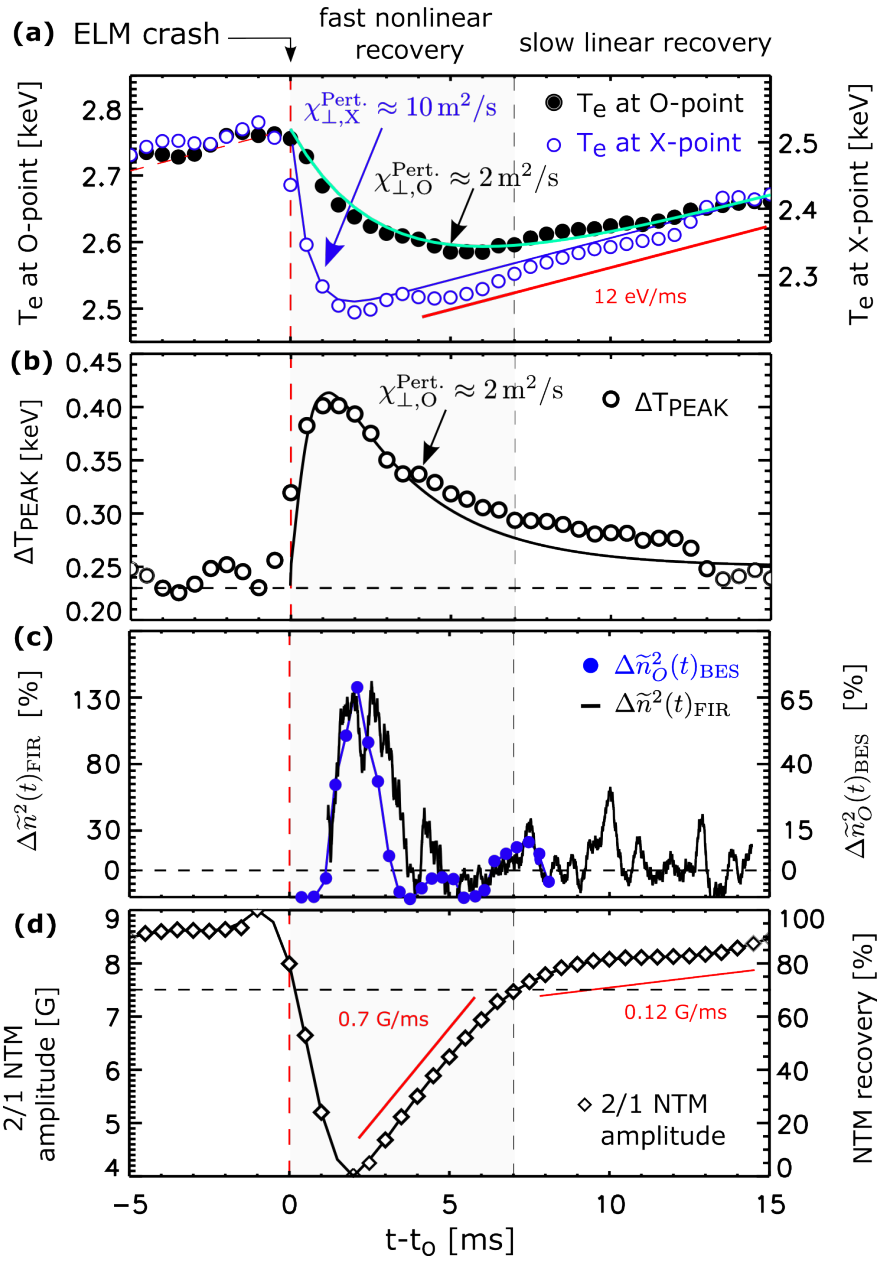

Figure 8.4: (a) Fast T_e drop at X-point is followed by slower drop at O-point (due to different local $\chi_\perp$) leading to an increase of T_e peak at the O-point shown in (b). (c) low-k fluctuations across the island increase $2-4$ ms after an ELM crash as seen from $\widetilde{n}^2_{\rm FIR}$ (#134375) as well as locally at the O-point as seen from $\widetilde{n}^2_{\rm BES}$ (#134360). (d) 2/1 NTM amplitude decreases and recovers in sync with the T_e peak. (Solid lines are analytic solutions of the transient heat transport model (equation. (3.16)) on (a) and (b).)

8.5.2 Low-k turbulence at the O-point

As mentioned in Section 8.2, the BES diagnostic allows the determination of $\widetilde{n}^2_O(t)_{\mathrm{BES}}$, the power of broadband, low-k turbulent density fluctuations at the O-point region of the island. Reference fluctuation levels $\overline{\widetilde{n}}^2_{\mathrm{O,BES}}$ and $\overline{\widetilde{n}}^2_{\mathrm{FIR}}$ were calculated from windows when the perturbations due to the ELMs have decayed:

$$\overline{\widetilde{n}}^2_{\mathrm{O,BES}} = \frac{1}{N}\sum_{i=1}^{N}\int_{t^i_\circ+\Delta t}^{t^{i+1}_\circ} \widetilde{n}^2_O(t)_{\mathrm{BES}}dt \tag{8.4}$$

$$\overline{\widetilde{n}}^2_{\mathrm{FIR}} = \frac{1}{N}\sum_{i=1}^{N}\int_{t^i_\circ+\Delta t}^{t^{i+1}_\circ} \widetilde{n}^2(t)_{\mathrm{FIR}}dt \tag{8.5}$$

Here $t^i_\circ$ is the time of the i^{th} ELM event, N is the number of ELMs and $\Delta t = 4$ ms. The change of fluctuation levels $\Delta\widetilde{n}^2_O(t)_{\mathrm{BES}}$ and $\Delta\widetilde{n}^2(t)_{\mathrm{FIR}}$ were calculated using these reference fluctuation levels as:

$$\Delta\widetilde{n}^2_O(t)_{\mathrm{BES}} = \frac{\widetilde{n}^2_O(t)_{\mathrm{BES}} - \overline{\widetilde{n}}^2_{\mathrm{O,BES}}}{\overline{\widetilde{n}}^2_{\mathrm{O,BES}}} \tag{8.6}$$

$$\Delta\widetilde{n}^2(t)_{\mathrm{FIR}} = \frac{\widetilde{n}^2(t)_{\mathrm{FIR}} - \overline{\widetilde{n}}^2_{\mathrm{FIR}}}{\overline{\widetilde{n}}^2_{\mathrm{FIR}}} \tag{8.7}$$

[FIG. 8.4 (c)] shows a significant increase of $\Delta\widetilde{n}^2_O(t)_{\mathrm{BES}}$ after an ELM event, meaning that turbulence is increased at the island O-point after an ELM. In accord with this, $\Delta\widetilde{n}^2(t)_{\mathrm{FIR}}$ also shows an overall increase of $\widetilde{n}^2$ along a chord encompassing the island region.
This increase of the measured low-k broadband fluctuations seen both in $\widetilde{n}^2(t)_{\mathrm{BES}}$ and $\widetilde{n}^2(t)_{\mathrm{FIR}}$ is consistent with low-k turbulence being increased at the O-point due to increased local gradients after an ELM crash. These increased fluctuations are likely responsible for the observed anomalous heat transport across the nested flux surfaces of the island, hence, accelerating the relaxation of $\Delta\mathrm{T}_{\mathrm{PEAK}}$ (compared to slow neoclassical transport).
Interestingly, both $\Delta\widetilde{n}^2_O(t)_{\mathrm{BES}}$ and $\Delta\widetilde{n}^2(t)_{\mathrm{FIR}}$ show nearly the same delay prior to increasing with $\Delta\mathrm{T}_{\mathrm{PEAK}}$ as well as decaying significantly earlier than the decay in $\Delta\mathrm{T}_{\mathrm{PEAK}}$. One possible explanation is multiple types of instabilities covering the same wavenumbers

(e.g. ITG with lower-k TEM) but with different critical gradient type response [104, 105] to ΔT_{PEAK}. This is beyond the scope of the present paper but will be explored in future publications.

8.5.3 Magnetic island dynamics

As mentioned in Section 8.4, the NTM magnetic amplitude decreases by as much as 50% (from 8 G to 4 G; island width shrinks by 30%) in sync with ELMs and O-point T_e peaking, see FIG. 8.4 (d). This shrinking could originate from the local drop of β at $q = 2$ due to the large ELM event (approximated by T_e at X-point shown in FIG. 8.4 (a)) and/or the decrease of δj_{BS} at the O-point due to increase of ΔT_{PEAK}. A theoretical model of δj_{BS} inside a peaked island has not been developed yet, therefore, here it is not verified/confirmed the second possibility on a theoretical basis. However, recall that the reduction of δj_{BS} at the O-point of 3/2 islands after an ELM crash has been measured in DIII-D plasma [103]. Also, notice that there is a characteristic breakpoint in the time history of the NTM amplitude, typically about 7 ms after each ELM crash [FIG. 8.3 (d) and FIG. 8.4 (d)]. This breakpoint suggests that there are two characteristic regimes in the NTM recovery:

- In the first regime ($t - t_\circ < 7$ ms), the NTM recovers by 70% with a growth rate of $\gamma_1 \approx 110$ Hz (≈ 0.70 G/ms). In this window, $\widetilde{n}$ is increased and ΔT_{PEAK} shrinks by 70% [FIG. 8.4 (b)].
- In the second regime ($t - t_\circ > 7$ ms), the NTM recovers by 30% only with a growth rate of $\gamma_2 \approx 15$ Hz (≈ 0.12 G/ms). In this window, turbulence is reduced at the O-point and ΔT_{PEAK} is small.

These observations suggest that during the early phase, NTM recovery is accelerated by local cross-field transport inside the island, potentially due to increased low-k $\widetilde{n}$ (via relaxing ΔT_{PEAK} and therefore recovering δj_{BS}). Later on, after ΔT_{PEAK} and $\widetilde{n}$ has decreased to the original level, the NTM grows resistively.

The observations reported in this section suggest that the recovery of a large NTM magnetic island after an ELM crash is accelerated by micro-instabilities driven transport. To investigate this possible relationship, solutions of the modified Rutherford equation (modeling the evolution of the NTM) coupled with the predator-prey equations (modeling the evolution of local turbulence power and pressure gradient at the O-point) was investigated for the first time in Section 8.6.

8.6 Model equations

The predator-prey model [10] of turbulence, zonal-flows and pressure gradient provides a fundamental set of equations to model the observations reported in Section 8.2. NTM evolution is included via the modified Rutherford equation [58] (MRE). Zonal-flows are removed for simplicity (and also due lack of measurement) which is reasonable as flows are not expected to be dominant at the O-point (however are predicted to regulate turbulence just outside the island separatrices [6, 18, 60]). The 3 coupled first order differential equations describing the evolution of $\widetilde{n}_{\mathrm{o}}^2$ (turbulence level at O-point), W (island width) and $\nabla \mathrm{p_o}$ (pressure gradient at O-point) are:

$$\partial_t \widetilde{n}_{\mathrm{O}}^2 = \mathrm{a_0}\nabla \mathrm{p_O} - \mathrm{a_1}\widetilde{n}_{\mathrm{O}}^2 \tag{8.8}$$

$$\partial_t \mathrm{W} = \frac{\eta}{\mu_{\circ}}\left(\Delta' + \mathrm{b_1}\frac{\mathrm{W}(\nabla \mathrm{p_X} - \nabla \mathrm{p_O})}{\mathrm{W_c^2} + \mathrm{W}^2}\right) \tag{8.9}$$

$$\partial_t(\nabla \mathrm{p_O}) = \mathrm{F}(\omega) - \mathrm{c_0}\widetilde{n}_{\mathrm{O}}^2 - \mathrm{c_1}\nabla \mathrm{p_O} \tag{8.10}$$

A flat density profile is assumed, meaning that at the O-point $\nabla \mathrm{p} \propto \nabla \mathrm{T_e} \propto \Delta \mathrm{T_{PEAK}}$. The pressure gradient at the X-point is assumed to be constant and is denoted by $\nabla \mathrm{p_X}$. The physical meaning of the parameters and terms are as follows. Equation (8.8) prescribes the evolution of $\widetilde{n}_{\mathrm{O}}^2$: turbulence is driven by $\nabla \mathrm{p_O}$ and is saturated via a linear dissipation. Equation (8.9) is the MRE. η and $\mu_{\circ}$ are the plasma resistivity and the vacuum permeability, respectively. $\mathrm{W_c} = 2\mathrm{w_c}$, where $\mathrm{w_c} = 1$ cm is the boundary layer width of the saturated island where gradients are maintained without localized heating [7, 56] and Δ' is

the linear stability parameter [37]. The numerical coefficient in the drive term is $b_1 = -2\sqrt{\varepsilon_{TR}}\mu_\circ L_q/(B_\theta^2 L_\circ)$, where ε_{TR} is the trapped electron fraction, L_q is the magnetic shear scale length, B_θ is the poloidal magnetic field and $L = R_\circ/n$. It is assumed that this model holds for the bootstrap current and variations of it are considered due to the temperature peaking. Equation (8.10) is the evolution of the pressure gradient at the O-point which is driven by a periodic external force describing the effect of ELMs ($F(\omega)$, here a sharp Gaussian perturbation) and is relaxed via turbulent (c_0) and diffusive (c_1) transport. The model has 6 fit parameters, 2 from each equation: a_0,a_1,$\eta\Delta'/\mu_\circ$,$\eta b_1/\mu_\circ$,c_0 and c_1. ∇p_x and W_c are directly obtained [7] from the DIII-D measurements and are fixed in this model.

Two set of solutions are shown in FIG. 8.5: one with turbulent transport (thick solid light lines) and one without (dotted lines). The experimental data (symbols) of FIG. 8.4 is re-plotted here, for a convenient comparison. First, the model parameters were estimated by fitting the model with turbulent transport term to the experimental data. Before $t = t_\circ$, the pressure gradient is small at the O-point, the turbulence level is constant and the NTM is saturated. Next, ΔT_{PEAK} grows due to a model ELM at $t_\circ$ and the island shrinks due to modification of the bootstrap current term via increased ∇p_O. Simultaneously, the turbulence level increases, which accelerates the peak relaxation and therefore the NTM recovery. A second set of solution (dotted lines) was calculated by turning the turbulent transport term off (setting $c_0 = 0$). In this case, turbulence does not have an effect on the peak relaxation, which results in a longer NTM recovery. These two types of solutions demonstrate that the growth of the NTM after an ELM crash is faster with turbulence compared to without turbulence.

This simple model replicates the experimental observations reported in Section 8.5, namely that after the ELM crash the pressure gradient grows at the O-point which is followed by the shrinking of the island and turbulence increase. The relaxation of the profile and the mode recovery take place on the same, turbulent transport time-scale. In this model, turbulence accelerates NTM recovery via rapid relaxation of the pressure profile and figure

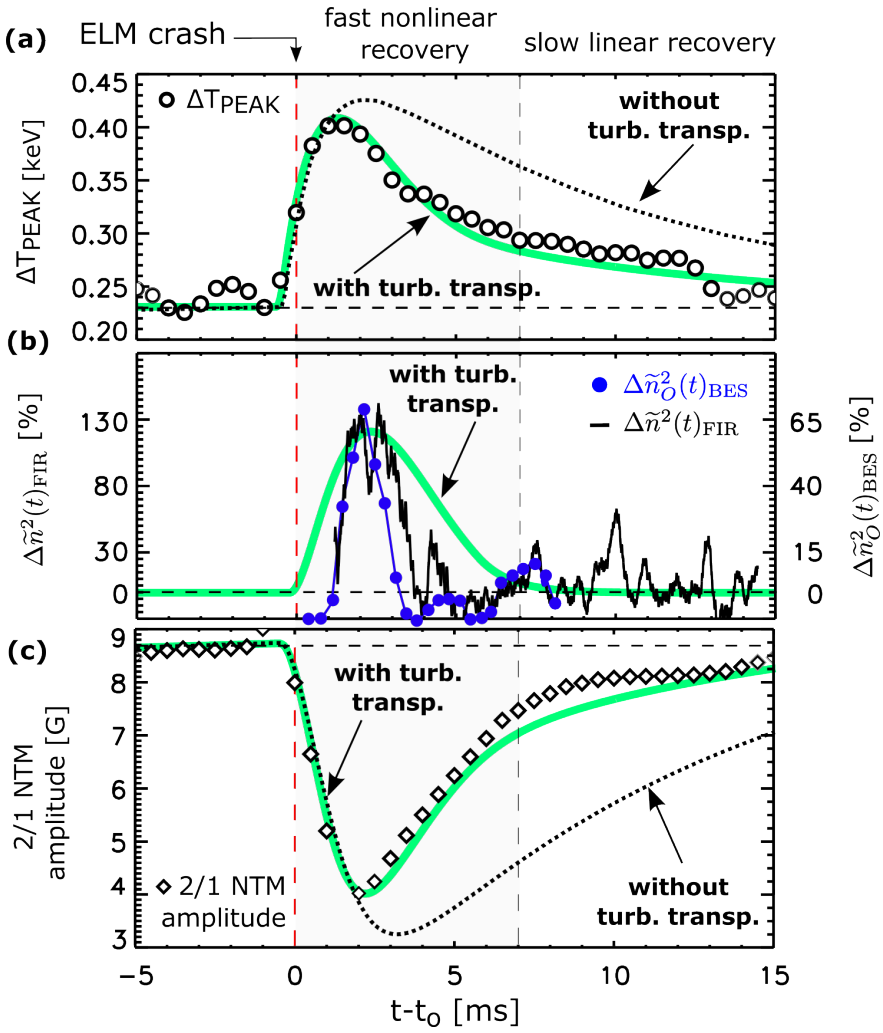

Figure 8.5: Solution of the coupled predator-prey and modified Rutherford equation (equations (8.8-8.10): (a) pressure gradient, (b) turbulence level and (c) NTM amplitude. Free parameters of the model were chosen to match experimental data. Solid thick light line: with turbulent transport, dotted line: without turbulent transport. (Parameters are: $a_0 = 0.01$, $a_1 = 0.005$, $\eta\Delta'/\mu_o = -1.3$, $\eta b_1/\mu_o = 0.5$, $\nabla p|_X = 150$, $w_c = 2.5$, $c_0 = 0.001$ and $c_1 = 0.007$, experimental data is a repeat of FIG 8.3.)

of the missing bootstrap current at the O-point.

8.7 Discussion

First, the effect of ECH on $m/n = 2/1$ islands in DIII-D H-mode plasmas was studied [Section 8.3]. The peaking of T_e at the O-point was observed, which indicates that the island has nested flux surfaces, as in the heat transport model [Subsection 3.3]. On top of a base value, this peak oscillates due to cold pulses generated by ELMs (Section 8.4). The experimental value of the perturbative $\chi_\perp$ at the O-point was constrained by comparing the time history of the peak to analytic solutions of the heat transport model [Subsection 8.5.1]. This found $\chi_{\perp,\mathrm{O}}^{\mathrm{Pert.}} \approx 2\,\mathrm{m}^2/\mathrm{s}$, unlike in flat islands where $\chi_{\perp,\mathrm{O}} = 0.1 - 0.01\ \mathrm{m}^2/\mathrm{s}$ was found [7]. Local BES measurements indicate that low-k density fluctuations at the O-point are increased when the island peak is increased [Subsection 8.5.2]. This suggests an explanation for the observed anomalous transport inside the island when the T_e peak is increased.

In sync with ELMs and O-point peaking, the island shrinks by as much as 30% [Subsection 8.5.3]. Comparison of the NTM amplitude recovery with the time history of the temperature peak suggests that the NTM recovery is connected to the local gradients at the O-point, as expected. As such, the growth rate of the NTM is linked to cross-field transport at the O-point region which is likely driven by the increased $\widetilde{n}$.

Finally, predator-prey equations coupled with the modified Rutherford equation were found to reproduce the experimental observations of coupled NTM-turbulence dynamics. In this model, increased gradient driven turbulence at the O-point accelerates NTM recovery via rapid relaxation of the pressure profile and therefore restoring the missing bootstrap current at the O-point. The key physics of the relationship between the temperature peak, turbulence level at the O-point region and the NTM magnetic island width has potentially far-reaching consequences:

Gyrokinetic code validation

Turbulent cross-field transport equilibrating the peak accelerates NTM recovery after ELMs; This observation could be used for testing and validation of nonlinear gyrokinetic turbulence simulations with magnetic islands, where a propagating cold

pulse could be realized e.g. by employing a transient boundary condition on the cold side of the simulation box. Validation is important as these models (investigating the multi-scale interaction of turbulence with islands) have been undergoing significant development in the past decade but only initial experimental validations [87] have been carried out so far.

Scenario development

ECH heating inside the island (without ECCD current drive) combined with localized cooling outside the island via pellet injection could stabilize NTM islands (via leading to a temperature peak and concomitant increase of gradients at the O-point, making the island shrink below W_c where it is neoclassically stable). This method could be used in scenario development to suppress 2/1 NTMs in ITER relevant plasmas, avoiding possible disruptions and therefore accessing higher β regimes.

CHAPTER 9

Ion temperature and rotation across slowly rotating NTMs

Measurements of $\delta \mathrm{T_i}(R,\xi)$ and $\delta \mathrm{v}_\phi(R,\xi)$ across rotating NTM islands can be accomplished using the CER diagnostic. However, helically resolved CER measurements of NTMs require steady state low torque high-β plasmas, which are advanced and challenging tokamak experiments requiring significant resources.

The island rotation frequency (f_{NTM}) must be below the sampling rate of the CER diagnostic, which is relatively low, $f_{\mathrm{CER}} \approx$ 1 kHz.

Rotating magnetic islands lead to the formation of eddy currents in the conducting tokamak wall, which, due to resistivity, dissipate the island rotation energy. If the associated drag is large, this effect can lead to progressive slowing until the islands eventually lock to the wall, which is often followed by disruption [8]. Typically, small f_{NTM} and large W lead to large drag. Therefore, slowly rotating islands must be small in order to avoid locking. f_{NTM} and W can be controlled by the beam torque and power, respectively. In practice, these two can be varied independently via manipulating the voltage of the 3 co- and 1 counter neutral beams of DIII-D. Here co- and counter refer to positive and negative torque, respectively.

In principle, it is possible to slowly increase β early in the discharge via a feedback loop until the islands grow to a target size and then reduce the torque at fixed β. However, the reproducibility of such plasmas would be extremely difficult, due to the random nature of NTM onset and coupled nonlinear dynamics of β with W.

It is a more reliable experimental approach to set up a target discharge with a large, stationary NTM (the same as the one used for turbulence measurements previously) and

then slow that island down while simultaneously decreasing β. The most difficult part is to avoid locking at slow rotation. An example of such experiment is shown in Fig. 9.1.

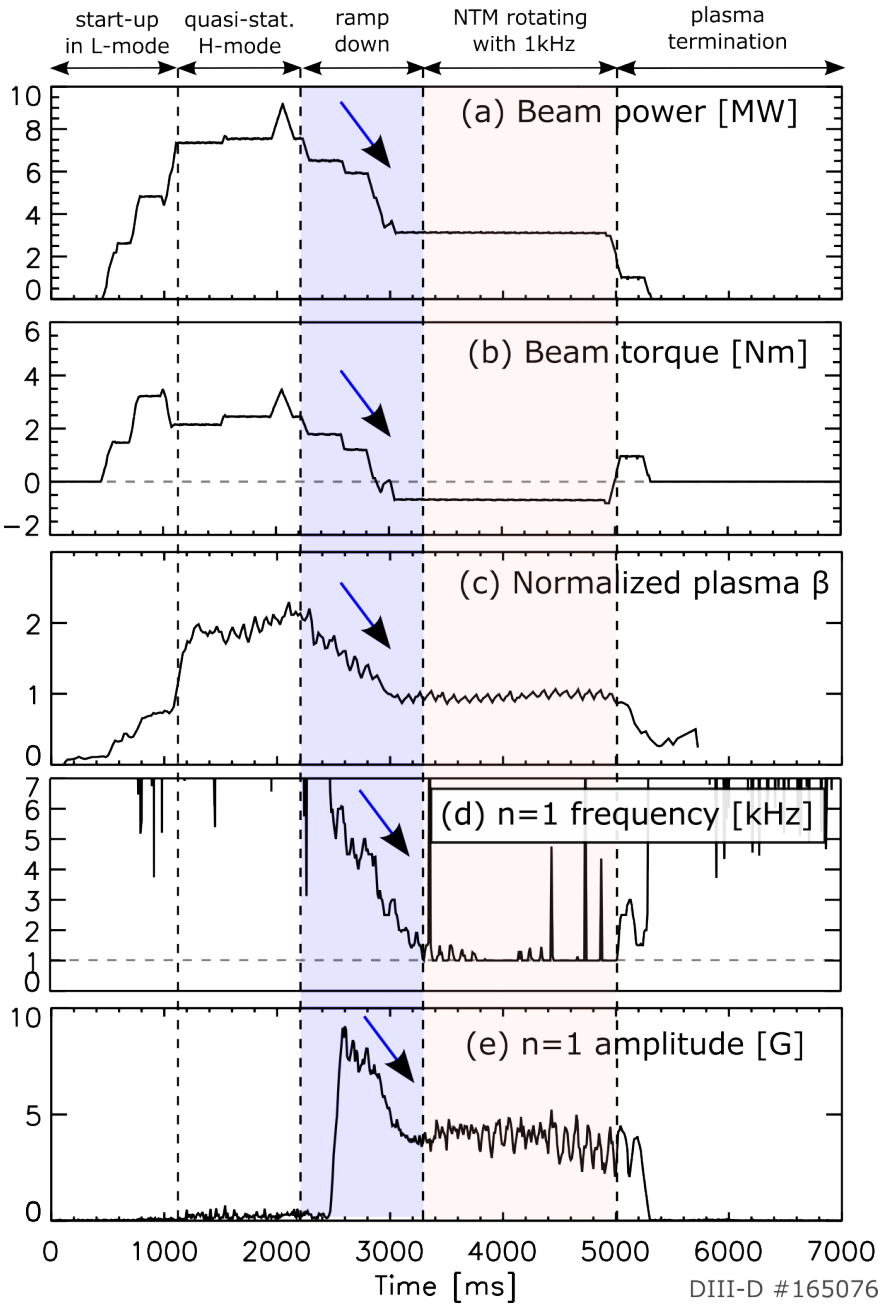

Figure 9.1: (a) Beam power, (b) beam torque, (c) normalized plasma β, (d) frequency and (e) amplitude of the rotating $m/n = 2/1$ islands.

Further, a few more constraints worth to be mentioned: (1) W must exceed the radial resolution of the CER, which is about 3 cm; (2) CER can record only 500 ms data (at 1 kHz

sampling rate) the timing of which must be matched with the window of slowly rotating NTM. The development of this plasma required 15 discharges (which cost about \$0.5M). Next, the scaling of required torque and beam power are derived vs f_{NTM}.

9.1 Scaling of drag vs island width, rotation and location

The rotating magnetic field perturbation (δB) generates an electric field perturbation (δE) in the wall as prescribed by Maxwell's equation:

$$\nabla \times \delta \mathrm{E} = -\delta \dot{\mathrm{B}} \tag{9.1}$$

This electric field drives a current ($\mathrm{I_{edd}}$) as prescribed by Ohm's law:

$$\mathrm{I_{edd}} = -\frac{\oint \delta \mathrm{E} dl}{\mathrm{R}_\Omega} = \frac{\int \delta \dot{\mathrm{B}} dS}{\mathrm{R}_\Omega} \tag{9.2}$$

Here the integral is calculated over the surface of the eddy current (S), l is the arc length on the circumference of S and R_Ω is the resistivity of the tokamak wall. The number of current loops are given by mn and the total Ohmic dissipation (P_Ω) of these currents are given by:

$$\mathrm{P}_\Omega = mn\mathrm{R}_\Omega \langle \mathrm{I}_{\mathrm{edd}}^2 \rangle_t = \frac{mn}{\mathrm{R}_\Omega} \left\langle \left(\int \delta \dot{\mathrm{B}} dS \right)^2 \right\rangle_t \tag{9.3}$$

This Ohmic loss acts to slow down the plasma rotation, therefore it can be expressed as a torque:

$$\mathrm{P}_\Omega = \frac{\mathrm{T_{isl}} \mathrm{v}}{\mathrm{R}_\circ} \longrightarrow \mathrm{T_{isl}} = \frac{\mathrm{P}_\Omega \mathrm{R}_\circ}{\mathrm{v}} \tag{9.4}$$

$\mathrm{R}_\circ$ is the plasma major radius and the velocity (v) is due to plasma toroidal rotation $\mathrm{v} = \omega \mathrm{R}_\circ$, which gives:

$$\mathrm{T}_{\mathrm{isl}} = \frac{\mathrm{P}_\Omega}{\omega} = \frac{mn}{\mathrm{R}_\Omega \omega} \left\langle \left(\int \delta \dot{\mathrm{B}} dS \right)^2 \right\rangle_t \tag{9.5}$$

Finally, one has to express $\delta\dot{\mathrm{B}}$ in terms of experimentally relevant parameters, such as W. For mathematical simplicity, it is reasonable to assume that $\widetilde{\mathrm{B}}_\theta$ is dominated by a single harmonic component at the wall ($r = \mathrm{a}$) due to the rapid decay of higher poloidal harmonics:

$$\delta\dot{\mathrm{B}}(\mathrm{a}) \approx -\frac{d}{dt}\left(\widetilde{\mathrm{B}}_\theta(\mathrm{a}) \cos(n\omega t + \xi) \right) = n\omega \widetilde{\mathrm{B}}_\theta(\mathrm{a}) \sin(n\omega t + \xi) \tag{9.6}$$

Expression (9.6) describes a 2D magnetic structure on the wall associated with one eddy current. This results from the projection of the 3D helical structure associated with the island, hence the $\xi = m\theta - n\phi$ dependence. This structure is rotated toroidally, hence the $n\omega t$ time-dependent phase. $\widetilde{\mathrm{B}}_\theta(\mathrm{a})$ is the amplitude of magnetic field fluctuation at the tokamak wall and is related to the island width:

$$\widetilde{\mathrm{B}}_\theta(\mathrm{a}) = \widetilde{\mathrm{B}}_r(r_s) \left(\frac{r_s}{\mathrm{a}} \right)^{m+1} = \frac{n\mathrm{W}^2}{2\mathrm{R}_\circ} \left(\frac{\mathrm{B}_\phi}{\mathrm{L}_\mathrm{q}} \right)_{r_s} \left(\frac{r_s}{\mathrm{a}} \right)^{m+1} \tag{9.7}$$

The torque becomes:

$$\begin{aligned} \mathrm{T}_{\mathrm{isl}} &= \frac{mn}{\mathrm{R}_\Omega \omega} \left\langle \left(\int n\omega \widetilde{\mathrm{B}}_\theta(\mathrm{a}) \sin(n\omega t + \xi) dS \right)^2 \right\rangle_t = \\ &= \frac{mn}{\mathrm{R}_\Omega \omega} \left\langle \left(\int n\omega \frac{n\mathrm{W}^2 \mathrm{B}_\phi}{2\mathrm{L}_\mathrm{q}\mathrm{R}_\circ} \left(\frac{r_s}{\mathrm{a}} \right)^{m+1} \sin(n\omega t + \xi) dS \right)^2 \right\rangle_t = \\ &= \frac{mn^5 \mathrm{W}^4 \mathrm{B}_\phi^2 \omega}{4\mathrm{L}_\mathrm{q}^2 \mathrm{R}_\circ^2 \mathrm{R}_\Omega} \left(\frac{r_s}{\mathrm{a}} \right)^{2m+2} \left\langle \left(\int \sin(n\omega t + \xi) dS \right)^2 \right\rangle_t \end{aligned} \tag{9.8}$$

Using the $\mathrm{G}_1 = \int \cos(\xi) dS$ and $\mathrm{G}_2 = \int \sin(\xi) dS$ notation and the

$\sin(\alpha+\beta) = \sin(\alpha)\cos(\beta) + \sin(\beta)\cos(\alpha)$ trigonometric identity, the integral becomes:

$$\begin{aligned}
\left\langle \left(\int \sin(n\omega t + \xi) dS \right)^2 \right\rangle_t &= \\
= \left\langle \left(\int \sin(n\omega t)\cos(\xi) + \cos(n\omega t)\sin(\xi) dS \right)^2 \right\rangle_t &= \\
= \left\langle sin^2(n\omega t)\mathrm{G}_1^2 + \cos(n\omega t)^2\mathrm{G}_2^2 + 2sin\mathrm{G}_1\mathrm{G}_2\sin(n\omega t)\cos(n\omega t) \right\rangle_t &= \\
= \frac{1}{2}(\mathrm{G}_1^2 + \mathrm{G}_2^2) \qquad (9.9)
\end{aligned}$$

The G_1 and G_2 integrals are numerical factors that describe the geometry of one eddy current on the tokamak wall. Recall that S is the surface of one eddy current, not the total toroidal surface, hence G_1 and G_2 are not necessarily zeros. With expression (9.9) the torque becomes:

$$\mathrm{T}_{\mathrm{isl}} = \frac{n^4 \mathrm{W}^4 \mathrm{B}_\phi^2 \omega}{8\mathrm{L}_\mathrm{q}^2 \mathrm{R}_\circ^2 \mathrm{R}_\Omega} \left(\frac{r_s}{\mathrm{a}} \right)^{2m+2} (\mathrm{G}_1^2 + \mathrm{G}_2^2) \propto \omega \mathrm{W}^4 r_s^{2m+2} \propto \omega \widetilde{\mathrm{B}}_\theta^2 r_s^{2m+2} \qquad (9.10)$$

In summary:

- the W^4 comes because $\mathrm{P}_\Omega \propto \delta\dot{\mathrm{B}}^2$ and $\widetilde{\mathrm{B}}_\theta \propto \mathrm{W}^2$
- r_s^{2m+2} comes because of the r_s^{m+1} radial decay of magnetic field perturbation with m poloidal mode number in cylindrical geometry and $\mathrm{P}_\Omega \propto \dot{\mathrm{B}}^2$
- finally the linear dependence in ω is because $\mathrm{P}_\Omega \propto \dot{\mathrm{B}}^2 \propto \omega^2$ but this is related to the drag as $\mathrm{P}_\Omega = \mathrm{T}\omega$

At high frequencies the wall acts more like an ideal conductor, which results in a correction to the above formula:

$$\mathrm{T}_{\mathrm{isl}} \propto \frac{\tau_s \omega}{1 + (\omega\tau_s)^2} \mathrm{W}^4 r_s^{2m+2} \propto \mathrm{W}^4 \omega^{-1} \propto \widetilde{\mathrm{B}}_\theta^2 \omega^{-1} \qquad (9.11)$$

Here $\tau_s \approx 3$ ms is the resistive decay time for induced currents in the wall [106]. The maximum of the drag occurs when $n\tau_s\omega = 1$ is satisfied as shown in Fig. 9.2 which yields 50 Hz for a $m/n = 2/1$ mode.

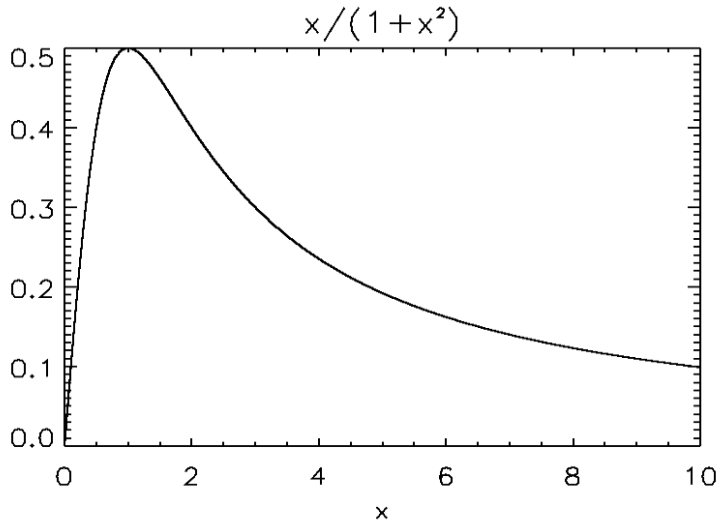

Figure 9.2: $F \propto \omega$ in the small ω limit, $F \propto \omega^{-1}$ in the large ω limit, and F has a maximum at $n\tau_s\omega = 1$.

9.2 Required torque for a given NTM frequency

It is assumed that in stationary conditions the beam torque (T_B) is balanced by a viscous torque (T_v) and the island torque ($\mathrm{T}_{\mathrm{isl}}$). Therefore, the dynamical equation for the rotation is give by:

$$\dot{\omega} \propto \mathrm{T_B} - \mathrm{T_v} - \mathrm{T_{isl}} \tag{9.12}$$

Assuming that $\mathrm{T}_{\mathrm{isl}}$ is small compared to $\mathrm{T_B}$ and that the viscous torque is a simple linear function of the plasma rotation frequency ($\mathrm{T_v} \propto f_p$), it follows:

$$\frac{\mathrm{T_{B,1}}}{\mathrm{T_{B,2}}} = \frac{f_{\mathrm{p,1}}}{f_{p,2}} \tag{9.13}$$

Here the indices 1 and 2 refer to the rapidly and slowly rotating plasma states, respectively. Assuming that the island rotates with the plasama $\omega = f_{\mathrm{p}}$ leads to:

$$\frac{\mathrm{T_{B,1}}}{\mathrm{T_{B,2}}} = \frac{\omega_1}{\omega_2} \tag{9.14}$$

Equation (9.14) shows that in order to slow down the island rotation (e.g.) from 7 kHz to 1 kHz, one must ramp down beam torque by a factor of 7.

9.3 Required β to avoid NTM locking at low rotation

When the island rotation is decreased, the island drag increases if the island width is kept constant. As it was shown in equation (9.11), $\mathrm{T_{isl}} \propto \omega^{-1}\mathrm{W}^4$. Therefore, to avoid mode locking, one must decrease W, which was done in practice by decreasing β via decreasing the beam input power.

A simplified estimation of the required W can be obtained by keeping the island drag constant: $\mathrm{T_{isl,1}} = \mathrm{T_{isl,2}}$, this gives:

$$\omega_1^{-1}\mathrm{W}_1^4 = \omega_2^{-1}\mathrm{W}_2^4 \tag{9.15}$$

On time scales much longer then the island evolution, $\mathrm{W} = \mathrm{W_{SAT}}$. The scaling of $\mathrm{W_{SAT}}$ vs β_θ is obtained simply from the MRE:

$$\gamma_M = \frac{\eta\Delta'}{\mu_\circ \mathrm{W}} + \frac{2\sqrt{\varepsilon}\eta \mathrm{L_q}}{(\mathrm{W}^2 + \mathrm{W_t^2})\mathrm{B}_\theta^2}(\nabla \mathrm{p}_X - \nabla \mathrm{p}_O) \tag{9.16}$$

with the $\gamma_M = 0$ condition. At large island size ($\mathrm{W} >> \mathrm{W_t}$) this gives:

$$\mathrm{W_{SAT}} \approx \frac{2\mu_\circ\sqrt{\varepsilon}\mathrm{L_q}}{\mathrm{B}_\theta^2}\left(\frac{\nabla \mathrm{p}_O - \nabla \mathrm{p}_X}{\Delta'}\right) \tag{9.17}$$

Therefore, $W \propto B_\theta^{-2} \propto \beta_\theta$, which, together with equation (9.15), gives:

$$\beta_{\theta,2} = \beta_{\theta,1} \left(\frac{\omega_2}{\omega_1} \right)^{1/4} \tag{9.18}$$

This means that if the island rotation is decreased by a factor of (e.g.) 7 (assuming $P_b \propto \beta_\theta$) one has to decrease P_b by a factor of about 1.6.

9.4 Perturbed ion temperature and rotation profiles

By simultaneously reducing the torque and beam power, the island rotation was slowed down to about 700 Hz and kept there for about 500 ms in shot 141951 [Fig. 9.3 (b)]. The CER measurement was well synchronized to the window of slowly rotating NTM, providing helical resolution for the $T_i(R)$ and $v_\phi(R)$ measurements [Fig. 9.3 (a)].

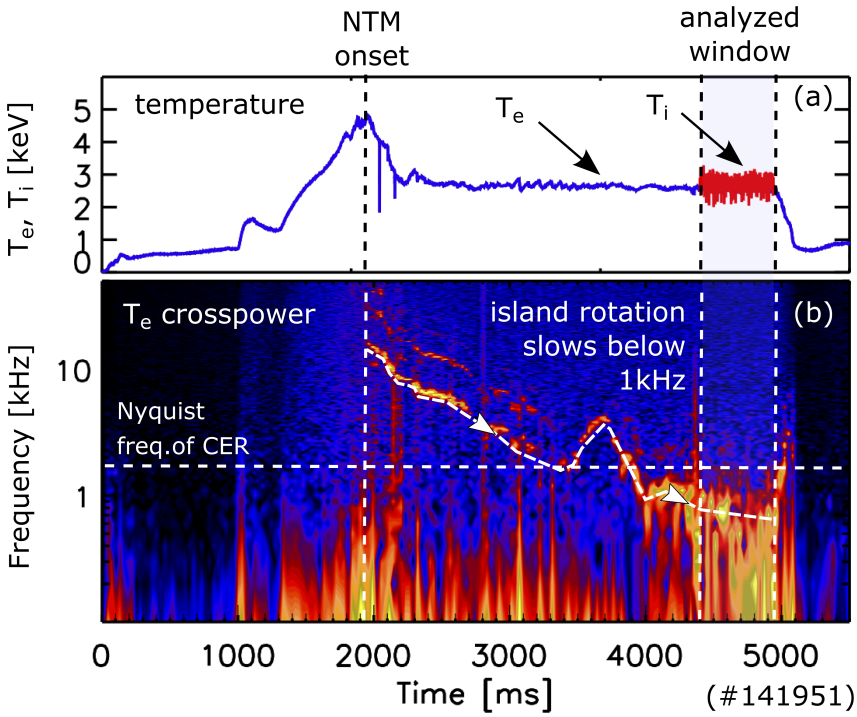

Figure 9.3: (a) Time history of T_e and T_i. (b) Cross-spectrogram of T_e signals measured across the islands.

The contours of $T_e(t, R)$ clearly show phase coupled islands [Fig. 9.4 (a)]. Taking into

account their locations vs q as well as the $m_1 + m_2 = m_3$ and $n_1 = n_2 = n_3$ coupling constraints [93], it follows that the islands have $m_1/n_1 = 1/1$, $m_2/n_2 = 2/1$ and $m_3/n_3 = 3/1$ mode numbers. The X-point times of the $m/n = 3/1$ island are marked with vertical dotted lines. Example of the reconstructed $\xi(t)$ is shown in Fig. 9.4 (b). $\xi(t)$ goes from 0 to 2π during each island cycle. $\xi = 2k\pi$ corresponds to the X-points of the $m/n = 3/1$ island and O-points of the $m/n = 2/1$ island (here k is an integer). $\xi = (2k+1)\pi$ corresponds to the O-points of the $m/n = 3/1$ island and X-points of the $m/n = 2/1$ island. This helical phase signal is used to phase lock-average T_e, T_i and v_ϕ across the $m/n = 3/1$ and $m/n = 2/1$ islands.

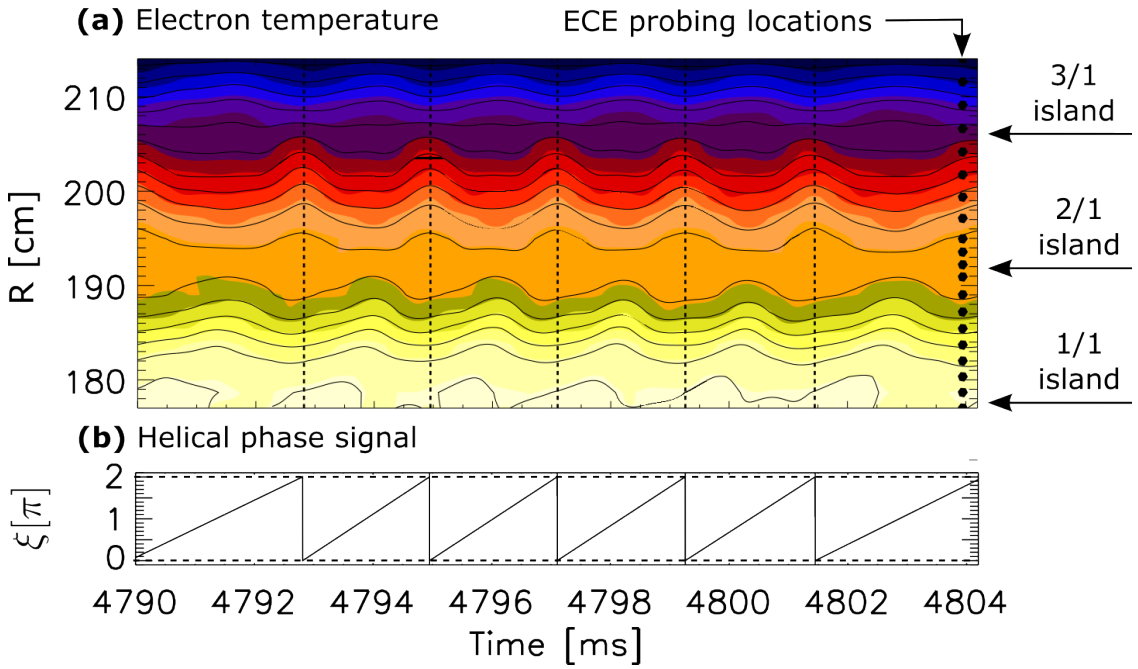

Figure 9.4: (a) Contours of electron temperature show coupled 3/1, 2/1 and 1/1 island structures. (b) Reconstructed helical phase of islands vs time.

The difference between X-point and O-point T_e profiles $\Delta T_e(R)_{X,O} = T_e(R, \xi = 0) - T_e(R, \xi = \pi)$ in Fig. 9.5 (a) shows 3 island structures. The zeros of $\Delta T_e(R)_{X,O}$ are well aligned with the $q = 1, 2, 3$ rational surfaces which are marked by vertical dotted lines. Over plotted is $\Delta T_i(R)_{X,O}$, which shows a similar structure as $\Delta T_e(R)_{X,O}$. $\Delta v_\phi(R)_{X,O}$ in Fig. 9.5 (d) has a qualitatively similar structure as $\Delta T_e(R)_{X,O}$ and $\Delta T_i(R)_{X,O}$ with zeros well aligned with the rational q surfaces. Notice that each island

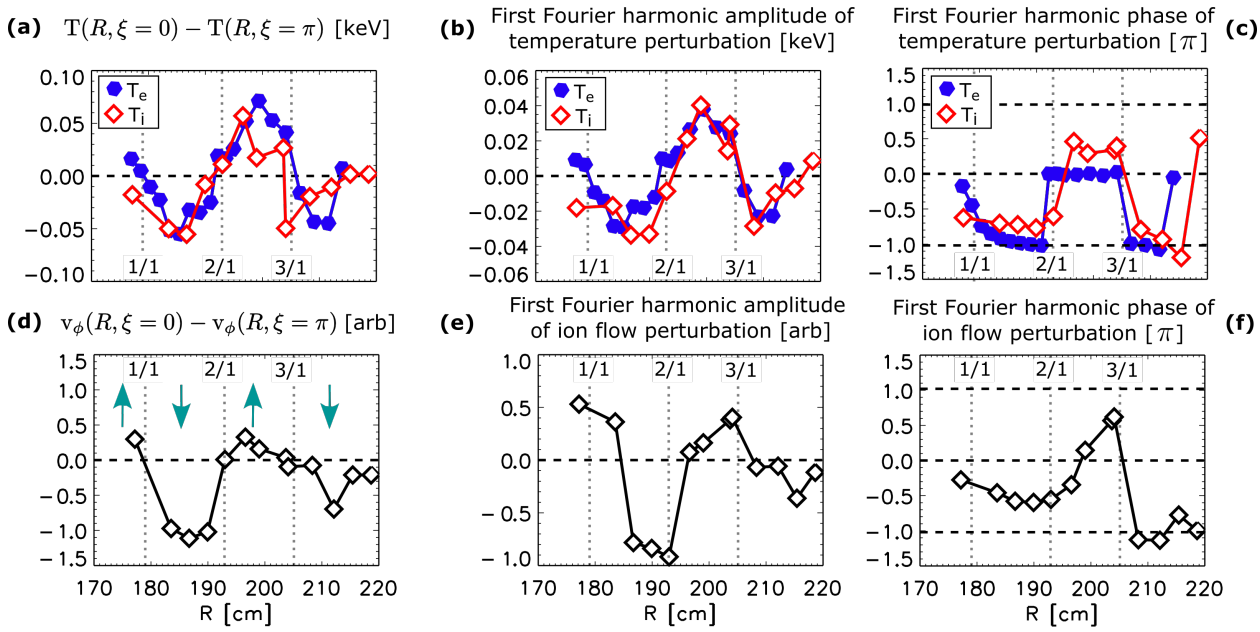

Figure 9.5: Temperature and ion flow perturbations due 2/1 and 3/1 coupled islands. (a) $\delta T_e(R)_{X,O}$ and $\delta T_i(R)_{X,O}$, (b) first Fourier harmonic amplitude and (c) phase of δT_e and δT_i. (d) Ion flow perturbation, (e) first Fourier harmonic amplitude and (f) phase of ion flow perturbation.

leads to a dominantly odd flow perturbation, i.e. $\Delta T_e(R-R_{s_i})_{X,O} \approx \Delta T_e(R_{s_i}-R)_{X,O}$ locally around R_{s_i} , where R_{s_i} are the major radius coordinates of the $q=3,2$ and 1 rational surfaces. The arrows in Fig. 9.5 (d) show that the flow direction reverses about the rational surfaces. This odd structure is similar to that seen around large islands in the GENE simulations [Chapter 6], where vortex modes developed about the O-point. Additionally, the amplitude and phase of the first Fourier harmonic of δT_e and δT_i is shown in Fig. 9.5 (b) and (c), respectively, and those of δv_ϕ in Fig. 9.5 (e) and (f), respectively. The first harmonic amplitude shows strong similarity with $\delta T_e(R)_{X,O}$ and $\delta T_i(R)_{X,O}$, meaning that the perturbation is dominantly due to the first harmonic. The first harmonic phase of T_e exhibits π jumps at rational surfaces, as expected. The phase of T_i has a very similar structure as T_e but there is an overall phase shift of about $\pi/3$, which is due to the toroidal offset of the ECE and CER diagnostics. The interpretation of the first harmonic amplitude and phase of v_ϕ is less clear and is left for future work. In principle, this flow can be different from that observed in the gyrokinetic simulation, as

here 3 islands are coupled to each other with different 3D helical structure that can modify the electrostatic potential and the flow around the islands.

9.5 Discussion

In this chapter, experiments with slowly rotating NTMs were presented. After calculating requirements on the beam torque and input power for a given island frequency, δT_i and δv_ϕ was reconstructed from CER measurements via the phase-locking technique using the ECE measurement as reference. This analysis found that δT_i is very similar to δT_e and the δv_ϕ is similar to the vortex modes seen previously in gyrokinetic simulations. Detailed investigation of the δv_ϕ spectrum and comparison with simulations is left for future work.

CHAPTER 10

Summary

As part of this thesis work, 5 major results have been accomplished:

- A new heat transport model of magnetic islands employing spatially non-uniform $\chi_\perp$ has been developed and used to derive the experimental value of $\chi_\perp$ at the O-point of rotating NTM islands for the first time.
- The first localized measurements of low- and intermediate-k $\tilde{n}$ and low-k $\widetilde{T}_e$ modified by magnetic islands were presented [87].

dedicated experiments were conducted utilizing the full complement of the DIII-D turbulence diagnostics to study the effect of Neoclassical Tearing Mode magnetic islands on turbulence as well as the effect of turbulence on NTM growth.
The first localized measurements of low- and intermediate-k $\tilde{n}$ and low-k $\widetilde{T}_e$ modified by magnetic islands were presented [87]. These long and intermediate wavelengths correspond to the expected ITG and TEM scales, respectively, as indicated by linear GENE gyrokinetic simulations.
Two regimes were observed when tracking $\tilde{n}$ during NTM evolution:

- **Small islands** are characterized by steep T_e radial profile and turbulence levels comparable to that of the background;
- **Large islands** have a flat T_e profile and reduced turbulence level at the O-point. Radially outside of the large island, the T_e profile is steeper and the turbulence level increased compared to the no or small island case.

It was also found that turbulence is reduced in the O-point region compared to the X-point region [86]. This helical structure of turbulence modification leads to a maximum 15%

modulation of $\widetilde{n}^2$ as the island rotates in the lab frame. This modulation is confined to the island region and is nearly in phase with the T_e modulation.

These turbulence measurements were also used to determine the turbulence penetration length scale ($L_{\widetilde{n}}$) at the island separatrix and was found that $L_{\widetilde{n}}$ is on the order of the threshold island width for temperature flattening and turbulence reduction to occur at the O-point [87]. This suggests that the physics of small to large island transition could be related to turbulence penetration into the island.

In addition, a novel, anisotropic, non-linear heat transport model of magnetic islands with spatially non-uniform $\chi_\perp$ was developed[7]. This model was utilized to derive $\chi_\perp$ at the O-point from measured T_e data and it was found that $\chi_\perp$ at the O-point is 1 to 2 orders of magnitude smaller than that of the background plasma. As the anomalously large values of $\chi_\perp$ are often attributed to turbulence driven transport, the reduction of $\chi_\perp$ is consistent with the found $\widetilde{n}$ and $\widetilde{T}_e$ reduction at the O-point.

Complementing the experimental results of turbulence-NTM interaction described in this thesis, qualitative comparisons were carried out for the first time to GENE non-linear gyrokinetic turbulence simulations employing static magnetic islands [6]. These simulations qualitatively replicate the measured 2D response of turbulence as well as the observed scaling with island size [87].

The consequences of the observed NTM-turbulence interaction on the global confinement were studied via analyses of simultaneous changes in NTM amplitude, plasma profiles, turbulence, fluxes and confinement. It was found that the global confinement degradation is intimately linked to the turbulence enhancement outside of the island region (induced by the island).

Experimentally observed local turbulence and transport reduction at the O-point, as well as the effect of global confinement decrease was incorporated in the dynamical equation of NTMs, which shows that the NTM growth rate increases when turbulence and gradients are reduced inside the island (right after the transition from small to large island regime). To further investigate the effects of turbulence on NTM growth, the recovery of NTM

islands and evolution of local low-k $\widetilde{\mathrm{n}}$ was investigated during ELM cycles for the first time. Synchronous peaking of $\mathrm{T_e}$ and island shrinking after the ELM crash suggest that local $\mathrm{T_e}$ perturbations at the O-point are linked to the NTM stability. These changes are followed by an increase of $\widetilde{\mathrm{n}}$, rapid relaxation of the $\mathrm{T_e}$ peak and island recovery. The analysis of $\widetilde{\mathrm{n}}(t)$, $\mathrm{T_e}(r,t)$ and NTM amplitude suggests that the increased $\widetilde{\mathrm{n}}$ accelerates NTM recovery after the ELM-crash by rapid restoration of the flat profile (and bootstrap current perturbation) at the O-point via fast turbulent cross-field transport. These observations were qualitatively replicated by coupled predator-prey equations and modified Rutherford equation. In this simple model, turbulence accelerates NTM recovery via relaxing $\nabla \mathrm{p}$ and therefore restoring $\delta \mathrm{j_{BS}}$ at the O-point. The key physics of the relationship between the $\mathrm{T_e}$ peak and NTM stability has potentially far-reaching consequences, such as NTM control via pellet injection in high-β tokamak plasmas.

Finally, to measure the perturbed ion temperature and toroidal flow profiles via CER, a series of low torque H-mode experiments were carried out with slowly rotating NTM islands. Comparison of the observed flow perturbation to the gyrokinetic simulations suggests that large islands develop a vortex like plasma flow circulating around the O-point.

Next, various heat transport models of magnetic islands are presented in Chapter 3. This effort extends beyond previous work, as a spatially non-uniform electron thermal diffusivity was introduced in an anisotropic heat diffusion model of magnetic islands for the first time.

Island structures are described in Chapter 4 via the analysis of measured 2D (R,ξ) perturbed electron temperature profiles. This is followed by the derivation of the cross-field electron thermal diffusivity in the O-point of the island from $\mathrm{T_e}$ data using a heat transport model presented previously in Chapter 3.

The major results of this thesis are presented in Chapter 5: the first localized measurements of low-k and intermediate-k $\widetilde{\mathrm{n}}$ and low-k $\widetilde{\mathrm{T}}_\mathrm{e}$ across naturally growing, freely rotating 2/1 NTM magnetic islands. Differences between O-point and X-point fluctuation levels, fluctuation levels inside vs outside the island region and scaling of turbulence modifications vs island width are all presented. Additionally, these measurements were

used to determine the turbulence penetration length scale at the island separatrix.

To help interpreting these experimental observations, GENE gyrokinetic simulations were run to study the effect of magnetic islands on turbulence in Chapter 6. These simulations were carried out by my collaborator A. Bañón Navarro and the output was analyzed by myself. We found that the measured turbulence modifications in DIII-D were qualitatively replicated by these simulations.

Consequences of the observed NTM-turbulence interaction on global plasma confinement were studied via analyses of simultaneous changes in NTM amplitude, plasma profiles, turbulence, fluxes and confinement and are described in Chapter 7. This is followed by discussing the effects of NTM-turbulence interaction on NTM growth rates via the dynamical equation of NTMs.

Additionally, the shrinking of NTM islands due to strong temperature perturbations associated with Edge Localized Modes was observed and is described in Chapter 8. Simultaneous changes in turbulence levels across the island were also observed and the potential implications of this turbulence level modification on the island recovery is discussed.

Finally, a series of low torque H-mode experiments were carried out to measure the perturbed ion temperature and toroidal flow profiles via CER across slowly rotating islands and the results are presented in Chapter 9.

CHAPTER 11

Open questions

The improved picture of NTM-turbulence physics emerging from this thesis work naturally gives rise to several question, some of which are elaborated in the following.

- What is the physics of transition from small to large island regimes? What is W_t set by? Hypotheses:

    1. Recall that gradients and turbulence at the O-point are linked to each other: the profile steepness is determined by the ratio of of $Q_\perp/Q_\parallel$ and turbulence is driven by local gradients. When the island grows, the connection length along the field line decreases, which leads to more effective $Q_\parallel$ and therefore flattens the island. It is expected that turbulence becomes stable when the local gradient at the O-point is equal to the critical gradient of the micro-instability. When turbulence decreases, $Q_\perp$ decreases (by about 1-2 orders of magnitude) and the island completely flattens.
    2. Turbulence can penetrate into the O-point region across the island separatrices. Significant $Q_\perp$ reduction is therefore expected only when the island width exceeds the turbulence penetration length scale.
    3. Finite banana width effects could prevent the island to flatten, when it is smaller than the ion banana orbit width.

- What is the physics of vortex modes and what is their effect on NTM stability? Hypotheses:

    1. The emergence of the vortex mode is suspected to be due to different neoclassical electron-ion transport across the island separatrix when the

transport is not turbulence dominated (when the island is flat). This could lead to a current perpendicular to the separatrix, which, interacting with the background magnetic field spins the plasma around the O-point.

2. The shear of the vortex can regulate turbulence, which in turn can lead to more flat islands and therefore more unstable NTMs. On the other hand, the vortex mode leads to the braking of turbulence isotropy, which then leads to finite Reynold's stress. This stress can drive energy from turbulence to the flow itself, leading to a time-dependent zonal flow component.
3. The vortex mode moves the turbulent eddies from the most unstable domain (outside of island in line with O-point) along the flow. This is in the opposite direction on the two sides of the island, leading to a helical asymmetry in the turbulence distribution, which then leads to helically asymmetric transport and profile flatness. This can further feed back into the bootstrap current and the magnetic island shape.

- Can gyrokinetic codes *quantitatively* predict turbulence - NTM interaction? This topic requires extensive computational effort and is underway in collaboration with A. B. Navarro.

Bibliography

[1] Euro fusion (www.euro-fusion.org).

[2] Jeff Candy. (w3.pppl.gov).

[3] A. W. Cook, W. Cabot, and P. L. Miller. The mixin transition in rayleigh-taylor instability. *J. Fluid Mech.*, 511:333–362, 2004.

[4] A. G. Peeters. The bootstrap current and its consequences. *Plasma Phys. Control. Fusion*, 42:B231–B243, 2000.

[5] K. Ida, N. Ohyabu, T. Morisaki, Y. Nagayama, S. Inagaki, K. Itoh, Y. Liang, K. Narihara, A.Yu. Kostrioukov, B. J. Peterson, K. Tanaka, T. Tokuzawa, K. Kawahata, H. Suzuki, A. Komori, and LHD Experimental Group. Observation of plasma flow at the magnetic island in the large helical device. *Phys. Rev. Lett.*, 88(1), 2002.

[6] A Bañón Navarro, L Bardóczi, T A Carter, F Jenko, and T L Rhodes. Effect of magnetic islands on profiles, flows, turbulence and transport in nonlinear gyrokinetic simulations. *Plasma Physics and Controlled Fusion*, 59(3):034004, 2017.

[7] L. Bardóczi, T. L. Rhodes, T. A. Carter, N. A. Crocker, W. A. Peebles, and B. A. Grierson. Non-perturbative measurement of cross-field thermal diffusivity reduction at the o-point of 2/1 neoclassical tearing mode islands in the diii-d tokamak. *Phys. Plasmas*, 23(052507), 2016.

[8] O. Sauter, R. J. La Haye, Z. Chang, D. A. Gates, Y. Kamada, H. Zohm, A. Bondeson, D. Boucher, J. D. Callen, M. S. Chu, T. A. Gianakon, O. Gruber, R. W. Harvey, C. C. Hegna, L. L. Lao, D. A. Monticello, F. Perkins, A. Pletzer, A. H. Reiman, M. Rosenbluth, E. J. Strait, T. S. Taylor, A. D. Turnbull, F. Waelbroeck, J. C. Wesley, H. R. Wilson, and R. Yoshinof. Beta limits in long-pulse tokamak discharges. *Phys. Plasmas*, 4:1654, 1997.

[9] R. Sweeney, W. Choi, R.J. La Haye, S. Mao, K.E.J. Olofsson, F.A. Volpe, and the DIII-D Team. Statistical analysis of m/n = 2/1 locked and quasi-stationary modes with rotating precursors at diii-d. *Nucl. Fusion*, 57(1), 2016.

[10] Eun-Jin Kim and P. H. Diamon. Zonal flows and transient dynamics of the l-h transition. *Phys. Rev. Lett.*, 90(185006), 2003.

[11] M. Shats and H. Xia. Spectrally condensed fluid turbulence and l-h transitions in plasma. *Plasma and Fusion Research*, 4(012), 2009.

[12] L. Bardóczi, M. Berta, and A. Bencze. Inverse energy cascade and turbulent transport in a quasi-two-dimensional magnetized electrolyte system: An experimental study. *Phys. Rev. E*, 85:056315, May 2012.

[13] L. Bardóczi, A. Bencze, M. Berta, and L. Schmitz. Experimental confirmation of self-regulating turbulence paradigm in two-dimensional spectral condensation. *Phys. Rev. E*, 90:063103, Dec 2014.

[14] L. Schmitz, L. Zeng, T. L. Rhodes, J. C. Hillesheim, E. J. Doyle, R. J. Groebner, W. A. Peebles, K. H. Burrell, and G. Wang. Role of zonal flow predator-prey oscillations in triggering the transition to h-mode confinement. *Phys. Rev. Lett.*, 108(155002), 2012.

[15] C. J. McDevitt and P. H. Diamond. Multiscale interaction of a tearing mode with drift wave turbulence: A minimal self-consistent model. *Phys. Plasmas*, 13(032302), 2006.

[16] M. Yagi, S.-I. Itoh, K. Itoh, M. Azumi, P. H. Diamond, A. Fukuyama, and T. Hayashi. Nonlinear drive of tearing mode by microscopic plasma turbulence. *Plasma and Fusion Research*, 2(025), 2007.

[17] F. Militello, F. L. Waelbroeck, R. Fitzpatrick, , and W. Horton. Interaction between

turbulence and a nonlinear tearing mode in the low beta regime. *Phys. Plasmas*, 15(050701), 2008.

[18] E. Poli, A. Bottino, and A.G. Peeters. Behaviour of turbulent transport in the vicinity of a magnetic island. *Nucl. Fusion*, 49(075010), 2009.

[19] H. R. Wilson and J W Connor. The influence of magnetic islands on drift mode stability in magnetized plasma. *Plasma Phys. Control. Fusion*, 51(115007), 2009.

[20] F L Waelbroeck, F Militello, R Fitzpatrick, and W Horton. Effect of electrostatic turbulence on magnetic islands. *Plasma Phys. Control. Fusion*, 51(015015), 2009.

[21] W A Hornsby, M Siccinio, A G Peeters, E Poli, A P Snodin, F J Casson, Y Camenen, and G Szepesi. Interaction of turbulence with magnetic islands: effect on bootstrap current. *Plasma Phys. Control. Fusion*, 53(054008), 2011.

[22] W. A. Hornsby, A. G. Peeters, M. Siccinio, and E. Poli. On the dynamics of vortex modes within magnetic islands. *Phys. Plasmas*, 19(032308), 2012.

[23] A. Ishizawa and F. L. Waelbroeck. Magnetic island evolution in the presence of ion-temperature gradient-driven turbulence. *Phys. Plasmas*, 20(122301), 2013.

[24] O. Agullo, M. Muraglia, A. Poye, S. Benkadda, M. Yagi, X. Garbet, and A. Sen. A signature of turbulence driven magnetic islands. *Phys. Plasmas*, 21(092303), 2014.

[25] Z. Q. Hu, Z. X. Wang, L. Wei, J. Q. Li, and Y. Kishimoto. Nonlinear mutual destabilization of the tearing mode and ion temperature gradient mode. *Nucl. Fusion*, 54(123018), 2014.

[26] D. Zarzoso, W.A. Hornsby, E. Poli, F.J. Casson, and A.G. Peetersand S. Nasr. Impact of rotating magnetic islands on density profile flattening and turbulent transport. *Nucl. Fusion*, 55(113018), 2015.

[27] P. Hill, F. Hariri, and M. Ottaviani. The effect of magnetic islands on ion temperature gradient turbulence driven transport. *Phys. Plasmas*, 22(042308), 2015.

[28] W. A. Hornsby, P. Migliano, R. Buchholz, D. Zarzoso, F. J. Casson, E. Poli, and A. G. Peeters. On seed island generation and the non-linear self-consistent interaction of the tearing mode with electromagnetic gyro-kinetic turbulence. *Plasma Phys. Control. Fusion*, 57(054018), 2015.

[29] W. A. Hornsby, P. Migliano, R. Buchholz, L. Kroenert, A. Weikl, A. G. Peeters, D. Zarzoso, E. Poli, and F. J. Casson. The linear tearing instability in three dimensional, toroidal gyro-kinetic simulations. *Phys. Plasmas*, 22(022118), 2015.

[30] Changxuan YU, D.L. BROWER, Shujun ZHAO, R.V. BRAVENEC, Jiayu CHEN, Hong LIN, N.C. LUHMANN Jr., W.A. PEEBLES, C.P. RITZ, P.M. SCHOCH, and Xuanzong YANG. Tearing instabilities and microturbulence in text. *Nucl. Fusion*, 32(9):1545, 1992.

[31] K.J. Zhao, Y.J. Shi, S.H. Hahnand P.H. Diamond, Y. Sun 5, J. Cheng, H. Liu, N. Lie, Z.P. Chen, Y.H. Ding, Z.Y. Chen, B. Rao, M. Leconte, J.G. Bak, Z.F. Cheng, L. Gao, X.Q. Zhang, Z.J. Yang, N.C. Wang, L. Wang, W. Jin, L.W. Yan, J.Q. Dong, G. Zhuang, and J-TEXT team. Plasma flows and fluctuations with magnetic islands in the edge plasmas of j-text tokamak. *Nucl. Fusion*, 55(073022), 2015.

[32] T. Estrada, E. Ascasibar, E. Blanco, A. Cappa, C. Hidalgo, K. Ida, A. Lopez-Fraguas, and B. Ph van Milligen. Plasma flow, turbulence and magnetic islands in tj-ii. *Nucl. Fusion*, 56(026011), 2016.

[33] S.P. Hirshman and D.J. Sigmar. Neoclassical transport of impurities in tokamak plasmas. *Nucl. Fusion*, 21(9), 1981.

[34] A. J. Wootton, B. A. Carreras, H. Matsumoto, K. McGuire, W. A. Peebles, Ch. P. Ritz, P. W. Terry, and S. J. Zweben. Fluctuations and anomalous transport in tokamaks. *Phys. Plasmas*, 2(2879), 1990.

[35] P. C. Liewer. Review paper measurements of microturbulence in tokamaks and

comparisons with theories of turbulence and anomalous transport. *Nucl. Fusion*, 25(5), 1985.

[36] W. Horton. Drift waves and transport. *Rev. Mod. Phys.*, 71(735), 1999.

[37] J. Wesson. *Tokamaks*. Oxford University Press, 2011.

[38] J.P. Freidberg. *Plasma Physics and Fusion Energy*. Cambridge University Press, isbn 0521851076 edition, 2007.

[39] F. Wagner, G. Becker, K. Behringer, D. Campbell, A. Eberhagen, W. Engelhardt, G. Fussmann, O. Gehre, J. Gernhardt., G. v. Gierke, G. Haas, M. Huang, F. Karger, M. Keilhacker, O. Klüber, M. Kornherr, K. Lackner, G. Lisitano, G. G. Lister, H. M. Mayer, D. Meisel, E. R. Müller, H. Murmann, H. Niedermeyer, W. Poschenrieder, H. Rapp, H. Röhr, F. Schneider, G. Siller, E. Speth, A. Stäbler, K. H. Steuer, G. Venus, O. Vollmer, and Z. Yü. Regime of improved confinement and high beta in neutral-beam-heated divertor discharges of the asdex tokamak. *Phys. Rev. Lett.*, 49(1408), 1982.

[40] A. E. White, L. Schmitz, G. R. McKee, C. Holland, W. A. Peebles, T. A. Carter, M. W. Shafer, M. E. Austin, K. H. Burrell, J. Candy, J. C. DeBoo, E. J. Doyle, M. A. Makowski, R. Prater, T. L. Rhodes, G. M. Staebler, G. R. Tynan, R. E. Waltz, and G. Wang. Measurements of core electron temperature and density fluctuations in diii-d and comparison to nonlinear gyrokinetic simulations. *Phys. Plasmas*, 15(056116), 2008.

[41] B. Coppi, M. N. Rosenbluth, and R. Z. Sagdeev. Instabilities due to temperature gradients in complex magnetic field configurations. *Phys. Fluids*, 10(582), 1967.

[42] R. Linsker. Integral-equation formulation for drift eigenmodes in cylindrically symmetric systems. *Phys. Fluids*, 24(1485), 1981.

[43] H. Nordman and J. Weiland. Transport due to toroidal ni mode turbulence in tokamaks. *Nucl. Fusion*, 29(251), 1989.

[44] A. M. Dimits, G. Bateman, M. A. Beer, B. I. Cohen, W. Dorland, G. W. Hammett, C. Kim, J. E. Kinsey, M. Kotschenreuther, A. H. Kritz, L. L. Lao, J. Mandrekas, W. M. Nevins, S. E. Parker, A. J. Redd, D. E. Shumaker, R. Sydora, and J. Weiland. Comparisons and physics basis of tokamak transport models and turbulence simulations. *Phys. Plasmas*, 7(969), 2000.

[45] A. Bencze, M. Berta, S. Zoletnik, J. Stockel, J. Adamek, and M. Hron. Observation of zonal flow-like structures using the autocorrelation-width technique. *Plasma Phys. Control. Fusion*, 48(4), 2006.

[46] S Zoletnik, L Bardoczi, A Krämer-Flecken, Y Xu, I Shesterikov, S Soldatov, G Anda, D Dunai, G Petravich, and the TEXTOR Team. Methods for the detection of zonal flows using one-point and two-point turbulence measurements. *Plasma Phys. Control. Fusion*, 54(6), 2012.

[47] L. Schmitz, G. Wang, J. C. Hillesheim, T. L. Rhodes, W. A. Peebles, A. E. White, L. Zeng, T. A. Carter, and W. Solomon. Detection of zonal flow spectra in diii-d by a dual-channel doppler backscattering system. *Rev. Sci. Instrum*, 79:10F113, 2008.

[48] D. R. Ernst, J. Lang, W. M. Nevins, M. Hoffman, Y. Chen, W. Dorland, and S. Parker. Role of zonal flows in trapped electron mode turbulence through nonlinear gyrokinetic particle and continuum simulations. *Phys. Plasmas*, 16(055906), 2009.

[49] A. Fujisawa. A review of zonal flow experiments. *Nucl. Fusion*, 49(1), 2008.

[50] B. Kadomtsev and O. Pogutse. Trapped particles in toroidal magnetic systems. *Nucl. Fusion*, 11(67), 1971.

[51] D. R. Ernst, P. T. Bonoli, P. J. Catto, W. Dorland, C. L. Fiore, R. S. Granetz, M. Greenwald, A. E. Hubbard, M. Porkolab, M. H. Redi, J. E. Rice, K. Zhurovich,

and Alcator C-Mod Group. Role of trapped electron mode turbulence in internal transport barrier control in the alcator c-mod tokamak. *Phys. Plasmas*, 11(2637), 2004.

[52] F. Jenko, W. Dorland, M. Kotschenreuther, and B. N. Rogers. Electron temperature gradient driven turbulence. *Phys. Plasmas*, 7(1904), 2000.

[53] F. Jenko, W. Dorland, and G. W. Hammett. Critical gradient formula for toroidal electron temperature gradient modes. *Phys. Plasmas*, 8(4096), 2001.

[54] Tom Neiser. Etg-dominated transport regimes in near-edge diii-d l-mode plasmas: Validation of multiscale gyrokinetic simulations. *Bulletin of the American Physical Society*, 2015.

[55] D De Lazarri and E Westerhof. The role of asymmetries in the growth and suppression of neoclassical tearing modes. *Plasma Phys. Control. Fusion*, 53(035020), 2011.

[56] R. Fitzpatrick. Helical temperature perturbations associated with tearing modes in tokamak plasmas. *Phys. Plasmas*, 2:825, 1995.

[57] C.C. Petty, R.J. Jayakumar, M.A. Makowski, C.T. Holcomb, D.A. Humphreys, R.J. La Haye, T.C. Luce, P.A. Politzer, R. Prater, M.R.Wade, and A.S.Welander. Spatiotemporal changes in the pressure-driven current densities on diii-d due magnetic islands. *Nucl. Fusion*, 52(013011), 2012.

[58] R. Carrera, R. D. Hazeltine, and M. Kotschenreuther. Island bootstrap current modification of the nonlinear dynamics of the tearing mode. *Phys. Fluids*, 29(899), 1986.

[59] R. J. La Haye and O. Sauter. Treshold for metastable tearing modes in diii-d. *Nucl. Fusion*, 38(987), 1998.

[60] W. A. Hornsby, A. G. Peeters, A. P. Snodin, F. J. Casson, Y. Camenen, G. Szepesi, M. Siccinio, and E. Poli. The nonlinear coupling between gyroradius scale turbulence and mesoscale magnetic islands in fusion plasmas. *Phys. Plasmas*, 17(092301), 2010.

[61] R. J. Hawryluk. An empirical approach to tokamak transport. *Physics of Plasmas close to thermonuclear conditions*, 1, 1980.

[62] S. Inagaki, N. Tamura, K. Ida, Y. Nagayama, K. Kawahata, S. Sudo, T. Morisaki, K. Tanaka, T. Tokuzawa, , and the LHD Experimental Group. Observation of reduced heat transport inside the magnetic island o point in the large helical device. *Phys. Rev. Lett.*, 92(5):055002, 2004.

[63] G.W. Spakman, G.M.D. Hogeweij, R.J.E. Jaspers, F.C. Schuller, E. Westerhof, J.E. Boom, I.G.J. Classen, E. Delabie, C. Domier, A.J.H. Donn'e, M.Yu. Kantor, A. Krämer-Flecken, Y. Liang, N.C. Luhmann Jr, H.K. Park, M.J. van de Pol, O. Schmitz, J.W. Oosterbeek, and the TEXTOR Team. Heat pulse propagation studies around magnetic islands induced by the dynamic ergodic divertor in textor. *Nucl. Fusion*, 48(115005), 2008.

[64] K. Ida, K. Kamiya, A. Isayama, Y. Sakamoto, and JT-60 Team. Reduction of ion thermal diffusivity inside a magnetic island in jt-60u tokamak plasma. *Phys. Rev. Lett.*, 109(065001), 2012.

[65] C. Ren, J. D. Callen, T. A. Gianakon, C. C. Hegna, Z. Chang, E. D. Fredrickson, K. M. McGuire, G. Taylor, and M. C. Zarnstorff. Measuring δ' from electron temperature fluctuations in the tokamak fusion test reactor. *Phys. Plasmas*, 5(450), 1998.

[66] J. P. Meskat, H. Yohm, G. Gantenbein, S. Gunter, M. Maraschek, W. Suttrop, Q. Yu, and ASDEX Upgrade Team. Analysis of the structure of neoclassical tearing modes in asdex upgrade. *Plasma Phys. Control. Fusion*, 43(1325), 2001.

[67] M. Holzl, S. Gunter, I.G.J. Classen, Q. Yu, the TEXTOR Team, and E. Delabie. Determination of the heat diffusion anysotropy by comparing measured and simulated electron temperature profiles across magnetic islands. *Nucl. Fusion*, 49(115009), 2009.

[68] J. A. Snape, K. J. Gibson, T. O'Gorman, N. C. Barratt, K. Imada, H. R. Wilson, G. J. Tallents, I. T. Chapman, and the MAST team. The influence of finite radial transport on the structure and evolution of m/n=2/1 neoclassical tearing modes on mast. *Plasma Phys. Control. Fusion*, 54(085001), 2012.

[69] M. J. Choi, G. S. Yun, W. Lee, H. K. Park, Y.-S. Park, S. A. Sabbagh, K. J. Gibson, C. Bowman, C. W. Domier, N. C. Luhmann Jr., J.-G. Bak, S. G. Lee, and the KSTAR Team. Improved accuracy in the estimation of the tearing mode stability parameters using 2d ecei data in kstar. *Nucl. Fusion*, 54(083010), 2014.

[70] K. Ida, S. Inagaki, N. Tamura, T. Morisaki, and N. Ohyabu. Radial electric field and transport near the rational surface and the magnetic island in lhd. *Nucl. Fusion*, 44(290-295), 2004.

[71] Genaral atomics - diii-d diagnostics, 2016.

[72] E. J. Strait. Magnetic diagnostic system of the diii-d tokamak. *Rev. Sci. Instrum*, 77(023502), 2006.

[73] C. M. Celata and D. A. Boyd. Cyclotron radiation as a diagnostic tool for tokamak plasmas. *Nuclear Fusion*, 17(4), 1977.

[74] M. Bornatici, R. Cano, O. De Barbieri, and F. Engelmann. Electron cyclotron emission and absorption in fusion plasmas. *Nucl. Fusion*, 23(9), 1983.

[75] T. N. Carlstrom, G. L. Campbell, J. C. DeBoo, R. Evanko, J. Evans, C. M. Greenfield, J. Haskovec, C. L. Hsieh, E. McKee, R. T. Snider, R. Stockdale, P. K. Trost, and M. P. Thomas. Design and operation of the multipulse thomson scattering diagnostic on diii-d. *Rev. Sci. Instrum*, 63(10):4901–4906, 1992.

[76] L.L. Lao, J.R. Ferron, R.J. Groebner, W. Howl, H. St. John, E.J. Strait, and T.S. Taylor. Equilibrium analysis of current profiles in tokamaks. *Nuclear Fusion*, 30:1035, 1990.

[77] M. E. Austin and J. Lohr. Electron cyclotron emission radiometer upgrade on the diii-d tokamak. *Rev. Sci. Instrum.*, 74:1457, 2003.

[78] T. L. Rhodes, W. A. Peebles, , X. Nguyen, M. A. VanZeeland, J. S. deGrassie, E. J. Doyle, G. Wang, and L. Zeng. Millimeter-wave backscatter diagnostic for the study of short scale length plasma fluctuations (invited). *Rev. Sci. Instrum.*, 77(10E922), 2006.

[79] G. R. McKee, R. J. Fonck, M. W. Shafer, I. U. Uzun-Kaymak, and Z. Yan. Wide-field turbulence imaging with beam emission spectroscopy. *Rev. Sci. Instrum.*, 81(10D741), 2010.

[80] P. Hennequin, C. Honore, A.Truc, A.Quemeneur, C. Fenzi-Bonizec, C. Bourdelle, X. Garbet, G.T. Hoang, and the Tore Supra team. Fluctuation spectra and velocity profile from doppler backscattering on tore supra. *Nuclear Fusion*, 46:S771–S779, 2006.

[81] J. C. Hillesheim, W. A. Peebles, T. L. Rhodes, L. Schmitz, T. A. Carter, P.-A. Gourdain, and G. Wang. A multichannel, frequency-modulated, tunable doppler backscattering and reflectometry system. *Rev. Sci. Instrum*, 80:083507, 2009.

[82] W. A. Peebles, T. L. Rhodes, J. C. Hillesheim, L. Zeng, and C. Wannberg. A novel, multichannel, comb-frequency doppler backscatter system. *Rev. Sci. Instrum*, 81:10D902, 2010.

[83] A. P. Smirnov and R. W. Harvey. The genray ray tracing code. *CompX Report*, pages 2000–1, 2001.

[84] C. Sung, W. A. Peebles, C. Wannberg, T. L. Rhodes, X. Nguyen, R. Lantsov, and L. Bardóczi. A frequency tunable, eight-channel correlation ece system for electron temperature turbulence measurements on the diii-d tokamak. *Rev. Sci. Instrum.*, 87(11E123), 2016.

[85] C. Watts. A review of ece correlation radiometry techniques for detection of core electron temperature fluctuations. *Fusion Science and Technology*, 52(176), 2007.

[86] L. Bardóczi, T. L. Rhodes, T. A. Carter, A. Bañón Navarro, W. A. Peebles, F. Jenko, and G. McKee. Modulation of core turbulent density fluctuations by large-scale neoclassical tearing mode islands in the diii-d tokamak. *Phys. Rev. Lett.*, 116:215001, May 2016.

[87] L. Bardóczi, T. L. Rhodes, A. Ba non Navarro, C. Sung, T. A. Carter, R. J. La Haye, C. Petty, C. Crystal, and F. Jenko. Multi-field/-scale interactions of turbulence with neoclassical tearing mode magnetic islands in the diii-d tokamak. *Phys. Plasmas - invited (accepted)*, 24(056106), 2017.

[88] L. Bardóczi, T. L. Rhodes, T. A. Carter, W. A. Peebles, and G. McKee. Shrinking of core neoclassical tearing mode magnetic islands due to edge localized modes and the role of low-k turbulence in island recovery in diii-d. *Phys. Plasmas (to be submitted)*, 2017.

[89] S. A. Orszag. Comparison of pseudospectral and spectral approximation. *Studies in Applied Mathematics*, 51:253–259, 1972.

[90] T S Hahm, P H Diamond, Z Lin, K Itoh, and S-I Itoh. Turbulence spreading into the linearly stable zone and transport scaling. *Plasma Phys. Control. Fusion*, 46(A323–A333), 2004.

[91] M. A. Van Zeeland, R. L. Boivin, T. N. Carlstrom, T. Deterly, and D. K. Finkenthal. Fiber optic two-color vibration compensated interferometer for plasma density measurements. *Rev. Sci. Instrum*, 77(10F325), 2006.

[92] K. H. Burrell, P. Gohil, R. J. Groebner, D. H. Kaplan, J. I. Robinson, and W. M. Solomon. Improved charge-coupled device detectors for high-speed, charge exchange spectroscopy studies on the diii-d tokamak. *Rev. Sci. Instrum*, 75(10):3455, 2004.

[93] R. Fitzpatrick. Phase locking of multi-helicity neoclassical tearing modes in tokamak plasmas. *Phys. Plasmas*, 22(042514), 2015.

[94] B. Tobias, B. A. Grierson, C. M. Muscatello, X. Ren, C. W. Domier, N. C. Luhmann Jr., S. E. Zemedkun, T. L. Munsat, and I. G. J. Classen. Phase-locking of magnetic islands diagnosed by ece-imaging. *Rev. Sci. Instrum*, 85(11D847), 2014.

[95] Julius S. Bendat and Allan G. Piersol. *Random Data: Analysis and Measurement Procedures*. Willey, 4th edition, March 2010.

[96] A. Ishizawa and N. Nakajima. Turbulence driven magnetic reconnection causing long-wavelength magnetic islands. *Phys. Plasmas*, 17(072308), 2010.

[97] Olivier Izacard, Christopher Holland, Spencer D. James, and Dylan P. Brennan. Dynamics of ion temperature gradient turbulence and transport with a static magnetic island. *Phys. Plasmas*, 23(022304), 2016.

[98] S. Zoeltnik and A. Bencze. Autocorrelation analysis and statistical consideration for the determination of velocity fluctuations in fusion plasmas. *Phys. Plasmas*, 12(052323), 2005.

[99] J. D. Callen Z. Chang. lobal energy confinement degradation due to macroscopic phenomena in tokamaks. *Nucl. Fusion*, 30(2), 1990.

[100] P. H. Rutherdord. Nonlinear growth of the tearing mode. *Phys. Fluids*, 16:1903, 1973.

[101] J. D. King, R. J. La Haye, C. C. Petty, T. H. Osborne, C. J. Lasnier, R. J. Groebner, F. A. Volpe, M. J. Lanctot, M. A. Makowski, C. T. Holcomb, W. M. Solomon, S. L. Allen, T. C. Luce, M. E. Austin, W. H. Meyer, and E. C. Morse. Hybrid-like 2/1

flux-pumping and magnetic island evolution due to edge localized mode-neoclassical tearing mode coupling in diii-d. *Phys. Plasmas*, 19(022503), 2012.

[102] G. McKee, R. Ashley, R. Durst, R. Fonck, M. Jakubowski, K. Tritz, K. Burrell, C. Greenfield, and J. Robinson. The beam emission spectroscopy diagnostic on the diii-d tokamak. *Rev. Sci. Instrum.*, 70(913), 1999.

[103] C. C. Petty, M. E. Austin, C. T. Holcomb, R. J. Jayakumar, R. J. La Haye, T. C. Luce, M. A. Makowski, P. A. Politzer, and M. R. Wade. Magnetic-flux pumping in high-performance, stationary plasmas with tearing modes. *Phys. Rev. Lett.*, 102(045005), 2009.

[104] J. C. Hillesheim, J. C. DeBoo, W. A. Peebles, T. A. Carter, G. Wang, T. L. Rhodes, L. Schmitz, G. R. McKee, Z. Yan, G. M. Staebler, K. H. Burrell, E. J. Doyle, C. Holland, C. C. Petty, S. P. Smith, A. E. White, and L. Zeng. Observation of a critical gradient threshold for electron temperature fluctuations in the diii-d tokamak. *Phys. Rev. Lett.*, 110(045003), 2013.

[105] J. C. DeBoo, C. C. Petty, A. E. White, K. H. Burrell, E. J. Doyle, J. C. Hillesheim, C. Holland, G. R. McKee, T. L. Rhodes, L. Schmitz, S. P. Smith, G. Wang, and L. Zeng. Electron profile stiffness and critical gradient studies. *Phys. Plasmas*, 19(082518), 2012.

[106] E. J. Strait, A. M. Garofalo, G. L. Jackson, M. Okabayashi, H. Reimerdes, M. S. Chu, R. Fitzpatrick, R. J. Groebner, Y. In, R. J. LaHaye, M. J. Lanctot, Y. Q. Liu, G. A. Navratil, W. M. Solomon, H. Takahashi, and the DIII-D Team. Resistive wall mode stabilization by slow plasma rotation in diii-d tokamak discharges with balanced neutral beam injection. *Phys. Plasmas*, 14(056101), 2007.